



universität  
wien

# DISSERTATION

Titel der Dissertation

The linear response function in density functional theory:  
Optical spectra and improved description of the electron correlation

angestrebter akademischer Grad

Doktorin der Naturwissenschaften (Dr. rer.nat.)

Verfasserin:	Mag. rer. nat. Judith Harl
Matrikel-Nummer:	9806788
Dissertationsgebiet:	Physik
Betreuer:	Univ.-Prof. Dipl.-Ing. Dr. Georg Kresse

Wien, am 31. Oktober 2008



# Abstract

The linear response function, which describes the change in the electron density induced by a change in the external potential, is the basis for a broad variety of applications. Three of these are addressed in the present thesis. In the first part, optical spectra of metallic surfaces are investigated. Quasiparticle energies, i.e., energies required to add or remove an electron from a system, are evaluated for selected metals in the second part. The final part of this thesis is devoted to an improved description of the ground-state electron correlation energy.

In the first part, the linear response function is used to evaluate optical properties of metallic surfaces. In recent years, reflectance difference (RD) spectroscopy has provided a sensitive experimental method to detect changes in the surface structure and morphology. The interpretation of the resulting spectra, which are linked to the anisotropy of the surface dielectric tensor, however, is often difficult. In the present thesis, we simulate RD spectra for the bare, as well as oxygen and carbon monoxide covered, Cu(110) surface, and assign features in these spectra to the corresponding optical transitions. A good qualitative agreement between our RD spectra and the experimental data is found.

Density functional theory (DFT) gives only access to the ground state energy. Quasiparticle energies should, however, be addressed within many body perturbation theory. In the second part of this thesis, we investigate quasiparticle energies for the transition metals Cu, Ag, Fe, and Ni using the Green's function based GW approximation, where the screened Coulomb interaction  $W$  is linked to the linear response function.

The fundamental limitation of density function theory is the approximation of the exchange-correlation energy. An exact expression for the exchange-correlation energy can be found by the adiabatic-connection fluctuation-dissipation theorem (ACFDT), linking the linear response function to the electron correlation energy. This expression has been implemented in the Vienna Ab-initio Simulation Package (VASP). Technical issues and ACFDT results obtained for molecules and extended systems, are addressed in the third and last part of this thesis. Although we make use of the random phase approximation (RPA), we find that the correct long-range van der Waals interaction for rare gas solids is reproduced and geometrical properties for insulators, semiconductors, and metals are in very good agreement with experiment. Atomization energies, however, are not significantly improved compared to standard DFT functionals like PBE.



# Zusammenfassung

Die Polarisationsfunktion, welche die lineare Dichteänderung durch eine kleine Änderung des äußeren Potentials beschreibt, ist die Grundlage zur Berechnung der unterschiedlichsten physikalischen Größen. Drei davon werden im Rahmen dieser Dissertation untersucht. Zuerst werden optische Spektren von metallischen Oberflächen berechnet. Im zweiten Teil werden für ausgewählte Metalle Quasiteilchenenergien berechnet, also diejenigen Energien, welche benötigt werden, um ein Elektron aus dem System zu entfernen bzw. hinzuzufügen. Der dritte Teil ist schließlich einer verbesserten Beschreibung der elektronischen Korrelationsenergie gewidmet.

Im ersten Teil dieser Dissertation werden optische Spektren von metallischen Oberflächen mit Hilfe der Polarisationsfunktion berechnet. In den letzten Jahren erwies sich die *reflectance difference* (RD) Spektroskopie als eine experimentelle Methode, die sehr empfindlich auf Änderungen der Oberflächenstruktur reagiert. Eine Interpretation der RD Spektren, welche auf die Anisotropie des dielektrischen Oberflächentensors zurückgehen, ist allerdings oftmals schwierig. Um eine Interpretation zu erleichtern, berechnen wir die RD Spektren sowohl für die reine, als auch für die Sauerstoff und Kohlenmonoxid bedeckte Cu(110) Oberfläche. Die berechneten Daten stimmen gut mit den experimentellen Werten überein und erlauben eine genaue Analyse der Spektren in Bezug auf die zugrunde liegenden optischen Übergänge.

Die Dichtefunktionaltheorie erlaubt allein die Bestimmung der Grundzustandsenergie. Zur Berechnung der Quasiteilchenenergien muss jedoch die Vielteilchenstörungstheorie herangezogen werden. Im zweiten Teil dieser Dissertation werden Quasiteilchenenergien für die Übergangsmetalle Cu, Ag, Fe und Ni berechnet. Dabei wird die auf der Greensfunktion basierende GW Näherung verwendet, wobei  $W$ , die abgeschirmte Coulombwechselwirkung, von der Polarisationsfunktion abhängt.

Das Fehlen einer exakten Beschreibung der Austausch- und Korrelationsenergie ist die fundamentale Schwachstelle der Dichtefunktionaltheorie. Ein exakter Ausdruck dieser Energie kann allerdings mit Hilfe des *adiabatic-connection fluctuation-dissipation* Theorems (ACFDT) aufgestellt werden. Dabei wird die Korrelationsenergie in Abhängigkeit von der Polarisationsfunktion dargestellt. Routinen zur Berechnung der ACFDT Korrelationsenergie wurden im *Vienna Ab-Initio Simulation Package* (VASP) implementiert. Details zur Implementierung und Ergebnisse für molekulare und ausgedehnte Systeme werden im dritten und letzten Teil dieser Dissertation behandelt. Obwohl die ACFDT Korrelationsenergie nur näherungsweise mit Hilfe der *random phase approximation* (RPA) berechnet wird, wird die langreichweitige van der Waals Wechselwirkung für Edeltgaskristalle richtig wiedergegeben, und die ACFDT Geometrien von Isolatoren, Halbleitern und Metallen stimmen sehr gut mit den experimentellen Werten überein.



# Contents

<b>Abstract</b>	<b>iii</b>
<b>I Theory</b>	<b>1</b>
<b>1 Density functional theory</b>	<b>5</b>
1.1 Theorem of Hohenberg-Kohn . . . . .	5
1.2 Kohn-Sham density functional theory . . . . .	5
1.3 DFT in practice . . . . .	8
1.3.1 Plane waves . . . . .	8
1.3.2 Projector augmented wave method . . . . .	8
<b>2 Optical properties within linear response theory</b>	<b>12</b>
2.1 Time-dependent density functional theory . . . . .	12
2.2 Linear response theory . . . . .	13
2.3 Dielectric function - macroscopic continuum considerations . . . . .	18
2.4 Macroscopic and microscopic quantities . . . . .	19
2.5 Longitudinal dielectric function . . . . .	21
2.6 Approximations . . . . .	22
2.7 Calculation of optical properties . . . . .	23
2.7.1 PAW response function . . . . .	25
2.7.2 Long-wavelength dielectric function . . . . .	27
2.8 Intraband transitions and the plasma frequency . . . . .	28
2.9 f-sum rule and interband transitions at small energies . . . . .	32
<b>3 Total energies from linear response theory</b>	<b>35</b>
3.1 Adiabatic connection dissipation-fluctuation theorem . . . . .	36
3.1.1 Adiabatic connection . . . . .	36
3.1.2 Fluctuation-dissipation theorem . . . . .	37
3.2 Random phase approximation . . . . .	40
3.3 Calculating the RPA correlation energy in practice . . . . .	41
<b>4 GW quasiparticle energies</b>	<b>44</b>
4.1 The GW approximation . . . . .	45
4.2 Solving the quasiparticle equation . . . . .	46

<b>II</b>	<b>Reflectance difference spectra</b>	<b>49</b>
<b>5</b>	<b>Calculating reflectance difference spectra</b>	<b>51</b>
5.1	Three-phase model . . . . .	51
5.2	Calculation of the dielectric function . . . . .	55
<b>6</b>	<b>Optical properties of bulk systems</b>	<b>58</b>
6.1	Plasma frequencies . . . . .	58
6.2	Dielectric function of bulk copper . . . . .	59
6.2.1	Bands . . . . .	60
6.2.2	$k$ -point convergence . . . . .	61
6.2.3	Hilbert transformation . . . . .	62
6.2.4	Final form of bulk dielectric function and comparison . . . . .	63
<b>7</b>	<b>Optical calculations for Cu(110) surfaces</b>	<b>66</b>
7.1	Geometry of surfaces . . . . .	66
7.2	Convergence tests . . . . .	68
7.2.1	Vacuum . . . . .	69
7.2.2	$k$ -points . . . . .	70
7.2.3	Interband transitions at small frequencies . . . . .	70
7.2.4	Number of layers . . . . .	72
7.3	RDS spectra and interpretation . . . . .	73
7.3.1	Band Structure . . . . .	75
7.3.2	Reflectance difference spectra . . . . .	78
<b>8</b>	<b>Conclusions and Summary</b>	<b>83</b>
<b>III</b>	<b>GW calculations</b>	<b>85</b>
<b>9</b>	<b>Quasiparticle energies for metals</b>	<b>86</b>
9.1	Noble metals - Cu and Ag . . . . .	86
9.2	Ferromagnets: Fe, Ni . . . . .	92
<b>IV</b>	<b>Total energies from ACFDT</b>	<b>99</b>
<b>10</b>	<b>Implementation of the ACFDT routines</b>	<b>101</b>
10.1	Dependence on dimension of the response function . . . . .	102
10.2	Frequency integration . . . . .	106
10.3	$k$ -point convergence and $\Gamma$ -point correction for metals . . . . .	109
10.3.1	$\Gamma$ -point corrections: Technical details . . . . .	111
<b>11</b>	<b>Application of the ACFDT</b>	<b>114</b>
11.1	Molecules - H <sub>2</sub> , O <sub>2</sub> , N <sub>2</sub> . . . . .	114
11.2	Rare-gas solids - Ne, Ar, Kr . . . . .	117
11.3	Homogenous electron gas . . . . .	122



---

11.4 Metals - Na, Al, Cu, Rh, Pd . . . . .	125
11.5 Solids . . . . .	130
11.5.1 Lattice constants and bulk moduli . . . . .	133
11.5.2 Atomization energies . . . . .	143
<b>12 Conclusions and Summary</b>	<b>150</b>
<b>Bibliography</b>	<b>153</b>
<b>List of Publications</b>	<b>161</b>
<b>Acknowledgments</b>	<b>163</b>
<b>Curriculum vitae</b>	<b>165</b>



# **Part I**

# **Theory**

The non-relativistic Schrödinger equation for  $N$  electrons moving in an external potential  $v_{\text{ext}}$  considering decoupling of ionic and electronic degrees of freedom (Born-Oppenheimer approximation) is given as:

$$\left( -\frac{\hbar^2}{2m} \sum_{i=1}^N \nabla_{\mathbf{r}_i}^2 + \frac{1}{2} \sum_{i \neq j} \frac{e^2}{|\mathbf{r}_i - \mathbf{r}_j|} + \sum_i v_{\text{ext}}(\mathbf{x}_i, \{\mathbf{R}\}) + E_{\text{ion}}(\{\mathbf{R}\}) \right) \Psi(\{\mathbf{x}\}) = E(\{\mathbf{R}\}) \Psi(\{\mathbf{x}\}), \quad (1)$$

where the electron energy is parametric depending on the ionic coordinates  $\{\mathbf{R}\}$  and  $\mathbf{x} = (\mathbf{r}, s)$  denotes both electron positions and spins. In the further discussion we will consider "spinless" electrons. Furthermore, we neglect the  $E_{\text{ion}}$  term, which describes the electrostatic interaction between the positive ions and which is constant for a fixed ionic configuration. The electronic Hamiltonian then reads:

$$\begin{aligned} \hat{H} &= -\frac{\hbar^2}{2m} \sum_{i=1}^N \nabla_{\mathbf{r}_i}^2 + \frac{1}{2} \sum_{i \neq j} \frac{e^2}{|\mathbf{r}_i - \mathbf{r}_j|} + \sum_i v_{\text{ext}}(\mathbf{r}_i) \\ &= \hat{T} + \hat{V}_{ee} + \hat{V}_{\text{ext}}. \end{aligned} \quad (2)$$

Instead of solving this eigenvalue problem, the ground state energy  $E_{\text{GS}}$  can be obtained by minimizing

$$\langle \Psi | \hat{H} | \Psi \rangle \quad \text{under the constraint} \quad \langle \Psi | \Psi \rangle = 1. \quad (3)$$

Such a minimization over the space of many-electron wavefunctions

$$\Psi(\{\mathbf{r}\}) = \Psi(\mathbf{r}_1, \mathbf{r}_2, \dots, \mathbf{r}_N) \quad (4)$$

is only possible for system containing a few electrons. For a larger number of electrons, the complexity of the electron problem becomes intractable due to the large number of degrees of freedom involved. It is therefore desirable to search for quantities of lower dimension which define the ground state energy uniquely. One possible quantity is the electron density

$$n(\mathbf{r}) = N \int d^3 r_2 d^3 r_3 \dots d^3 r_N \Psi^*(\mathbf{r}, \mathbf{r}_2, \dots, \mathbf{r}_N) \Psi(\mathbf{r}, \mathbf{r}_2, \dots, \mathbf{r}_N) \quad (5)$$

which can also be written as

$$n(\mathbf{r}) = \langle \Psi | \hat{n}(\mathbf{r}) | \Psi \rangle \quad \text{with the density operator} \quad \hat{n}(\mathbf{r}) = \sum_i^N \delta(\mathbf{r} - \mathbf{r}_i). \quad (6)$$

The density  $n(\mathbf{r})$  describes the probability to find an electron at place  $\mathbf{r}$ , if all other electrons are located at any place, and it, therefore, contains much less information than the full many-body wavefunction  $\Psi(\{\mathbf{r}\})$ . It is not straightforward that the ground state energy can be expressed as a quantity solely depending on the density. This can only be the case if different external potentials inevitably result in different densities for a  $N$  electron system. The validity of this requirement has been first proven by Hohenberg and Kohn [1] in 1964. A more general proof was provided by Levy in 1979 [2]. On these foundations all methods summarized under the name "density functional theories" are based. We will later come back

to the theorem of Hohenberg and Kohn and to its practical realization as proposed by Kohn and Sham [3].

But also for the straightforward evaluation of the ground state energy, the entire many-body wavefunction is not required. Three parts contribute to the electronic energy

$$E = \underbrace{\langle \Psi | \hat{T} | \Psi \rangle}_{\text{kinetic energy}} + \underbrace{\langle \Psi | \hat{V}_{ee} | \Psi \rangle}_{\text{e-e interaction}} + \underbrace{\langle \Psi | \hat{V}_{\text{ext}} | \Psi \rangle}_{\text{external potential}}. \quad (7)$$

The energy resulting from the external potential,  $\langle \Psi | \hat{V}_{\text{ext}} | \Psi \rangle$ , is given as

$$\begin{aligned} \langle \Psi | \hat{V}_{\text{ext}} | \Psi \rangle &= \sum_{i=1}^N \int d^3 r_1 \dots d^3 r_N \Psi^*(\mathbf{r}_1, \mathbf{r}_2, \dots, \mathbf{r}_N) v_{\text{ext}}(\mathbf{r}_i) \Psi(\mathbf{r}_1, \mathbf{r}_2, \dots, \mathbf{r}_N) = \\ &= N \int d^3 r d^3 r_2 \dots d^3 r_N \Psi^*(\mathbf{r}, \mathbf{r}_2, \dots, \mathbf{r}_N) v_{\text{ext}}(\mathbf{r}) \Psi(\mathbf{r}, \mathbf{r}_2, \dots, \mathbf{r}_N) = \\ &= \int d^3 r v_{\text{ext}}(\mathbf{r}) n(\mathbf{r}) \end{aligned} \quad (8)$$

and is consequently only depending on the electron density  $n(\mathbf{r})$ . The kinetic energy is also a "one-electron" quantity:

$$\begin{aligned} \langle \Psi | \hat{T} | \Psi \rangle &= -\frac{\hbar^2}{2m} \sum_{i=1}^N \int d^3 r_1 d^3 r_2 \dots d^3 r_N \Psi^*(\mathbf{r}_1, \mathbf{r}_2, \dots, \mathbf{r}_N) \nabla_{\mathbf{r}_i}^2 \Psi(\mathbf{r}_1, \mathbf{r}_2, \dots, \mathbf{r}_N) = \\ &= -\frac{N\hbar^2}{2m} \int d^3 r' d^3 r d^3 r_2 \dots d^3 r_N \delta(\mathbf{r} - \mathbf{r}') \Psi^*(\mathbf{r}', \mathbf{r}_2, \dots, \mathbf{r}_N) \nabla_{\mathbf{r}}^2 \Psi(\mathbf{r}, \mathbf{r}_2, \dots, \mathbf{r}_N) \\ &= -\frac{\hbar^2}{2m} \int d^3 r' d^3 r \delta(\mathbf{r} - \mathbf{r}') \nabla_{\mathbf{r}}^2 \gamma(\mathbf{r}, \mathbf{r}') = -\frac{\hbar^2}{2m} \int d^3 r [\nabla_{\mathbf{r}}^2 \gamma(\mathbf{r}, \mathbf{r}')]_{\mathbf{r}'=\mathbf{r}} \end{aligned} \quad (9)$$

where  $\gamma(\mathbf{r}, \mathbf{r}')$  is the one-particle density matrix:

$$\gamma(\mathbf{r}, \mathbf{r}') = N \int d^3 r_2 d^3 r_3 \dots d^3 r_N \Psi^*(\mathbf{r}', \mathbf{r}_2, \dots, \mathbf{r}_N) \Psi(\mathbf{r}, \mathbf{r}_2, \dots, \mathbf{r}_N). \quad (10)$$

The remaining term, the electron-electron interaction, links the coordinates of every two electrons:

$$\begin{aligned} \langle \Psi | \hat{V}_{ee} | \Psi \rangle &= \frac{1}{2} \sum_{i \neq j} \int d^3 r_1 d^3 r_2 \dots d^3 r_N \Psi^*(\mathbf{r}_1, \mathbf{r}_2, \dots, \mathbf{r}_N) \frac{e^2}{|\mathbf{r}_i - \mathbf{r}_j|} \Psi(\mathbf{r}_1, \mathbf{r}_2, \dots, \mathbf{r}_N) = \\ &= \frac{N(N-1)}{2} \int d^3 r_1 d^3 r_2 \frac{e^2}{|\mathbf{r}_1 - \mathbf{r}_2|} \int d^3 r_3 \dots d^3 r_N \Psi^*(\mathbf{r}_1, \mathbf{r}_2, \dots, \mathbf{r}_N) \Psi(\mathbf{r}_1, \mathbf{r}_2, \dots, \mathbf{r}_N) = \\ &= \frac{e^2}{2} \int d^3 r_1 d^3 r_2 \frac{n^2(\mathbf{r}_1, \mathbf{r}_2)}{|\mathbf{r}_1 - \mathbf{r}_2|} \end{aligned} \quad (11)$$

where  $n^2(\mathbf{r}_1, \mathbf{r}_2)$  is the pair density which can be defined as the trace of the two-electron density matrix,  $n^2(\mathbf{r}_1, \mathbf{r}_2) = \Gamma(\mathbf{r}_1, \mathbf{r}_2; \mathbf{r}_1, \mathbf{r}_2)$ :

$$\Gamma(\mathbf{r}_1, \mathbf{r}_2; \mathbf{r}'_1, \mathbf{r}'_2) = N(N-1) \int d^3 r_3 \dots d^3 r_N \Psi^*(\mathbf{r}_1, \mathbf{r}_2, \dots, \mathbf{r}_N) \Psi(\mathbf{r}'_1, \mathbf{r}'_2, \dots, \mathbf{r}_N). \quad (12)$$

If the classical electrostatic energy (Hartree-Term)

$$E_H = \frac{e^2}{2} \int d^3r d^3r' \frac{n(\mathbf{r}) n(\mathbf{r}')}{|\mathbf{r} - \mathbf{r}'|} \quad (13)$$

is subtracted from  $\langle \Psi | \hat{V}_{ee} | \Psi \rangle$  and the exchange-correlation hole  $n_{xc}(\mathbf{r}_1, \mathbf{r}_2)$  is introduced

$$n_{xc}(\mathbf{r}_1, \mathbf{r}_2) = \frac{n^2(\mathbf{r}_1, \mathbf{r}_2)}{n(\mathbf{r}_1)} - n(\mathbf{r}_2) \quad (14)$$

the total energy of the electronic system reads

$$E = -\frac{\hbar^2}{2m} \int d^3r [\nabla_{\mathbf{r}}^2 \gamma(\mathbf{r}', \mathbf{r})]_{\mathbf{r}'=\mathbf{r}} + \frac{e^2}{2} \int d^3r d^3r' \frac{n(\mathbf{r}) n(\mathbf{r}')}{|\mathbf{r} - \mathbf{r}'|} + \frac{e^2}{2} \int d^3r d^3r' \frac{n(\mathbf{r}) n_{xc}(\mathbf{r}, \mathbf{r}')}{|\mathbf{r} - \mathbf{r}'|} + \int d^3r v_{\text{ext}}(\mathbf{r}) n(\mathbf{r}). \quad (15)$$

This suggests that there should be ways to calculate the energy without considering the whole many-body wavefunction. Besides the already mentioned density functional theories (DFT), methods based on the pair density  $n^2(\mathbf{r}_1, \mathbf{r}_2)$  and the two-electron density matrix  $\Gamma(\mathbf{r}_1, \mathbf{r}_2; \mathbf{r}'_1, \mathbf{r}'_2)$  have been considered. Whereas in DFT the exact density dependent form for the kinetic energy term and the electron-electron interaction is not known, theories based on the pair density lack an exact expression for the kinetic energy term only (see e.g., [4]). Introducing the two-electron density matrix  $\Gamma(\mathbf{r}_1, \mathbf{r}_2; \mathbf{r}'_1, \mathbf{r}'_2)$  lifts this problem, but the  $N$ -representability problem (which conditions must a two-electron density matrix obey to be derived from a many-body wavefunction) comes to the fore (e.g., [5]).

# Chapter 1

## Density functional theory

### 1.1 Theorem of Hohenberg-Kohn

The term density functional theory (DFT) refers to all methods that express the ground-state energy as a functional of the electronic density  $n(\mathbf{r})$ . The validity of such an approach was first proven by Hohenberg and Kohn in 1964 [1] and later generalized by Levy [2]. Hohenberg and Kohn introduced the energy functional

$$E_{HK}[n] := F[n] + \int d^3r n(\mathbf{r}) v(\mathbf{r}) \quad F[n] := \min_{\Psi \rightarrow n} \langle \Psi | \hat{T} + \hat{V}_{ee} | \Psi \rangle \quad (1.1)$$

and proved that

1.  $F[n]$  is a unique functional of the density  $n(\mathbf{r})$  i.e., for an  $N$  electron system, there do not exist two ground state wavefunctions  $\Psi_1 \neq \Psi_2$  (potentials  $v_1 \neq v_2$ ) resulting in the same density  $n(\mathbf{r})$ .

2.

$$E_{HK}[n] \geq E_{GS}$$

The energy functional  $E_{HK}$  obeys a variational principle and always results in energies larger or equal to the ground state energy  $E_{GS}$ .

3.

$$E_{HK}[n_{GS}] = E_{GS}$$

The energy functional  $E_{HK}$  reaches the ground state energy at the ground state density  $n_{GS}$ .

### 1.2 Kohn-Sham density functional theory

The Hohenberg-Kohn (HK) theorem provides a theoretical justification for the construction of an energy functional that depends on the electron density only, but it does not provide a concrete expression for the energy functional  $F[n] = \min_{\Psi \rightarrow n} \langle \Psi | \hat{T} + \hat{V}_{ee} | \Psi \rangle$ . Actually, density functionals as the Thomas-Fermi functional [6, 7] have been used before the HK theorem. In the Thomas-Fermi functional three terms are considered: the classical electron-electron

repulsion (Hartree term), the energy resulting from the external potential, and a kinetic energy term, which is approximated in a local density approximation by the kinetic energy of the homogenous electron gas  $\propto n^{1/3}$ . This approximation allowed an exact mathematical treatment of the resulting integral equation, but it could also be shown [8, 9] that binding of atoms to form molecules and solids can not be described within Thomas-Fermi theory.

In 1965, Kohn and Sham [3] proposed a different approximation for the functional  $F[n]$  that maps the problem of a system of interacting particles onto a system of independent electrons with the same density  $n(\mathbf{r})$  moving in an effective local potential that mimics the influence of the other electrons. The energy of an electron system [Eq. (7)] can be reformulated to

$$E[n] = T_s[n] + E_H[n] + E_{xc}[n] + E_{\text{ext}}[n] \quad \text{with}$$

$$E_{xc}[n] := \langle \Psi_{MB} | \hat{T} | \Psi_{MB} \rangle - T_s[n] + \langle \Psi_{MB} | \hat{V}_{ee} | \Psi_{MB} \rangle - E_H[n]. \quad (1.2)$$

The wavefunction of the true, interacting, system is thereby denoted as  $\Psi_{MB}$ , whereas the wavefunction of the reference system of independent particles is a Slater determinant built from one-electron wavefunctions  $\{\psi_n\}$ . The independent particle kinetic energy  $T_s[n] = -\hbar^2/2m \sum_{n(\text{occ})} \langle \psi_n | \nabla^2 | \psi_n \rangle$  thereby depends only implicitly on the electron density

$$n(\mathbf{r}) = 2 \sum_{n(\text{occ})} |\psi_n(\mathbf{r})|^2 \quad (1.3)$$

via the one-electron wavefunctions  $\psi_n$ . By introducing the Hartree potential

$$v_H[n](\mathbf{r}) = e^2 \int d^3r' \frac{n(\mathbf{r}')}{|\mathbf{r} - \mathbf{r}'|} \quad (1.4)$$

and the (abstract)  $\mu_{xc}[n](\mathbf{r})$  energy density per particle, the energy can also be written as

$$E[n] = T_s[n] + \underbrace{\int d^3r n(\mathbf{r}) \left[ \frac{1}{2} v_H[n](\mathbf{r}) + \mu_{xc}[n](\mathbf{r}) + v_{\text{ext}}(\mathbf{r}) \right]}_{v_{KS}[n](\mathbf{r})} \quad (1.5)$$

The ground state energy  $E_{GS}$  can be found by minimizing Eq. (1.5) with respect to the density  $n(\mathbf{r})$  or solving the so called Kohn-Sham equations:

$$\begin{aligned} \left( -\frac{\hbar^2}{2m} \nabla^2 + v_{KS}[n](\mathbf{r}) + \int d^3r' n(\mathbf{r}') \frac{\delta v_{KS}[n]}{\delta n(\mathbf{r}')} \right) \psi_n &= \epsilon_n \psi_n \\ \Downarrow \\ \left( -\frac{\hbar^2}{2m} \nabla^2 + \underbrace{v_H[n](\mathbf{r}) + v_{xc}[n](\mathbf{r}) + v_{\text{ext}}(\mathbf{r})}_{v_{\text{eff}}[n](\mathbf{r})} \right) \psi_n &= \epsilon_n \psi_n, \end{aligned} \quad (1.6)$$

where the exchange correlation potential  $v_{xc}[n](\mathbf{r})$  is defined as:

$$v_{xc}[n](\mathbf{r}) = \frac{\delta E_{xc}[n]}{\delta n(\mathbf{r})}. \quad (1.7)$$



Due to the dependence of the KS Hamiltonian on the density and thus on the wavefunctions themselves, Eq. (1.6) have to be solved selfconsistently. By introducing the occupation function  $f_n$ ,

$$f_n = \begin{cases} 1 & \text{if state } n \text{ is occupied} \\ 0 & \text{if state } n \text{ is unoccupied,} \end{cases} \quad (1.8)$$

the ground state energy  $E_{GS}$  can be written as

$$E_{GS} = 2 \sum_n f_n \epsilon_n - E_H[n_{GS}] - \int d^3r n_{GS}(\mathbf{r}) v_{xc}[n_{GS}](\mathbf{r}) + E_{xc}[n_{GS}] \quad (1.9)$$

with the ground state density

$$n_{GS}(\mathbf{r}) = 2 \sum_n f_n |\psi_n(\mathbf{r})|^2 \quad (1.10)$$

given by the wavefunctions solving Eq. (1.6).

By applying the Kohn-Sham density functional theory, the ground state energy and ground state density can thus be calculated by solving a set of one-electron Schrödinger equations. However, the exchange-correlation energy functional  $E_{xc}[n]$  or the exchange-correlation potential, respectively, have to be approximated. The earliest approach has been the so called local density approximation (LDA) [3], which assumes that the exchange-correlation energy can be locally approximated by the exchange-correlation energy density of the homogeneous electron gas  $\epsilon_{xc}^{\text{unif}}[n]$  (energy per particle) at the respective density:

$$E_{xc}[n(\mathbf{r})] = \int d^3r n(\mathbf{r}) \epsilon_{xc}^{\text{unif}}[n]. \quad (1.11)$$

The exchange-correlation energy of the homogenous electron gas has been calculated by Ceperley and Alder for a set of densities using quantum Monte Carlo methods [10]. The parametrisation of these energies suggested by Perdew and Wang [11] will be used in the following.

The LDA assumes that the exchange correlation energy of an inhomogenous system can be approximated at each point by the energy of a homogenous electron gas. In the more sophisticated generalized gradient approximation (GGA) not only the density but also the variation of the density, the density gradient, is considered for the calculation of the exchange-correlation energy

$$E_{xc}^{GGA}[n] = \int d^3r f(n, \nabla n). \quad (1.12)$$

GGA functionals can be either constructed as to fulfill (some) exact conditions, or by fitting to energies calculated on a higher level of theory or experimental values. The GGA introduced by Perdew, Burke, and Ernzerhof (PBE) [12], which is used in the present work, belongs to the first class of GGAs.

### 1.3 DFT in practice

In the present section, we will briefly describe how the Kohn-Sham equations are solved in the Vienna ab-initio simulation package (VASP) used throughout this thesis. More details about the plane wave approach can be found e.g., in the review of Payne *et al.* [13]. The PAW method is discussed in Ref. [14] and with respect to the VASP code in Ref. [15].

#### 1.3.1 Plane waves

For the actual solution of the Kohn-Sham equations the wavefunctions are usually expanded in a basis set. In our case, this basis set consists of plane waves. For a periodic system, each wavefunction can be written as a Bloch function  $\psi_{n\mathbf{k}}(\mathbf{r}) = u_{n\mathbf{k}}(\mathbf{r}) e^{i\mathbf{k}\mathbf{r}}$  where  $u_{n\mathbf{k}}(\mathbf{r})$  exhibits the same periodicity as the system itself and can therefore be expanded with respect to reciprocal lattice vectors  $\mathbf{G}$ :  $u_{n\mathbf{k}}(\mathbf{r}) = \sum_{\mathbf{G}} c_{n\mathbf{k}}(\mathbf{G}) e^{i\mathbf{G}\mathbf{r}}$ . The wave vector  $\mathbf{k}$  lies within the first Brillouin zone. In practice, a finite grid of  $k$ -points, in the form of e.g., a Monkhorst-Pack grid [16], is used for the sampling of the Brillouin zone. Applying the concept of periodicity on the Kohn-Sham equations, they split up into  $N_{\mathbf{k}}$  (number of  $k$ -points) equations, which can be solved separately. For finite or aperiodic systems the concept of periodicity is certainly artificial. But these systems can be treated within the supercell approach where the respective systems are placed in large three-dimensional supercells in order to avoid interactions between the repeated images.

Due to the plane wave approach it is costly to describe strongly localized electrons with rapid oscillations, such as electrons close to the core. They require a large number of plane waves in the expansion of the cell periodic function

$$u_{n\mathbf{k}}(\mathbf{r}) = \sum_{\mathbf{G}}^{|k+\mathbf{G}|^2/2 < E_{\text{cut}}} c_{n\mathbf{k}}(\mathbf{G}) e^{i\mathbf{G}\mathbf{r}} \quad (1.13)$$

and consequently a large value for the plane wave energy cutoff  $E_{\text{cut}}$ , slowing the DFT calculations drastically. To circumvent this problem, we do not consider the KS equations for energetically deeper lying electrons, core electrons, (frozen core approximation) and describe the remaining electrons, valence electrons, within the projector augmented-wave method (PAW) [14, 15].

#### 1.3.2 Projector augmented wave method

The main idea of the PAW method is to divide space into two regions: the augmentation region  $\Omega_a$  (atom-centered spheres) and the interstitial region  $\Omega_I$  between these spheres. Within the augmentation regions  $\Omega_a$  the all-electron (AE) wavefunction  $|\psi_{n\mathbf{k}}\rangle$  of state  $n$  and  $k$ -point  $\mathbf{k}$  can be expanded with respect to a set for AE partial-waves  $|\phi_i\rangle$

$$|\psi_{n\mathbf{k}}\rangle = \sum_i c_{i,n\mathbf{k}} |\phi_i\rangle \quad \text{in} \quad \Omega_a. \quad (1.14)$$

The AE partial waves are solutions to the all-electron KS-DFT equation for a spherical reference atom of type  $N$  situated at the atomic site  $\mathbf{R}$  for different angular momentum numbers  $L = l, m$  and reference energies  $\epsilon_{al}$ . The index  $i$  is an abbreviation for  $\mathbf{R}, N, L$ ,

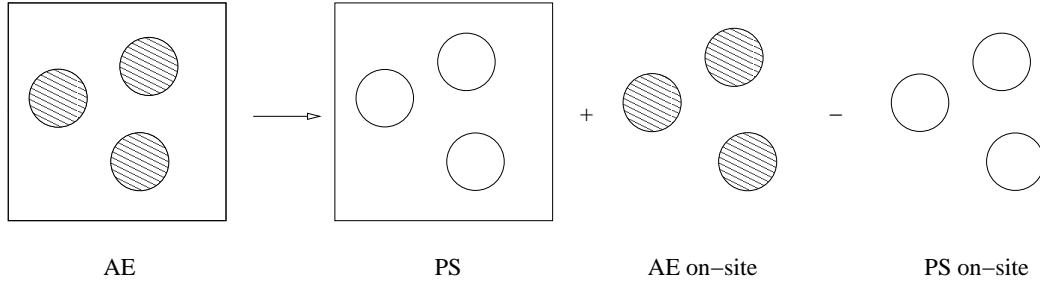


Figure 1.1: Wavefunction/density representation in the projector augmented-wave method.

and the index of the reference energy  $\alpha$ . The radial part of the solution can be split off and by means of the spherical harmonics  $Y_{lm}$  the AE partial-wave can be written as:

$$\langle \mathbf{r} | \phi_i \rangle = \phi_i(\mathbf{r}) = Y_{lm}(\widehat{\mathbf{r} - \mathbf{R}}) \phi_{Nl\alpha}(|\mathbf{r} - \mathbf{R}|). \quad (1.15)$$

Additionally pseudo (PS) partial waves

$$\langle \mathbf{r} | \tilde{\phi}_i \rangle = \tilde{\phi}_i(\mathbf{r}) = Y_{lm}(\widehat{\mathbf{r} - \mathbf{R}}) \tilde{\phi}_{Nl\alpha}(|\mathbf{r} - \mathbf{R}|) \quad (1.16)$$

are generated, which are smooth functions inside the augmentation-spheres and match the AE partial-waves outside  $\Omega_a$ . This is achieved by expanding  $\tilde{\phi}_{Nl\alpha}(r)$  with respect to Bessel functions  $j_l(qr)$ . For more details see [15] Sec. IV B.

Pseudo wavefunctions  $|\tilde{\psi}_{n\mathbf{k}}\rangle$  represented using plane waves are finally introduced. These are defined as:

$$\begin{aligned} |\tilde{\psi}_{n\mathbf{k}}\rangle &= \sum_i c_{i,n\mathbf{k}} |\tilde{\phi}_i\rangle \quad \text{in } \Omega_a \\ |\tilde{\psi}_{n\mathbf{k}}\rangle &= |\psi_{n\mathbf{k}}\rangle \quad \text{in } \Omega_I. \end{aligned} \quad (1.17)$$

The representation of the PS wavefunction  $|\tilde{\psi}_{n\mathbf{k}}\rangle$  requires only a modest number of plane waves because the AE partial waves  $|\phi_i\rangle$  with their rapid oscillations near the atomic core region  $\Omega_a$  are replaced by the smooth PS partial waves  $|\tilde{\phi}_i\rangle$ . By introducing projector functions  $|\tilde{p}_i\rangle$  that are dual to the PS partial waves

$$\langle \tilde{p}_i | \tilde{\phi}_j \rangle = \delta_{ij}, \quad (1.18)$$

the coefficients  $c_{i,n\mathbf{k}}$  can be obtained by

$$\langle \tilde{p}_i | \tilde{\psi}_{n\mathbf{k}} \rangle = \sum_j c_{j,n\mathbf{k}} \langle \tilde{p}_i | \tilde{\phi}_j \rangle = c_{i,n\mathbf{k}}. \quad (1.19)$$

Combining Eq. (1.14) and Eq. (1.17), the AE wavefunction  $|\psi_{n\mathbf{k}}\rangle$  can be written as:

$$|\psi_{n\mathbf{k}}\rangle = |\tilde{\psi}_{n\mathbf{k}}\rangle + \sum_i \langle \tilde{p}_i | \tilde{\psi}_{n\mathbf{k}} \rangle |\phi_i\rangle - \sum_i \langle \tilde{p}_i | \tilde{\psi}_{n\mathbf{k}} \rangle |\tilde{\phi}_i\rangle. \quad (1.20)$$

This splitting of the AE wavefunction is visualized schematically in Fig. 1.1. The AE wavefunction  $|\psi_{n\mathbf{k}}\rangle$  with large oscillations (slashed spheres) in  $\Omega_a$  is described by a PS wavefunction  $|\tilde{\psi}_{n\mathbf{k}}\rangle$  which is smooth in the entire space and corresponds to the AE wavefunction in the interstitial region  $\Omega_I$ . It is expanded with respect to a plane-wave basis set. To correct for the PS error an AE on-site term is added inside the augmentation regions  $\Omega_a$ . Contributions already accounted for by the PS wavefunctions are finally expressed by PS partial waves and subtracted. The same separation as for the wavefunctions approximately holds also for the density

$$n(\mathbf{r}) = \sum_{n\mathbf{k}} f_{n\mathbf{k}} \langle \psi_{n\mathbf{k}} | \mathbf{r} \rangle \langle \mathbf{r} | \psi_{n\mathbf{k}} \rangle, \quad (1.21)$$

which can be written as

$$\begin{aligned} n(\mathbf{r}) &= \sum_{n\mathbf{k}} f_{n\mathbf{k}} \langle \tilde{\psi}_{n\mathbf{k}} | \mathbf{r} \rangle \langle \mathbf{r} | \tilde{\psi}_{n\mathbf{k}} \rangle + \sum_{ij} \rho_{ij} \langle \phi_i | \mathbf{r} \rangle \langle \mathbf{r} | \phi_j \rangle - \sum_{ij} \rho_{ij} \langle \tilde{\phi}_i | \mathbf{r} \rangle \langle \mathbf{r} | \tilde{\phi}_j \rangle = \\ &= \tilde{n}(\mathbf{r}) + n^1(\mathbf{r}) - \tilde{n}^1(\mathbf{r}) \end{aligned}$$

with

$$\rho_{ij} = \sum_{n\mathbf{k}} f_{n\mathbf{k}} \langle \tilde{\psi}_{n\mathbf{k}} | \tilde{p}_i \rangle \langle \tilde{p}_j | \tilde{\psi}_{n\mathbf{k}} \rangle = \sum_{n\mathbf{k}} f_{n\mathbf{k}} c_{i,n\mathbf{k}}^* c_{j,n\mathbf{k}}. \quad (1.22)$$

The pseudo density  $\tilde{n}(\mathbf{r})$  is thereby described on a regular grid spanning the entire supercell volume. A Fast Fourier Transform is used to switch between the plane wave coefficient  $c_{i,n\mathbf{k}}$  and the real space representation of the PS wavefunction  $\tilde{\psi}_{n\mathbf{k}}(\mathbf{r})$ . The plane wave grid on which the PS wavefunction is thereby evaluated in real space is closely related to the regular grid. The on-site PS and AE densities  $\tilde{n}^1(\mathbf{r})$  and  $n^1(\mathbf{r})$  are represented on radial grids in the augmentation spheres  $\Omega_a$  centered around the ions. The separation into terms arising from contributions represented on regular and radial grids holds (approximately) also for the total energy, if one introduces the compensation charge density  $\hat{n}(\mathbf{r})$  (see [15] Sec. II B, C). The compensation charge density  $\hat{n}$  is added to the PS charge density  $\tilde{n}(\mathbf{r})$  in order to restore the AE monopole and multipoles up to a certain angular momentum number  $L$ . Consequently,  $\hat{n}$  has to fulfill the requirement:

$$\int_{\Omega_a(\mathbf{R}_i)} (n^1 - \tilde{n}^1 - \hat{n}) |\mathbf{r} - \mathbf{R}_i|^l Y_L^*(\widehat{\mathbf{r} - \mathbf{R}_i}) d^3r = 0. \quad (1.23)$$

The compensation charge  $\hat{n}$  should therefore reproduce the multipoles of the augmentation charge density  $Q_{ij}$

$$n^1(\mathbf{r}) - \tilde{n}^1(\mathbf{r}) = \sum_{ij} \rho_{ij} Q_{ij}(\mathbf{r}) \quad Q_{ij}(\mathbf{r}) = \phi_i^*(\mathbf{r}) \phi_j(\mathbf{r}) - \tilde{\phi}_i^*(\mathbf{r}) \tilde{\phi}_j(\mathbf{r}), \quad (1.24)$$

but at the same time its shape has to be smoother than the one of the fast varying  $Q_{ij}(\mathbf{r})$ , because it has to be represented on a regular grid in order to add it to the PS charge density. By introducing the moments of the augmentation charge

$$q_{ij}^L = \int_{\Omega_a(\mathbf{R}_i)} Q_{ij}(\mathbf{r}) |\mathbf{r} - \mathbf{R}_i|^l Y_L^*(\widehat{\mathbf{r} - \mathbf{R}_i}) d^3r, \quad (1.25)$$

the compensation charge density can be expressed as

$$\hat{n} = \sum_{ij} \rho_{ij} \hat{Q}_{ij}^L(\mathbf{r}) \quad \hat{Q}_{ij}^L(\mathbf{r}) = q_{ij}^L g_l(|\mathbf{r} - \mathbf{R}|) Y_L(\widehat{\mathbf{r} - \mathbf{R}}), \quad (1.26)$$

where  $g_l(|\mathbf{r} - \mathbf{R}|)$  is a smooth function which a  $l$ -moment of one. For more details about the construction of  $g_l(|\mathbf{r} - \mathbf{R}|)$  see [15] Sec. IV D.

## Chapter 2

# Optical properties within linear response theory

### 2.1 Time-dependent density functional theory

Time-dependent density functional theory (TDDFT) aims at mapping the time-dependent Schrödinger equation

$$i\frac{\partial}{\partial t}\Psi(t) = \hat{H}\Psi(t) \quad (2.1)$$

onto an effective one-electron problem, as density functional theory does for the static Schrödinger equation. In 1984, Runge and Gross [17] proved that, for a given initial state, a one-to-one correspondence exists between the time-dependent density  $n(\mathbf{r}, t)$  and the time-dependent external potential  $v_{\text{ext}}(\mathbf{r}, t)$ . The Runge-Gross theorem is the fundament of TDDFT as the Hohenberg-Kohn theorem [1] is the justification for (static) DFT. Analogous to static DFT, time-dependent Kohn-Sham equations can be introduced, which map the problem of interacting electrons moving in a time-dependent external potential  $v_{\text{ext}}$  onto a system of independent electrons moving in a time-dependent effective potential  $v_{\text{eff}}$ . The resulting time-dependent Kohn-Sham equations take the form:

$$i\frac{\partial\psi_n(\mathbf{r}, t)}{\partial t} = \left[ -\frac{\hbar^2}{2m}\nabla^2 + v_{\text{eff}}[n](\mathbf{r}, t) \right] \psi_n(\mathbf{r}, t) \quad n(\mathbf{r}, t) = 2 \sum_{n(\text{occ})} |\psi_n(\mathbf{r}, t)|^2. \quad (2.2)$$

The effective potential  $v_{\text{eff}}$  can be split into the external potential, the (via the density) time-dependent Hartree potential, and the exchange-correlation potential

$$v_{\text{eff}}[n](\mathbf{r}, t) = v_{\text{ext}}(\mathbf{r}, t) + v_H[n](\mathbf{r}, t) + v_{xc}[n](\mathbf{r}, t). \quad (2.3)$$

The time-dependent Hartree potential is defined as

$$v_H[n](\mathbf{r}, t) = e^2 \int d^3r' \frac{n(\mathbf{r}', t)}{|\mathbf{r} - \mathbf{r}'|}. \quad (2.4)$$

The time-dependent exchange-correlation potential  $v_{xc}$  is a quantity that depends on the history of the density  $n(\mathbf{r}, t)$  and the initial interacting many-electron and Kohn-Sham wavefunctions. In the following we will only consider the influence of a weak external potential

(linear response regime), but a detailed overview on TDDFT and various applications can be found in Ref. [18].

## 2.2 Linear response theory

Both in the calculation of the reflectance difference spectra (part II of this thesis) and in the improved description of the DFT exchange-correlation energy (part IV) we have to evaluate the response of the material to an external perturbation. If this perturbation is weak compared to the internal electric fields caused by the ions, as usually in spectroscopic experiments, the induced change in the density can be described within perturbation theory as linearly dependent on the applied perturbation.

The key quantity of linear response theory is the response function  $\chi(\mathbf{r}, \mathbf{r}', t - t')$ , which describes the change of the density  $\delta n$  at  $(\mathbf{r}, t)$  if the external potential undergoes a small change  $\delta v_{\text{ext}}$  at  $(\mathbf{r}', t')$ .

$$\delta n(\mathbf{r}, t) = \int dt' \int d^3r' \chi(\mathbf{r}, \mathbf{r}', t - t') \delta v_{\text{ext}}(\mathbf{r}', t') \quad (2.5)$$

$$\chi(\mathbf{r}, \mathbf{r}', t - t') = \frac{\delta n(\mathbf{r}, t)}{\delta v_{\text{ext}}(\mathbf{r}', t')}. \quad (2.6)$$

Within the Kohn-Sham formulation it is easier to calculate the Kohn-Sham (KS) response function  $\chi^{KS}(\mathbf{r}, \mathbf{r}', t - t')$ , which describes the response of the KS system to a small change of the effective Kohn-Sham potential  $v_{\text{eff}}[n]$ :

$$\delta n(\mathbf{r}, t) = \int dt' \int d^3r' \chi^{KS}(\mathbf{r}, \mathbf{r}', t - t') \delta v_{\text{eff}}(\mathbf{r}', t') \quad (2.7)$$

$$\chi^{KS}(\mathbf{r}, \mathbf{r}', t - t') = \frac{\delta n(\mathbf{r}, t)}{\delta v_{\text{eff}}(\mathbf{r}', t')}. \quad (2.8)$$

The requirement that the change of the density  $\delta n(\mathbf{r}, t)$  is the same in both descriptions links the response function of the interacting system  $\chi(\mathbf{r}, \mathbf{r}', t - t')$  to the KS response function  $\chi^{KS}(\mathbf{r}, \mathbf{r}', t - t')$ . In order to write this relation explicitly, we introduce the exchange-correlation kernel  $f_{xc}$

$$v_{xc}[n_{GS} + \delta n](\mathbf{r}, t) = v_{xc}[n_{GS}](\mathbf{r}) + \int dt' \int d^3r' f_{xc}[n_{GS}](\mathbf{r}, \mathbf{r}', t - t') \delta n(\mathbf{r}', t') \quad (2.9)$$

$$f_{xc}[n_{GS}](\mathbf{r}, \mathbf{r}', t - t') = \left. \frac{\delta v_{xc}(\mathbf{r}, t)}{\delta n(\mathbf{r}', t')} \right|_{n=n_{GS}}, \quad (2.10)$$

which is defined as the derivative of the time-dependent exchange-correlation potential with respect to the time-dependent density evaluated at the ground state density  $n_{GS}$ . By requiring that Eq. (2.5) and Eq. (2.7) are the same, the link between  $\chi$  and  $\chi^{KS}$  is given as [see Eq. (2.3)]:

$$\begin{aligned} \int dt' \int d^3r' \chi(\mathbf{r}, \mathbf{r}', t - t') \delta v_{\text{ext}}(\mathbf{r}', t') &= \\ &= \int dt' \int d^3r' \chi^{KS}(\mathbf{r}, \mathbf{r}', t - t') \{ \delta v_{\text{ext}}(\mathbf{r}', t') + \delta v_H(\mathbf{r}', t') + \delta v_{xc}(\mathbf{r}', t') \}. \end{aligned} \quad (2.11)$$

Applying the chain rule on  $\delta v_H$  and  $\delta v_{xc}$ ,

$$\delta v_H(\mathbf{r}', t') = \int dt_1 dt_2 \int d^3 r_1 d^3 r_2 \frac{\delta v_H(\mathbf{r}', t')}{\delta n(\mathbf{r}_1, t_1)} \frac{\delta n(\mathbf{r}_1, t_1)}{\delta v_{\text{ext}}(\mathbf{r}_2, t_2)} \delta v_{\text{ext}}(\mathbf{r}_2, t_2) \quad (2.12)$$

$$\begin{aligned} &= \int dt_1 dt_2 \int d^3 r_1 d^3 r_2 \frac{1}{|\mathbf{r}_1 - \mathbf{r}'|} \chi(\mathbf{r}_1, \mathbf{r}_2, t_1 - t_2) \delta v_{\text{ext}}(\mathbf{r}_2, t_2) \\ \delta v_{xc}(\mathbf{r}', t') &= \int dt_1 dt_2 \int d^3 r_1 d^3 r_2 \frac{\delta v_{xc}(\mathbf{r}', t')}{\delta n(\mathbf{r}_1, t_1)} \frac{\delta n(\mathbf{r}_1, t_1)}{\delta v_{\text{ext}}(\mathbf{r}_2, t_2)} \delta v_{\text{ext}}(\mathbf{r}_2, t_2) = \\ &= \int dt_1 dt_2 \int d^3 r_1 d^3 r_2 f_{xc}(\mathbf{r}', \mathbf{r}_1, t' - t_1) \chi(\mathbf{r}_1, \mathbf{r}_2, t_1 - t_2) \delta v_{\text{ext}}(\mathbf{r}_2, t_2), \end{aligned} \quad (2.13)$$

changing the names of the integration variables, and going to frequency space finally leads to the relationship:

$$\begin{aligned} \chi(\mathbf{r}, \mathbf{r}', \omega) &= \chi^{KS}(\mathbf{r}, \mathbf{r}', \omega) + \\ &+ \int d^3 r_1 d^3 r_2 \chi^{KS}(\mathbf{r}, \mathbf{r}_1, \omega) \left( \frac{e^2}{|\mathbf{r}_1 - \mathbf{r}_2|} + f_{xc}(\mathbf{r}_1, \mathbf{r}_2, \omega) \right) \chi(\mathbf{r}_2, \mathbf{r}', \omega). \end{aligned} \quad (2.14)$$

This relationship is generally referred to as Dyson equation. For the evaluation of the response function of an interacting electron system the response function of the respective Kohn-Sham system is calculated and afterwards the interacting response function is estimated by applying the Dyson equation with some approximated exchange-correlation kernel. The easiest approximation for  $f_{xc}$  is to ignore the effect of the exchange-correlation at all ( $f_{xc} = 0$ ). This simplification is called random phase approximation (RPA) or Hartree approximation (because only the Hartree term  $\delta v_H$  contributes).

Following the derivation of Pines and Nozière [19] (see also [20]), an explicit formula for the response to an external (time-dependent) potential  $\delta v(\mathbf{r}, t)$ , leading to a small perturbation in the Hamiltonian

$$\delta \hat{H}(t) = e^{\eta t} \sum_{i=1}^N \delta v(\mathbf{r}_i, t) \quad 0 < \eta \ll 1, \quad (2.15)$$

can be found. The factor  $e^{\eta t}$  is introduced to guarantee an adiabatic, slow switching from the unperturbed Hamiltonian for  $t \rightarrow -\infty$  ( $e^{\eta t} = 0$ ) to 1 for  $t = 0$ . With the density operator  $\hat{n}(\mathbf{r}) = \sum_{i=1}^N \delta(\mathbf{r} - \mathbf{r}_i)$ , the perturbation can be written in frequency space as

$$\delta \hat{H}(t) = \int d^3 r \int \frac{d\omega}{2\pi} e^{-i\tilde{\omega}t} \delta v(\mathbf{r}, \omega) \hat{n}(\mathbf{r}) \quad \tilde{\omega} := \omega + i\eta. \quad (2.16)$$

If  $|\Psi_0^0\rangle$  and  $E_0^0$  are the ground state wavefunction and ground state energy of the stationary Schrödinger equation  $\hat{H}^0 |\Psi_j^0\rangle = E_j |\Psi_j^0\rangle$ , where  $\hat{H}^0$  is the unperturbed Hamiltonian, the solution of the (unperturbed) time-dependent Schrödinger equation is given as

$$|\Psi^0(t)\rangle = e^{-iE_0 t} |\Psi_0^0\rangle. \quad (2.17)$$

Introducing the time-dependent perturbation  $\delta \hat{H}(t)$ , the Schrödinger equation reads:

$$i \frac{\partial |\Psi(t)\rangle}{\partial t} = (\hat{H}^0 + \delta \hat{H}(t)) |\Psi(t)\rangle. \quad (2.18)$$



Within first-order perturbation theory,  $|\Psi(t)\rangle$  can be written as

$$|\Psi(t)\rangle = \underbrace{e^{-iE_0t} |\Psi_0^0\rangle}_{|\Psi^0(t)\rangle} + \sum_{j \neq 0} a_j(t) e^{-iE_jt} |\Psi_j^0\rangle. \quad (2.19)$$

It can be described as the unperturbed time-dependent solution  $|\Psi^0(t)\rangle$  plus an admixture of components resulting from excited states of the unperturbed Schrödinger equation  $e^{-iE_jt} |\Psi_j^0\rangle$ . The time-dependent coefficients are given by:

$$\begin{aligned} a_j(t) &= -i \int_{-\infty}^t dt' e^{i\omega_{0j}t'} \langle \Psi_j^0 | \delta \hat{H}(t') | \Psi_0^0 \rangle = \\ &= -i \int d^3r' \int \frac{d\omega}{2\pi} \int_{-\infty}^t dt' e^{i(\omega_{0j}-\tilde{\omega})t'} \delta v(\mathbf{r}', \omega) \langle \Psi_j^0 | \hat{n}(\mathbf{r}') | \Psi_0^0 \rangle = \\ &= - \int d^3r' \int \frac{d\omega}{2\pi} \delta v(\mathbf{r}', \omega) \langle \Psi_j^0 | \hat{n}(\mathbf{r}') | \Psi_0^0 \rangle \frac{e^{i(\omega_{0j}-\tilde{\omega})t}}{\omega_{0j} - \tilde{\omega}}, \end{aligned} \quad (2.20)$$

where  $\omega_{0j}$  denotes the difference between the energy of an excited state and the ground state,  $\omega_{0j} = E_j - E_0$ . The change of the density resulting from the time-dependent perturbation

$$n_{\text{ind}}(\mathbf{r}, t) = \delta n(\mathbf{r}, t) = \langle \Psi(t) | \hat{n}(\mathbf{r}) | \Psi(t) \rangle - \langle \Psi^0(t) | \hat{n}(\mathbf{r}) | \Psi^0(t) \rangle \quad (2.21)$$

can be written as

$$\begin{aligned} n_{\text{ind}}(\mathbf{r}, t) &= \sum_{j \neq 0} [a_j(t) \langle \Psi_0^0 | \hat{n}(\mathbf{r}) | \Psi_j^0 \rangle e^{-i\omega_{0j}t} + a_j^*(t) \langle \Psi_j^0 | \hat{n}(\mathbf{r}) | \Psi_0^0 \rangle e^{i\omega_{0j}t}] = \\ &= - \int d^3r' \int \frac{d\omega}{2\pi} \delta v(\mathbf{r}', \omega) e^{-i\tilde{\omega}t} \times \\ &\quad \times \sum_{j \neq 0} \left( \frac{\langle \Psi_j^0 | \hat{n}(\mathbf{r}') | \Psi_0^0 \rangle \langle \Psi_0^0 | \hat{n}(\mathbf{r}) | \Psi_j^0 \rangle}{\omega_{0j} - \tilde{\omega}} + \frac{\langle \Psi_0^0 | \hat{n}(\mathbf{r}') | \Psi_j^0 \rangle \langle \Psi_j^0 | \hat{n}(\mathbf{r}) | \Psi_0^0 \rangle}{\omega_{0j} + \tilde{\omega}} \right), \end{aligned} \quad (2.22)$$

if terms proportional to the square of  $|\Psi(t)\rangle - |\Psi^0(t)\rangle$  are neglected. The induced density in frequency space becomes

$$\begin{aligned} n_{\text{ind}}(\mathbf{r}, \omega) &= - \int d^3r' \delta v(\mathbf{r}', \omega) \times \\ &\quad \times \sum_{j \neq 0} \left( \frac{\langle \Psi_j^0 | \hat{n}(\mathbf{r}') | \Psi_0^0 \rangle \langle \Psi_0^0 | \hat{n}(\mathbf{r}) | \Psi_j^0 \rangle}{\omega_{0j} - \tilde{\omega}} + \frac{\langle \Psi_0^0 | \hat{n}(\mathbf{r}') | \Psi_j^0 \rangle \langle \Psi_j^0 | \hat{n}(\mathbf{r}) | \Psi_0^0 \rangle}{\omega_{0j} + \tilde{\omega}} \right). \end{aligned} \quad (2.23)$$

The change of the density  $n_{\text{ind}} = \delta n$  with respect to the change of the potential  $\delta v$  induced by the external perturbation is exactly the response function

$$\begin{aligned} \frac{\delta n(\mathbf{r}, \omega)}{\delta v(\mathbf{r}', \omega)} &= \chi(\mathbf{r}, \mathbf{r}', \omega) = \\ &= - \sum_{j \neq 0} \left( \frac{\langle \Psi_j^0 | \hat{n}(\mathbf{r}') | \Psi_0^0 \rangle \langle \Psi_0^0 | \hat{n}(\mathbf{r}) | \Psi_j^0 \rangle}{\omega_{0j} - \tilde{\omega}} + \frac{\langle \Psi_0^0 | \hat{n}(\mathbf{r}') | \Psi_j^0 \rangle \langle \Psi_j^0 | \hat{n}(\mathbf{r}) | \Psi_0^0 \rangle}{\omega_{0j} + \tilde{\omega}} \right). \end{aligned} \quad (2.24)$$

For a system of non-interacting electrons (and the KS system can be considered as a system of independent electrons moving in an effective potential), the ground state wavefunction  $\Psi_0^0$  can be written as a product of one-particle wavefunctions  $\psi_n$  (or as a Slater determinant, respectively):

$$\Psi_0^0(\mathbf{r}_1, \mathbf{r}_2, \dots, \mathbf{r}_{N/2}) = \psi_1(\mathbf{r}_1) \psi_2(\mathbf{r}_2) \dots \psi_n(\mathbf{r}_i) \dots \psi_{N/2}(\mathbf{r}_{N/2}), \quad (2.25)$$

where the functions  $\{\psi_1 \dots \psi_{N/2}\}$  are the  $N/2$  lowest solutions of the one-particle Schrödinger equation (or KS equation). Orthonormality holds for the one-particle wavefunctions  $\psi_n$ . An excited state of the system can be generated by "moving" one electron from an occupied state to an unoccupied state generating the excited wavefunction

$$\Psi_j^0(\mathbf{r}_1, \mathbf{r}_2, \dots, \mathbf{r}_{N/2}) = \psi_1(\mathbf{r}_1) \psi_2(\mathbf{r}_2) \dots \psi_m(\mathbf{r}_i) \dots \psi_{N/2}(\mathbf{r}_{N/2}) \quad m > N/2. \quad (2.26)$$

For the system of independent electrons, the expression  $\langle \Psi_0^0 | \hat{n}(\mathbf{r}) | \Psi_j^0 \rangle$  then reads

$$\begin{aligned} \sum_k \langle \psi_1(\mathbf{r}_1) \dots \psi_n(\mathbf{r}_i) \dots \psi_{N/2}(\mathbf{r}_{N/2}) | \delta(\mathbf{r} - \mathbf{r}_k) | \psi_1(\mathbf{r}_1) \dots \psi_m(\mathbf{r}_i) \dots \psi_{N/2}(\mathbf{r}_{N/2}) \rangle = \\ = \psi_n^*(\mathbf{r}) \psi_m(\mathbf{r}). \end{aligned} \quad (2.27)$$

The difference of the ground-state energy and the energy of the excited state,  $\omega_{0j} = E_j - E_0$ , can be described as the difference between one-electron energies  $\omega_{nm} = \epsilon_m - \epsilon_n$ . The independent particle response function of the KS system is consequently given as

$$\chi^{KS}(\mathbf{r}, \mathbf{r}', \omega) = - \sum_{\substack{n \\ occ}} \sum_{\substack{m \\ uocc}} 2 \left( \frac{\psi_m^*(\mathbf{r}') \psi_n(\mathbf{r}') \psi_n^*(\mathbf{r}) \psi_m(\mathbf{r})}{\epsilon_m - \epsilon_n - \tilde{\omega}} + \frac{\psi_n^*(\mathbf{r}') \psi_m(\mathbf{r}') \psi_m^*(\mathbf{r}) \psi_n(\mathbf{r})}{\epsilon_m - \epsilon_n + \tilde{\omega}} \right) \quad (2.28)$$

or

$$\begin{aligned} \chi^{KS}(\mathbf{r}, \mathbf{r}', \omega) = - \sum_{\substack{n \\ all}} \sum_{\substack{m \\ all}} 2 f_n (1 - f_m) \times \\ \times \left( \frac{\psi_m^*(\mathbf{r}') \psi_n(\mathbf{r}') \psi_n^*(\mathbf{r}) \psi_m(\mathbf{r})}{\epsilon_m - \epsilon_n - \tilde{\omega}} + \frac{\psi_n^*(\mathbf{r}') \psi_m(\mathbf{r}') \psi_m^*(\mathbf{r}) \psi_n(\mathbf{r})}{\epsilon_m - \epsilon_n + \tilde{\omega}} \right), \end{aligned}$$

where  $f_n$  is 1 for occupied and 0 for unoccupied states.

As we will consider the response function of a periodic crystal, the Fourier transform of Eq. (2.28),  $\chi(\mathbf{q}, \mathbf{q}', \omega)$ , is more convenient for our purpose. Due to the invariance of the real space response function with respect to a shift by a lattice vector  $\chi(\mathbf{r} + \mathbf{R}, \mathbf{r}' + \mathbf{R}) = \chi(\mathbf{r}, \mathbf{r}')$ , it can be shown that  $\chi(\mathbf{q}, \mathbf{q}', \omega)$  is only nonzero if  $\mathbf{q}$  and  $\mathbf{q}'$  differ by a reciprocal lattice vector  $\mathbf{G}$ . Consequently, one can replace  $\mathbf{q} \rightarrow \mathbf{q} + \mathbf{G}$  and  $\mathbf{q}' \rightarrow \mathbf{q} + \mathbf{G}'$ , with  $\mathbf{q}$  lying within the first Brillouin zone. According to the Bloch theorem, the sum over states in Eq. (2.28) can be replaced by a sum over states and  $k$ -points ( $n \rightarrow n\mathbf{k}$  and  $m \rightarrow m\mathbf{k}'$ ) where  $\mathbf{k}$  lies within the first Brillouin zone. Combining all this, the response function in momentum space can be written as

$$\begin{aligned} \chi_{\mathbf{G}, \mathbf{G}'}^{KS}(\mathbf{q}, \omega) = \\ = - \frac{1}{V} \sum_{n\mathbf{k}} \sum_{m\mathbf{k}'} 2 f_{n\mathbf{k}} (1 - f_{m\mathbf{k}'}) \left( \frac{\langle \psi_{m\mathbf{k}'} | e^{i(\mathbf{q} + \mathbf{G})\mathbf{r}} | \psi_{n\mathbf{k}} \rangle \langle \psi_{n\mathbf{k}} | e^{-i(\mathbf{q} + \mathbf{G}')\mathbf{r}'} | \psi_{m\mathbf{k}'} \rangle}{\epsilon_{m\mathbf{k}'} - \epsilon_{n\mathbf{k}} - \tilde{\omega}} + \right. \\ \left. + \frac{\langle \psi_{n\mathbf{k}} | e^{i(\mathbf{q} + \mathbf{G})\mathbf{r}} | \psi_{m\mathbf{k}'} \rangle \langle \psi_{m\mathbf{k}'} | e^{-i(\mathbf{q} + \mathbf{G}')\mathbf{r}'} | \psi_{n\mathbf{k}} \rangle}{\epsilon_{m\mathbf{k}'} - \epsilon_{n\mathbf{k}} + \tilde{\omega}} \right) \end{aligned} \quad (2.29)$$

where

$$\begin{aligned}\langle \psi_{m\mathbf{k}'} | e^{i(\mathbf{q}+\mathbf{G})\mathbf{r}} | \psi_{n\mathbf{k}} \rangle &\equiv \int_V d^3r \psi_{m\mathbf{k}'}^*(\mathbf{r}) e^{i(\mathbf{q}+\mathbf{G})\mathbf{r}} \psi_{n\mathbf{k}}(\mathbf{r}) = \\ &= \int_V d^3r u_{m\mathbf{k}'}^*(\mathbf{r}) e^{-i\mathbf{k}'\mathbf{r}} e^{i(\mathbf{q}+\mathbf{G})\mathbf{r}} e^{i\mathbf{k}\mathbf{r}} u_{n\mathbf{k}}(\mathbf{r})\end{aligned}\quad (2.30)$$

is calculated as an integral over the unit cell with volume  $V$ . The relationship between the induced density  $n_{\text{ind}} = \delta n$  and the change in the potential  $\delta v$  is consequently given as:

$$\delta n(\mathbf{q} + \mathbf{G}, \omega) = \sum_{\mathbf{G}'} \chi_{\mathbf{G}, \mathbf{G}'}(\mathbf{q}, \omega) \delta v(\mathbf{q} + \mathbf{G}', \omega). \quad (2.31)$$

By changing the summation index in the second term ( $n\mathbf{k} \rightarrow m\mathbf{k}'$ ,  $m\mathbf{k}' \rightarrow n\mathbf{k}$ ) the response function can also be written as

$$\begin{aligned}\chi_{\mathbf{G}, \mathbf{G}'}^{KS}(\mathbf{q}, \omega) &= \frac{1}{V} \sum_{n\mathbf{k}} \sum_{m\mathbf{k}'} 2(f_{m\mathbf{k}'} - f_{n\mathbf{k}}) \times \\ &\times \frac{\langle \psi_{m\mathbf{k}'} | e^{i(\mathbf{q}+\mathbf{G})\mathbf{r}} | \psi_{n\mathbf{k}} \rangle \langle \psi_{n\mathbf{k}} | e^{-i(\mathbf{q}+\mathbf{G}')\mathbf{r}'} | \psi_{m\mathbf{k}'} \rangle}{\epsilon_{m\mathbf{k}'} - \epsilon_{n\mathbf{k}} - \tilde{\omega}}.\end{aligned}\quad (2.32)$$

Due to the translational invariance of the crystal only terms  $\mathbf{k}' = \mathbf{k} + \mathbf{q}$  are allowed as can be seen by performing the integration in Eq. (2.30) over a supercell shifted by a lattice vector  $\mathbf{R}$ . The response function finally reads (see also Ref. [21]):

$$\begin{aligned}\chi_{\mathbf{G}, \mathbf{G}'}^{KS}(\mathbf{q}, \omega) &= \frac{1}{V} \sum_{nm; \mathbf{k}} 2(f_{m\mathbf{k}+\mathbf{q}} - f_{n\mathbf{k}}) \times \\ &\times \frac{\langle \psi_{m\mathbf{k}+\mathbf{q}} | e^{i(\mathbf{q}+\mathbf{G})\mathbf{r}} | \psi_{n\mathbf{k}} \rangle \langle \psi_{n\mathbf{k}} | e^{-i(\mathbf{q}+\mathbf{G}')\mathbf{r}'} | \psi_{m\mathbf{k}+\mathbf{q}} \rangle}{\epsilon_{m\mathbf{k}+\mathbf{q}} - \epsilon_{n\mathbf{k}} - \tilde{\omega}}.\end{aligned}\quad (2.33)$$

From Eq. (2.33) it is evident that transitions between states that are either both filled or both empty do not contribute to the response function, because the difference in the occupation number,  $f_{m\mathbf{k}+\mathbf{q}} - f_{n\mathbf{k}}$ , is zero for these cases.

Sometimes the response function in Eq. (2.33) is written in a slightly different form and we will in the following briefly sketch the intermediate steps for the derivation of this reformulation. First, the term  $\langle \psi_{m\mathbf{k}+\mathbf{q}} | e^{i(\mathbf{q}+\mathbf{G})\mathbf{r}} | \psi_{n\mathbf{k}} \rangle$  can be expressed as  $\langle u_{m\mathbf{k}+\mathbf{q}} | e^{i\mathbf{G}\mathbf{r}} | u_{n\mathbf{k}} \rangle$ . This can be seen from combining the definition given in Eq. (2.30) and the fact that  $\mathbf{k}' = \mathbf{k} + \mathbf{q}$ . Furthermore, expression Eq. (2.33) can be split into two terms  $\sum_{nm; \mathbf{k}} 2f_{m\mathbf{k}+\mathbf{q}} - \sum_{nm; \mathbf{k}} 2f_{n\mathbf{k}}$ . By changing the summation index in the first sum  $n \leftrightarrow m$ , and performing the Brillouin zone integration over  $-\mathbf{k} - \mathbf{q}$  instead of  $\mathbf{k}$  (this corresponds to  $\mathbf{k} + \mathbf{q} \rightarrow -\mathbf{k}$  and  $\mathbf{k} \rightarrow -\mathbf{k} - \mathbf{q}$ ), Eq. (2.33) reads:

$$\begin{aligned}\chi_{\mathbf{G}, \mathbf{G}'}^{KS}(\mathbf{q}, \omega) &= \frac{1}{V} \sum_{nm; \mathbf{k}} 2f_{n(-\mathbf{k})} \frac{\langle u_{n(-\mathbf{k})} | e^{i\mathbf{G}\mathbf{r}} | u_{m(-\mathbf{k}-\mathbf{q})} \rangle \langle u_{m(-\mathbf{k}-\mathbf{q})} | e^{-i\mathbf{G}'\mathbf{r}'} | u_{n(-\mathbf{k})} \rangle}{\epsilon_{n(-\mathbf{k})} - \epsilon_{m(-\mathbf{k}-\mathbf{q})} - \tilde{\omega}} - \\ &- \frac{1}{V} \sum_{nm; \mathbf{k}} 2f_{n\mathbf{k}} \frac{\langle u_{m\mathbf{k}+\mathbf{q}} | e^{i\mathbf{G}\mathbf{r}} | u_{n\mathbf{k}} \rangle \langle u_{n\mathbf{k}} | e^{-i\mathbf{G}'\mathbf{r}'} | u_{m\mathbf{k}+\mathbf{q}} \rangle}{\epsilon_{m\mathbf{k}+\mathbf{q}} - \epsilon_{n\mathbf{k}} - \tilde{\omega}}.\end{aligned}\quad (2.34)$$

Both, the one-particle energy and the occupation function, are symmetric with respect to the crystal momentum  $\mathbf{k}$ , so that  $\epsilon_{-\mathbf{k}} = \epsilon_{\mathbf{k}}$  and  $f_{-\mathbf{k}} = f_{\mathbf{k}}$ . For the cell periodic part of the wavefunction,  $u_{-\mathbf{k}} = u_{\mathbf{k}}^*$  holds. By means of these relations the response function can be alternatively written as

$$\chi_{\mathbf{G},\mathbf{G}'}^{KS}(\mathbf{q},\omega) = -\frac{1}{V} \sum_{nm;\mathbf{k}} 2 f_{n\mathbf{k}} \langle u_{m\mathbf{k}+\mathbf{q}} | e^{i\mathbf{G}\mathbf{r}} | u_{n\mathbf{k}} \rangle \langle u_{n\mathbf{k}} | e^{-i\mathbf{G}'\mathbf{r}'} | u_{m\mathbf{k}+\mathbf{q}} \rangle \times \left( \frac{1}{\epsilon_{m\mathbf{k}+\mathbf{q}} - \epsilon_{n\mathbf{k}} - \tilde{\omega}} + \frac{1}{\epsilon_{m\mathbf{k}+\mathbf{q}} - \epsilon_{n\mathbf{k}} + \tilde{\omega}} \right), \quad (2.35)$$

where  $\tilde{\omega}$  has been defined in Eq. (2.16) as  $\tilde{\omega} = \omega + i\eta$ .

## 2.3 Dielectric function - macroscopic continuum considerations

The macroscopic dielectric function  $\varepsilon$  couples the total electric field  $\mathbf{E}$  in a material to the external electric field  $\mathbf{E}_{\text{ext}}$ :

$$\mathbf{E} = \varepsilon^{-1} \mathbf{E}_{\text{ext}}. \quad (2.36)$$

In general,  $\varepsilon$  is a  $3 \times 3$  Cartesian tensor. For a (macroscopic) homogenous material, Eq. (2.36) is a product in momentum and frequency space. If the external electric field is caused by stationary external charges, the electric field can be described as a gradient of an electric potential (longitudinal case),  $\mathbf{E} = \nabla\phi$ , and the relation between these potentials and the underlying charge densities is given by the Poisson equation:  $\nu\phi = \hat{e}n$  with the Coulomb-kernel  $\nu = 4\pi e^2/q^2$ . The mechanical potential  $v$  acting on the electrons is simply  $\phi$  times the unit charge  $\hat{e}$ . In momentum space and in the long-wavelength limit Eq. (2.36) can therefore be reformulated as:

$$v_{\text{tot}} = \varepsilon^{-1} v_{\text{ext}}, \quad (2.37)$$

where  $v_{\text{ext}}$  is the potential caused by the external charge density  $n_{\text{ext}}$ , whereas  $v_{\text{tot}} = v_{\text{ext}} + v_{\text{ind}}$  is the total, "screened" potential generated by the external plus the induced charge density  $n_{\text{ind}}$ . For weak external fields (linear response regime) one assumes that the induced charge is proportional to the external or the total potential, respectively:

$$n_{\text{ind}} = \chi v_{\text{ext}} \quad (\chi = \text{reducible polarizability}) \quad (2.38)$$

$$n_{\text{ind}} = P v_{\text{tot}} \quad (P = \text{irreducible polarizability}). \quad (2.39)$$

The dielectric function  $\varepsilon$  and its inverse  $\varepsilon^{-1}$  can then be expressed as:

$$\varepsilon^{-1} = \frac{v_{\text{tot}}}{v_{\text{ext}}} = \frac{v_{\text{ext}} + v_{\text{ind}}}{v_{\text{ext}}} = 1 + \nu \frac{n_{\text{ind}}}{v_{\text{ext}}} = 1 + \nu \chi \quad (2.40)$$

$$\varepsilon = \frac{v_{\text{ext}}}{v_{\text{tot}}} = \frac{v_{\text{tot}} - v_{\text{ind}}}{v_{\text{tot}}} = 1 - \nu \frac{n_{\text{ind}}}{v_{\text{tot}}} = 1 - \nu P. \quad (2.41)$$

Additionally a relation between the reducible and irreducible polarizability can be established:

$$1 = \varepsilon \varepsilon^{-1} = (1 - \nu P) (1 + \nu \chi) = 1 - \nu P + \nu \chi - \nu P \nu \chi = 1 - \nu(\chi - P - P\nu\chi) \rightarrow \chi = P + P\nu\chi \quad (2.42)$$

The relation between  $\chi$  and  $P$  has the form of a Dyson equation and is similar to the relation between  $\chi$  and  $\chi^{KS}$  which has been established in Eq. (2.14). According to Eq. (2.40) and Eq. (2.41) the dielectric function can thus be calculated if the response of the system to a change in the external or total potential is known.

A more detailed derivation will be given in Sec. 2.5. But first we will briefly describe the relation between the macroscopic and the microscopic dielectric function, both times following closely Ref. [20].

## 2.4 Macroscopic and microscopic quantities

In the present work, we will calculate the response function and the dielectric function for a periodic system. For a periodic system, the response function is homogenous on a coarse scale and the total macroscopic electric field follows the periodicity of the external perturbation, but the microscopic total electric field additionally exhibits rapid oscillations on the scale of the primitive cell. Therefore, the distinction between the macroscopic and the microscopic dielectric function becomes important. More details can be found in Ref. [20]. The dielectric function can be more formally written as:

$$\mathbf{E}(\mathbf{r}, \omega) = \int d^3r' \varepsilon_{\text{mac}}^{-1}(\mathbf{r} - \mathbf{r}', \omega) \mathbf{E}_{\text{ext}}(\mathbf{r}', \omega). \quad (2.43)$$

Here  $\mathbf{E}$  and  $\mathbf{E}_{\text{ext}}$  are the total and the external macroscopic electric fields that are connected by the macroscopic dielectric function  $\varepsilon_{\text{mac}}$ . Because the material is homogenous from a macroscopic point of view, the dielectric function depends only on the difference of the positions. The microscopic total electric field  $\mathbf{e}(\mathbf{r}, t)$  has large oscillations on the atomic scale. The corresponding microscopic dielectric function  $\varepsilon(\mathbf{r}, t)$  fulfills:

$$\mathbf{e}(\mathbf{r}, \omega) = \int d^3r' \varepsilon^{-1}(\mathbf{r}, \mathbf{r}', \omega) \mathbf{E}_{\text{ext}}(\mathbf{r}', \omega). \quad (2.44)$$

Because the macroscopic dielectric function only depends on the position difference, Eq. (2.43) transferred to momentum space is simply

$$\mathbf{E}(\mathbf{q}, \omega) = \varepsilon_{\text{mac}}^{-1}(\mathbf{q}, \omega) \mathbf{E}_{\text{ext}}(\mathbf{q}, \omega). \quad (2.45)$$

The microscopic dielectric function is only invariant under translations by a lattice vector

$$\begin{aligned} \varepsilon(\mathbf{r}, \mathbf{r}', \omega) &= \int \frac{d^3q'}{(2\pi)^3} \frac{d^3q''}{(2\pi)^3} e^{i\mathbf{q}'\mathbf{r}} \varepsilon(\mathbf{q}', \mathbf{q}'', \omega) e^{-i\mathbf{q}''\mathbf{r}'} = \\ &= \int \frac{d^3q'}{(2\pi)^3} \frac{d^3q''}{(2\pi)^3} e^{i\mathbf{q}'(\mathbf{r}+\mathbf{R})} \varepsilon(\mathbf{q}', \mathbf{q}'', \omega) e^{-i\mathbf{q}''(\mathbf{r}'+\mathbf{R})} = \varepsilon(\mathbf{r} + \mathbf{R}, \mathbf{r}' + \mathbf{R}, \omega) \end{aligned} \quad (2.46)$$

so that the difference between  $\mathbf{q}'$  and  $\mathbf{q}''$  has to be a reciprocal lattice vector. By setting  $\mathbf{q}' = \mathbf{q} + \mathbf{G}$  and  $\mathbf{q}'' = \mathbf{q} + \mathbf{G}'$ , one may write:

$$\begin{aligned} \mathbf{e}(\mathbf{q} + \mathbf{G}, \omega) &= \sum_{\mathbf{G}'} \varepsilon^{-1}(\mathbf{q} + \mathbf{G}, \mathbf{q} + \mathbf{G}', \omega) \mathbf{E}_{\text{ext}}(\mathbf{q} + \mathbf{G}', \omega) = \\ &= \sum_{\mathbf{G}'} \varepsilon_{\mathbf{G}, \mathbf{G}'}^{-1}(\mathbf{q}, \omega) \mathbf{E}_{\text{ext}}(\mathbf{q} + \mathbf{G}', \omega). \end{aligned} \quad (2.47)$$

The microscopic dielectric function is the quantity directly accessible in ab-initio calculations. In order to evaluate the macroscopic dielectric function we link the macroscopic electric field to the microscopic one:

$$\mathbf{E}(\mathbf{R}, \omega) = \frac{1}{V} \int_{V(\mathbf{R})} d^3r \mathbf{e}(\mathbf{r}, \omega) \quad (2.48)$$

where  $V(\mathbf{R})$  indicates integration over the unit cell at (around)  $\mathbf{R}$ . By Fourier transforming the microscopic electric field, the macroscopic electric field can be expressed as:

$$E(\mathbf{R}, \omega) = \sum_{\mathbf{G}} \int_{BZ} \frac{d^3q}{(2\pi)^3} \mathbf{e}(\mathbf{q} + \mathbf{G}, \omega) \frac{1}{V} \int_{V(\mathbf{R})} d^3r e^{i(\mathbf{q}+\mathbf{G})\mathbf{r}}. \quad (2.49)$$

If one assumes that the external field varies on a much larger length scale than the atomic distances ( $\mathbf{q} \ll \mathbf{G}_{\min}$ ), the term  $e^{i\mathbf{q}\mathbf{r}}$  can be placed in front of the unit cell integral:

$$\mathbf{E}(\mathbf{R}, \omega) = \sum_{\mathbf{G}} \int_{BZ} \frac{d^3q}{(2\pi)^3} \mathbf{e}(\mathbf{q} + \mathbf{G}, \omega) e^{i\mathbf{q}\mathbf{R}} \frac{1}{V} \int_{V(\mathbf{R})} d^3r e^{i\mathbf{G}\mathbf{r}} = \int_{BZ} \frac{d^3q}{(2\pi)^3} e^{i\mathbf{q}\mathbf{R}} \mathbf{e}(\mathbf{q}, \omega). \quad (2.50)$$

On the other hand,

$$\mathbf{E}(\mathbf{R}, \omega) = \sum_{\mathbf{G}} \int_{BZ} \frac{d^3q}{(2\pi)^3} e^{i(\mathbf{q}+\mathbf{G})\mathbf{R}} \mathbf{E}(\mathbf{q} + \mathbf{G}, \omega). \quad (2.51)$$

Comparison between Eq. (2.50) and Eq. (2.51) shows that the relationship between macroscopic and microscopic total electric field is

$$\mathbf{E}(\mathbf{q} + \mathbf{G}, \omega) = \mathbf{e}(\mathbf{q}, \omega) \delta_{\mathbf{G},0}. \quad (2.52)$$

Because the external field  $\mathbf{E}_{\text{ext}}$  is macroscopic,

$$\mathbf{E}_{\text{ext}}(\mathbf{q} + \mathbf{G}, \omega) = \mathbf{E}_{\text{ext}}(\mathbf{q}, \omega) \delta_{\mathbf{G},0}, \quad (2.53)$$

the relation between the macroscopic total and external field can be written as

$$\mathbf{E}(\mathbf{q}, \omega) = \mathbf{e}(\mathbf{q}, \omega) = \sum_{\mathbf{G}'} \varepsilon_{0\mathbf{G}'}^{-1}(\mathbf{q}, \omega) \mathbf{E}_{\text{ext}}(\mathbf{q}, \omega) \delta_{\mathbf{G}',0} = \varepsilon_{00}^{-1}(\mathbf{q}, \omega) \mathbf{E}_{\text{ext}}(\mathbf{q}, \omega). \quad (2.54)$$

Combining Eq. (2.54) and Eq. (2.45) the relation between microscopic and macroscopic dielectric function is given as:

$$\begin{aligned} \varepsilon_{\text{mac}}^{-1}(\mathbf{q}, \omega) &= \varepsilon_{00}^{-1}(\mathbf{q}, \omega) \\ \varepsilon_{\text{mac}}(\mathbf{q}, \omega) &= (\varepsilon_{00}^{-1}(\mathbf{q}, \omega))^{-1}. \end{aligned} \quad (2.55)$$

The macroscopic dielectric function is therefore obtained by inverting the microscopic dielectric function with respect to  $\mathbf{G}, \mathbf{G}'$ , taking the head ( $\mathbf{G} = \mathbf{G}' = 0$ ) of the resulting matrix and inverting this  $3 \times 3$  tensor. The fact that slowly varying external fields cause rapid oscillations on the macroscopic scale and the resulting effect on the macroscopic dielectric function are called local field effects. Only for materials that are also homogenous on the microscopic scale (like the homogenous electron gas), the off-diagonal elements of  $\varepsilon_{\mathbf{G},\mathbf{G}'}^{-1}$  are zero and no local field effects are present:

$$\varepsilon_{\text{mac}}(\mathbf{q}, \omega) = \varepsilon_{00}(\mathbf{q}, \omega). \quad (2.56)$$

In many cases, the microscopic dielectric function is calculated by Eq. (2.56). This approximation is usually referred to as "neglect of local field effects".

## 2.5 Longitudinal dielectric function

In Sec. 2.3 it has been sketched how to calculate the microscopic dielectric function. Here we show in more detail how the longitudinal dielectric function can be calculated. A longitudinal electric field  $\mathbf{E}$  is parallel to the wave vector  $\mathbf{q}$ . Related to this property is the requirement that  $\text{rot } \mathbf{E} = 0$ , and, as a consequence,  $\mathbf{E}$  can be described as a gradient field resulting from a scalar potential  $\mathbf{E} = \nabla \phi$ , and  $\hat{e} \nabla \mathbf{E} = 4\pi e^2 n$  [ $e^2 = \hat{e}^2 / (4\pi\epsilon_0)$ ]. The potential caused by the longitudinal electric field is given as  $v = \hat{e} \phi$ . Longitudinal fields result from only slowly moving charges. Transversal electric fields, as e.g., electromagnetic waves in vacuum, obey  $\text{div } \mathbf{E} = 0$  and the wave vector is perpendicular to the field vector. Nevertheless, for slowly varying fields ( $\mathbf{q} \rightarrow 0$ ) the longitudinal and transversal components of the dielectric function become equal (see Ref. [22] for a derivation of the transversal dielectric function). Considering Eq. (2.47) and replacing the electric fields by the densities through the Poisson equation

$$i \hat{e} \mathbf{q} \mathbf{E}(\mathbf{q}) = 4\pi e^2 n(\mathbf{q}) \quad (2.57)$$

we obtain a direct relation between external and induced charge densities

$$n_{\text{ext}}(\mathbf{q} + \mathbf{G}) = \sum_{\mathbf{G}'} (\mathbf{q} + \mathbf{G}) \varepsilon(\mathbf{q} + \mathbf{G}, \mathbf{q} + \mathbf{G}') (\mathbf{q} + \mathbf{G}') \frac{n_{\text{ext}}(\mathbf{q} + \mathbf{G}') + n_{\text{ind}}(\mathbf{q} + \mathbf{G}')}{(\mathbf{q} + \mathbf{G}')^2}. \quad (2.58)$$

In the present work we will concentrate on the longitudinal dielectric function  $\varepsilon^{LL}$ , which links the longitudinal component of the external electric field to the longitudinal component of the total electric field. For a longitudinal electric field the Poisson equation reads  $i \hat{e} |\mathbf{q}| |\mathbf{E}^L(\mathbf{q})| = 4\pi e^2 n(\mathbf{q})$  and Eq. (2.58) becomes:

$$n_{\text{ext}}(\mathbf{q} + \mathbf{G}) = \sum_{\mathbf{G}'} |\mathbf{q} + \mathbf{G}| \varepsilon^{LL}(\mathbf{q} + \mathbf{G}, \mathbf{q} + \mathbf{G}') |\mathbf{q} + \mathbf{G}'| \frac{n_{\text{ext}}(\mathbf{q} + \mathbf{G}') + n_{\text{ind}}(\mathbf{q} + \mathbf{G}')}{(\mathbf{q} + \mathbf{G}')^2}. \quad (2.59)$$

In the following, we will denote the longitudinal part of the dielectric function  $\varepsilon^{LL}$  simply as  $\varepsilon$ . By multiplying with the inverse of the dielectric function and using the Poisson equation  $n_{\text{ext}}(\mathbf{q} + \mathbf{G}) = (\mathbf{q} + \mathbf{G})^2 v_{\text{ext}}(\mathbf{q} + \mathbf{G}) / (4\pi e^2)$  [the Coulomb kernel  $\nu_{\mathbf{G}, \mathbf{G}'}(\mathbf{q})$  is defined as  $4\pi e^2 / (\mathbf{q} + \mathbf{G})^2 \delta_{\mathbf{G}, \mathbf{G}'}$ ], the external density can be written as

$$\sum_{\mathbf{G}'} [\varepsilon^{-1}(\mathbf{q} + \mathbf{G}, \mathbf{q} + \mathbf{G}') - \delta_{\mathbf{G}, \mathbf{G}'}] \frac{|\mathbf{q} + \mathbf{G}| |\mathbf{q} + \mathbf{G}'|}{4\pi e^2} v_{\text{ext}}(\mathbf{q} + \mathbf{G}') = n_{\text{ind}}(\mathbf{q} + \mathbf{G}). \quad (2.60)$$

Taking the derivative with respect to the Fourier component  $v_{\text{ext}}(\mathbf{q} + \mathbf{G}')$ , the inverse of the microscopic (symmetric<sup>1</sup>) dielectric function can be expressed as:

$$\varepsilon_{\mathbf{G}, \mathbf{G}'}^{-1}(\mathbf{q}, \omega) := \varepsilon^{-1}(\mathbf{q} + \mathbf{G}, \mathbf{q} + \mathbf{G}', \omega) = \delta_{\mathbf{G}, \mathbf{G}'} + \frac{4\pi e^2}{|\mathbf{q} + \mathbf{G}| |\mathbf{q} + \mathbf{G}'|} \frac{\partial n_{\text{ind}}(\mathbf{q} + \mathbf{G}, \omega)}{\partial v_{\text{ext}}(\mathbf{q} + \mathbf{G}', \omega)}. \quad (2.61)$$

---

<sup>1</sup>There exists a slightly different definition of the longitudinal dielectric function (as e.g., used by Adler [22] and Wiser [23]) where the term  $4\pi e^2 / (|\mathbf{q} + \mathbf{G}| |\mathbf{q} + \mathbf{G}'|)$  in Eq. (2.61) is replaced by the Coulomb kernel  $\nu_{\mathbf{G}, \mathbf{G}'}(\mathbf{q})$ ; in contrast to the present definition the dielectric function is then not symmetric anymore with respect to  $\mathbf{G}, \mathbf{G}'$

By similar manipulations one finds that:

$$\varepsilon_{\mathbf{G},\mathbf{G}'}(\mathbf{q},\omega) := \varepsilon(\mathbf{q} + \mathbf{G}, \mathbf{q} + \mathbf{G}', \omega) = \delta_{\mathbf{G},\mathbf{G}'} - \frac{4\pi e^2}{|\mathbf{q} + \mathbf{G}||\mathbf{q} + \mathbf{G}'|} \frac{\partial n_{\text{ind}}(\mathbf{q} + \mathbf{G}, \omega)}{\partial v_{\text{tot}}(\mathbf{q} + \mathbf{G}', \omega)}. \quad (2.62)$$

These formulas have been written in a simplified way in Eq. (2.40) and Eq. (2.41). The reducible polarizability (also density-density response function)  $\chi$  and the irreducible polarizability (also screened response function)  $P$  are defined as

$$\frac{\partial n_{\text{ind}}(\mathbf{q} + \mathbf{G}, \omega)}{\partial v_{\text{ext}}(\mathbf{q} + \mathbf{G}', \omega)} =: \chi_{\mathbf{G},\mathbf{G}'}(\mathbf{q}, \omega) \quad \frac{\partial n_{\text{ind}}(\mathbf{q} + \mathbf{G}, \omega)}{\partial v_{\text{tot}}(\mathbf{q} + \mathbf{G}', \omega)} =: P_{\mathbf{G},\mathbf{G}'}(\mathbf{q}, \omega). \quad (2.63)$$

With  $\nu_{\mathbf{G},\mathbf{G}'}^s(\mathbf{q}) := \frac{4\pi e^2}{|\mathbf{q} + \mathbf{G}||\mathbf{q} + \mathbf{G}'|}$ , the dielectric function and its inverse become:

$$\varepsilon_{\mathbf{G},\mathbf{G}'}^{-1}(\mathbf{q}, \omega) = \delta_{\mathbf{G},\mathbf{G}'} + \nu_{\mathbf{G},\mathbf{G}'}^s(\mathbf{q}) \chi_{\mathbf{G},\mathbf{G}'}(\mathbf{q}, \omega) \quad (2.64)$$

$$\varepsilon_{\mathbf{G},\mathbf{G}'}(\mathbf{q}, \omega) = \delta_{\mathbf{G},\mathbf{G}'} - \nu_{\mathbf{G},\mathbf{G}'}^s(\mathbf{q}) P_{\mathbf{G},\mathbf{G}'}(\mathbf{q}, \omega). \quad (2.65)$$

By combining the last two equations, one finds that the density-density response function  $\chi$  and the screened response function  $P$  are connected by a Dyson like equation:

$$\chi_{\mathbf{G},\mathbf{G}'}(\mathbf{q}, \omega) = P_{\mathbf{G},\mathbf{G}'}(\mathbf{q}, \omega) + \sum_{\mathbf{G}_1 \mathbf{G}_2} P_{\mathbf{G},\mathbf{G}_1}(\mathbf{q}, \omega) \nu_{\mathbf{G}_1,\mathbf{G}_2}^s(\mathbf{q}) \chi_{\mathbf{G}_2,\mathbf{G}'}(\mathbf{q}, \omega). \quad (2.66)$$

In this section we have derived an expression for the longitudinal dielectric function (following closely the procedure in [20]) depending on the momentum transfer  $\mathbf{q}$  caused by a perturbation with frequency  $\omega$  and spatial periodicity  $\mathbf{q}$ . The transversal component of the dielectric function is e.g., derived in the work by Adler [22].

## 2.6 Approximations

Because neither  $\chi$  nor  $P$  are known for a general system, an approximation has to be considered in order to calculate the dielectric function. The quantity accessible in DFT calculations is the independent particle response function  $\chi^{KS}$  as defined in Eq. (2.33), which describes the response of a system of independent electrons moving in an effective potential to a change in this potential.

Two approximations for the calculation of the longitudinal dielectric function seem straightforward: On the one hand,  $\chi$  could be replaced by  $\chi^{KS}$  in Eq. (2.64), which is equivalent to the assumption that the system responds to a change of the external potential like a system of independent particles. On the other hand, the screened response function  $P$  can be replaced by the  $KS$  response function  $\chi^{KS}$  in Eq. (2.65). This procedure, which is called random phase approximation (RPA) or Hartree approximation, has been shown to be more accurate because it mimics the true reaction of the system as an independent particle response to the screened potential, which guarantees that the electron-electron interaction is taken at least partly into account. Within the random phase approximation, the dielectric function is given as

$$\varepsilon_{\mathbf{G},\mathbf{G}'}^{RPA}(\mathbf{q}, \omega) = \delta_{\mathbf{G},\mathbf{G}'} - \nu_{\mathbf{G},\mathbf{G}'}^s(\mathbf{q}) \chi_{\mathbf{G},\mathbf{G}'}^{KS}(\mathbf{q}, \omega). \quad (2.67)$$



An equation similar to Eq. (2.66) has been already established for the density response to an external potential  $\chi$  and the independent particle response to the effective KS potential  $\chi^{KS}$  in Eq. (2.14). Translated to momentum space Eq. (2.14) reads

$$\begin{aligned} \chi_{\mathbf{G},\mathbf{G}'}(\mathbf{q},\omega) &= \chi_{\mathbf{G},\mathbf{G}'}^{KS}(\mathbf{q},\omega) + \\ &+ \sum_{\mathbf{G}_1\mathbf{G}_2} \chi_{\mathbf{G},\mathbf{G}_1}^{KS}(\mathbf{q},\omega) \left( \nu_{\mathbf{G}_1,\mathbf{G}_2}^s(\mathbf{q}) + f_{xc,\mathbf{G}_1\mathbf{G}_2}(\mathbf{q},\omega) \right) \chi_{\mathbf{G}_2,\mathbf{G}'}(\mathbf{q},\omega). \end{aligned} \quad (2.68)$$

The term random phase approximation is also used if one neglects the exchange-correlation kernel  $f_{xc}(\mathbf{q},\omega)$  in Eq. (2.68).

If going beyond the RPA, the dielectric function is evaluated from Eq. (2.65) and the irreducible polarizability  $P$  is calculated using the relation<sup>1</sup>

$$P_{\mathbf{G},\mathbf{G}'}(\mathbf{q},\omega) = \chi_{\mathbf{G},\mathbf{G}'}^{KS}(\mathbf{q},\omega) + \sum_{\mathbf{G}_1\mathbf{G}_2} \chi_{\mathbf{G},\mathbf{G}_1}^{KS}(\mathbf{q},\omega) f_{xc,\mathbf{G}_1\mathbf{G}_2}(\mathbf{q},\omega) P_{\mathbf{G}_2,\mathbf{G}'}(\mathbf{q},\omega). \quad (2.69)$$

An accurate description of the screened response function and consequently the dielectric function therefore relies on a reasonable approximation for the exchange-correlation kernel  $f_{xc}$ . The most widely used approximation for the exchange-correlation kernel (beside the random phase approximation) is the adiabatic local density approximation (ALDA), which is also called time-dependent local density approximation, where the exchange-correlation kernel  $f_{xc}$  is approximated by a frequency independent, local expression

$$f_{xc}^{ALDA}(\mathbf{r}_1, \mathbf{r}_2) = \delta(\mathbf{r}_1 - \mathbf{r}_2) \frac{\partial v_{xc}^{LDA}(n)}{\partial n(\mathbf{r}_1)}. \quad (2.70)$$

For localized systems, the ALDA seems to provide reasonable results (see e.g. Ref. [24]), but it does not improve the description of the long-wavelength limit ( $\mathbf{q} \rightarrow 0$ ) of the macroscopic dielectric function in extended systems. One possibility to calculate the macroscopic dielectric function is to evaluate the head of the inverse of the microscopic dielectric function as given in Eq. (2.64), and the required reducible polarizability  $\chi$  by Eq. (2.68). It can be shown that the ALDA exchange-correlation kernel approaches a finite value as  $\mathbf{q} \rightarrow 0$ , while the Coulomb kernel diverges as  $1/|\mathbf{q}|^2$ . The influence of the exchange-correlation kernel thus vanishes in the long-wavelength limit for the ALDA, which is known to be incorrect (e.g. excitonic effects are not accounted for).

## 2.7 Calculation of optical properties

In this section the calculation of the response function and the dielectric function in the VASP code will be addressed. Both the response function and the dielectric function are represented in reciprocal space and the projector augmented-wave method (PAW) is used.

---

<sup>1</sup>Eq. (2.66), Eq. (2.68), and Eq. (2.69) can be formulated in a more convenient way by multiplying the equations from the right and the left by the inverse of the contributing response functions. The equations then read:  $P^{-1} = \chi^{-1} + \nu$  [Eq. (2.66)],  $(\chi^{KS})^{-1} = \chi^{-1} + (\nu + f_{xc})$  [Eq. (2.68)],  $(\chi^{KS})^{-1} = P^{-1} + f_{xc}$  [Eq. (2.69)]. These equations can be easily derived by the relations between the external, total, induced, and effective KS potential.

The present summary follows closely the publication by Gajdoš *et al.* [21] and Shishkin *et al.* [25].

In part II of this thesis, the dielectric function of surfaces will be calculated. If one assumes that the response to the screened external perturbation,  $P$ , equals the independent particle response function  $\chi^{KS}$  as given in Eq. (2.35), namely if one applies the random phase approximation, the dielectric function is given by [see Eq. (2.67)]:

$$\varepsilon_{\mathbf{G},\mathbf{G}'}(\mathbf{q},\omega) = \varepsilon_{\mathbf{G},\mathbf{G}'}^{RPA}(\mathbf{q},\omega) = \delta_{\mathbf{G},\mathbf{G}'} - \frac{4\pi e^2}{|\mathbf{G} + \mathbf{q}||\mathbf{G}' + \mathbf{q}|} \chi_{\mathbf{G},\mathbf{G}'}^{KS}(\mathbf{q},\omega). \quad (2.71)$$

For the reflectance difference spectra the long-wavelength macroscopic dielectric function  $\varepsilon_{\infty}(\hat{\mathbf{q}},\omega) = 1/(\lim_{q \rightarrow 0} \varepsilon_{0,0}^{-1}(\mathbf{q},\omega))$ , which describes the response of a material to a perturbation with slow spatial variations, has to be calculated. We will, in the following, neglect local field effects (see section 2.5) and will evaluate the macroscopic dielectric function directly from the head of the microscopic dielectric function:

$$\varepsilon_{\text{mac}}(\hat{\mathbf{q}},\omega) \approx \lim_{\mathbf{q} \rightarrow 0} \varepsilon_{00}(\mathbf{q},\omega) = 1 - \lim_{\mathbf{q} \rightarrow 0} \frac{4\pi e^2}{q^2} \chi_{0,0}^{KS}(\mathbf{q},\omega). \quad (2.72)$$

Within these approximations the imaginary part of the dielectric function ( $\varepsilon = \varepsilon^{(1)} + i\varepsilon^{(2)}$ ), the absorption spectrum  $\varepsilon^{(2)}(\omega)$ , can be evaluated as a sum over  $\delta$ -like peaks (Lorentzian peaks with width  $\eta$ , respectively) at transition energies  $\omega = \epsilon_{m\mathbf{k}} - \epsilon_{n\mathbf{k}}$ , which are weighted by the transition probability  $|\langle u_{m\mathbf{k}+\mathbf{q}} | u_{n\mathbf{k}} \rangle|^2$ :

$$\begin{aligned} \varepsilon^{(2)}(\hat{\mathbf{q}},\omega) &= \frac{4\pi^2 e^2}{V} \lim_{q \rightarrow 0} \frac{1}{q^2} \sum_{\substack{nm \\ \mathbf{k}}} 2 f_{n\mathbf{k}} |\langle u_{m\mathbf{k}+\mathbf{q}} | u_{n\mathbf{k}} \rangle|^2 \times \\ &\quad \times [\delta(\epsilon_{m\mathbf{k}} - \epsilon_{n\mathbf{k}} - \omega) - \delta(\epsilon_{m\mathbf{k}} - \epsilon_{n\mathbf{k}} + \omega)]. \end{aligned} \quad (2.73)$$

While  $\mathbf{q} \rightarrow 0$ , the dielectric function  $\varepsilon^{(2)}$  still depends on the direction of  $\mathbf{q}$ , described by the unit vector  $\hat{\mathbf{q}} = \mathbf{q}/|\mathbf{q}|$ . One can introduce the dielectric tensor  $\varepsilon_{\alpha\beta}$  by setting:

$$\varepsilon^{(2)}(\hat{\mathbf{q}},\omega) =: \sum_{\alpha,\beta} \hat{\mathbf{q}}_{\alpha} \varepsilon_{\alpha\beta}^{(2)}(\hat{\mathbf{q}},\omega) \hat{\mathbf{q}}_{\beta}. \quad (2.74)$$

The imaginary part of the dielectric function is then fully described by the Cartesian tensor  $\varepsilon_{\alpha\beta}$

$$\begin{aligned} \varepsilon_{\alpha,\beta}^{(2)}(\hat{\mathbf{q}},\omega) &= \frac{4\pi^2 e^2}{V} \lim_{q \rightarrow 0} \frac{1}{q^2} \sum_{\substack{nm \\ \mathbf{k}}} 2 f_{n\mathbf{k}} \langle u_{m\mathbf{k}+\mathbf{e}_{\alpha}q} | u_{n\mathbf{k}} \rangle \langle u_{n\mathbf{k}} | u_{m\mathbf{k}+\mathbf{e}_{\beta}q} \rangle \times \\ &\quad \times [\delta(\epsilon_{m\mathbf{k}} - \epsilon_{n\mathbf{k}} - \omega) - \delta(\epsilon_{m\mathbf{k}} - \epsilon_{n\mathbf{k}} + \omega)]. \end{aligned} \quad (2.75)$$

Often, only interband transitions ( $n \neq m$ ) are considered in Eq. (2.75). For metals, where partially occupied states exist, also transitions within one band are possible. These transitions, referred to as intraband transitions, are discussed in more detail at the end of this section. For metals, they lead to the so called Drude term, which is responsible for the large metallic screening at small frequencies and small wavevectors  $\mathbf{q}$  and is determined by the intraband plasma frequency.

The calculation of the real part of the dielectric function  $\varepsilon^{(1)}$  is performed by a Hilbert transformation:

$$\varepsilon^{(1)}(\omega) = 1 + \frac{2}{\pi} P \int_0^\infty \frac{\varepsilon^{(2)}(\omega') \omega'}{\omega'^2 - \omega^2} d\omega', \quad (2.76)$$

resulting in

$$\begin{aligned} \varepsilon^{(1)}(\hat{\mathbf{q}}, \omega) = 1 + \frac{4\pi e^2}{V} \lim_{q \rightarrow 0} \frac{1}{q^2} \sum_{nm} 2 f_{n\mathbf{k}} |\langle u_{m\mathbf{k}+\mathbf{q}} | u_{n\mathbf{k}} \rangle|^2 \times \\ \times \left( \frac{1}{\epsilon_{m\mathbf{k}} - \epsilon_{n\mathbf{k}} - \omega} + \frac{1}{\epsilon_{m\mathbf{k}} - \epsilon_{n\mathbf{k}} + \omega} \right), \end{aligned} \quad (2.77)$$

or in tensor form

$$\begin{aligned} \varepsilon_{\alpha\beta}^{(1)}(\hat{\mathbf{q}}, \omega) = 1 + \frac{4\pi e^2}{V} \lim_{q \rightarrow 0} \frac{1}{q^2} \sum_{nm} 2 f_{n\mathbf{k}} \langle u_{m\mathbf{k}+\mathbf{e}_\alpha q} | u_{n\mathbf{k}} \rangle \langle u_{n\mathbf{k}} | u_{m\mathbf{k}+\mathbf{e}_\beta q} \rangle \times \\ \times \left( \frac{1}{\epsilon_{m\mathbf{k}} - \epsilon_{n\mathbf{k}} - \omega} + \frac{1}{\epsilon_{m\mathbf{k}} - \epsilon_{n\mathbf{k}} + \omega} \right). \end{aligned} \quad (2.78)$$

### 2.7.1 PAW response function

For the calculation of the response function as given in Eq. (2.33) and Eq. (2.35), the transition probabilities

$$\begin{aligned} \langle u_{m\mathbf{k}+\mathbf{q}} | e^{i\mathbf{G}\mathbf{r}} | u_{n\mathbf{k}} \rangle &= \int_V d^3r e^{i\mathbf{G}\mathbf{r}} u_{m\mathbf{k}+\mathbf{q}}^*(\mathbf{r}) u_{n\mathbf{k}}(\mathbf{r}) = \\ &= \int_V d^3r e^{i(\mathbf{G}+\mathbf{q})\mathbf{r}} \psi_{m\mathbf{k}+\mathbf{q}}^*(\mathbf{r}) \psi_{n\mathbf{k}}(\mathbf{r}) = \langle \psi_{m\mathbf{k}+\mathbf{q}} | e^{i(\mathbf{G}+\mathbf{q})\mathbf{r}} | \psi_{n\mathbf{k}} \rangle \end{aligned} \quad (2.79)$$

have to be evaluated. For this reason, we introduce  $B$  (instead of the index  $m$  we write  $n'$  in order to avoid confusion with the magnetic quantum number  $m$  which will be used later):

$$B_{n'\mathbf{k}+\mathbf{q}, n\mathbf{k}}(\mathbf{r}) = e^{i\mathbf{q}\mathbf{r}} \psi_{n'\mathbf{k}+\mathbf{q}}^*(\mathbf{r}) \psi_{n\mathbf{k}}(\mathbf{r}). \quad (2.80)$$

In the PAW method, the all-electron (AE) wavefunction  $|\psi_{n\mathbf{k}}\rangle$  is separated into a pseudo (PS) wavefunction  $|\tilde{\psi}_{n\mathbf{k}}\rangle$  and on-site terms expanded into AE partial waves  $|\phi_i\rangle$  and PS partial waves  $|\tilde{\phi}_i\rangle$  as introduced in subsection 1.3.2 [see Eq. (1.20)]. Here the  $\mathbf{k}$ -dependent projector functions  $|\tilde{p}_{i\mathbf{k}}\rangle$ , as used in VASP,

$$|\tilde{p}_{i\mathbf{k}}\rangle = e^{-i\mathbf{k}(\mathbf{r}-\mathbf{R}_i)} |\tilde{p}_i\rangle. \quad (2.81)$$

are additionally defined where  $\mathbf{R}_i$  is the position of the ion  $i$ . The coefficient of the expansion with respect to AE and PS partial waves is consequently given by

$$\langle \tilde{p}_i | \tilde{\psi}_{n\mathbf{k}} \rangle = e^{i\mathbf{k}\mathbf{R}_i} \langle \tilde{p}_{i\mathbf{k}} | \tilde{u}_{n\mathbf{k}} \rangle. \quad (2.82)$$

Within the PAW framework  $B$  can be written as

$$B_{n'\mathbf{k}+\mathbf{q},n\mathbf{k}}(\mathbf{r}) = \tilde{u}_{n'\mathbf{k}+\mathbf{q}}^*(\mathbf{r})\tilde{u}_{n\mathbf{k}}(\mathbf{r}) + \sum_{ij} \langle \tilde{u}_{n'\mathbf{k}+\mathbf{q}} | \tilde{p}_{i\mathbf{k}+\mathbf{q}} \rangle \langle \tilde{p}_{j\mathbf{k}} | \tilde{u}_{n\mathbf{k}} \rangle e^{i\mathbf{q}(\mathbf{r}-\mathbf{R}_i)} \left[ \phi_i^*(\mathbf{r})\phi_j(\mathbf{r}) - \tilde{\phi}_i^*(\mathbf{r})\tilde{\phi}_j(\mathbf{r}) \right] \quad (2.83)$$

where we have used that the PS wavefunction  $|\tilde{\psi}_{n\mathbf{k}}\rangle$  equals  $\sum_i \langle p_i | \tilde{\psi}_{n\mathbf{k}} \rangle |\tilde{\phi}_i\rangle$  inside  $\Omega_a$ . The first part of Eq. (2.83) is a relatively smooth function and is represented on a regular, plane wave grid. The second term in Eq. (2.83) exhibits rapid oscillations because it is related to the difference between AE and PS partial waves  $Q_{ij}(\mathbf{r}) = \phi_i^*(\mathbf{r})\phi_j(\mathbf{r}) - \tilde{\phi}_i^*(\mathbf{r})\tilde{\phi}_j(\mathbf{r})$ . It is usually described on a radial grid around the ions. A transformation of this term to the regular grid would require a very dense plane wave grid or a very high plane wave cutoff, respectively. For the head ( $\mathbf{G} + \mathbf{q} \rightarrow 0$  and  $\mathbf{G}' + \mathbf{q} \rightarrow 0$ ) and the wings ( $\mathbf{G} + \mathbf{q} \rightarrow 0$  or  $\mathbf{G}' + \mathbf{q} \rightarrow 0$ ) of the dielectric function, the on-site terms are correctly taken into account (see Sec. 2.7.2). For the body of the polarizability some approximations to Eq. (2.83) have to be applied:

By default  $B$  is approximated by

$$B_{n'\mathbf{k}+\mathbf{q},n\mathbf{k}}(\mathbf{r}) = \tilde{u}_{n'\mathbf{k}+\mathbf{q}}^*(\mathbf{r})\tilde{u}_{n\mathbf{k}}(\mathbf{r}) + \sum_{ij,lm} \langle \tilde{u}_{n'\mathbf{k}+\mathbf{q}} | \tilde{p}_{i\mathbf{k}+\mathbf{q}} \rangle \langle \tilde{p}_{j\mathbf{k}} | \tilde{u}_{n\mathbf{k}} \rangle e^{i\mathbf{q}(\mathbf{r}-\mathbf{R}_i)} \hat{Q}_{ij}^{lm}(\mathbf{r}). \quad (2.84)$$

where  $\hat{Q}_{ij}^{lm}(\mathbf{r})$  [see Eq. (1.26)] and  $Q_{ij}(\mathbf{r})$  have the same monopole/multipole moments  $lm$  but their shapes do not coincide. Per construction,  $\hat{Q}_{ij}^{lm}(\mathbf{r})$  is smooth and can be easily represented on a regular grid. This construction allows the accurate calculation of electrostatic (Hartree) energies, but it does not suffice to obtain very accurate dielectric functions  $\varepsilon_{\mathbf{G},\mathbf{G}'}(\mathbf{q},\omega)$ . A more sophisticated treatment of the augmentation charges is possible by trying to conserve the Fourier development of the charge density at small Fourier components  $\mathbf{q}$ . In this case, not only the correct moments but also the shape of the augmentation charge  $Q_{ij}(\mathbf{r})$  is approximatively reproduced. For each momentum number ( $lm$ ) accessible:

$$m = m_i + m_j, \quad l = |l_i - l_j|, |l_i - l_j| + 2, \dots, l_i + l_j \quad (2.85)$$

an additional function  $\Delta Q_{ij}^{lm}(\mathbf{r}) = \Delta g_l^{ij}(|\mathbf{r}-\mathbf{R}|)Y_L(\widehat{\mathbf{r}-\mathbf{R}})$  is introduced. The radial function  $\Delta g_l^{ij}(r)$  is written as a sum of spherical Bessel functions

$$\Delta g_l^{ij}(r) = \sum_i j_l(q_i r) \alpha_{ij}. \quad (2.86)$$

The coefficients are chosen such that the multipole  $lm$  vanishes and that the Bessel transform of  $\Delta g_l^{ij}(r)$  is the same as the Bessel transform of  $Q_{ij}(r) - \hat{Q}_{ij}(r)$  at  $q = 6 \text{ \AA}^{-1}$  (70 eV). In a calculation such an improved description of the response function can be selected by setting LMAXFOCKAE in the INCAR file. The value of LMAXFOCKAE specifies the maximal angular momentum number  $l$  up to which this correction is applied. As values up to  $l_i + l_j$  can occur, LMAXFOCKAE should be chosen larger if partial waves with high angular momentum numbers exist. With the LMAXFOCKAE correction  $B$  is approximated as

$$B_{n'\mathbf{k}+\mathbf{q},n\mathbf{k}}(\mathbf{r}) = \tilde{u}_{n'\mathbf{k}+\mathbf{q}}^*(\mathbf{r})\tilde{u}_{n\mathbf{k}}(\mathbf{r}) + \sum_{ij,lm} \langle \tilde{u}_{n'\mathbf{k}+\mathbf{q}} | \tilde{p}_{i\mathbf{k}+\mathbf{q}} \rangle \langle \tilde{p}_{j\mathbf{k}} | \tilde{u}_{n\mathbf{k}} \rangle e^{i\mathbf{q}(\mathbf{r}-\mathbf{R}_i)} \left( \hat{Q}_{ij}^{lm}(\mathbf{r}) + \Delta Q_{ij}^{lm}(\mathbf{r}) \right). \quad (2.87)$$

For both, GW calculations (part III) and the evaluation of the RPA-ACFDT correlation energy (part IV), setting LMAXFOCKAE leads to noticeable changes in the resulting spectra and energies and therefore will, except for test calculations, be set throughout the following sections.

### 2.7.2 Long-wavelength dielectric function

For the head ( $\mathbf{G} + \mathbf{q}$  and  $\mathbf{G}' + \mathbf{q} \rightarrow 0$ ) and the wings ( $\mathbf{G} + \mathbf{q}$  or  $\mathbf{G}' + \mathbf{q} \rightarrow 0$ ) of the dielectric function (and  $\nu\chi$ ) the direct multiplication of the response function with the Coulomb kernel leads to a division by zero. Due to this reason, the behavior of  $\langle u_{n'\mathbf{k}+\mathbf{q}} | e^{i\mathbf{q}\mathbf{r}} | u_{n\mathbf{k}} \rangle$  for  $\mathbf{G} = 0$  and  $\mathbf{q} \rightarrow 0$  will be expanded with respect to  $\mathbf{q}$  in the following. More details concerning the implementation in VASP can be found again in Ref. [21]. For the calculation of

$$\lim_{\mathbf{q} \rightarrow 0} \langle \Psi_{n'\mathbf{k}+\mathbf{q}} | e^{i\mathbf{q}\mathbf{r}} | \Psi_{n\mathbf{k}} \rangle = \lim_{\mathbf{q} \rightarrow 0} \int_V d^3r B_{n'\mathbf{k}+\mathbf{q},n\mathbf{k}}(\mathbf{r}), \quad (2.88)$$

the phase factor  $e^{i\mathbf{q}(\mathbf{r}-\mathbf{R}_i)}$  in Eq. (2.83) can be expanded to first order in  $\mathbf{q}$ :

$$e^{i\mathbf{q}(\mathbf{r}-\mathbf{R}_i)} = 1 + i\mathbf{q}(\mathbf{r} - \mathbf{R}_i) + \mathbf{O}(\mathbf{q}^2). \quad (2.89)$$

This leads to

$$\lim_{\mathbf{q} \rightarrow 0} \langle \Psi_{n'\mathbf{k}+\mathbf{q}} | e^{i\mathbf{q}\mathbf{r}} | \Psi_{n\mathbf{k}} \rangle = \langle \tilde{u}_{n'\mathbf{k}+\mathbf{q}} | \tilde{u}_{n\mathbf{k}} \rangle + \sum_{ij} \langle \tilde{u}_{n'\mathbf{k}+\mathbf{q}} | \tilde{p}_{i\mathbf{k}+\mathbf{q}} \rangle q_{ij} \langle \tilde{p}_{j\mathbf{k}} | \tilde{u}_{n\mathbf{k}} \rangle + \quad (2.90)$$

$$+ i\mathbf{q} \sum_{ij} \langle \tilde{u}_{n'\mathbf{k}+\mathbf{q}} | \tilde{p}_{i\mathbf{k}+\mathbf{q}} \rangle \vec{\tau}_{ij} \langle \tilde{p}_{j\mathbf{k}} | \tilde{u}_{n\mathbf{k}} \rangle, \quad (2.91)$$

where  $q_{ij}$  and  $\vec{\tau}_{ij}$  are short notations for the difference of the norm and the dipole moments of the AE and PS partial waves:

$$q_{ij} = \int_{\Omega_a} \left[ \phi_i^*(\mathbf{r}) \phi_j(\mathbf{r}) - \tilde{\phi}_i^*(\mathbf{r}) \tilde{\phi}_j(\mathbf{r}) \right] d^3r \quad (2.92)$$

$$\vec{\tau}_{ij} = \int_{\Omega_a} (\mathbf{r} - \mathbf{R}_i) \left[ \phi_i^*(\mathbf{r}) \phi_j(\mathbf{r}) - \tilde{\phi}_i^*(\mathbf{r}) \tilde{\phi}_j(\mathbf{r}) \right] d^3r. \quad (2.93)$$

In a next step,  $\tilde{u}_{n\mathbf{k}}(\mathbf{r})$  is expanded for small values of the momentum  $\mathbf{q}$ :

$$\tilde{u}_{n\mathbf{k}+\mathbf{q}}(\mathbf{r}) = \tilde{u}_{n\mathbf{k}}(\mathbf{r}) + \mathbf{q} \nabla_{\mathbf{k}} \tilde{u}_{n\mathbf{k}}(\mathbf{r}) + \mathbf{O}(\mathbf{q}^2). \quad (2.94)$$

For the  $\mathbf{k}$ -dependent projector functions  $\tilde{p}_{i\mathbf{k}}$  [see Eq. (2.81) and Eq. (2.89)] one obtains:

$$|\tilde{p}_{i\mathbf{k}+\mathbf{q}}\rangle = [1 - i\mathbf{q}(\mathbf{r} - \mathbf{R}_i)] |\tilde{p}_{i\mathbf{k}}\rangle + \mathbf{O}(\mathbf{q}^2). \quad (2.95)$$

Applying these two expansions we find:

$$\lim_{\mathbf{q} \rightarrow 0} \langle \Psi_{n'\mathbf{k}+\mathbf{q}} | e^{i\mathbf{q}\mathbf{r}} | \Psi_{n\mathbf{k}} \rangle = \langle u_{n'\mathbf{k}}(\mathbf{r}) | \left( 1 + \sum_{ij} |\tilde{p}_{i\mathbf{k}}\rangle q_{ij} \langle \tilde{p}_{j\mathbf{k}} | \right) | u_{n\mathbf{k}}(\mathbf{r}) \rangle + |\mathbf{q}| \langle \hat{\mathbf{q}} | \vec{\beta}_{n'\mathbf{k}} | \tilde{u}_{n\mathbf{k}} \rangle, \quad (2.96)$$

with

$$|\vec{\beta}_{n\mathbf{k}}\rangle = \left(1 + \sum_{ij} |\tilde{p}_{i\mathbf{k}}\rangle q_{ij} \langle \tilde{p}_{j\mathbf{k}}|\right) |\nabla_{\mathbf{k}} \tilde{u}_{n\mathbf{k}}\rangle + i \left( \sum_{ij} |\tilde{p}_{i\mathbf{k}}\rangle q_{ij} \langle \tilde{p}_{j\mathbf{k}}|(\mathbf{r} - \mathbf{R}_i) \right) |\tilde{u}_{n\mathbf{k}}\rangle - i \sum_{ij} |\tilde{p}_{i\mathbf{k}}\rangle \tilde{\tau}_{ij} \langle \tilde{p}_{j\mathbf{k}}| \tilde{u}_{n\mathbf{k}}\rangle. \quad (2.97)$$

Due to the orthogonality relation between the PS wavefunctions (see Sec. III A in [15]), the first term on the right hand side of Eq. (2.96) is zero so that the final expression becomes:

$$\lim_{\mathbf{q} \rightarrow 0} \langle \Psi_{n'\mathbf{k}+\mathbf{q}} | e^{i\mathbf{q}\mathbf{r}} | \Psi_{n\mathbf{k}} \rangle = |\mathbf{q}| \langle \hat{\mathbf{q}} | \vec{\beta}_{n'\mathbf{k}} | \tilde{u}_{n\mathbf{k}} \rangle, \quad (2.98)$$

and is consequently linear in  $|\mathbf{q}|$ . Because always a product of two terms like Eq. (2.98) occurs, the  $1/q^2$  term resulting from the Coulomb kernel is canceled. The derivative of the cell periodic part of the PS wavefunctions  $|\nabla_{\mathbf{k}} \tilde{u}_{n\mathbf{k}}\rangle$  is calculated using first-order perturbation theory. For more details see Section II F in Ref. [21].

## 2.8 Intraband transitions and the plasma frequency

In the previous section, the calculation of the long-wavelength dielectric function was discussed. But only interband transitions, i.e., transitions between different bands  $n \neq m$  have been considered. For semiconductors and insulators this accounts for all possible transitions, because every band is either fully occupied ( $f = 1$ ) or fully unoccupied ( $f = 0$ ) and therefore transitions within one band do not occur.

For metallic systems there exists a non-vanishing probability that an electron is excited from one state below the Fermi level to a state above the Fermi level both belonging to one and the same band. These transitions are called intraband transitions and lead to the so called Drude term for the long-wavelength limit.

The calculation of intraband contributions for  $\mathbf{q} \neq 0$  does not lead to any complications and the same treatment as discussed in the previous section can be applied. But for the long-wavelength limit  $\mathbf{q} \rightarrow 0$ , the head of the dielectric function  $\mathbf{G} = \mathbf{G}' = 0$  (which equals the macroscopic dielectric function if local field effects are neglected)

$$\varepsilon_{\text{intra}}^{(1)}(\hat{\mathbf{q}}, \omega) = \frac{4\pi e^2}{V} \lim_{q \rightarrow 0} \frac{1}{q^2} \sum_{n,\mathbf{k}} 2 f_{n\mathbf{k}} |\langle u_{n\mathbf{k}+\mathbf{q}} | u_{n\mathbf{k}} \rangle|^2 \times \left( \frac{1}{\epsilon_{n\mathbf{k}+\mathbf{q}} - \epsilon_{n\mathbf{k}} - \omega} + \frac{1}{\epsilon_{n\mathbf{k}+\mathbf{q}} - \epsilon_{n\mathbf{k}} + \omega} \right) \quad (2.99)$$

becomes indefinite because  $1/q^2 \rightarrow \infty$  and at the same time the term in parenthesis goes to zero ( $-1/\omega + 1/\omega \rightarrow 0$ ). To avoid this indefiniteness, all quantities depending on  $\mathbf{q}$  will be expanded around  $\mathbf{q} = 0$ . For the transition probability  $\langle u_{n\mathbf{k}+\mathbf{q}} | u_{n\mathbf{k}} \rangle$  one finds that

$$\langle u_{n\mathbf{k}+\mathbf{q}} | u_{n\mathbf{k}} \rangle = \langle u_{n\mathbf{k}} | u_{n\mathbf{k}} \rangle + \mathbf{q} \langle \nabla_{\mathbf{k}} u_{n\mathbf{k}} | u_{n\mathbf{k}} \rangle + \mathcal{O}(q^2) = 1 + \mathcal{O}(q^2), \quad (2.100)$$

because  $\nabla_{\mathbf{k}} u_{n\mathbf{k}}$  is orthogonal to  $u_{n\mathbf{k}}$  and  $\langle u_{n\mathbf{k}} | u_{n\mathbf{k}} \rangle = 1$ . Using  $\Delta\omega_{\mathbf{k};\mathbf{q}} = \epsilon_{n\mathbf{k}+\mathbf{q}} - \epsilon_{n\mathbf{k}}$  and considering  $\Delta\omega_{\mathbf{k};\mathbf{q}} \ll \omega$  the term in parenthesis in Eq. (2.99) can be approximated as

$$\frac{1}{\Delta\omega_{\mathbf{k};\mathbf{q}} - \omega} + \frac{1}{\Delta\omega_{\mathbf{k};\mathbf{q}} + \omega} = \quad (2.101)$$

$$= \frac{1}{\omega} \left( - \left( 1 + \frac{\Delta\omega_{\mathbf{k};\mathbf{q}}}{\omega} \right) + \left( 1 - \frac{\Delta\omega_{\mathbf{k};\mathbf{q}}}{\omega} \right) + \mathcal{O}\left(\frac{\Delta\omega_{\mathbf{k};\mathbf{q}}^2}{\omega^2}\right) \right) \approx -\frac{2\Delta\omega_{\mathbf{k};\mathbf{q}}}{\omega^2}. \quad (2.102)$$

A Taylor expansion of  $\Delta\omega_{\mathbf{k};\mathbf{q}}$  gives

$$\Delta\omega_{\mathbf{k};\mathbf{q}} = \epsilon_{n\mathbf{k}+\mathbf{q}} - \epsilon_{n\mathbf{k}} = \mathbf{q} \nabla_{\mathbf{k}} \epsilon_{n\mathbf{k}} + \frac{1}{2} \mathbf{q}^2 \nabla_{\mathbf{k}}^2 \epsilon_{n\mathbf{k}} + \mathcal{O}(\mathbf{q}^3). \quad (2.103)$$

Only terms symmetric in  $\mathbf{k}$  contribute to the  $k$ -point sum in Eq. (2.99), so that the term  $\nabla_{\mathbf{k}} \epsilon_{n\mathbf{k}}$  can be neglected. By inserting the expanded terms in Eq. (2.99), the head of the long-wavelength intraband dielectric function becomes:

$$\varepsilon_{\text{intra}}^{(1)}(\hat{\mathbf{q}}, \omega) = -\frac{1}{\omega^2} \frac{4\pi e^2}{V} \sum_{n,\mathbf{k}} 2 f_{n\mathbf{k}} \nabla_{\mathbf{k}}^2 \epsilon_{n\mathbf{k}}, \quad (2.104)$$

or in tensor form:

$$\varepsilon_{\alpha,\beta}^{(1)}(\omega) = -\frac{1}{\omega^2} \frac{4\pi e^2}{V} \sum_{n,\mathbf{k}} 2 f_{n\mathbf{k}} \frac{\partial^2 \epsilon_{n\mathbf{k}}}{\partial \mathbf{k}_\alpha \partial \mathbf{k}_\beta}. \quad (2.105)$$

The real part of the intraband dielectric function, therefore, only depends on the frequency of the incident light  $\omega$  and on the energy dispersion. The material specific prefactor is called plasma frequency (tensor) and is defined as:

$$\bar{\omega}_{\alpha\beta}^2 := \frac{4\pi e^2}{V} \sum_{n\mathbf{k}} 2 f_{n\mathbf{k}} \frac{\partial^2 \epsilon_{n\mathbf{k}}}{\partial \mathbf{k}_\alpha \partial \mathbf{k}_\beta}. \quad (2.106)$$

Using this definition, the real part of the intraband dielectric function is given as:

$$\varepsilon_{\alpha,\beta}^{(1)}(\omega) = -\frac{\bar{\omega}_{\alpha\beta}^2}{\omega^2}. \quad (2.107)$$

In practice, the expression Eq. (2.106) for the plasma frequency is not that convenient to calculate, because it includes second derivatives of the energy. Therefore, we make use of the Green's theorem for periodic functions (see e.g. Ref. [26]) which states that for  $u(\mathbf{k})$  and  $v(\mathbf{k})$  being periodic functions in reciprocal space:

$$\int_{BZ} d^3k u(\mathbf{k}) \nabla v(\mathbf{k}) = - \int_{BZ} d^3k v(\mathbf{k}) \nabla u(\mathbf{k}) \quad (2.108)$$

$$\int_{BZ} d^3k u(\mathbf{k}) \nabla^2 v(\mathbf{k}) = \int_{BZ} d^3k v(\mathbf{k}) \nabla^2 u(\mathbf{k}). \quad (2.109)$$

As special cases one finds:

$$\int_{BZ} d^3k u(\mathbf{k}) \nabla^2 v(\mathbf{k}) = - \int_{BZ} d^3k \nabla u(\mathbf{k}) \nabla v(\mathbf{k}) \quad (2.110)$$

$$\int_{BZ} d^3k \nabla^2 u(\mathbf{k}) = 0. \quad (2.111)$$

If we set  $f_{n\mathbf{k}} = f(\epsilon_n(\mathbf{k}))$  to  $u(\mathbf{k})$  and  $\epsilon_{n\mathbf{k}} = \epsilon_n(\mathbf{k})$  to  $v(\mathbf{k})$ , we can reformulate Eq. (2.106) by considering:

$$\begin{aligned} \int_{BZ} d^3k f(\epsilon_n(\mathbf{k})) \nabla^2 \epsilon_n(\mathbf{k}) &=^{(2.110)} - \int_{BZ} d^3k \frac{\partial f(\epsilon_n(\mathbf{k}))}{\partial \mathbf{k}} \nabla \epsilon(\mathbf{k}) = \\ &= \int_{BZ} d^3k \left( -\frac{\partial f(\epsilon_n)}{\partial \epsilon_n} \right) (\nabla \epsilon(\mathbf{k}))^2 \end{aligned} \quad (2.112)$$

and write

$$\bar{\omega}_{\alpha\beta}^2 = -\frac{4\pi e^2}{V} \sum_{n\mathbf{k}} 2 \frac{\partial f(\epsilon_n)}{\partial \epsilon_n} \left( \mathbf{e}_\alpha \frac{\partial \epsilon_n(\mathbf{k})}{\partial \mathbf{k}} \right) \left( \mathbf{e}_\beta \frac{\partial \epsilon_n(\mathbf{k})}{\partial \mathbf{k}} \right). \quad (2.113)$$

Due to relation Eq. (2.111) it can be furthermore shown that fully occupied bands do not contribute to the plasma frequency. We can see this also from Eq. (2.113), if we consider that the occupation function  $f$  has a non-vanishing derivative only in the case of partially filled bands. It is also evident that contributions from fully occupied bands vanish because we presently consider only intraband transitions and excitations within a fully occupied band are not possible. Instead of  $\sum_{n,\mathbf{k}}$  in Eq. (2.113) we can thus safely write  $\sum_{n-pf,\mathbf{k}}$  ( $pf$  = partial filled bands).

In the case of an ideal, free Fermi gas, the plasma frequency is a scalar and Eq. (2.106) and Eq. (2.113) reduce to the Drude plasma frequency

$$\bar{\omega}_{\text{Drude}}^2 = \frac{4\pi e^2 n \hbar^2}{m}, \quad (2.114)$$

and the strength of the optical response thus only depends on the electron density  $n$ . Generally, the plasma frequency of every metal can be written in a Drude like form

$$\bar{\omega}_{\alpha\beta}^2 = \frac{4\pi e^2 n \hbar^2}{m_{\alpha\beta}^*} \quad (2.115)$$

by introducing the tensor  $m_{\alpha\beta}^*$

$$\frac{1}{m_{\alpha\beta}^*} = \frac{1}{N \hbar^2} \sum_{n\mathbf{k}} 2 f_{n\mathbf{k}} \frac{\partial^2 \epsilon_{n\mathbf{k}}}{\partial \mathbf{k}_\alpha \partial \mathbf{k}_\beta}. \quad (2.116)$$

and setting  $N$  to the number of valence electrons per unit cell volume. Often the factor  $m^*/m$  is quoted instead of the plasma frequency  $\bar{\omega}$ . The quantity defined in Eq. (2.116) is referred to as optical or effective mass, but should not be mixed up with the effective mass tensor:

$$\frac{1}{M_{\alpha\beta}} = \frac{1}{\hbar^2} \frac{\partial^2 \epsilon(\mathbf{k})}{\partial \mathbf{k}_\alpha \partial \mathbf{k}_\beta}. \quad (2.117)$$



The equality only holds, if the tensor defined in Eq. (2.117) does not depend on  $\mathbf{k}$ , which is the case for a quadratic dependence of  $\epsilon$  on the crystal momentum  $\mathbf{k}$ .

In the following, the relation between the real plasma frequency of a material (calculated within the independent particle approach) and the corresponding Drude plasma frequency will be discussed in more detail. By using second order perturbation theory, the second derivative of the energy can be evaluated by:

$$\frac{1}{2} \frac{\partial^2 \epsilon_{n\mathbf{k}}}{\partial \mathbf{k}^2} = \sum_{m \neq n} \frac{|\langle u_{m\mathbf{k}} | H^1 | u_{n\mathbf{k}} \rangle|^2}{\epsilon_{n\mathbf{k}} - \epsilon_{m\mathbf{k}}} + \langle u_{m\mathbf{k}} | H^2 | u_{n\mathbf{k}} \rangle. \quad (2.118)$$

with

$$H^1 = \frac{\partial H}{\partial \mathbf{k}} \quad H^2 = \frac{1}{2} \frac{\partial^2 H}{\partial \mathbf{k}^2} \quad (2.119)$$

and  $u_{n\mathbf{k}}$  and  $\epsilon_{n\mathbf{k}}$  being the unperturbed wavefunctions and eigenenergies. The Hamiltonian  $H(\mathbf{k})$  for the cell periodic wave function is given as:

$$H(\mathbf{k}) = -\frac{\hbar^2}{2m} (\nabla + i\mathbf{k})^2 + V(\mathbf{r}), \quad (2.120)$$

if we assume a local potential  $V(\mathbf{r})$ . In the PAW method the expressions become more complicated (see also [21]), but this will not be discussed here. With the Hamiltonian in Eq. (2.120) the second derivative of the one-electron energy can be approximately written as:

$$\frac{\partial^2 \epsilon_{n\mathbf{k}}}{\partial \mathbf{k}_\alpha \partial \mathbf{k}_\beta} = \frac{2\hbar^4}{m^2} \sum_{m \neq n} \frac{\langle u_{m\mathbf{k}} | (\mathbf{k}_\alpha - i\nabla_\alpha) | u_{n\mathbf{k}} \rangle \langle u_{n\mathbf{k}} | (\mathbf{k}_\beta - i\nabla_\beta) | u_{m\mathbf{k}} \rangle}{\epsilon_{n\mathbf{k}} - \epsilon_{m\mathbf{k}}} + \frac{\hbar^2}{m} \langle u_{n\mathbf{k}} | u_{n\mathbf{k}} \rangle. \quad (2.121)$$

Assuming  $\alpha$  being a principle axes and making use of  $\langle u_{n\mathbf{k}} | u_{n\mathbf{k}} \rangle = 1$  the tensor element  $\bar{\omega}_{\alpha\alpha}$  can be expressed as:

$$\begin{aligned} \bar{\omega}_{\alpha\alpha}^2 &= \underbrace{\frac{8\pi e^2 \hbar^4}{Vm^2} \sum_{n-pf} \sum_{\mathbf{k}} \sum_{m \neq n} 2f_{n\mathbf{k}} \frac{|\langle u_{m\mathbf{k}} | (\mathbf{k}_\alpha - i\nabla_\alpha) | u_{n\mathbf{k}} \rangle|^2}{\epsilon_{n\mathbf{k}} - \epsilon_{m\mathbf{k}}}}_{-A} + \underbrace{\frac{4\pi e^2 n_{\text{val}} \hbar^2}{m}}_{\bar{\omega}_{\text{Drude}}^2(n_{\text{val}})} \\ &= -A + \bar{\omega}_{\text{Drude}}^2(n_{\text{val}}). \end{aligned} \quad (2.122)$$

The independent particle plasma frequency  $\bar{\omega}_{\alpha\alpha}^2$  therefore equals the Drude plasma frequency,  $\bar{\omega}_{\text{Drude}}^2$ , minus a correction term  $A$ . The correction term  $A$  is positive, because for every pair of occupied states  $n = i$  and  $m = j$  also the pair  $n = j$  and  $m = i$  appears in the sum in Eq. (2.122), and the corresponding terms are equally large but have opposite signs. The only contributing terms are transitions from occupied bands  $n$  to unoccupied bands  $m$ , so that  $\epsilon_{n\mathbf{k}} - \epsilon_{m\mathbf{k}} < 0$  and consequently  $A > 0$ . The independent particle plasma frequency is therefore always smaller than the corresponding Drude like one. Because all contributions from fully occupied bands vanish, one can also consider the sum over all bands in Eq. (2.122):

$$\begin{aligned} \bar{\omega}_{\alpha\alpha}^2 &= \underbrace{\frac{8\pi e^2 \hbar^4}{Vm^2} \sum_{n\mathbf{k}} \sum_{m \neq n} 2f_{n\mathbf{k}} \frac{|\langle u_{m\mathbf{k}} | (\mathbf{k}_\alpha - i\nabla_\alpha) | u_{n\mathbf{k}} \rangle|^2}{\epsilon_{n\mathbf{k}} - \epsilon_{m\mathbf{k}}}}_{-A^{\text{all}}} + \underbrace{\frac{4\pi e^2 n_{\text{all}} \hbar^2}{m}}_{\bar{\omega}_{\text{Drude}}^2(n_{\text{all}})} \\ &= -A^{\text{all}} + \bar{\omega}_{\text{Drude}}^2(n_{\text{all}}). \end{aligned} \quad (2.123)$$

This result will be used later for relating the interband and the intraband dielectric functions by the so called  $f$ -sum rule.

The imaginary part of the intraband dielectric function  $\varepsilon^{(2)}$  is obtained by a Kramers-Kronig transformation:

$$\varepsilon_{\alpha,\beta}^{(2)} = -\pi \bar{\omega}_{\alpha\alpha}^2 \frac{\partial \delta(\omega)}{\partial \omega} \quad (2.124)$$

and has therefore non-vanishing elements only in the vicinity of  $\omega = 0$ . As electron-electron and electron-phonon scattering are neglected in the present theoretical approach, the experimental absorption due to intraband excitations is non-vanishing also for  $\omega > 0$ . By introducing the relaxation time  $\tau$ , which in a semi-classical model gives the average time between collisions, the real and imaginary part of the intraband dielectric function can be written as:

$$\varepsilon^{(1)}(\omega) = 1 - \frac{\bar{\omega}^2 \tau^2}{1 + \omega^2 \tau^2} \quad (2.125)$$

$$\varepsilon^{(2)}(\omega) = \bar{\omega}^2 \tau / (\omega(1 + \omega^2 \tau^2)). \quad (2.126)$$

So far, we have always considered the head ( $\mathbf{G} = \mathbf{G}' = 0$ ) of the long-wavelength dielectric function. The body ( $\mathbf{G} \neq 0$  and  $\mathbf{G}' \neq 0$ ) and the wing ( $\mathbf{G} = 0$  or  $\mathbf{G}' = 0$ ) of the long-wavelength intraband dielectric function are both zero. For the wing, the part resulting from the Coulomb kernel,  $1/q^2$ , is replaced by  $1/(|\mathbf{q}||\mathbf{G} + \mathbf{q}|)$  and  $|\langle u_{n\mathbf{k}+\mathbf{q}} | u_{n\mathbf{k}} \rangle|^2$  by  $\langle u_{n\mathbf{k}+\mathbf{q}} | u_{n\mathbf{k}} \rangle \langle u_{n\mathbf{k}} | e^{i\mathbf{G}\mathbf{r}} | u_{n\mathbf{k}+\mathbf{q}} \rangle$  in Eq. (2.99). For sufficiently small frequencies  $\omega$  the eigenenergy term stays the same as in Eq. (2.103), and depends quadratically on  $\mathbf{q}$ . Because neither  $\langle u_{n\mathbf{k}+\mathbf{q}} | u_{n\mathbf{k}} \rangle$  nor  $\langle u_{n\mathbf{k}} | e^{i\mathbf{G}\mathbf{r}} | u_{n\mathbf{k}+\mathbf{q}} \rangle$  approach zero the wing vanishes like  $q^2/q = q$ . The body decays as  $q^2$ , which can be shown by analogous considerations.

## 2.9 $f$ -sum rule and interband transitions at small energies

The  $f$ -sum rule states that

$$\int_0^\infty d\omega \omega \varepsilon^{(2)}(\omega) = \int_0^\infty d\omega \omega [\varepsilon_{\text{inter}}^{(2)}(\omega) + \varepsilon_{\text{intra}}^{(2)}(\omega)] = \frac{2\pi^2 e^2 n_{\text{all}}}{m} = \frac{\pi}{2} \bar{\omega}_{\text{Drude}}^2 (n_{\text{all}}) \quad (2.127)$$

and thereby couples the interband and intraband dielectric function. In order to prove Eq. (2.127) we consider the interband dielectric function as defined in Eq. (2.73) and rewrite the expression  $|\langle u_{m\mathbf{k}+\mathbf{q}} | u_{n\mathbf{k}} \rangle|^2$  using perturbation theory. In a first step, the term  $u_{m\mathbf{k}+\mathbf{q}}$  is Taylor expanded

$$u_{m\mathbf{k}+\mathbf{q}} = u_{m\mathbf{k}} + \mathbf{q} \nabla_{\mathbf{k}} u_{m\mathbf{k}} + \mathbf{O}(q^2) \quad (2.128)$$

and using the orthogonality of wavefunctions  $u_{m\mathbf{k}}$  and  $u_{n\mathbf{k}}$ ,  $\langle u_{m\mathbf{k}+\mathbf{q}} | u_{n\mathbf{k}} \rangle$  becomes

$$\langle u_{m\mathbf{k}+\mathbf{q}} | u_{n\mathbf{k}} \rangle \approx \mathbf{q} \langle \nabla_{\mathbf{k}} u_{m\mathbf{k}} | u_{n\mathbf{k}} \rangle. \quad (2.129)$$

The scalar product  $\langle \nabla_{\mathbf{k}} u_{m\mathbf{k}} | u_{n\mathbf{k}} \rangle$  is within first order perturbation theory given by

$$\langle \nabla_{\mathbf{k}} u_{m\mathbf{k}} | u_{n\mathbf{k}} \rangle = \frac{\langle u_{m\mathbf{k}} | \nabla_{\mathbf{k}} H | u_{n\mathbf{k}} \rangle}{\epsilon_{m\mathbf{k}} - \epsilon_{n\mathbf{k}}}. \quad (2.130)$$

Assuming the same local Hamiltonian as in Eq. (2.120), the long-wavelength interband dielectric function can be expressed as [see Eq. (2.75)]:

$$\begin{aligned} \varepsilon_{\text{inter}}^{(2)}(\omega) = & \frac{4\pi^2 e^2}{\hbar^2 V} \frac{\hbar^4}{m^2} \sum_{n\mathbf{k}} \sum_{m \neq n} 2f_{n\mathbf{k}} \frac{|\langle u_{m\mathbf{k}} | (\mathbf{k} + i\nabla) | u_{n\mathbf{k}} \rangle|^2}{|\epsilon_{m\mathbf{k}} - \epsilon_{n\mathbf{k}}|^2} \times \\ & \times [\delta(\epsilon_{m\mathbf{k}} - \epsilon_{n\mathbf{k}} - \omega) - \delta(\epsilon_{m\mathbf{k}} - \epsilon_{n\mathbf{k}} + \omega)]. \end{aligned} \quad (2.131)$$

Integration of  $\omega \varepsilon_{\text{inter}}^{(2)}(\omega)$  from zero to infinity results in

$$\begin{aligned} \int_0^\infty d\omega \omega \varepsilon_{\text{inter}}^{(2)}(\omega) = & \frac{4\pi^2 e^2}{\hbar^2 V} \frac{\hbar^4}{m^2} \sum_{n\mathbf{k}} \sum_{m \neq n} 2f_{n\mathbf{k}} \frac{|\langle u_{m\mathbf{k}} | (\mathbf{k} + i\nabla) | u_{n\mathbf{k}} \rangle|^2}{|\epsilon_{m\mathbf{k}} - \epsilon_{n\mathbf{k}}|^2} (\epsilon_{m\mathbf{k}} - \epsilon_{n\mathbf{k}}) = \\ = & \frac{4\pi^2 e^2}{\hbar^2 V} \frac{\hbar^4}{m^2} \sum_{n\mathbf{k}} \sum_{m \neq n} 2f_{n\mathbf{k}} \frac{|\langle u_{m\mathbf{k}} | (\mathbf{k} + i\nabla) | u_{n\mathbf{k}} \rangle|^2}{\epsilon_{m\mathbf{k}} - \epsilon_{n\mathbf{k}}} = \frac{\pi}{2} A^{\text{all}} \end{aligned} \quad (2.132)$$

where  $A^{\text{all}}$  already occurred as part of the intraband plasma frequency in Eq. (2.123). Combining Eq. (2.124) and Eq. (2.123) results in

$$\int_0^\infty d\omega \omega \varepsilon_{\text{intra}}^{(2)}(\omega) = \frac{\pi}{2} \bar{\omega}^2 = -\frac{\pi}{2} A^{\text{all}} + \frac{\pi}{2} \bar{\omega}_{\text{Drude}}^2(n_{\text{all}}). \quad (2.133)$$

and consequently

$$\int_0^\infty d\omega \omega \varepsilon^{(2)}(\omega) = \frac{\pi}{2} A^{\text{all}} + \left( -\frac{\pi}{2} A^{\text{all}} + \frac{\pi}{2} \bar{\omega}_{\text{Drude}}^2(n_{\text{all}}) \right) = \frac{\pi}{2} \bar{\omega}_{\text{Drude}}^2(n_{\text{all}}). \quad (2.134)$$

For the proof of the  $f$ -sum rule we have made use of the locality of the external potential entering the Hamiltonian. If the PAW method is used, the  $f$ -sum rule does not (exactly) hold anymore.

The concepts used for the proof of the  $f$ -sum rule remain relevant when discussing interband transitions between states with small energy differences. Whereas the  $f$ -sum rule only states that the integrated intraband and interband dielectric function sums up to a fixed value, for interband transitions between bands with small energy differences it can be furthermore shown that the intra- and interband dielectric functions themselves are coupled to each other. We start from the real part of the interband dielectric function:

$$\begin{aligned} \varepsilon_{\text{inter}}^{(1)}(\omega) = & 1 + \frac{4\pi e^2}{V} \lim_{q \rightarrow 0} \frac{1}{q^2} \sum_{n\mathbf{k}} \sum_{m \neq n} 2f_{n\mathbf{k}} |\langle u_{m\mathbf{k}+\mathbf{q}} | u_{n\mathbf{k}} \rangle|^2 \times \\ & \times \left( \frac{1}{\epsilon_{m\mathbf{k}} - \epsilon_{n\mathbf{k}} - \omega} + \frac{1}{\epsilon_{m\mathbf{k}} - \epsilon_{n\mathbf{k}} + \omega} \right). \end{aligned} \quad (2.135)$$

We now consider interband transitions between states near the Fermi edge with small energy differences. The contributing states are given the indices  $n'$  and  $m'$ . For frequencies much larger than the energy difference ( $\Delta\epsilon = \epsilon_{m'\mathbf{k}} - \epsilon_{n'\mathbf{k}} \ll \omega$ ) the eigenenergy term in Eq. (2.135) can be expanded [see Eq. (2.101)]. The transition probability  $|\langle u_{m'\mathbf{k}+\mathbf{q}} | u_{n'\mathbf{k}} \rangle|^2$  is reformulated using perturbation theory [Eq. (2.129)] so that the interband dielectric function for small transition energies  $\epsilon_{m'\mathbf{k}} - \epsilon_{n'\mathbf{k}}$  reads:

$$\varepsilon_{\text{inter}}^{(1)}(\omega) = 1 - \frac{1}{\omega^2} \frac{8\pi e^2}{\hbar^2 V} \frac{\hbar^4}{m^2} 2f_{n'\mathbf{k}} \frac{|\langle u_{m'\mathbf{k}} | (\mathbf{k} + i\nabla) | u_{n'\mathbf{k}} \rangle|^2}{\epsilon_{m'\mathbf{k}} - \epsilon_{n'\mathbf{k}}} = 1 - \frac{A^{n'm'}}{\omega^2}. \quad (2.136)$$

The interband dielectric function resulting from transitions between states with small energy differences therefore exhibit the same behavior as the intraband dielectric function with a squared "plasma frequency" of  $A^{n'm'}$ . Because the intraband plasma frequency is

$$\varepsilon_{\text{intra}}^{(1)}(\omega) = -\frac{\bar{\omega}_{\text{Drude}}^2(n_{\text{all}}) - A^{\text{all}}}{\omega^2} \quad (2.137)$$

and  $A^{n'm'}$  is one contribution to  $A^{\text{all}}$ , interband transitions between bands with small energy differences result in a reduction of the intraband plasma frequency with respect to the Drude plasma frequency. This is in essence a consequence of the  $f$ -sum rule.

## Chapter 3

# Total energies from linear response theory

In most density functional theory calculations, the exchange-correlation energy  $E_{xc}$  is approximated within the LDA [Eq. (1.11)] or GGA [Eq. (1.12)] (e.g., using the PBE exchange-correlation functional). This results in a fast method for calculating ground state properties for a large variety of systems. Nevertheless, LDA and PBE can not provide chemical accuracy (0.05 eV) for atomization energies, and bond lengths are too small in LDA ( $\approx 1-2\%$ ) and too large in PBE ( $\approx 1\%$ ). Negative ions are not or much too weakly bound within LDA and PBE which is related to the wrong asymptotic behavior of the exchange potential caused by the (semi)local approximation. Furthermore, long-range correlation effects, as the van der Waals interaction between distant fragments, are neither included in the LDA nor GGA description. This can be easily seen from the fact that for both, LDA and PBE, no correlation contributions arise from two fragments with non-overlapping densities. The introduction of functionals that partly include exact exchange (e.g., PBE0) can not cure this failure in the description of the long-range contribution to the correlation energy.

This has initiated efforts to find a more fundamental expression for the (exchange)-correlation energy than given by the LDA, GGA, or hybrid functionals. In this chapter, we will introduce the adiabatic connection dissipation-fluctuation theorem (ACFDT). This theorem provides a possibility to calculate the energy of an interacting electron system (and especially the complicated part of this energy, the correlation energy) by the knowledge of the answer of this system to an external perturbation as described by the response function of the system. The knowledge of the response function as provided within TDDFT, therefore, also includes an access to the total energy of a system and an improved approximation of the DFT exchange-correlation energy. In the TDDFT context, Refs. [27, 28, 29] (late 1970s) are cited as the original ACFDT papers. Nevertheless, this approach is closely connected to total energy calculation within many-body perturbation theory (MBPT) going back to the work by Pines and Nozières [19] and to coupled cluster theory routinely used by quantum chemists [30].

### 3.1 Adiabatic connection dissipation-fluctuation theorem

In the Kohn-Sham density functional theory (see section 1.2) the problem of interacting electrons is mapped onto a system of non-interacting electrons moving in an effective (local) potential. In the Hamiltonian assigned to the KS system, therefore, the electron-electron interaction operator is set to zero, and a modified external potential is introduced such that the KS density and energy correspond to the one of the fully interacting system. The aim of the adiabatic connection fluctuation-dissipation theorem (ACFDT) is to find an exact expression for the exchange-correlation energy  $E_{xc}$  by smoothly switching the electron-electron interaction from 0 (KS system) to 1 (fully interacting system). In subsection 3.1.1, it will be shown that the exchange-correlation energy can be expressed as an integral over the expectation value of the electron-electron interaction when going from the non-interacting KS system to the fully interacting system. The expectation value can be related to the response function of the corresponding system as will be derived in subsection 3.1.2. The results of TDDFT can be used to evaluate the response function of the interacting system. In the present case, we apply the random phase approximation (RPA) and the expression of the RPA correlation energy will be reported in Sec. 3.2.

#### 3.1.1 Adiabatic connection

In this subsection, we will discuss how to find an expression for the exchange-correlation energy by introducing a set of systems interacting via the Hamiltonian

$$\hat{H}(\lambda) = \hat{T} + \hat{V}(\lambda) + \lambda \hat{V}_{ee}. \quad (3.1)$$

The coupling constant  $\lambda$  thereby determines the strength of the electron-electron interaction  $\hat{V}_{ee} = \sum_{i < j} e^2 / |\mathbf{r}_i - \mathbf{r}_j|$ . The local potential  $v_\lambda(\mathbf{r})$  underlying the operator  $\hat{V}(\lambda) = \sum_i v_\lambda(\mathbf{r}_i)$  is chosen as to keep the groundstate density of the  $\lambda$  system at the same value as the density of the fully interacting system. For  $\lambda = 1$ , the fully interacting Hamiltonian  $\hat{H}(1)$  is recovered and by considering  $\hat{V}(1) = \sum_i v_{\text{ext}}(\mathbf{r}_i)$ , the ground state energy is given by

$$E = \langle \Psi(1) | \hat{H}(1) | \Psi(1) \rangle = \langle \Psi(1) | \hat{T} + \hat{V}_{ee} + \hat{V}(1) | \Psi(1) \rangle = \langle \Psi(1) | \hat{T} + \hat{V}_{ee} | \Psi(1) \rangle + E_{\text{ext}}, \quad (3.2)$$

with the (fully) interacting ground state wavefunction  $\Psi(1)$ . For  $\lambda = 0$ ,  $\hat{H}(0)$  becomes the KS Hamiltonian and  $\Psi(0)$  the KS wavefunction, a single Slater determinant. The respective local potential is  $\hat{V}(0) = \sum_i v_{KS}(\mathbf{r}_i)$  [see Eq. (1.5)]. The energy of the KS system can be expressed as

$$E = \langle \Psi(0) | \hat{H}(0) | \Psi(0) \rangle = \langle \Psi(0) | \hat{T} + \hat{V}(0) | \Psi(0) \rangle = T_s + E_H + E_{\text{ext}} + E_{xc}. \quad (3.3)$$

By combining Eq. (3.2) and Eq. (3.3), the Hartree and exchange-correlation energy can therefore be written as

$$\begin{aligned} E_H + E_{xc} &= E - E_{\text{ext}} - T_s = \\ &= \langle \Psi(1) | \hat{H}(1) | \Psi(1) \rangle - \langle \Psi(1) | \hat{V}(1) | \Psi(1) \rangle - \langle \Psi(0) | \hat{H}(0) | \Psi(0) \rangle + \langle \Psi(0) | \hat{V}(0) | \Psi(0) \rangle = \\ &= \int_0^1 d\lambda \frac{d}{d\lambda} \left( \langle \Psi(\lambda) | \hat{H}(\lambda) | \Psi(\lambda) \rangle - \langle \Psi(\lambda) | \hat{V}(\lambda) | \Psi(\lambda) \rangle \right). \end{aligned} \quad (3.4)$$

Because  $\Psi(\lambda)$  is an eigenstate of  $\hat{H}(\lambda)$  one can make use of the Hellmann-Feynmann theorem and rewrite the first integrand of Eq. (3.4) as

$$\frac{d}{d\lambda} \langle \Psi(\lambda) | \hat{H}(\lambda) | \Psi(\lambda) \rangle = \langle \Psi(\lambda) | \frac{d\hat{H}(\lambda)}{d\lambda} | \Psi(\lambda) \rangle = \langle \Psi(\lambda) | \hat{V}_{ee} | \Psi(\lambda) \rangle + \langle \Psi(\lambda) | \frac{d\hat{V}(\lambda)}{d\lambda} | \Psi(\lambda) \rangle. \quad (3.5)$$

Because  $n(\mathbf{r})$  does not depend on  $\lambda$  the second part of the integrand in Eq. (3.4) can be reformed to

$$\begin{aligned} \frac{d}{d\lambda} \langle \Psi(\lambda) | \hat{V}(\lambda) | \Psi(\lambda) \rangle &= \frac{d}{d\lambda} \int d^3r n(\mathbf{r}) v_\lambda(\mathbf{r}) = \\ &= \int d^3r n(\mathbf{r}) \frac{dv_\lambda(\mathbf{r})}{d\lambda} = \langle \Psi(\lambda) | \frac{d\hat{V}(\lambda)}{d\lambda} | \Psi(\lambda) \rangle. \end{aligned} \quad (3.6)$$

Inserting Eq. (3.5) and Eq. (3.6) in Eq. (3.4) results in a Hartree-exchange-correlation energy, which is given as a coupling constant integral over the expectation value of the electron-electron Coulomb interaction  $\hat{V}_{ee}$ :

$$E_{Hxc} = \int_0^1 d\lambda \langle \Psi(\lambda) | \hat{V}_{ee} | \Psi(\lambda) \rangle. \quad (3.7)$$

A main achievement is that this expression circumvents any reference to the kinetic energy operator, and thus the need for an explicit construction of the one-particle density matrix [Eq. (10)] is entirely avoided.

### 3.1.2 Fluctuation-dissipation theorem

The fluctuation-dissipation theorem [31] states that the response of a system to a small external perturbation described by the linear response properties of the system is the same as its response to a spontaneous fluctuation. The fluctuation-dissipation theorem is a general one and has many examples in thermodynamics. In our case, the fluctuation is a density fluctuation within the system, and the external perturbation a small time-dependent additional potential that creates a density response described by the density-density response function  $\chi$  [as e.g., introduced in Eq. (2.23)]. After applying the fluctuation-dissipation theorem, the exchange-correlation energy can be written as (see proof below):

$$E_{xc} = -\frac{e^2}{2} \int_0^1 d\lambda \int d^3r d^3r' \frac{1}{|\mathbf{r} - \mathbf{r}'|} \left\{ n(\mathbf{r}) \delta(\mathbf{r} - \mathbf{r}') + \frac{1}{\pi} \int_0^\infty d\omega \chi^\lambda(\mathbf{r}, \mathbf{r}', i\omega) \right\}, \quad (3.8)$$

where  $\chi^\lambda$  is the response function of the system interacting via the scaled electron-electron interaction  $\lambda \hat{V}_{ee}$  and moving in the local potential given by the operator  $\hat{V}(\lambda)$ .

In the following, we derive the density fluctuation-dissipation theorem in a similar way as Dobson in Ref. [34]. If one rewrites the expectation value of the Coulomb operator in Eq. (3.7) making use of the pair density [see Eq. (11)]

$$\langle \Psi(\lambda) | \hat{V}_{ee} | \Psi(\lambda) \rangle = \frac{e^2}{2} \int d^3r d^3r' \frac{n^{2,\lambda}(\mathbf{r}, \mathbf{r}')}{|\mathbf{r} - \mathbf{r}'|}, \quad (3.9)$$

the Hartree-exchange-correlation energy reads:

$$E_{Hxc} = \frac{e^2}{2} \int_0^1 d\lambda \int d^3r d^3r' \frac{n^{2,\lambda}(\mathbf{r}, \mathbf{r}')}{|\mathbf{r} - \mathbf{r}'|}. \quad (3.10)$$

The pair density can be expressed via the density operator  $\hat{n}(\mathbf{r}) = \sum_i \delta(\mathbf{r} - \mathbf{r}_i)$  as

$$\begin{aligned} n^{2,\lambda}(\mathbf{r}, \mathbf{r}') &= \langle \Psi(\lambda) | \sum_{ij, i \neq j} \delta(\mathbf{r} - \mathbf{r}_i) \delta(\mathbf{r}' - \mathbf{r}_j) | \Psi(\lambda) \rangle = \\ &= \langle \Psi(\lambda) | \sum_{ij} \delta(\mathbf{r} - \mathbf{r}_i) \delta(\mathbf{r}' - \mathbf{r}_j) | \Psi(\lambda) \rangle - \delta(\mathbf{r} - \mathbf{r}') \langle \Psi(\lambda) | \sum_i \delta(\mathbf{r} - \mathbf{r}_i) | \Psi(\lambda) \rangle = \\ &= \langle \Psi(\lambda) | \hat{n}(\mathbf{r}) \hat{n}(\mathbf{r}') | \Psi(\lambda) \rangle - n(\mathbf{r}) \delta(\mathbf{r} - \mathbf{r}'). \end{aligned} \quad (3.11)$$

In order to evaluate the expectation value of the product  $\hat{n}(\mathbf{r}) \hat{n}(\mathbf{r}')$  for an arbitrary system we consider the following expression containing the density-density response function  $\chi$  at imaginary frequencies:

$$\int_0^\infty d\omega [\chi(\mathbf{r}, \mathbf{r}', i\omega) + \chi(\mathbf{r}', \mathbf{r}, i\omega)]. \quad (3.12)$$

An expression for the response function  $\chi$  has been derived in Sec. 2.2 and we will make use of Eq. (2.24) (replacing  $\tilde{\omega} \rightarrow i\omega$ ) but use the shorter notation  $|0\rangle$  for the ground state wavefunction  $|\Psi_0^0\rangle$  and  $|J\rangle$  for the excited state  $|\Psi_j^0\rangle$ . The difference in eigenenergies  $E_j - E_0$  will be further denoted as  $\omega_{0j}$ . The integrand of Eq. (3.12) can then be written as

$$- \sum_{J \neq 0} \{ \langle 0 | \hat{n}(\mathbf{r}) | J \rangle \langle J | \hat{n}(\mathbf{r}') | 0 \rangle + \langle 0 | \hat{n}(\mathbf{r}') | J \rangle \langle J | \hat{n}(\mathbf{r}) | 0 \rangle \} \left( \frac{1}{\omega_{0j} - i\omega} + \frac{1}{\omega_{0j} + i\omega} \right). \quad (3.13)$$

The only frequency dependent term is the expression in parenthesis, which can be reformed to  $2\omega_{0j}/(\omega_{0j}^2 + \omega^2)$ . Performing the frequency integration results in a factor  $\pi/2$  so that Eq. (3.12) becomes:

$$\begin{aligned} \int_0^\infty d\omega [\chi(\mathbf{r}, \mathbf{r}', i\omega) + \chi(\mathbf{r}', \mathbf{r}, i\omega)] &= \\ &= -\pi \sum_J \{ \langle 0 | \hat{n}(\mathbf{r}) | J \rangle \langle J | \hat{n}(\mathbf{r}') | 0 \rangle + \langle 0 | \hat{n}(\mathbf{r}') | J \rangle \langle J | \hat{n}(\mathbf{r}) | 0 \rangle \} + \\ &\quad + \pi \{ \langle 0 | \hat{n}(\mathbf{r}) | 0 \rangle \langle 0 | \hat{n}(\mathbf{r}') | 0 \rangle + \langle 0 | \hat{n}(\mathbf{r}') | 0 \rangle \langle 0 | \hat{n}(\mathbf{r}) | 0 \rangle \}. \end{aligned} \quad (3.14)$$

Here we have included the  $J = 0$  term in the sum and subtracted it afterwards. The states  $|J\rangle$  form a complete basis set ( $\sum_J |J\rangle \langle J| = 1$ ) so that Eq. (3.14) can be rewritten as:

$$\begin{aligned} \int_0^\infty d\omega (\chi(\mathbf{r}, \mathbf{r}', i\omega) + \chi(\mathbf{r}', \mathbf{r}, i\omega)) &= \\ &= -\pi \{ \langle 0 | \hat{n}(\mathbf{r}) \hat{n}(\mathbf{r}') | 0 \rangle + \langle 0 | \hat{n}(\mathbf{r}') \hat{n}(\mathbf{r}) | 0 \rangle \} + 2\pi n(\mathbf{r}) n(\mathbf{r}'). \end{aligned} \quad (3.15)$$

where we have used that  $\langle 0 | \hat{n}(\mathbf{r}) | 0 \rangle = n(\mathbf{r})$ . This relation holds for all systems and by replacing  $|0\rangle$  by  $|\Psi(\lambda)\rangle$  and  $\chi$  by  $\chi^\lambda$  (describing the density change to the change of the



potential  $v_\lambda$ ) we can write Eq. (3.10) as:

$$E_{Hxc} = \frac{e^2}{2} \int_0^1 d\lambda \int d^3r d^3r' \frac{1}{|\mathbf{r} - \mathbf{r}'|} \times \\ \times \left[ n(\mathbf{r}) n(\mathbf{r}') - \left\{ \frac{1}{\pi} \int_0^\infty \chi^\lambda(\mathbf{r}, \mathbf{r}', i\omega) d\omega \right\} - n(\mathbf{r}) \delta(\mathbf{r} - \mathbf{r}') \right]. \quad (3.16)$$

The first term is simply the Hartree energy as given in Eq. (13), so that Eq. (3.8) has been proven.

In many cases, the ACFDT exchange-correlation energy is written in a slightly different form. For this purpose, one considers the  $\lambda$  integrand of Eq. (3.8) for the KS case  $\lambda = 0$  ( $\chi^{KS} = \chi^0$ ):

$$-\frac{e^2}{2} \int d^3r d^3r' \frac{1}{|\mathbf{r} - \mathbf{r}'|} \left\{ n(\mathbf{r}) \delta(\mathbf{r} - \mathbf{r}') + \frac{1}{\pi} \int_0^\infty d\omega \chi^{KS}(\mathbf{r}, \mathbf{r}', i\omega) \right\}. \quad (3.17)$$

The response function  $\chi^{KS}$  is the independent-particle response function as given in Eq. (2.28) (here for imaginary frequencies). By a similar procedure as applied in Eq. (3.12) and Eq. (3.13) we can write

$$-\frac{e^2}{2\pi} \int d^3r d^3r' \frac{1}{|\mathbf{r} - \mathbf{r}'|} \int_0^\infty d\omega \chi^{KS}(\mathbf{r}, \mathbf{r}', i\omega) = \\ = \frac{e^2}{2\pi} \sum_{\substack{n \\ occ}} \sum_{\substack{m \\ uocc}} 2 \int d^3r d^3r' \frac{\psi_m^*(\mathbf{r}') \psi_n(\mathbf{r}') \psi_n^*(\mathbf{r}) \psi_m(\mathbf{r})}{|\mathbf{r} - \mathbf{r}'|} \int_0^\infty d\omega \left( \frac{2\omega_{nm}}{\omega_{nm}^2 + \omega^2} \right) = \\ = \frac{e^2}{2} \sum_{\substack{n \\ occ}} \sum_{\substack{m \\ uocc}} 2 \int d^3r d^3r' \frac{\psi_m^*(\mathbf{r}') \psi_n(\mathbf{r}') \psi_n^*(\mathbf{r}) \psi_m(\mathbf{r})}{|\mathbf{r} - \mathbf{r}'|}, \quad (3.18)$$

where  $n$  is summed over occupied and  $m$  over unoccupied states. By making use of

$$\sum_m \psi_m^*(\mathbf{r}') \psi_m(\mathbf{r}) = \delta(\mathbf{r} - \mathbf{r}') \quad \text{and} \quad n(\mathbf{r}) = \sum_{\substack{n \\ occ}} 2 \psi_n^*(\mathbf{r}) \psi_n(\mathbf{r}), \quad (3.19)$$

the first term in Eq. (3.17) is given by

$$-\frac{e^2}{2} \int d^3r d^3r' \frac{n(\mathbf{r}) \delta(\mathbf{r} - \mathbf{r}')}{|\mathbf{r} - \mathbf{r}'|} = -\frac{e^2}{2} \sum_{\substack{n \\ occ}} \sum_m 2 \int d^3r d^3r' \frac{\psi_m^*(\mathbf{r}') \psi_n(\mathbf{r}') \psi_n^*(\mathbf{r}) \psi_m(\mathbf{r})}{|\mathbf{r} - \mathbf{r}'|}. \quad (3.20)$$

Combining Eq. (3.18) and Eq. (3.20), Eq. (3.17) becomes:

$$-\frac{e^2}{2} \sum_{\substack{n \\ occ}} \sum_{\substack{m \\ occ}} 2 \int d^3r d^3r' \frac{\psi_m^*(\mathbf{r}') \psi_n(\mathbf{r}') \psi_n^*(\mathbf{r}) \psi_m(\mathbf{r})}{|\mathbf{r} - \mathbf{r}'|} = E_x[\{\psi^{KS}\}], \quad (3.21)$$

which is the exchange energy evaluated for DFT wavefunctions. The exchange-correlation energy described in Eq. (3.8) can thus also be written as:

$$E_{xc} = E_x[\{\psi^{KS}\}] - \\ - \underbrace{\int_0^1 d\lambda \int d^3r \int d^3r' \frac{e^2}{|\mathbf{r} - \mathbf{r}'|} \int_0^\infty \frac{d\omega}{2\pi} \left\{ \chi^\lambda(\mathbf{r}, \mathbf{r}', i\omega) - \chi^{KS}(\mathbf{r}, \mathbf{r}', i\omega) \right\}}_{E_c}. \quad (3.22)$$

In reciprocal space the correlation energy per unit cell is given as:

$$E_c = - \int_0^1 d\lambda \int_0^\infty \frac{d\omega}{2\pi} \sum_{\mathbf{q} \in \text{BZ}} \sum_{\mathbf{G}} \frac{4\pi e^2}{|\mathbf{q} + \mathbf{G}|^2} \left\{ \chi_{\mathbf{G},\mathbf{G}}^\lambda(\mathbf{q}, i\omega) - \chi_{\mathbf{G},\mathbf{G}}^{KS}(\mathbf{q}, i\omega) \right\} \quad (3.23)$$

$$= - \int_0^1 d\lambda \int_0^\infty \frac{d\omega}{2\pi} \text{Tr} \left\{ \nu \left[ \chi^\lambda(i\omega) - \chi^{KS}(i\omega) \right] \right\} \quad (3.24)$$

with the trace defined as

$$\text{Tr}\{AB\} = \sum_{\mathbf{q} \in \text{BZ}} \sum_{\mathbf{G}, \mathbf{G}'} A_{\mathbf{G}, \mathbf{G}'} B_{\mathbf{G}', \mathbf{G}} \quad (3.25)$$

and the Coulomb kernel given as  $\nu_{\mathbf{G}, \mathbf{G}'}(\mathbf{q}) = 4\pi e^2 / |\mathbf{G} + \mathbf{q}|^2 \delta_{\mathbf{G}, \mathbf{G}'}$ . Due to the fact that the real space Coulomb kernel depends only on the difference  $|\mathbf{r} - \mathbf{r}'|$ ,  $\nu_{\mathbf{G}, \mathbf{G}'} \propto \delta_{\mathbf{G}, \mathbf{G}'}$ .

### 3.2 Random phase approximation

Eq. (3.22) is exact, in principle, as long as one can evaluate the response function of the interacting electron system  $\chi^\lambda$ . The response function of the  $\lambda$  interacting system,  $\chi^\lambda$ , and of the KS system of independent electrons,  $\chi^{KS}$ , are linked by the Dyson equation

$$\begin{aligned} \chi^\lambda(\mathbf{r}, \mathbf{r}', i\omega) &= \chi^{KS}(\mathbf{r}, \mathbf{r}', i\omega) + \\ &+ \int d^3r_1 d^3r_2 \chi^{KS}(\mathbf{r}, \mathbf{r}_1, i\omega) \left( \frac{\lambda e^2}{|\mathbf{r}_1 - \mathbf{r}_2|} + f_{xc}^\lambda(\mathbf{r}_1, \mathbf{r}_2, i\omega) \right) \chi^\lambda(\mathbf{r}_2, \mathbf{r}', i\omega), \end{aligned} \quad (3.26)$$

which in reciprocal space reads:

$$\begin{aligned} \chi_{\mathbf{G}, \mathbf{G}'}^\lambda(\mathbf{q}, i\omega) &= \chi_{\mathbf{G}, \mathbf{G}'}^{KS}(\mathbf{q}, i\omega) + \\ &+ \sum_{\mathbf{G}_1 \mathbf{G}_2} \chi_{\mathbf{G}, \mathbf{G}_1}^{KS}(\mathbf{q}, i\omega) \left( \frac{4\pi e^2 \lambda}{|\mathbf{q} + \mathbf{G}_1|^2} \delta_{\mathbf{G}_1, \mathbf{G}_2} + f_{xc, \mathbf{G}_1, \mathbf{G}_2}^\lambda(\mathbf{q}, i\omega) \right) \chi_{\mathbf{G}_2, \mathbf{G}'}^\lambda(\mathbf{q}, i\omega). \end{aligned} \quad (3.27)$$

Similar relations have already been introduced in Eq. (2.14) and Eq. (2.69), but now the exchange-correlation kernel  $f_{xc}$  additionally depends on the coupling constant  $\lambda$ . It can be shown [35] that the  $\lambda$  dependent exchange-correlation kernel obeys the scaling relation

$$f_{xc}^\lambda[n](\mathbf{r}, \mathbf{r}', \omega) = \lambda^2 f_{xc}[n'](\lambda\mathbf{r}, \lambda\mathbf{r}', \omega/\lambda^2) \quad \text{with} \quad n'(\mathbf{r}) = \lambda^{-3} n(\mathbf{r}/\lambda), \quad (3.28)$$

so that for any approximation of the fully interacting exchange-correlation kernel,  $f_{xc}$ , also the one depending on the coupling constant  $\lambda$ ,  $f_{xc}^\lambda$ , can be evaluated. Throughout this work we use the random phase approximation (RPA), which has already been introduced in Sec. 2.6, and thus set the exchange-correlation kernel to zero ( $f_{xc} = 0$ ). The relation between  $\chi^\lambda$  and  $\chi^{KS}$  in the RPA is given by

$$\begin{aligned} \chi^{RPA, \lambda}(\mathbf{r}, \mathbf{r}', i\omega) &= \chi^{KS}(\mathbf{r}, \mathbf{r}', i\omega) + \\ &+ \int d^3r_1 d^3r_2 \chi^{KS}(\mathbf{r}, \mathbf{r}_1, i\omega) \frac{\lambda e^2}{|\mathbf{r}_1 - \mathbf{r}_2|} \chi^{RPA, \lambda}(\mathbf{r}_2, \mathbf{r}', i\omega). \end{aligned} \quad (3.29)$$

or in reciprocal space

$$\chi_{\mathbf{G},\mathbf{G}'}^{RPA,\lambda}(\mathbf{q}, i\omega) = \chi_{\mathbf{G},\mathbf{G}'}^{KS}(\mathbf{q}, i\omega) + \sum_{\mathbf{G}_1} \chi_{\mathbf{G},\mathbf{G}_1}^{KS}(\mathbf{q}, i\omega) \frac{4\pi e^2 \lambda}{|\mathbf{q} + \mathbf{G}_1|^2} \chi_{\mathbf{G}_1,\mathbf{G}'}^{RPA,\lambda}(\mathbf{q}, i\omega). \quad (3.30)$$

In the following we will omit the index *RPA* and the use of the RPA is implicitly assumed. By rearranging Eq. (3.30), the RPA response of the interacting system can be written as

$$\chi_{\mathbf{G},\mathbf{G}'}^\lambda(\mathbf{q}, i\omega) = \sum_{\mathbf{G}_1} (1 - \lambda \chi_{\mathbf{G},\mathbf{G}_1}^{KS} \nu)^{-1} \chi_{\mathbf{G}_1,\mathbf{G}'}^{KS}(\mathbf{q}, i\omega). \quad (3.31)$$

For the RPA, the  $\lambda$  integration in Eq. (3.24) can be avoided by making use of the fact that

$$\text{Tr}\{\nu \chi^\lambda\} = -\frac{\partial}{\partial \lambda} \text{Tr}\{\ln[1 - \lambda \chi^{KS} \nu]\}. \quad (3.32)$$

Eq. (3.32) can be shown straightforwardly by considering

$$\begin{aligned} -\frac{\partial}{\partial \lambda} \sum_{\mathbf{G}} \ln[1 - \lambda \chi_{\mathbf{G},\mathbf{G}}^{KS} \nu] &= \sum_{\mathbf{G}} \sum_{\mathbf{G}_1, \mathbf{G}_2} (1 - \lambda \chi_{\mathbf{G},\mathbf{G}_1}^{KS} \nu)^{-1} \chi_{\mathbf{G}_1,\mathbf{G}_2}^{KS} \nu_{\mathbf{G}_2,\mathbf{G}} = \\ &= \sum_{\mathbf{G}, \mathbf{G}_1} (1 - \lambda \chi_{\mathbf{G},\mathbf{G}_1}^{KS} \nu)^{-1} \chi_{\mathbf{G}_1,\mathbf{G}}^{KS} \nu_{\mathbf{G},\mathbf{G}} = \sum_{\mathbf{G}} \nu_{\mathbf{G},\mathbf{G}} \chi_{\mathbf{G},\mathbf{G}}^\lambda. \end{aligned} \quad (3.33)$$

The  $\lambda$ -integration of the first term in Eq. (3.24) can then be written as

$$-\int_0^1 d\lambda \left[ \frac{\partial}{\partial \lambda} \text{Tr}\{\ln[1 - \lambda \chi^{KS} \nu]\} \right] = -\text{Tr}\{\ln[1 - \chi^{KS} \nu]\}, \quad (3.34)$$

and the RPA correlation energy finally is given as

$$\begin{aligned} E_c &= \int_0^\infty \frac{d\omega}{2\pi} \text{Tr} \{ \ln[1 - \chi^{KS} \nu] + \chi^{KS} \nu \} = \\ &= \int_0^\infty \frac{d\omega}{2\pi} \sum_{\mathbf{q} \in BZ} \sum_{\mathbf{G}} \left\{ (\ln[1 - \chi_{\mathbf{G},\mathbf{G}}^{KS}(\mathbf{q}, i\omega) \nu(\mathbf{q})])_{\mathbf{G},\mathbf{G}} + \nu_{\mathbf{G},\mathbf{G}}(\mathbf{q}) \chi_{\mathbf{G},\mathbf{G}}^{KS}(\mathbf{q}, i\omega) \right\} \end{aligned} \quad (3.35)$$

and no numerical  $\lambda$  integration has to be considered. If one introduces an exchange-correlation kernel different from zero, this is not the case anymore.

### 3.3 Calculating the RPA correlation energy in practice

The total ACFDT energy in the RPA is given by

$$E = T_s[\{\psi^{KS}\}] + E_H[n] + E_x[\{\psi^{KS}\}] + E_c^{RPA}[\chi^{KS}] = E_{HF}[\{\psi^{KS}\}] + E_c^{RPA}, \quad (3.36)$$

where the first three terms represent the Hartree-Fock energy expression evaluated for the KS wavefunctions and the second term the RPA correlation energy as given in Eq. (3.35). In principle, the energy functional should be evaluated at the "true" Kohn-Sham wavefunctions and eigenenergies fulfilling:

$$H_{KS} \psi_n^{KS}(\mathbf{r}) = \epsilon_n \psi_n^{KS}(\mathbf{r}) \quad v_{xc}(\mathbf{r}) = \delta E_{xc}[n] / \delta n(\mathbf{r}). \quad (3.37)$$

A derivation for the compatible RPA exchange-correlation potential can be found in the work of Niquet *et al.* [36], but the practical introduction of selfconsistency is very demanding. Therefore, it is common to evaluate Eq. (3.36) at the PBE, LDA, or some hybrid functional (e.g., PBE0) wavefunctions and eigenenergies. In the present work, we usually use PBE wavefunctions and eigenenergies as an input, but tests applying LDA values will also be presented. More details concerning the evaluation of the Hartree-Fock Hamiltonian in VASP can be found in Ref. [37].

The evaluation of the correlation energy is the most demanding part in Eq. (3.36). In the following, we will discuss the calculation of  $E_c$  and the computational cost involved in more detail. In the practical implementation we closely follow the expression Eq. (3.35) for the evaluation of the correlation energy. Thereby the term<sup>1</sup>

$$\text{Tr}\{\ln[1 - AB]\} = \sum_i (\ln[1 - AB])_{ii} := \sum_{\mathbf{G}} (\ln[1 - \chi^{\text{KS}} \nu])_{\mathbf{G}, \mathbf{G}} \quad (3.38)$$

has to be calculated. The logarithm of a matrix can be written as

$$\ln[1 - AB]_{ij} = -(AB)_{ij} - \frac{1}{2} \sum_k (AB)_{ik} (AB)_{kj} - \frac{1}{3} \sum_{kl} (AB)_{ik} (AB)_{kl} (AB)_{kj} - \dots \quad (3.39)$$

and the trace

$$\text{Tr}\{\ln[1 - AB]\} = -\text{Tr}\{AB\} - \frac{1}{2} \text{Tr}\{ABAB\} - \frac{1}{3} \text{Tr}\{ABABAB\} - \dots \quad (3.40)$$

For later considerations it is useful to replace  $\chi^{\text{KS}} \nu$  by the symmetric expression  $\nu^{1/2} \chi^{\text{KS}} \nu^{1/2}$ , which does not change the trace in Eq. (3.38). This can easily be shown by using

$$\text{Tr}\{ABC\} = \text{Tr}\{CAB\} \quad (3.41)$$

or

$$\text{Tr}\{\chi^{\text{KS}} \nu\} = \text{Tr}\{\chi^{\text{KS}} \nu^{1/2} \nu^{1/2}\} = \text{Tr}\{\nu^{1/2} \chi^{\text{KS}} \nu^{1/2}\}. \quad (3.42)$$

Applying the same transformation to expression Eq. (3.40) one finds

$$\text{Tr}\{\ln[1 - \chi^{\text{KS}} \nu] + \chi^{\text{KS}} \nu\} = \text{Tr}\{\ln[1 - \nu^{1/2} \chi^{\text{KS}} \nu^{1/2}]\} + \text{Tr}\{\nu^{1/2} \chi^{\text{KS}} \nu^{1/2}\}. \quad (3.43)$$

Because  $S := \nu^{1/2} \chi^{\text{KS}} \nu^{1/2}$  is hermitian, it can be diagonalized yielding real eigenvalues  $d_i$  and an orthogonal (unitary) matrix of eigenvectors  $C_{ij}$ :

$$\sum_{kl} C_{ik}^{-1} S_{kl} C_{lj} = d_{ii} \delta_{ij}, \quad (3.44)$$

and due to Eq. (3.40) and Eq. (3.41)

$$\text{Tr}\{\ln[1 - \chi^{\text{KS}} \nu]\} + \text{Tr}\{\chi^{\text{KS}} \nu\} = \sum_i \ln(1 - d_{ii}) + d_{ii}. \quad (3.45)$$

---

<sup>1</sup>Here  $\text{Tr}$  denotes simply the sum over diagonal matrix elements, and no  $q$  integration is taken into account as has been done in the definition Eq. (3.32)

Consequently, in order to evaluate Eq. (3.35) two steps have to be performed (for the moment ignoring the frequency integration): The term  $\nu_{\mathbf{G},\mathbf{G}}^{1/2}(\mathbf{q}) \chi_{\mathbf{G},\mathbf{G}'}^{KS}(\mathbf{q}) \nu_{\mathbf{G}',\mathbf{G}'}^{1/2}(\mathbf{q})$  has to be set up for all  $q$ -points ( $N_q$ ) and reciprocal lattice vectors  $\mathbf{G}$  and  $\mathbf{G}'$ . The number of reciprocal lattice vectors  $N_{PW}^\chi$  is determined by  $|\mathbf{G} + \mathbf{q}|^2/2 < E_{\text{cut}}^\chi$ , where  $E_{\text{cut}}^\chi$  is chosen by setting ENCUTGW (eV) in the INCAR file. Considering Eq. (2.33) the total cost for this step scales like  $N_q N_k N_{occ} N_{uocc} (N_{PW}^\chi)^2$  where  $N_{occ}$  and  $N_{uocc}$  are the number of occupied and unoccupied bands, respectively. On the other hand,  $\nu_{\mathbf{G},\mathbf{G}}^{1/2}(\mathbf{q}) \chi_{\mathbf{G},\mathbf{G}'}^{KS}(\mathbf{q}) \nu_{\mathbf{G}',\mathbf{G}'}^{1/2}(\mathbf{q})$  has to be diagonalized with respect to  $\mathbf{G}, \mathbf{G}'$  for all  $q$ -points in order to evaluate the eigenenergies and consequently the trace given by Eq. (3.45). This step scales like  $N_q (N_{PW}^\chi)^3$ . Both steps scale like  $V^3$  for a fixed number of  $k$ -points and electrons, which makes the evaluation of the RPA correlation energies for molecules and atoms expensive, because in this case rather large unit cells have to be employed.

As will be shown in section 10.1, the correlation energy slowly converges with the rank of the response function and  $E_{\text{cut}}^\chi$ , respectively. But in many cases, the correlation energy (difference) for sufficiently large values of  $E_{\text{cut}}^\chi$  behaves as

$$E_c(E_{\text{cut}}^\chi) = E_c^\infty + \frac{A}{(E_{\text{cut}}^\chi)^{3/2}}. \quad (3.46)$$

For the homogenous electron gas this behaviour is exactly observed, and it also holds for correlation energy differences of arbitrary systems. For simple systems without deep lying core states it is even approximatively observed for the correlation energy itself. For RPA correlation energy calculations, 8 values of  $E_{\text{cut}}^\chi$  are automatically chosen starting from the value ENCUTGW in the INCAR file and decreasing in steps of 5%. For each value of  $E_{\text{cut}}^\chi$ , the correlation energy  $E_c(E_{\text{cut}}^\chi)$  is calculated and the extrapolated value  $E_c^\infty$  using Eq. (3.46) is determined. In contrast to a set of full calculations, each time setting ENCUTGW to a different value in the INCAR file, this procedure saves the cost to set up the response function in each of the calculations. This is especially useful for small volumes or calculations using many  $k$ -points where the cost for setting up of the response function exceeds the cost for the diagonalization by far. The frequency integration is rather straightforward and will be discussed in Sec. 10.2.

## Chapter 4

# GW quasiparticle energies

Density functional theory provides a good description of ground state properties by mapping the problem of interacting electrons onto a KS system of independent particles moving in an effective potential caused by the other electrons. For the calculation of (inverse) photoemission spectra, the energy to add or remove an electron to or from a system is required. For a system of non-interacting electrons, these energies correspond to the one-electron energies. For a system of interacting electrons, the KS system can be used to calculate the ground state energy, but no theorem links the KS one-electron energies to the electron addition and removal energies. Instead, a system of quasiparticles that interact via the non-local and energy-dependent self-energy  $\Sigma$  should be considered. The fundament of the resulting quasiparticle equations is provided by many-body perturbation theory. In the widely used GW approximation, the self-energy operator is described as a product of the Green's ( $G$ ) function and the screened Coulomb kernel  $W = \varepsilon^{-1} \nu$ . Especially for the description of band gaps, which are generally underestimated in KS-DFT, the GW approximation leads to drastically improved results. E.g., for Si, LDA yields a band gap of 0.6 eV, whereas GW gives a band gap around 1.15 eV close to the experimentally observed gap of 1.25 eV.

In the following, a brief overview on the Green's function approach and the quasiparticle equations will be given. In Sec. 4.2 the actual evaluation of the quasiparticle equations will be outlined with a focus on the implementation of the GW routines in the VASP code [25]. More details about many-body perturbation theory and applications are provided in the reviews Refs. [38, 39, 40] where Ref. [39] focuses specifically on the comparison of many-body perturbation theory and time-dependent density functional theory.

In part III of this thesis, GW calculations for the transition metals Cu, Ag, Fe, and Ni will be presented. Former calculations by Marini *et al.* for Cu [41] and Ag [42] yielded a good agreement between GW quasiparticle energies and experimental photoemission data, whereas our results suggest that this was most likely fortuitous and related to the pseudopotential approximation used in Ref. [41] and Ref. [42]. For Ni [43], previous GW calculations have shown that the large LDA exchange splitting could not be corrected, which we found confirmed in the present study. Furthermore,  $d$  bands might not be as well described as  $sp$  like states as suggested by a recent work of Louie *et al.* [44].

## 4.1 The GW approximation

The Green's function  $G(\mathbf{x}, \mathbf{x}', t, t')$ , which is the fundamental quantity of many-body perturbation theory, describes the probability of finding an electron with spin  $\xi$  at time  $t$  and position  $\mathbf{r}$ , if another electron with spin  $\xi'$  is added (or removed) at position  $\mathbf{r}'$  at time  $t'$ . It can be shown that the poles of the Green's function describe the energies needed to add/remove an electron from the system and that the imaginary part of the Green's function - the spectral function - is proportional to the photoemission spectrum. For a system of non-interacting electrons moving in the external potential  $v(\mathbf{x})$ , the energies to add or remove an electron are given by the eigenenergies of

$$[T + v(\mathbf{x})] \psi_n = \epsilon_n \psi_n \quad T + v(\mathbf{x}) =: H_0(\mathbf{x}), \quad (4.1)$$

with the kinetic energy operator  $T = -(\hbar^2/2m) \nabla^2$ , and the corresponding Green's function  $G_H$  (Hartree Green's function) becomes

$$G_H^{-1}(\mathbf{x}, \mathbf{x}', \omega) = \delta(\mathbf{x} - \mathbf{x}') [\omega - H_0] \quad G_H(\mathbf{x}, \mathbf{x}', \omega) = \sum_n \frac{\psi_n(\mathbf{x}) \psi_n^*(\mathbf{x}')}{\omega - \epsilon_n + i\eta \operatorname{sgn}(\epsilon_n - \mu)}, \quad (4.2)$$

where  $\eta$  is a positive infinitesimal and  $\mu$  is the Fermi energy of the system. The spectral function of a non-interacting system, therefore, consists of  $\delta$ -like functions at the one-electron energies  $\epsilon_n$ . For a system of interacting electrons, the perturbation caused by the addition or removal of an electron is screened and the sharp independent particle peaks in the spectral function are replaced by quasiparticle (QP) peaks with finite widths. Additionally, the weights of the QP peaks are reduced and further structures, satellites, appear at other energies. The relation between the non-interacting Green's function  $G_H$  and the Green's function of the interacting system  $G$  is given by the Dyson equation

$$G^{-1}(\mathbf{x}, \mathbf{x}', \omega) = G_H^{-1}(\mathbf{x}, \mathbf{x}', \omega) - \Sigma(\mathbf{x}, \mathbf{x}', \omega), \quad (4.3)$$

where the self-energy operator  $\Sigma$  includes the many-body effects due to exchange and correlation. The poles of the interacting Green's function can be found by solving the QP equation:

$$H_0(\mathbf{x}) \psi_n^{QP}(\mathbf{x}) + \int d\mathbf{x}' \Sigma(\mathbf{x}, \mathbf{x}', E_n^{QP}) \psi_n^{QP}(\mathbf{x}') = E_n^{QP} \psi_n^{QP}(\mathbf{x}) \quad (4.4)$$

where the QP energies are complex quantities describing the position ( $\operatorname{Re} E_n^{QP}$ ) and width ( $\operatorname{Im} E_n^{QP}$ ) of the QP peaks.

The relation between the Green's function  $G$ , the self-energy  $\Sigma$ , the irreducible polarizability  $P$  (see Sec. 2.5), the screened Coulomb interaction  $W = \epsilon^{-1} \nu$ , and the so-called vertex

function  $\Gamma$ , is given by Hedin's equations  $[(\mathbf{x}_i, t_i) = i]$ :

$$P(12) = -i \int d(34) G(13) G(41^+) \Gamma(342) \quad (4.5)$$

$$W(12) = \nu(12) + \int d(34) W(13) P(34) \nu(42) \quad (4.6)$$

$$\Sigma(12) = i \int d(34) G(14^+) W(13) \Gamma(423) \quad (4.7)$$

$$\Gamma(123) = \delta(12) \delta(13) + \int d(4567) \frac{\delta \Sigma(12)}{\delta G(45)} G(46) G(75) \Gamma(673) \quad (4.8)$$

$$G(12) = G_{KS}(12) + \int d(34) G_{KS}(13) \Sigma(34) G(42). \quad (4.9)$$

The Dyson equation for the relation between the interacting and non-interacting Green's function, Eq. (4.3), is thereby rephrased in Eq. (4.9) for the case that the KS-DFT system is taken as the reference system, as usually done in practical calculations. Hedin's equations should in principle be solved selfconsistently, but this is involved. The most common approximation to simplify this approach is the so-called GW approximation. The vertex corrections are thereby excluded which corresponds to setting  $\Gamma(123) = \delta(12) \delta(13)$  in Eq. (4.8). Consequently, the irreducible polarizability [see Eq. (4.5)] is described by  $P(12) = -i G(12) G(21^+)$ , which equals the RPA approximation and the neglect of electron-hole interactions. The self-energy, finally, is approximated by

$$\Sigma(12) = i G(12^+) W(12), \quad (4.10)$$

explaining the name of the "GW" approximation.

## 4.2 Solving the quasiparticle equation

The QP equations for a periodic crystal can be written as:

$$(T + v_{\text{ext}} + v_H) \psi_{n\mathbf{k}}^{QP}(\mathbf{r}) + \int d^3 r' \Sigma(\mathbf{r}, \mathbf{r}', E_{n\mathbf{k}}^{QP}) \psi_{n\mathbf{k}}^{QP}(\mathbf{r}') = E_{n\mathbf{k}}^{QP} \psi_{n\mathbf{k}}^{QP}(\mathbf{r}). \quad (4.11)$$

Normally, the wavefunctions are taken from a KS calculation ( $\psi_{n\mathbf{k}}$  instead of  $\psi_{n\mathbf{k}}^{QP}$ ) and are not updated throughout the calculations. Self-consistency with respect to the wavefunctions can nevertheless be introduced (see the scQPGW method described in Refs. [45, 46, 47]). Additionally, Eq. (4.11) is solved only on the real axis, i.e., imposing the constraint that  $E_{n\mathbf{k}}^{QP}$  is real. If the DFT wavefunctions are considered, the quasiparticle energies equal the solution of

$$E_{n\mathbf{k}}^{QP} = \text{Re}[\langle \psi_{n\mathbf{k}} | T + v_{\text{ext}} + v_H + \Sigma(E_{n\mathbf{k}}^{QP}) | \psi_{n\mathbf{k}} \rangle]. \quad (4.12)$$

An iterative solution to Eq. (4.12) can be found by

$$\begin{aligned} E_{n\mathbf{k}}^{N+1} &= \text{Re}[\langle \psi_{n\mathbf{k}} | T + v_{\text{ext}} + v_H + \Sigma(E_{n\mathbf{k}}^{N+1}) | \psi_{n\mathbf{k}} \rangle] = \\ &= \text{Re}[\langle \psi_{n\mathbf{k}} | T + v_{\text{ext}} + v_H + \Sigma(E_{n\mathbf{k}}^N) | \psi_{n\mathbf{k}} \rangle] + (E_{n\mathbf{k}}^{N+1} - E_{n\mathbf{k}}^N) \text{Re}[\langle \psi_{n\mathbf{k}} | \frac{\partial \Sigma(\omega)}{\partial \omega} \Big|_{\omega=E_{n\mathbf{k}}^N} | \psi_{n\mathbf{k}} \rangle], \end{aligned} \quad (4.13)$$



i.e., by linearizing  $\Sigma(E_{n\mathbf{k}}^{N+1})$  around  $\Sigma(E_{n\mathbf{k}}^N)$ . The superscript QP has and will be omitted in the following. By introducing the normalization factor  $Z$  that accounts for the fact that the weights of the QP peaks are reduced at the cost of emerging satellites

$$Z_{n\mathbf{k}}^N = \left( 1 - \text{Re}[\langle \psi_{n\mathbf{k}} | \frac{\partial \Sigma(\omega)}{\partial \omega} \Big|_{\omega=E_{n\mathbf{k}}^N} | \psi_{n\mathbf{k}} \rangle] \right)^{-1}, \quad (4.14)$$

the QP energies can be approximated as

$$E_{n\mathbf{k}}^{N+1} = E_{n\mathbf{k}}^N + Z_{n\mathbf{k}}^N \text{Re}[\langle \psi_{n\mathbf{k}} | T + v_{\text{ext}} + v_H + \Sigma(E_{n\mathbf{k}}^N) | \psi_{n\mathbf{k}} \rangle - E_{n\mathbf{k}}^N]. \quad (4.15)$$

Several degrees of selfconsistency can be distinguished depending on how the expectation value of the self-energy operator [see also Eq. (4.10)]

$$\begin{aligned} \Sigma(\omega)_{n\mathbf{k},n\mathbf{k}} &= \langle \psi_{n\mathbf{k}} | \Sigma(E_{n\mathbf{k}}^N) | \psi_{n\mathbf{k}} \rangle = \\ &= \frac{i}{2\pi V} \sum_{\mathbf{q}, \mathbf{G}, \mathbf{G}'} \sum_{n'} 2 \int_0^\infty d\omega' W_{\mathbf{q}}(\mathbf{G}, \mathbf{G}', \omega') \langle \psi_{n\mathbf{k}} | e^{i(\mathbf{G}+\mathbf{q})\mathbf{r}} | \psi_{n'\mathbf{k}+\mathbf{q}} \rangle \langle \psi_{n'\mathbf{k}+\mathbf{q}} | e^{-i(\mathbf{G}'+\mathbf{q})\mathbf{r}'} | \psi_{n\mathbf{k}} \rangle \\ &\quad \times \left( \frac{1}{\omega + \omega' - \epsilon_{n'\mathbf{k}+\mathbf{q}} + i\eta \text{sgn}[\epsilon_{n'\mathbf{k}+\mathbf{q}} - \mu]} + \frac{1}{\omega - \omega' - \epsilon_{n'\mathbf{k}+\mathbf{q}} + i\eta \text{sgn}[\epsilon_{n'\mathbf{k}+\mathbf{q}} - \mu]} \right) \end{aligned} \quad (4.16)$$

is calculated. In the most common approximation,  $G_0W_0$ , only one iteration step of Eq. (4.15) is performed and DFT eigenenergies are chosen as a starting point. The dielectric function for the evaluation of the screened Coulomb interaction  $W$  is calculated using DFT eigenvalues. In the  $GW_0$  approximation, several circles of Eq. (4.15) are considered and the eigenvalues in Eq. (4.16) are approximated by  $E_{n\mathbf{k}}^N$  of the previous iteration. The dielectric function  $\epsilon$ , which enters the screened Coulomb kernel  $W$ , is thereby fixed at the DFT level. Finally,  $W$  in Eq. (4.16) can also be updated in each iteration. The GW calculations presented in part III of this thesis have mostly been performed applying the  $G_0W_0$  approximation, but in selected cases  $G$  [eigenvalues in Eq. (4.16)] has been updated as well.

In the following, we will discuss how to evaluate Eq. (4.16) in more detail. In Eq. (4.16) the screened Coulomb kernel  $W_{\mathbf{q}}(\mathbf{G}, \mathbf{G}', \omega)$  enters. For large frequencies  $\omega$  or large wave vectors  $\mathbf{G}$  the dielectric function  $\epsilon$  becomes 1 and  $W_{\mathbf{q}}(\mathbf{G}, \mathbf{G}', \omega)$  approaches the unscreened Coulomb kernel  $\nu_{\mathbf{q}}(\mathbf{G}, \mathbf{G}')$ . In order to make the frequency integration well behaved, the screened Coulomb kernel  $W$  in Eq. (4.16) is replaced by

$$\bar{W}_{\mathbf{q}}(\mathbf{G}, \mathbf{G}', \omega) = W_{\mathbf{q}}(\mathbf{G}, \mathbf{G}', \omega) - \nu_{\mathbf{q}}(\mathbf{G}, \mathbf{G}') \quad (4.17)$$

and the resulting quantity,  $\bar{\Sigma}_{n\mathbf{k},n\mathbf{k}}(\omega)$ , is calculated. The total self-energy  $\Sigma_{n\mathbf{k},n\mathbf{k}}(\omega)$  is obtained by

$$\Sigma_{n\mathbf{k},n\mathbf{k}}(\omega) = \bar{\Sigma}_{n\mathbf{k},n\mathbf{k}}(\omega) - \underbrace{\sum_{n'\mathbf{k}'} 2f_{n'\mathbf{k}'} e^2 \int d^3r d^3r' \frac{\psi_{n\mathbf{k}}^*(\mathbf{r}) \psi_{n'\mathbf{k}'}(\mathbf{r}) \psi_{n'\mathbf{k}'}^*(\mathbf{r}') \psi_{n\mathbf{k}}(\mathbf{r}')}{|\mathbf{r} - \mathbf{r}'|}}_{\langle \psi_{n\mathbf{k}} | v_x | \psi_{n\mathbf{k}} \rangle}. \quad (4.18)$$

The second term on the right side of Eq. (4.18) stems from replacing the screened by the unscreened Coulomb kernel  $\nu$  in Eq. (4.16), and it equals the non-local exchange potential

$v_x(\mathbf{r}, \mathbf{r}')$  evaluated for the state  $\psi_{n\mathbf{k}}$ ,  $\langle \psi_{n\mathbf{k}} | v_x | \psi_{n\mathbf{k}} \rangle$ . The determination of this term within the PAW framework is discussed in Refs. [37, 140]. For the evaluation of the one-center terms of the self-energy, the screened Coulomb kernel is replaced by the bare Coulomb kernel  $\nu$  and the one-center terms are thus approximated by the Hartree-Fock expression. This approximation is expected to lead to relatively small errors, since differences in the pseudo wave function and the AE wave function are only present for large vectors  $\mathbf{G}$  and the dielectric function is close to 1 for these cases.

The sum over states  $n'$  in Eq. (4.16) and Eq. (4.18) is only performed for states which are treated as valence. But although we make use of the frozen-core approximation, the core-valence interaction ( $n'$  describing a core state) can be approximatively calculated within the PAW framework. In order to evaluate the core-valence interaction, we again assume that the screened Coulomb kernel  $W$  can be replaced by the bare Coulomb kernel  $\nu$  and evaluate the core-valence interaction by the Hartree-Fock exchange contribution. As the core states are confined in the spheres around the atoms, it is sufficient to calculate the one-center term

$$\langle \psi_{n\mathbf{k}} | v_{x \text{ core-val}}^{(1)} | \psi_{n\mathbf{k}} \rangle = - \sum_{ij,c} 2e^2 \langle \tilde{\psi}_{n\mathbf{k}} | \tilde{p}_i \rangle \langle \tilde{p}_j | \tilde{\psi}_{n\mathbf{k}} \rangle \int d^3r d^3r' \frac{\phi_i^*(\mathbf{r}) \phi_c(\mathbf{r}) \phi_c^*(\mathbf{r}') \phi_j(\mathbf{r}')}{|\mathbf{r} - \mathbf{r}'|}, \quad (4.19)$$

where  $\psi_c(\mathbf{r})$  are core-electron orbitals  $c$ , centered on the same atom as the partial waves and projectors with the indices  $i$  and  $j$ . For deriving Eq. (4.19), the second term on the right side of Eq. (4.18) is considered and the projection of the pseudo wave function onto AE partial waves Eq. (1.20) is performed.

More details about the GW implementation in VASP are summarized in Refs. [25, 48, 47]. Terms like  $\langle \psi_{n'\mathbf{k}+\mathbf{q}} | e^{-i(\mathbf{G}'+\mathbf{q})\mathbf{r}'} | \psi_{n\mathbf{k}} \rangle$ , which are required for the calculation of the self energy and the dielectric function, can be treated within the same approximations as discussed in subsection 2.7. Approximately restoring the AE charge density on a plane wave grid by setting LMAXFOCKAE will effect the QP energies of the considered metals, as will be shown in part III of this thesis.

## Part II

# Reflectance difference spectra

Reflectance difference (RD) spectroscopy (also reflectance anisotropy (RA) spectroscopy) measures the difference in reflectance  $\Delta r = r_x - r_y$  between two orthogonal directions in the surface plane ( $x, y$ ) for normal incident light:

$$\frac{\Delta r}{\bar{r}} = \frac{2(r_x - r_y)}{r_x + r_y}. \quad (4.20)$$

The first RD/RA spectrometer was developed by Aspnes and co-workers [49, 50]. The incident light, which is chosen to be linearly polarized in an  $45^\circ$  angle with respect to the  $x$  and the  $y$ -direction, becomes elliptically polarized when reflected, if the material responds anisotropically to light polarized along the  $x$ - and  $y$ -direction. By measuring the polarization state for different wavelengths  $\lambda$ , one has access to the frequency dependent RD spectrum. It is easier to measure the real part of the reflectance difference,  $\text{Re}(\Delta r / \bar{r})$ , which in the following will be referred to as the actual RD signal. For more details about the experimental setup, we refer e.g., to Ref. [51].

RD spectroscopy is surface sensitive, if the bulk exhibits no optical anisotropy. This is e.g., the case for surfaces of fcc or bcc bulk structures. The anisotropy can arise from the bare surface itself. Examples are the (110) surface or faceted surfaces. But also adsorbate induced structures can give rise to an anisotropic optical response. The RD spectrum is determined by the optical response of the surface, and therefore linked to surface electronic transitions. Also small changes in the surface structure lead to a change in the electronic structure and consequently to a change in the RD spectrum. This makes RD spectroscopy a very sensitive probe for the surface region. Nevertheless, an interpretation of the RD spectrum with respect to the underlying electronic transitions and consequently an assignment of a RD spectrum to a specific surface geometry is not straightforward. First-principles calculations of the surface optical response and the resulting RD spectrum can provide a more detailed understanding. How to calculate the RD spectra from first-principles and which approximations have to be made will be the subject of the next chapter, but at this point it is already emphasised that all calculations are performed in the DFT and independent particle approximation, since more involved calculations (GW + Bethe-Salpeter) are not routinely possible for metallic surfaces.

In this part of my thesis, I will present RD spectra for the bare and adsorbate covered Cu(110) surface. The Cu(110) surface represents a good starting point for the calculation of RD spectra for several reasons, as it has been experimentally studied in detail [52, 53, 54, 55, 56, 57, 58]. Additionally, theoretical work exists in the literature which allows straightforward comparison [59, 60, 61]. In the last section of this part, the electronic structure of all considered surfaces will be discussed and the resulting RD spectra will be analyzed with respect to important electronic transitions.

## Chapter 5

# Calculating reflectance difference spectra

In order to calculate the RD spectrum theoretically, it has to be described by quantities that are directly and easily accessible using first-principles methods. Since the dielectric function  $\varepsilon$  determines the material's response to light completely, a relationship between the RD signal and the difference of the (macroscopic) dielectric function  $\Delta\varepsilon = \varepsilon_{xx} - \varepsilon_{yy}$  is expected to hold.

### 5.1 Three-phase model

For the situation considered in an RD experiment, namely a thin film with an anisotropic optical response between an isotropic bulk and a transparent environment (here: vacuum), such a relationship can be derived under the assumption that the thickness  $d$  of the anisotropic film is much smaller than the wavelength  $\lambda$  of the incident light. Within the three-phase model [62] the reflectance anisotropy is approximately given as<sup>1</sup>

$$\frac{\Delta r}{\bar{r}} = -\frac{4\pi i d}{\lambda} \frac{\Delta\varepsilon}{\varepsilon_b - 1} = -\frac{2id\omega}{c} \frac{\Delta\varepsilon}{\varepsilon_b - 1}, \quad (5.1)$$

where  $\omega$  and  $c$  are the frequency of the incident light and the vacuum light velocity, respectively. The surface dielectric anisotropy (SDA)  $\Delta\varepsilon = \varepsilon_{xx} - \varepsilon_{yy}$  and the bulk dielectric function  $\varepsilon_b$  are complex quantities. In the following we will give a short outline how this formula can be derived. We use the convention that

1. the time phase of the electromagnetic wave is chosen negative, the space phase positive:  $\mathbf{E}(\mathbf{r}, t) = \mathbf{E}_0 e^{-i(\omega t - \mathbf{k}\mathbf{r})}$ . This is in contrast to the convention used in most optical textbooks.
2. complex numbers are defined as:  $z = x + iy$ , in contrast to the convention  $z = x - iy$  often employed in optics textbooks.

The permeability  $\mu$  is set to 1.

---

<sup>1</sup>In some/most publications [54, 53, 51] these formula are given without a minus. The minus is due to the negative space phase used in the present work:  $\mathbf{E}(\mathbf{r}, t) = \mathbf{E}_0 e^{-i(\omega t - \mathbf{k}\mathbf{x})}$

We first introduce the Fresnel coefficient of a three-phase model [63], then apply the thin film approximation [62] and finally express the reflectance difference in terms of the dielectric function [Eq. (5.1)]. Before considering the reflectance of a three-phase model, we summarize the Fresnel formulas for the reflection and transmission coefficients of light at an interface between two materials. The reflectance  $r$  (transmission  $t$ ) coefficient is defined as the ratio between the amplitude of the reflected (transmitted) and the incident wave. Depending on the polarization direction of the incident light, different relations are found for light polarized parallel ( $p$ ) or normal ( $n$ ) to the plane of incidence:

$$r_{12}^n = \frac{n_1 \cos \alpha - n_2 \cos \beta}{n_1 \cos \alpha + n_2 \cos \beta} \quad (5.2)$$

$$t_{12}^n = \frac{2 n_1 \cos \alpha}{n_1 \cos \alpha + n_2 \cos \beta} \quad (5.3)$$

$$r_{12}^p = \frac{n_1 \cos \beta - n_2 \cos \alpha}{n_1 \cos \beta + n_2 \cos \alpha} \quad (5.4)$$

$$t_{12}^p = \frac{2 n_1 \cos \alpha}{n_1 \cos \beta + n_2 \cos \alpha}. \quad (5.5)$$

The (complex) refraction index of the initial and final material are referred to as  $n_1$  and  $n_2$ , the angle of incidence and refraction as  $\alpha$  and  $\beta$ , respectively. In the present case, we only consider normal incidence so that  $\alpha = \beta = 0$  and consequently no distinction between parallel and normal Fresnel coefficients exists:

$$r_{12} = \frac{n_1 - n_2}{n_1 + n_2} \quad (5.6)$$

$$t_{12} = \frac{2 n_1}{n_1 + n_2}. \quad (5.7)$$

The reflectance for a three-phase model  $r_{123}$  can be expressed by reflectance and transmission coefficients of the phase 1 - phase 2 and the phase 2 - phase 3 interface, respectively. The

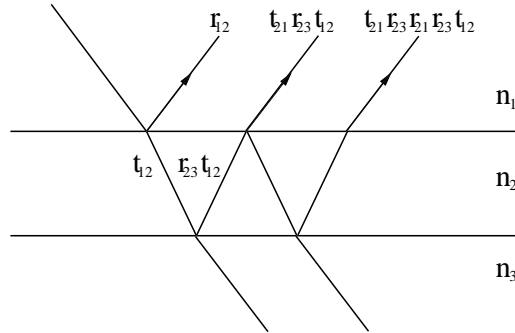


Figure 5.1: Schematic view of the three-phase model. Although we consider normal incidence, a non-zero incidence angle is chosen for reasons of clarity. The sum over the all (multi-)scattered wave components results in the total amplitude of the reflected wave.  $r_{21}$  and  $r_{23}$  denote the reflectance coefficients when going from phase 2 to phase 1 and phase 3, respectively. The transmission coefficients  $t_{12}$  and  $t_{21}$  describe the transmission from phase 1 to phase 2, and from phase 2 to phase 1, respectively.

procedure is schematically sketched in Fig. 5.1. If one considers (again assuming normal incidence), that the amplitude of a wave propagating inside a medium behaves as

$$A(z) = A_0 e^{2\pi i z n_2 / \lambda}, \quad (5.8)$$

the wave undergoes a change of  $e^{2i\beta}$  with  $\beta = 2d\pi n_2 / \lambda$ , when going from one side of the thin film and back again.<sup>2</sup> The total amplitude of the reflected wave  $A_r$  therefore is given by:

$$\begin{aligned} A_r = & r_{12}A_0 + t_{21}r_{23}t_{12}e^{2i\beta}A_0 + t_{21}r_{23}r_{21}e^{2i\beta}r_{23}t_{12}e^{2i\beta}A_0 + \\ & + t_{21}r_{23}r_{21}e^{2i\beta}r_{23}r_{21}e^{2i\beta}r_{23}t_{12}e^{2i\beta}A_0 + \dots \end{aligned} \quad (5.9)$$

The reflectance coefficient of the three-phase model  $r_{123} = A_r/A_0$  consequently becomes:

$$r_{123} = r_{12} + t_{21}r_{23}t_{12}e^{2i\beta} \left( 1 + r_{21}r_{23}e^{2i\beta} + (r_{21}r_{23}e^{2i\beta})^2 + (r_{21}r_{23}e^{2i\beta})^3 + \dots \right). \quad (5.10)$$

By writing the sum of the geometrical series explicitly and replacing  $r_{21}$  by  $-r_{12}$ ,  $r_{123}$  becomes:

$$r_{123} = r_{12} + \frac{t_{21}r_{23}t_{12}e^{2i\beta}}{1 + r_{12}r_{23}e^{2i\beta}}. \quad (5.11)$$

This expression can be transformed by applying Eq. (5.6) and Eq. (5.7)<sup>3</sup>:

$$r_{123} = \frac{r_{12} + r_{23}e^{2i\beta}}{1 + r_{12}r_{23}e^{2i\beta}}. \quad (5.12)$$

For  $d \rightarrow 0$ , the reflectance coefficient  $r_{13}$  has to be restored, so that

$$r_{13} = \frac{r_{12} + r_{23}}{1 + r_{12}r_{23}}. \quad (5.13)$$

Until now, we have derived the reflectance of a three-phase model in terms of the reflectance of two phases each. In order to obtain an explicit formula depending on the dielectric function  $\varepsilon = n^2$ , we assume that the thickness of the film,  $d$ , is much smaller than the wavelength  $\lambda$  of the incident light. As we will calculate the RD spectrum for light with energies ranging from 1 to 5 eV (corresponding to  $\lambda \approx 1250$  nm and  $\approx 250$  nm) and consider surface regions of a few nm thickness, this assumption is reasonable. For the thin film case, the exponential function can be expanded and by neglecting terms of order  $O(d^2/\lambda^2)$  one finds:

$$r_{123} = \frac{r_{12} + r_{23}(1 + 2i\beta)}{1 + r_{12}r_{23}(1 + 2i\beta)}. \quad (5.14)$$

Additionally, we consider the ratio between the reflectance of a three-phase model  $r_{123}$  and the reflectance for  $d \rightarrow 0$ ,  $r_{13}$ :

$$\frac{r_{123}}{r_{13}} = \frac{1 + 2i\beta [r_{23}/(r_{12} + r_{23})]}{1 + 2i\beta [r_{12}r_{23}/(1 + r_{12}r_{23})]}. \quad (5.15)$$

<sup>2</sup>If the space phase is chosen negative, as done in most optics text books,  $e^{2i\beta}$  is replaced by  $e^{-2i\beta}$

<sup>3</sup>see also Heavens [63]. Again: different space phase.

Expansion of the denominator with respect to  $d/\lambda$  and again neglecting terms of higher order in  $d/\lambda$ , the ratio becomes

$$\frac{r_{123}}{r_{13}} = 1 + 2i\beta \left[ \frac{r_{23}(1 - r_{12}^2)}{(r_{12} + r_{23})(1 + r_{12}r_{23})} \right]. \quad (5.16)$$

Using the Fresnel formulas given in Eq. (5.6) and Eq. (5.7), we obtain:

$$\frac{r_{123}}{r_{13}} = 1 + 2i\beta \left( \frac{n_1 n_2}{n_2^2} \right) \left( \frac{n_2^2 - n_3^2}{n_1^2 - n_3^2} \right) = 1 + 2i\beta \left( \frac{n_1 n_2}{n_2^2} \right) \left( \frac{\varepsilon_2 - \varepsilon_3}{\varepsilon_1 - \varepsilon_3} \right). \quad (5.17)$$

Replacing  $\beta$  by  $2d\pi n_2/\lambda$  the ratio becomes<sup>4</sup>

$$\frac{r_{123}}{r_{13}} = 1 + \frac{4\pi i d n_1}{\lambda} \left( \frac{\varepsilon_2 - \varepsilon_3}{\varepsilon_1 - \varepsilon_3} \right). \quad (5.18)$$

If we consider the first phase to be vacuum, than  $\varepsilon_1 = 1$  and  $n_1 = 1$ . Additionally, we assume the bulk dielectric function (corresponding to  $\varepsilon_3$ ) to be isotropic and set  $\varepsilon_3 = \varepsilon_b$ . The anisotropic dielectric tensor of the thin film  $\varepsilon_2$  will be referred to as  $\varepsilon_{ij}$ . Instead of  $r_{123}$  we write  $r_i$  for the reflectance of light polarized in the (principle) direction  $i$ :

$$\frac{r_i}{r_{13}} = 1 + \frac{4\pi i d}{\lambda} \left( \frac{\varepsilon_{ii} - \varepsilon_b}{1 - \varepsilon_b} \right) \quad (5.19)$$

The reflectance difference is then given by:

$$\begin{aligned} 2 \frac{r_x - r_y}{r_x + r_y} &= 2 \left[ \frac{r_x}{r_{13}} - \frac{r_y}{r_{13}} \right] / \left[ \frac{r_x}{r_{13}} + \frac{r_y}{r_{13}} \right] = \\ &= \left[ \frac{4\pi i d}{\lambda} \left( \frac{\varepsilon_{xx} - \varepsilon_{yy}}{1 - \varepsilon_b} \right) \right] / \left[ 1 + \frac{2\pi i d}{\lambda} \left( \frac{\varepsilon_{xx} + \varepsilon_{yy} - 2\varepsilon_b}{1 - \varepsilon_b} \right) \right] \end{aligned} \quad (5.20)$$

Applying again  $d/\lambda \ll 1$ , one finds:

$$\frac{\Delta r}{\bar{r}} = -\frac{4\pi i d}{\lambda} \frac{\varepsilon_{xx} - \varepsilon_{yy}}{\varepsilon_b - 1} \quad (5.21)$$

proving Eq. (5.1).

Sometimes, the RD signal is not described via the reflectance  $r$ , but by considering the reflectivity  $R$  (see e.g., [64]), which describes the ratio between the squared amplitudes of the incident and reflected waves. Applying the relation  $R = |r|^2$  and neglect terms of higher order in  $d/\lambda$  the relative difference of reflectivities becomes:

$$\frac{\Delta R}{\bar{R}} = -\frac{8\pi d}{\lambda} \text{Im} \left[ \frac{\varepsilon_{xx} - \varepsilon_{yy}}{\varepsilon_b - 1} \right] \quad (5.22)$$

and consequently  $\Delta R/\bar{R} = -2 \text{Re}[\Delta r/\bar{r}]$ .

---

<sup>4</sup>see also [62]. Different sign due to different space phase convention



By writing real and imaginary parts explicitly,  $\varepsilon_b = \varepsilon_b^{(1)} + i \varepsilon_b^{(2)}$  and  $\Delta\varepsilon = \Delta\varepsilon^{(1)} + i \Delta\varepsilon^{(2)}$ , the imaginary and real part of the RD signal are given by:

$$\operatorname{Re} \left[ \frac{\Delta r}{\bar{r}} \right] = \frac{4\pi d}{\lambda} \left( \frac{\Delta\varepsilon^{(2)} (\varepsilon_b^{(1)} - 1) - \Delta\varepsilon^{(1)} \varepsilon_b^{(2)}}{(\varepsilon_b^{(1)} - 1)^2 + (\varepsilon_b^{(2)})^2} \right) \quad (5.23)$$

$$\operatorname{Im} \left[ \frac{\Delta r}{\bar{r}} \right] = -\frac{4\pi d}{\lambda} \left( \frac{\Delta\varepsilon^{(2)} \varepsilon_b^{(2)} + \Delta\varepsilon^{(1)} (\varepsilon_b^{(1)} - 1)}{(\varepsilon_b^{(1)} - 1)^2 + (\varepsilon_b^{(2)})^2} \right). \quad (5.24)$$

Thanks to the three-phase model, first-principles calculations of the reflectance anisotropy are possible, if one has access to the frequency dependent surface and bulk dielectric function. The surface dielectric anisotropy  $\Delta\varepsilon$  of the thin film, the surface region, is thereby calculated by modeling the surface as a slab consisting of several atomic layers. Following the derivation carefully, it becomes clear that the only relevant quantity is  $d \Delta\varepsilon = d (\varepsilon_{xx} - \varepsilon_{yy})$ , which is a surface intrinsic property. As long as the depth, where the dielectric function is modified is small compared to the wavelength, the derivation is accurate. Also note, that  $\varepsilon$  is proportional to the polarizability per volume element [see Eq. (2.75)]. Thus  $d \Delta\varepsilon$  describes the difference of the polarizability per *surface area* and is a well defined microscopic surface quantity. In the independent particle approximation (see below) one simply needs to normalize the polarizability  $\chi^{KS}$  to the surface area [ $1/A$  instead of  $1/V$ ] to determine  $d \Delta\varepsilon$ .

## 5.2 Calculation of the dielectric function

By considering the three-phase model, we have obtained an expression for the reflectance difference spectrum which depends on the dielectric function of the bulk and the (anisotropic) optical response of the surface. Because we are interested in the interaction of light and matter at optical wavelengths, the long-wavelength limit ( $\mathbf{q} \rightarrow 0$ ) is assumed in the following.

In an ab-initio calculation of the dielectric function several steps of increasing accuracy, but also complexity, can be considered. A detailed overview about different ways to calculate the dielectric function and the relation between these methods can be found in [65]:

1. The dielectric function is calculated within the independent particle (IP) approximation on top of KS-DFT eigenenergies and wavefunctions. The dielectric tensor is then given by Eq. (2.75).
2. Instead of the KS-DFT eigenenergies, quasiparticle energies calculated within Green's function theory are used for the evaluation of the dielectric function. Normally, the  $G_0W_0$  approximation is applied, and the quasiparticle energies are calculated as perturbation to the KS-DFT energies. The dielectric function is again derived within the IP approximation, but the KS-DFT eigenenergies are now replaced by quasiparticle energies.
3. Local field effects are included.
4. The inclusion of electron-hole interactions is realized by solving the Bethe-Salpeter equation. In the framework of Green's function theory this can be described as the inclusion of vertex corrections in the description of the dielectric function.

Because calculations of surface optical properties are involved, most RD spectra of semiconductors and insulators (e.g., [66, 67, 68, 69, 70, 71]) and all theoretical RD spectra of metals [59, 60, 61, 72, 73, 74, 75] have been obtained applying the first and simplest approximation, so far. For exemplary semiconductor surfaces, as e.g., InP(001)-(2 × 4) and GaAs(110), also calculations employing the more involved independent quasiparticle approach exist [76, 67] (step 2) resulting in an improved, but not perfect alignment with experiment. Local field effects (step 3) and electron-hole interactions (step 4) have e.g., been included for the model Si(110):H surface [77, 78, 79]. While the inclusion of local field effects has only a minor influence on the Si(110):H RD spectrum, the inclusion of electron-hole interactions via the solution of the Bethe-Salpeter equation improves the correspondence with the experimental spectrum. The Si(111)-(2 × 1) [80] and Ge(111)-(2 × 1) [81] surfaces are two further examples where electron-hole interactions have been considered in the evaluation of the RD spectrum.

For the calculation of the bare and adsorbate covered Cu(110) RD spectra presented in the following sections, we used the independent particle approximation applied on top of KS-DFT wavefunctions and eigenenergies (step 1). As a dense  $k$ -point grid and a large number of slab layers are required to obtain convergence of the RD signal, even at this level of simplification, RD calculations for metallic surfaces are involved.

Nevertheless, two of the approximations applied for the calculation of the dielectric function, namely the neglect of local field effects (step 3) and the electron-hole interaction (step 4), are most likely more reliable for metals than for semiconductors. As calculations by Marini and co-workers [82] have shown, local field effects are negligible for the macroscopic dielectric function of bulk Cu. The reason for this can be found in the relatively homogeneous screening in metals. The electron-hole interaction, on the other side, can be seen as an electrostatic interaction between a negative (electron) and positive (hole) charged particle screened by the dielectric function of the material. For metals the screening is large, so that excitonic effects should not be as important as for semiconductors and insulators.

Consequently, the approximation of the excitation energies by one-electron eigenenergies obtained from KS-DFT remains the most important one. Not considering electron-hole interactions, the use of KS-DFT eigenenergies will in particular result in a (not necessarily uniform) shift of theoretical and experimental RD features whenever the calculated band structure does not match the measured photo emission (PE)/ inverse photo emission (IPE) spectrum.

Within the applied approximations, the imaginary part of the dielectric function  $\varepsilon^{(2)}$  is calculated via Eq. (2.73). The real part  $\varepsilon^{(1)}$  is evaluated by a Kramers-Kronig transformation [Eq. (2.76)]. The wavefunctions and eigenenergies stem from KS-DFT calculations using the GGA-PBE approximation for the exchange-correlation potential. The theoretical lattice constant (3.638 Å) was used for the bulk calculations. For the surfaces, symmetric slabs with up to 25 layers have been considered and the topmost 6 substrate layers and adsorbate positions have been relaxed prior to the optical calculations. More details on the geometrical properties of the bare Cu(110), the oxygen induced Cu(110)-(2 × 1)O added-row reconstruction, and the carbon monoxide covered Cu(110)-(2 × 1)CO and Cu(110)-(3 × 1)CO surfaces will be given in Sec. 7.1. The intraband contributions to the dielectric functions are included by calculating the intraband plasma tensor [Eq. (2.113)]. We found that an ab-initio treatment of the anisotropic surface plasma frequency is essential in order to reduce the strong thickness dependence due to band crossings near the Fermi-surface (see Sec. 2.9). The RD spectrum

was finally evaluated by applying Eq. (5.1).

For the interpretation of the resulting RD spectra in Sec. 7.3, we analyzed RD contributions arising from specific  $k$ -point and energy regions. Important contributions to the theoretical spectra could consequently be traced back to transitions between specific electronic states. The agreement between experimental and theoretical RD spectra is not always perfect, but the characteristic line-shapes could be qualitatively reproduced for all surfaces.

## Chapter 6

# Optical properties of bulk systems

### 6.1 Plasma frequencies

For metals, the long-wavelength dielectric function at small frequencies is dominated by intraband transitions. In the independent particle approximation the real part of the dielectric function exhibits a  $-\bar{\omega}^2/\omega^2$  decay [Eq. (2.107)], where  $\bar{\omega}$  is the intraband plasma frequency [Eq. (2.113)]. This term is often referred to as Drude like term. In general, the plasma frequency is a tensor, but for the cubic metals considered in this chapter, it reduces to a scalar quantity. For the anisotropic surfaces treated in chapter 7, this is not the case anymore.

The intraband plasma frequency is calculated from a surface integral [see Eq. (2.113)]. In order to generate a sufficient number of  $k$ -points in the vicinity of the Fermi surface, a very dense  $k$ -point mesh is required, so that the intraband plasma frequency converges significantly slower with the number of  $k$ -points than quantities which are evaluated from an integral over the Brillouin zone volume (like energy and density). Faster convergence with the number of  $k$ -points can be reached, if the smearing width  $\sigma$  for the determination of the one electron occupancies

$$f(\epsilon_n) = \frac{1}{1 + e^{\frac{\epsilon_n - \mu}{\sigma}}} \quad (6.1)$$

is chosen larger (in practice often Gaussian broadening or, as in the present case, a Methfessel-Paxton broadening is chosen). In Tab 6.1, we report the copper plasma frequency (at the experimental volume) for different sets of  $k$ -points and smearing widths. The  $k$ -point grid has been generated using the Monkhorst-Pack scheme and for the broadening a Methfessel-Paxton method of first order with a smearing width  $\sigma$  has been applied.

For a relatively modest  $16 \times 16 \times 16$   $k$ -point grid, a standard smearing width of 0.2 eV leads to an error of 0.5 eV in the intraband plasma frequency, whereas a  $32 \times 32 \times 32$  grid gives effectively converged plasma frequencies for all considered widths. For larger cells, where such dense  $k$ -point grids may not be practicable anymore, a large value of  $\sigma \approx 0.4$  eV seems to be a good compromise.

The same trend as is observed for copper has also been found for the other metals considered in this chapter. The plasma frequencies  $\bar{\omega}$  obtained for a 32  $k$ -point grid and  $\sigma = 0.2$  eV are summarized in Tab. 6.2. Additionally the number of electrons in partially filled bands is given. If the band structure of a metal does not deviate too much from the free-electron

Table 6.1: Convergence test for the plasma frequency (in eV) of copper. The dependence on the smearing width  $\sigma$  (in eV) and the number of  $k$ -points is shown.

$\sigma/k$ -points	16	24	32
0.1	7.7	9.7	9.0
0.2	8.6	9.2	9.1
0.3	8.9	9.0	9.1
0.4	9.0	9.1	9.1

gas, the plasma frequency  $\bar{\omega}$  should be close to the Drude plasma frequency  $\bar{\omega}_{\text{Drude}}$  [see Eq. (2.114)] obtained for the corresponding electron density. For the transition metals, the number of electrons in partially filled bands is not straightforwardly determined, so that the comparison with a Drude plasma frequency is not meaningful. Consequently, also the ratio between the relative mass  $m^*$  and the electron mass  $m$  can not be calculated. Furthermore, comparison between the theoretical (intraband) plasma frequency and the experimental one is not straightforward for transition metals, because interband transitions at small frequencies cause also a decay  $\propto -1/\omega^2$  [see Eq. (2.136)] and it is not possible to disentangle the effect of interband and intraband transitions in the measured dielectric functions. In the case of Ca and Al, where interband transitions at small frequencies are also present, the authors of Ref. [83] and Ref. [84] aimed explicitly on subtracting the effect of the interband transitions.

In most experimental articles cited in Tab. 6.2, either the plasma frequency or the mass ratio are given. The missing quantity was added using the experimental volume in Tab. 6.2 for the calculation of the corresponding Drude frequency or the effective mass, respectively. The complemented value is set in parenthesis. Overall, the agreement between theoretical and experimental plasma frequencies is quite good. Only for Ca, the difference between the theoretical plasma frequency of 4.3 eV and the experimental one (5.7 eV) is significant. Apart from possible inadequacies of the one-electron picture, this might simply be due to a contaminated probe in the experiment. The theoretical intraband plasma frequencies of Cu [82] and Ag [42] have also been calculated by Marini and co-workers. They find a plasma frequency of 9.27 eV and 9.48 eV for Cu and Ag, respectively. Our values are slightly smaller which might be a consequence of the fact that Marini *et al.* used an LDA exchange-correlation functional, whereas we apply the PBE throughout the present chapter. But possibly, the discrepancy is also related to their pseudopotential description.

## 6.2 Dielectric function of bulk copper

In this section, I will present the frequency dependent dielectric function of copper. We make use of the IP approximation so that the imaginary part of the macroscopic dielectric function is described by Eq. (2.75). The real part of the dielectric function [Eq. (2.78)] is obtained by a Hilbert transformation.

Additionally, I will address some technical issues concerning the convergence of the frequency dependent dielectric function with respect to the number of bands, the  $k$ -point grid and the parameters chosen in the Hilbert transformation. The results will give guidance

Table 6.2: Theoretical intraband plasma frequencies  $\bar{\omega}$  for some representative metals calculated at the experimental volume. Besides the Drude plasma frequency  $\bar{\omega}_{\text{Drude}} = (4\pi e^2 n/m)^{(1/2)}$  (eV), which is directly calculated from the number of valence electrons and the experimental volume, the calculated plasma frequency  $\bar{\omega} = (4\pi e^2 n/m^*)^{(1/2)}$  (eV) and the ratio  $M_{\text{eff}} = m^*/m$  are presented. In the last two columns experimental values are shown. Values in brackets correspond to derived numbers. For the transition metals, the definition of the number of valence electrons is questionable and no disentanglement between intraband and interband transitions is possible, so that only the calculated intraband plasma frequencies are shown.

<sup>a</sup> [85]; <sup>b</sup> [86]; <sup>c</sup> [87]; <sup>d</sup> [88]; <sup>e</sup> [84]; <sup>f</sup> [83]

	exp. V [ $\text{\AA}^3$ ]	valence	$\bar{\omega}_{\text{Drude}}$	$\bar{\omega}$	$M_{\text{eff}}$	$\bar{\omega}$ -exp	$M_{\text{eff}}$ -exp
Li	21.02	1	8.1	6.5	1.6	(6.4) <sup>a</sup>	1.6 <sup>a</sup>
Na	37.71	1	6.0	5.9	1.1	(5.7) <sup>a</sup>	1.1 <sup>a</sup>
Cu	11.69	1	10.9	9.1	1.4	(8.9) <sup>b</sup> , 8.8 <sup>c</sup> , 8.9 <sup>d</sup>	1.5 <sup>b</sup> (1.6) <sup>c</sup> , (1.5) <sup>d</sup>
Ag	16.84	1	9.0	9.2	1.0	(9.2) <sup>b</sup> , 8.9 <sup>d</sup>	1.0 <sup>b</sup> , (1.0) <sup>d</sup>
Au	16.96	1	9.0	9.0	1.0	(9.1) <sup>b</sup> , 8.7 <sup>d</sup>	1.0 <sup>b</sup> , (1.1) <sup>d</sup>
Ca	43.44	2	8.0	4.3	3.4	(5.7) <sup>e</sup>	2.0 <sup>e</sup>
Al	16.39	3	15.9	12.6	1.6	12.3 <sup>c</sup> , 12.5 <sup>f</sup>	(1.7) <sup>c</sup> , (1.6) <sup>f</sup>
Rh	13.70			10.1			
Pd	14.61			7.4			
Pt	15.09			8.8			

to the settings that guarantee (technically) converged reflectance difference spectra for the surface dielectric function. Specific tests for the surface dielectric function with respect to the number of layers and the thickness of the vacuum will be presented in a later chapter.

Finally, we compare our dielectric function to experimental spectra and to an older theoretical work by Marini and co-workers [82]. The origin of the deviations between experiment and our calculations is traced back to the difference of experimental photo-emission measurements and DFT band structure calculations, or slightly different band structures compared to Ref. [82]. The following calculations have been performed at the theoretical PBE lattice constant of 3.638  $\text{\AA}$  (exp. 3.605  $\text{\AA}$ ). Therefore the plasma frequency differs slightly from the one presented in the previous section and becomes 8.92 eV instead of 9.1 eV.

### 6.2.1 Bands

If one does not explicitly define the number of bands, this quantity is set to half of the number of electrons plus some additional bands in a conventional (VASP) DFT calculation. For the primitive copper cell with 11 electrons e.g., 9 bands would be chosen. For the imaginary part of the dielectric function this is sufficient, because bands up to 8.9 eV are included, so that frequencies of interest (max. 8 eV) are accounted for. The real part of the dielectric function, however, requires the integration of the imaginary dielectric function over the whole frequency space via the Hilbert transformation. A smaller number of bands implies that the imaginary dielectric function becomes zero at smaller frequencies introducing errors in the frequency dependent real dielectric function and reducing the static dielectric

function. The required number of bands for a well converged real dielectric function up to a frequency of 8 eV was determined by choosing 12, 16, 20, 24, and 32 bands and comparing the corresponding real dielectric functions. All curves looked very similar, and even for 12 bands the value of the interband contribution to the static dielectric function differs only by 0.1 compared to the value obtained for 32 bands. For 16 bands, the error decreases to 0.05, which is accurate enough for the present purpose. Based on this fact, we chose the number of bands to be 1.5 times the number of electrons in all following bulk and surface optical calculations.

### 6.2.2 $k$ -point convergence

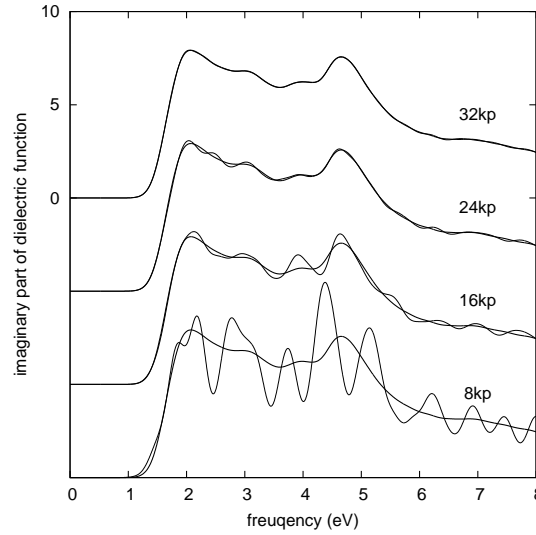


Figure 6.1: Comparison of the imaginary dielectric function obtained for different  $k$ -point grids (thin lines) with the result for  $(40 \times 40 \times 40)$   $k$ -points (bold line).

The dependence of the dielectric function on the number of  $k$ -points is an important issue, if well converged spectra should be obtained. Because the transition strengths might depend critical on the position in  $k$ -space, the dielectric function converges slower than e.g., the charge density, and a coarse  $k$ -point sampling introduces additional features in the dielectric function. The choice of the smearing method and the applied smearing width is also closely linked to the  $k$ -point convergence. We used a Gaussian smearing for the optical calculations throughout this work. In the pre-run in which we determined the charge density, a Methfessel-Paxton smearing as normally used for metals was applied. In principle, this method could also be used for the optical calculations, but it can result in (small) negative values of the imaginary dielectric function which we tried to avoid. Concerning the chosen smearing width, it is generally observed that larger widths lead to faster  $k$ -point convergence, but at the same time all features are broadened. We found that  $\sigma = 0.2$  eV is a reasonable compromise. In Fig. 6.1 the imaginary dielectric function for different  $k$ -point grids are compared to the "converged" spectrum obtained for  $40 \times 40 \times 40$   $k$ -points (corresponds to 5740  $k$ -points in the IBZ). For the  $8 \times 8 \times 8$   $k$ -point grid the artificial features due to the coarse  $k$ -point sampling

are significant. Only for  $24 \times 24 \times 24$   $k$ -points ( $= 1300$   $k$ -points IBZ), the dielectric function becomes smooth and approaches the converged result. The dielectric function calculated by Marini and coworkers [82], which we will compare to in Fig. 6.4 (left), was obtained utilizing 3000  $k$ -points in the IBZ and a smearing width of 0.2 eV.

### 6.2.3 Hilbert transformation

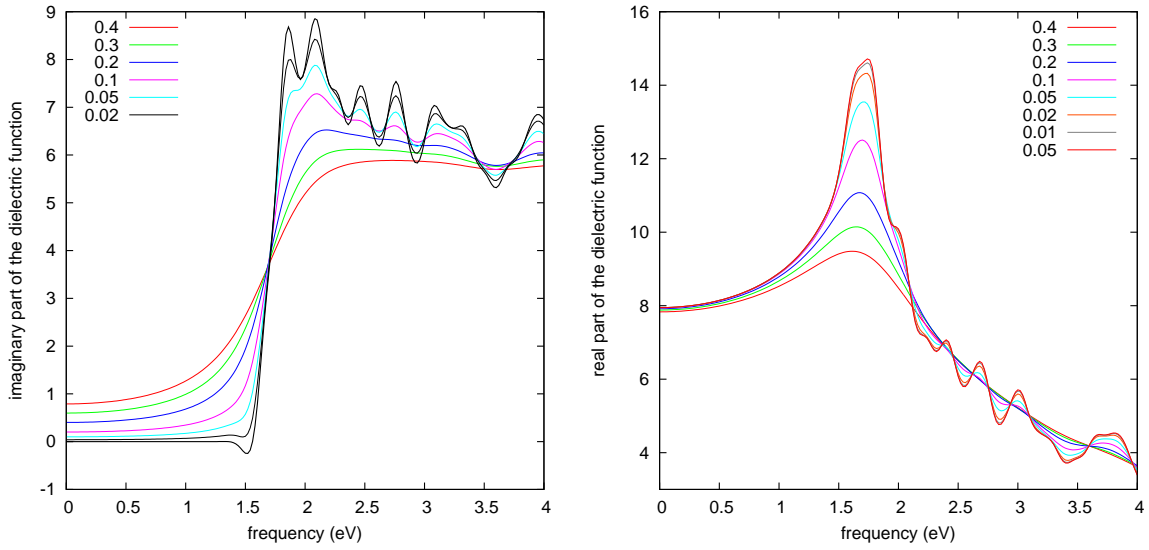


Figure 6.2: Imaginary (left) and real part of the interband dielectric function for different smearing parameters  $\eta$  used in the Hilbert transformation. The initial imaginary dielectric function is plotted using a bold line.

The real part of the dielectric function is obtained via a Hilbert transformation. Originally also the imaginary dielectric function was recalculated in VASP by applying

$$\varepsilon_{\alpha\beta}(\omega) = 1 + \frac{2}{\pi} \int_0^\infty \frac{\varepsilon_{\alpha\beta}^{(2)}(\omega') (\omega' - i\eta)}{(\omega' - i\eta)^2 - \omega^2} d\omega'. \quad (6.2)$$

for a small value of  $\eta$ . The integration is performed applying a simple rectangle formula with supporting points defined by the maximal frequency (OMEGAMAX) and the number of frequency points (NEDOS). The quantity  $\eta$  (CSHIFT) causes a smoothening of the spectra and is set to 0.1 eV by default. In Fig. 6.2 the imaginary (left) and real (right) part of the dielectric function obtained by Eq. (6.2) using different values of  $\eta$  are shown.

For the final calculation of the real dielectric function we use a small  $\eta$  (CSHIFT = 0.02 eV). The maximal frequency is throughout this work chosen to be 100 eV, and the number of frequency points set to the (very) large number of 20 000 frequencies. The imaginary part of the dielectric function is not recalculated applying Eq. (6.2).



### 6.2.4 Final form of bulk dielectric function and comparison

In Fig. 6.3, the imaginary and real dielectric function are compared to two experimental spectra. The calculation was performed using a  $40 \times 40 \times 40$   $k$ -point grid and a smearing width of 0.2 eV. For the theoretical intraband dielectric function, the relaxation time was set to  $\tau = \infty$  [corresponding to Eq. (2.107) and Eq. (2.124)]. For the real part, this should give an intraband contribution that does not differ too much from the experimental one, if the plasma frequencies are the same. As the imaginary part of the intraband dielectric function is zero for  $\omega \neq 0$ , theory does not capture the characteristic rise towards small frequencies as present for the experimental absorption spectrum (a lifetime broadening effect).

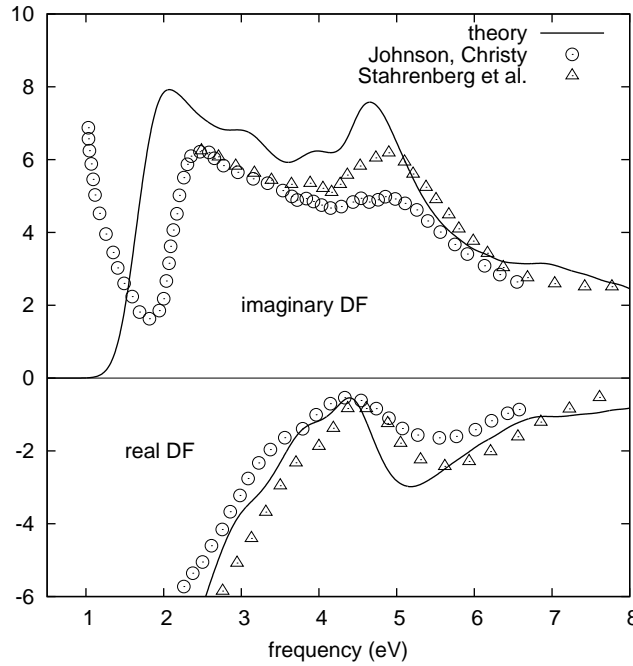


Figure 6.3: Real and imaginary part of the copper dielectric function. The theoretical spectrum is compared to the experimental data by Johnson and Christy [86] and Stahrenberg *et al.* [89]. The intraband part of the real dielectric function is accounted for by adding [Eq. (2.107)] with the theoretical plasma frequency of  $\bar{\omega} = 8.92$  eV.

Agreement between the theoretical and the experimental dielectric function is good, if one considers the overall shape of the dielectric function. The experimental spectra themselves differ concerning the height of the feature at about 5 eV. Stahrenberg *et al.* [89] attribute this to an oxygen contamination of the sample used by Johnson and Christy [86], which would strengthen the agreement of experiment and theory further. Absolute energy positions of specific features, however, are not exactly reproduced by theory. We find that the absorption sets in at an energy of about 1.5 eV which is about 0.5 eV lower than in experiment. Also the peak at 4.5 eV is about 0.3 eV red-shifted. This implies that the theoretical spectrum is overall slightly red-shifted compared to experiment, as usually observed for DFT.

For analyzing single features in the theoretical (IPA) dielectric function, the one-electron band structure of the respective material is of relevance. To the absorption spectrum, only

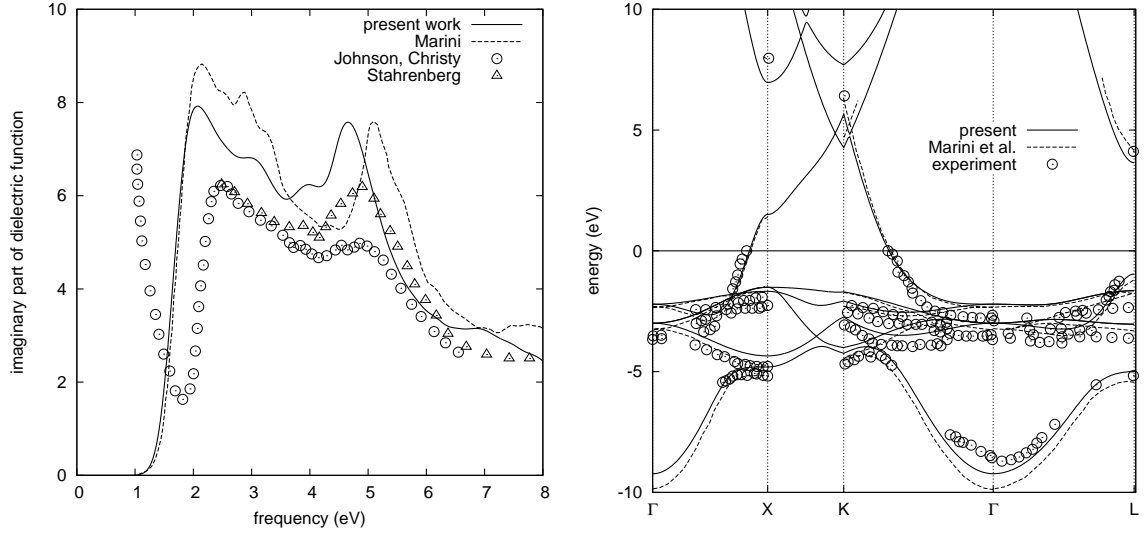


Figure 6.4: Left: Absorption spectrum for bulk copper. Our spectrum is compared to the theoretical dielectric function by Marini *et al.* [82] and the experimental spectra by Johnson and Christy [86] and Stahrenberg *et al.* [89]. Right: Band structure of bulk copper. The energies obtained in the present work are compared to other theoretical results by Marini *et al.* [82] and to photo emission data [90].

transitions between bands with an energy difference corresponding to the considered frequency contribute, and this enables to trace an absorption peak back to its original electronic transition. The transitions underlying the "true" (experimental) spectrum correspond to excitations between quasiparticle states if excitonic effects are neglected. If the quasiparticle energies (or experimental (inverse) photo emission data) and the one-electron band structure are equal, the theoretical and experimental dielectric function should be the same. On the other hand, deviations between the theoretical band structure and photoemission data can explain differences of the theoretical spectrum and the measured one. The same holds for spectra stemming from different theoretical band structures. In Fig. 6.4 (right) the theoretical band structures of Marini *et al.* [82] and experimental photoemission data [90] are shown together with our results. The comparison of the band structure calculated by Marini *et al.* and our one-electron energies shows that Marini's spectrum is slightly expanded away from the Fermi energy. As they apply the LDA exchange-correlation potential, it might be possible that they use the LDA volume, which is smaller than the experimental one and therefore leads to an increase of the bandwidth. Both theoretical spectra, nevertheless, give too large *d*-band widths and the onset for *d*-bands is shifted upwards from  $-2$  eV in experiment to  $-1.5$  eV in the theoretical band structures.

Before considering the effect of these deviations on the absorption spectrum, we interpret our spectrum with respect to the underlying transitions. Therefore we have decomposed the imaginary part of the dielectric functions (here:  $24 \times 24 \times 24$  *k*-point calculation) into contributions arising from specific energy ranges (see Fig. 6.5). The initial part of the absorption spectrum arises from transitions between (flat) *d*-bands at energies between  $-1.5$  eV and  $-4.0$  eV and the Fermi surface. The form of this initial part is very similar to the *d*-band density of states when changing the energy sign. A large joined density of states is obtained

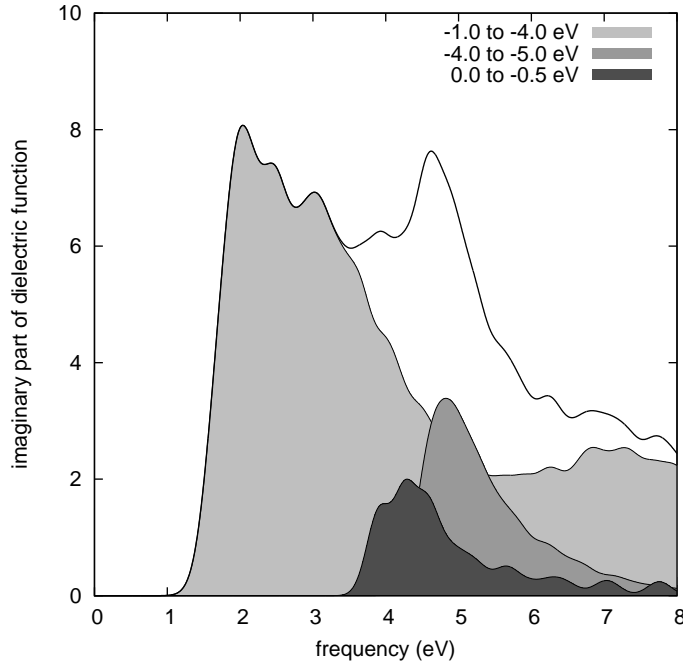


Figure 6.5: Contributions to the absorption spectrum arising from different energy regions below the Fermi energy.

for a low lying  $d$ -band (between  $-4.0$  eV and  $-5.0$  eV) and the  $s/p$ -like band crossing the Fermi surface resulting in the second larger feature at about 5 eV. An additional contribution at slightly smaller energies arises from excitations from bands at the Fermi-energy to an unoccupied  $s$  band. A more detailed assignment of absorption features and band structure can e.g., be found in Ref. [89].

In Fig. 6.4 (left side), our absorption spectrum is compared to the one obtained by Marini and co-workers [82] and again to experimental data. The early onset of both theoretical spectra can now be explained by the too high energies of the top-most  $d$ -bands. The reason for the different energy position of the second maximum in the theoretical spectra is twofold. On the one hand, Marini's unoccupied bands are shifted to higher energies, so that also the transitions from the Fermi sphere to these bands are blue-shifted. On the other side, low lying  $d$ -bands have smaller energies than in our band structure, thus again resulting in a larger frequency. Additionally to the various energy shifts, both Marini's and our spectrum overestimate the dielectric function. For the RD spectra this error cancels out, because there we consider only the relative difference in the reflectance. Finally, we should emphasize that we have neglected local field effects in this section and we will use this approximation also for the surface calculations. Test calculations have shown that, at least for the Cu bulk, this simplification is justified. The same calculations have also been considered by Marini *et al.* and the respective spectra can be found in Ref. [82].

## Chapter 7

# Optical calculations for Cu(110) surfaces

In this chapter, we will present reflectance difference spectra for the bare, the oxygen, and the carbon monoxide covered Cu(110) surface. The Cu(110) surface has been one of the first metallic surfaces studied with RD spectroscopy [52] and has evoked numerous experimental studies since [53, 54, 55, 56, 57, 58]. Additionally the electronic structure of the bare and oxygen covered Cu(110) surface is well studied by (inverse) photoemission spectroscopy [92, 93, 94, 95], thus allowing an easy check of the validity of the theoretical one-electron band structure. This makes the bare Cu(110) and its adsorbate covered surfaces a good test case for surface optical calculations. RD spectra have already been evaluated for the bare [59, 60] and carbon-monoxide covered [61] Cu(110) surface by Monachesi and coworkers. Their linear muffin tin orbital (LMTO) calculations were based on the independent particle approximation for the (surface) dielectric function, as is the case in the present work. The RD spectra of Monachesi *et al.* shared some features with the experimental spectra, but due to their small number of slab layers (11 layers) the overall agreement with experiment was modest.

In the following section, we first give a brief overview of the geometry of the bare Cu(110), the Cu(110)-(2×1)O, the Cu(110)-(2×1)CO, and the Cu(110)-(3×1)CO surface. Afterwards, convergence tests for the surface optical response with respect to the number of  $k$ -points, the vacuum layer thickness, and the number of slab layers will be presented. Finally, the RD spectra of the considered surface structure are shown in Sec. 7.3 and interpreted with respect to the theoretical band structure presented in Sec. 7.3.1.

### 7.1 Geometry of surfaces

In this section, a brief overview of the considered surface structures will be given. Fig. 7.1 shows the bare Cu(110) surface in top view. Here and in the following sections the  $[1\bar{1}0]$ ,  $[001]$ , and  $[110]$  direction will be referred to as  $x$ -,  $y$ -, and  $z$ -direction, respectively. The anisotropy of the bare (110) surface arises from the different distance of surface atoms in  $x$ - and  $y$ - direction (2.572 Å along the  $x$ -direction, 3.638 Å along the  $y$ -direction). For the bare Cu(110) surface the distance of the two topmost layers  $d_{12}$  is 1.16 Å, which is −10 % smaller than the bulk layer distance of 1.286 Å. For the second and third layer, the layer distance  $d_{23}$  is increased by 4.5 %.

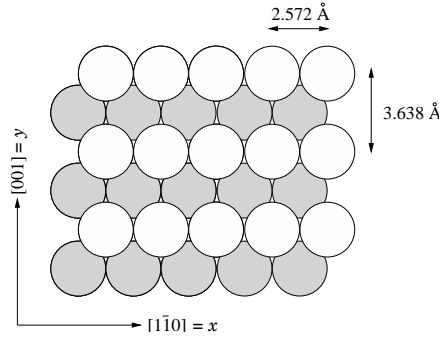


Figure 7.1: Top view onto the bare Cu(110) surface. In the following the  $[1\bar{1}0]$  and  $[001]$  direction will be referred to as  $x$ - and  $y$ - direction respectively.

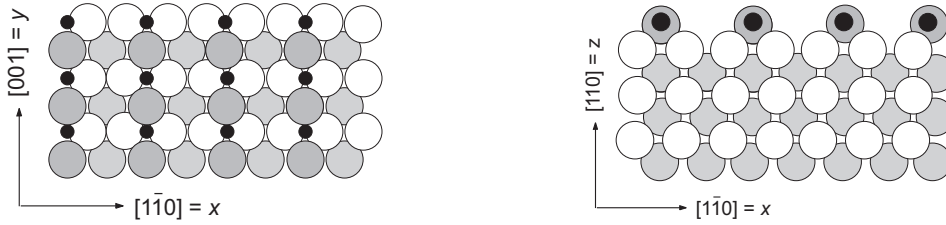


Figure 7.2: Cu(110)- $(2 \times 1)$ O added-row reconstruction in top (left) and side (right) view. Oxygen atoms are drawn as black circles, Cu atoms forming the linear chains with the oxygen atoms are shown in grey, Cu atoms in the first and second Cu(110) layer are white and light grey, respectively.

In Fig. 7.2 the Cu(110)- $(2 \times 1)$ O added-row reconstruction is shown in top (left) and side (right) view. This structure is formed of Cu-O-Cu rows along the  $y$ -direction, with oxygen atoms situated in short bridge sites and additional Cu atoms in hollow sites. The oxygen atom is situated slightly higher than the added-row Cu atom. The distance between the added-row Cu atom and the top most Cu(110) layer amounts to 1.42 Å. Due to the presence of the Cu-O-Cu rows the distances between the first and second Cu(110) layer comes closer to the bulk distance  $d_{12} = 1.24$  Å for the Cu atom directly below the Cu-O-Cu rows and 1.27 Å for the other Cu atom. More details about the geometry of the Cu(110)- $(2 \times 1)$ O added-row reconstruction and a comparison with experimental values can be found in [96] and [97].

The Cu(110)- $(2 \times 1)$ CO and Cu(110)- $(3 \times 1)$ CO surface are shown in Fig. 7.3 and Fig. 7.4, respectively. Experimentally, CO is found to adsorb on the top site with a C-Cu distance of 1.87 Å and a C-O bond length of 1.11 Å for the Cu(110)- $(2 \times 1)$ CO geometry (see e.g., [98]). Because the theoretical geometry of the  $(2 \times 1)$ CO and  $(3 \times 1)$ CO structure is very similar, we will concentrate on the Cu(110)- $(2 \times 1)$ CO atomic positions. We find that the CO molecule is situated 1.84 Å above the Cu(110) surface with a C-O bond length of 1.16 Å. The distance between the Cu atom directly below the CO molecule and the next Cu layer is with 1.29 Å exactly the same as the bulk like distance of 1.286 Å (increased compared to the bare surface). For the copper atom between the CO adsorbates the layer distance is 1.15

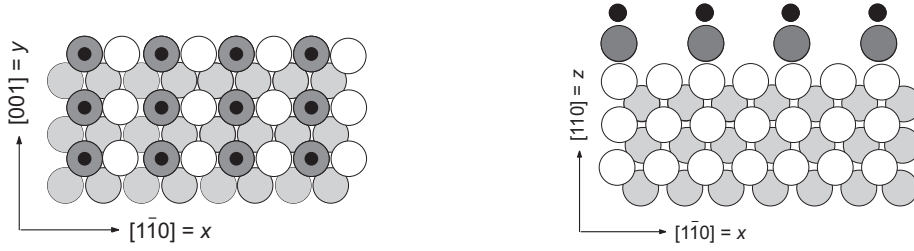


Figure 7.3: Cu(110)-(2 × 1)CO surface in top (left) and side (right) view. Cu atoms in the first and second Cu(110) layer are shown using white and light grey balls, oxygen atoms are shown using black and carbon atoms using dark grey balls.

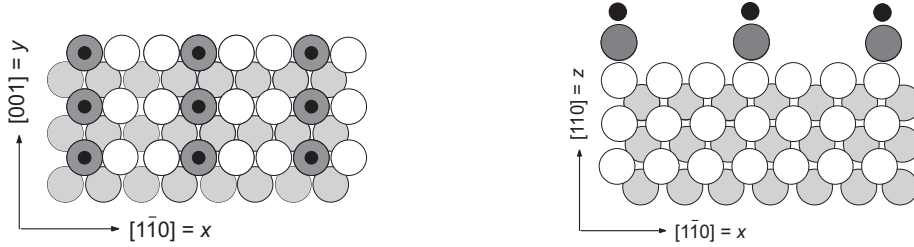


Figure 7.4: Cu(110)-(3 × 1)CO surface in top (left) and side (right) view.

Å and therefore very similar to the bare Cu(110) surface (1.16 Å).

## 7.2 Convergence tests

The reflectance difference spectrum is calculated according to Eq. (5.1) as

$$\frac{\Delta r}{\bar{r}} = -\frac{2id\omega}{c} \frac{\varepsilon_{xx} - \varepsilon_{yy}}{\varepsilon_b - 1}.$$

The quantity which is easier accessible in experiment - and simply referred to as RD spectrum in the following - is the real part [Eq. (5.23)]:

$$\text{Re} \left[ \frac{\Delta r}{\bar{r}} \right] = \frac{2\omega d}{c} \left( \frac{\Delta\varepsilon^{(2)}(\varepsilon_b^{(1)} - 1) - \Delta\varepsilon^{(1)}\varepsilon_b^{(2)}}{(\varepsilon_b^{(1)} - 1)^2 + (\varepsilon_b^{(2)})^2} \right). \quad (7.1)$$

with  $\varepsilon_b = \varepsilon_b^{(1)} + i\varepsilon_b^{(2)}$  and  $\Delta\varepsilon = \Delta\varepsilon^{(1)} + i\Delta\varepsilon^{(2)}$ . Because the RD spectrum depends on both, the imaginary and real part of the surface and bulk dielectric function, a direct interpretation of single features is not always straightforward. In many cases it is easier to consider the surface dielectric anisotropy (SDA)  $\Delta\varepsilon = \varepsilon_{xx} - \varepsilon_{yy}$  that underlies the RD spectrum. Its imaginary part directly tells whether light polarized along the  $x$ - or  $y$ - direction is stronger absorbed at a specific frequency  $\omega$ . For small frequencies, where the imaginary part of the bulk dielectric function is small compared to the real part  $\varepsilon_b^{(2)} \ll |(\varepsilon_b^{(1)} - 1)|$  the RD spectrum

can be approximately written as:

$$\text{Re} \left[ \frac{\Delta r}{\bar{r}} \right] \approx \frac{2\pi\omega d}{c} \frac{\Delta\epsilon^{(2)}}{(\epsilon_b^{(1)} - 1)}, \quad (7.2)$$

so that for  $\Delta\epsilon^{(2)} < 0$  (stronger absorption in  $y$ -direction) the RD spectrum becomes positive (stronger reflectance in  $x$ -direction) and vice versa.

Technically, converged RD spectra can only be achieved, if the surface dielectric anisotropy or the surface dielectric function, respectively, is well converged. As for the bulk dielectric function, the  $k$ -point sampling has to be tested. Additionally, since the surface is modeled as repeated slabs separated by vacuum regions, the dependence of the dielectric function on the thickness of the vacuum and on the number of slab layers has to be analyzed.

### 7.2.1 Vacuum

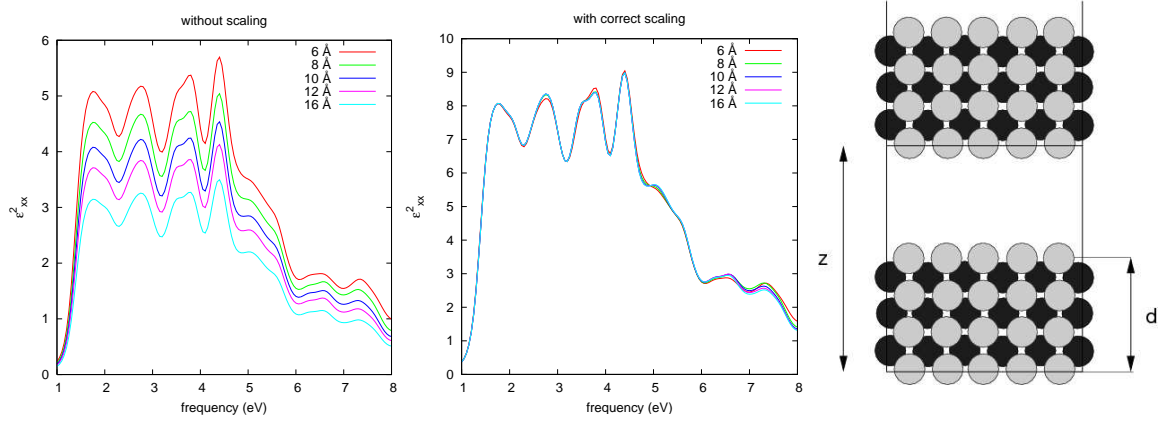


Figure 7.5: In the left and middle panel, the imaginary surface dielectric component  $\epsilon_{xx}^{(2)}$  of a 8 layer bare Cu(110) slab, once without correct scaling (left), once scaled by  $z/d$  (middle) is shown for different thicknesses of the vacuum regions. On the very right, a schematic view of the slab representation is shown.

In the optical routines, the dielectric function is obtained by dividing the sum over transitions by the volume of the supercell [see Eq. (2.75)]. This makes the dielectric function an intrinsic quantity and independent of a cell replication. In the case of a surface optical calculation, however, the dielectric function is averaged over both the slab and the vacuum region (see schematic in the very right panel of Fig. 7.5), thus resulting in a too small value of the dielectric function. On the left hand side of Fig. 7.5, the imaginary dielectric function  $\epsilon_{xx}^2$  for an 8 layer slab is shown for different vacuum thicknesses as normally calculated by the optics routines. In the middle panel of Fig. 7.5, the same spectra scaled by  $z/d$  are plotted. The convergence with the vacuum thickness is already obtained for 8 Å, if the correct rescaling is performed.

For the final calculations, a distance of about 13 Å between the Cu slabs has been chosen to guarantee that the opposite surfaces do not influence each other. In summary, the convergence with the thickness of the vacuum region is fast and well controlled.



### 7.2.2 $k$ -points

As for the bulk (see Fig. 6.1), the calculation of the surface dielectric tensor requires a dense  $k$ -point grid in order to avoid spurious oscillations in the spectra, whereas converged values for geometries and charge densities are already obtained for a much coarser Brillouin zone sampling. Only at  $40 \times 24 \times 1$   $k$ -points for a  $(1 \times 1)$  geometry [ $20 \times 24 \times 1$  for  $(2 \times 1)$  and  $12 \times 24 \times 1$  for  $(3 \times 1)$ ], these oscillations become negligible. Unfortunately, such a dense  $k$ -point grid exceeds the memory limits especially if a large number of slab layers is used in the representation of the surface. Therefore, we divide the Brillouin zone into sub-grids and evaluate the corresponding contributions to the dielectric function at each segment of the sub-grid separately. As the contributions to the dielectric function arising from different  $k$ -points are independent from each other, the sum over all these parts results in the correct dielectric function. This procedure furthermore allows to attribute features in the SDA and consequently in the RD spectrum to transitions from specific  $k$ -point regions.

In summary, the calculation of the RD spectrum of a specific surface proceeds in the following steps. A symmetric slab representation of the surface is set up (using usually 23-25 layers) and the outermost 6 Cu layers and the adsorbates are allowed to relax. This step is performed for a coarser  $k$ -point grid of e.g.,  $20 \times 12 \times 1$   $k$ -points for the  $(1 \times 1)$  cell. For the optical calculation, the charge density of this pre-run is read in, and, in a non-self consistent manner, the wavefunctions, their derivatives, and finally the contributions to the dielectric function are evaluated for one  $k$ -point region. The Fermi energy is thereby fixed to the value obtained in the pre-run. In a final step, the total dielectric function is obtained by averaging over all partial dielectric functions.

### 7.2.3 Interband transitions at small frequencies

In the following, we will emphasize the importance of including the ab-initio surface **in**-**tr**aband dielectric function in the evaluation of the SDA and the RD spectrum. The reason for this is not that experiments suggest an anisotropic surface plasma tensor, but that **in**-**ter**band transitions at small frequencies strongly effect the theoretical dielectric anisotropy.

For metals, there is no lower boundary for interband transition frequencies because of the lack of a bandgap between occupied and unoccupied states. Such small frequency interband excitations normally occur at bands that cross near the Fermi sphere. Although not present for bulk Cu, these interband transitions have been subject of previous publications [99, 100] for Al bulk and occur for all Cu(110) surfaces. As an example, the band structure of the bare Cu(110) surface is plotted in Fig. 7.6 between two high symmetry  $k$ -points for a 23 and a 24 layer slab. The strength of the small frequency interband contributions critically depends on the position of the band crossings relative to the Fermi level, and thus is strongly affected by the number of slab layers (see Fig. 7.6) and the  $k$ -point positions. Furthermore, this dependence is anisotropic with respect to the polarization state of the incident light. In Sec. 2.9, I have shown that interband transitions at small energies lead to a real dielectric function which has the same form as the intraband dielectric function and depends on the (square of the) interband plasma frequency  $\bar{\omega}_{\text{inter}}^2$ . At the same time, second order perturbation theory shows that such small interband transitions lead to a reduction of the (square of the) intraband plasma frequency  $\bar{\omega}_{\text{intra}}^2$  by  $\bar{\omega}_{\text{inter}}^2$  (see Sec. 2.8 and Sec. 2.9). As the strength of the small frequency interband transitions is sensitive to the number of layers, to the chosen  $k$ -point



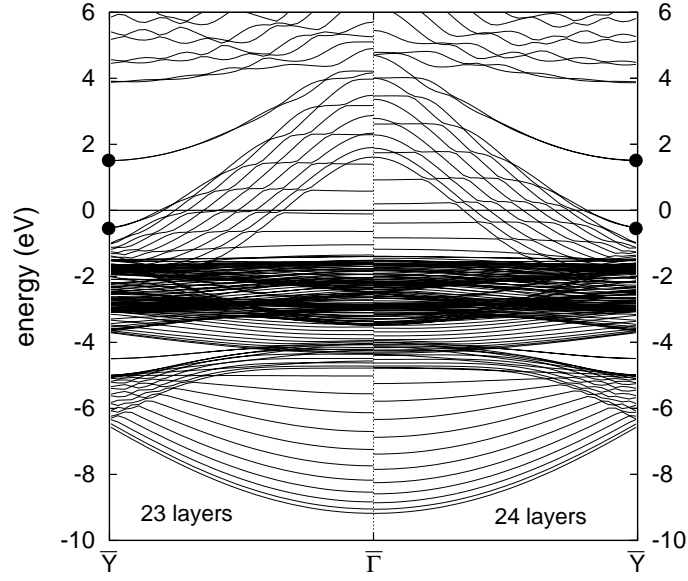


Figure 7.6: The band structure between the  $\bar{\Gamma}$  and  $\bar{Y}$  high symmetry  $k$ -point is shown for the bare Cu(110) surface modeled by a 23 and 24 layer slab. Black circles indicate two surface states.

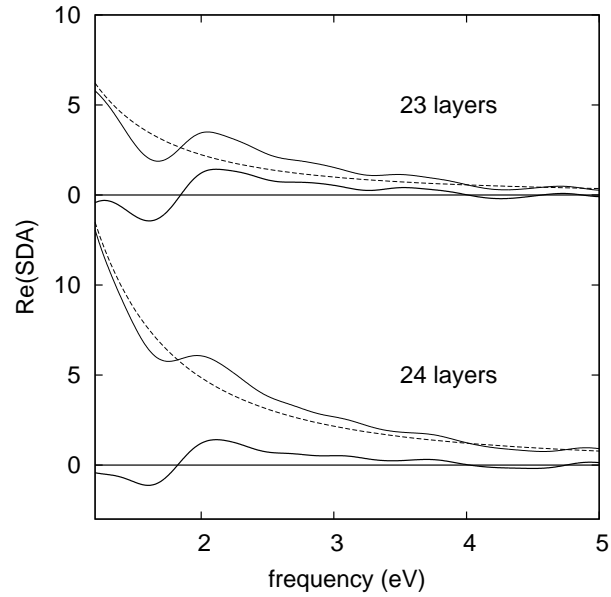


Figure 7.7: Real part of the SDA for a 23 and a 24 layer slab. Thin solid lines indicate the SDA arising only from interband transitions. The real SDA considering both the interband and the intraband dielectric function is shown in bold. The dashed line shows the error introduced by neglecting the intraband contributions.

grid, and furthermore is anisotropic for light polarized along the  $x$ - and the  $y$ -direction, the difference of the real interband SDA  $\Delta\epsilon^{\text{inter}} = \epsilon_{xx}^{\text{inter}} - \epsilon_{yy}^{\text{inter}}$  exhibits a spurious  $-\Delta\bar{\omega}_{\text{inter}}^2/\omega^2$  behavior with  $\Delta\bar{\omega}_{\text{inter}}^2 = \bar{\omega}_{\text{inter}}^{2,xx} - \bar{\omega}_{\text{inter}}^{2,yy}$ . This behavior can be corrected by consistently including both the interband and the intraband dielectric function in the calculation of the SDA, because large contributions by small frequency interband transitions imply a lowering in the corresponding component of the intraband plasma frequency.

As an example, we discuss the bare Cu(110) 23 and 24 layer SDA spectrum in more detail. In Fig. 7.7 the real part of the SDA arising only from interband excitations is plotted using a thin solid line. For both, the 23 and 24 layer calculations, a  $-\Delta\bar{\omega}_{\text{inter}}^2/\omega^2$  decay is superimposed on the spectra. This decay is stronger for 24 layers because here  $\Delta\bar{\omega}_{\text{inter}}^2$  is significantly larger than for 23 layers. Interband transitions at small frequencies lead to a reduction of the intraband plasma frequency. The intraband plasma frequency element  $\bar{\omega}_{\text{intra}}^{xx}$  and  $\bar{\omega}_{\text{intra}}^{yy}$  are 7.2 eV and 6.7 eV for 23 layers, and 7.2 eV and 6.3 eV for 24 layers, respectively. For both, 23 and 24 layers, the plasma frequency component  $\bar{\omega}_{\text{intra}}^{yy}$  is smaller than  $\bar{\omega}_{\text{intra}}^{xx}$ , related to the larger amount of small frequency interband transitions for the  $y$ -direction. Additionally the difference between the intraband plasma frequency components is larger for 24 layers than for 23 layers. The inclusion of the intraband dielectric function in the evaluation of the real SDA spectrum leads to an additional term  $(\bar{\omega}_{\text{intra}}^{2,xx} - \bar{\omega}_{\text{intra}}^{2,yy})/\omega^2$ . The resulting SDA is shown as a thick line in Fig. 7.7, the correction term introduced by the intraband dielectric function is plotted by a dashed line. Including intraband and interband terms consistently improves the agreement between the 23 and the 24 layer SDA spectra.

#### 7.2.4 Number of layers

In the present case, we approximate a surface of macroscopic thickness as a slab consisting of only a few atomic layers. The first and most important requirement on the slab representation is that surface states that contribute to the RD spectrum are reproduced. Taking the surface states of the bare surface at the  $\bar{Y}$ -point as an example, we find that they are present already for a slabs with 12 layers. In Fig. 7.6 these surface states are highlighted with black dots for 23 and 24 layers, and we see that the onset energy and dispersion is the same for both cases.

The second kind of states from or to which optical transitions can occur are bulk like bands. In the surface Brillouin zone they fill up energy-momentum areas that correspond to a projection of the three-dimensional bulk band structure onto the two-dimensional surface Brillouin zone. While these areas are continuously populated for a (semi)infinite surface, only a discretized number of bands are present, if one models the surface by a slab consisting of a few layers. This discretized representation of the bulk-like band structure can be also observed in Fig. 7.6. While the energy areas of the bulk bands are the same for 23 and 24 layers, the bulk bands become denser for 24 layers and change their energy position slightly. Connected to these energy shifts with increasing layers are small oscillations in the dielectric function and consequently in the RD spectrum. Therefore, RD spectra are slightly different even for layer numbers as large as 23 and 24, as can be seen in Fig. 7.8. The strong peak at about 2 eV is due to a surface state to surface state transition and is therefore not affected by the discretized bulk bands. In the higher energy region the spurious oscillations due to the finite slab thickness become evident. For the case of Cu(110), we have shown in Ref. [97] that the onset positions of the  $sp$ -like bands are roughly alternating for slabs with one layer difference. Transitions between localized bands or surface states and  $sp$ -like bands, therefore,

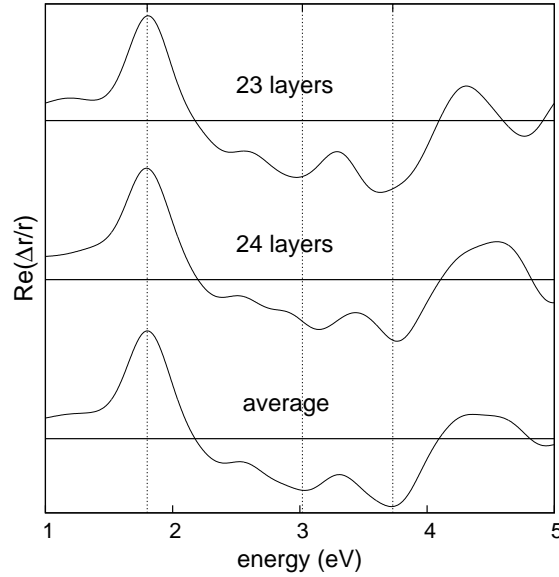


Figure 7.8: RD spectrum evaluated for a 23 and 24 layers slab and the average of these two spectra.

show alternating onsets for slabs with one layer difference. These artifacts, arising from the coarse spacing of bulk-like bands, can be reduced by averaging over spectra obtained for slabs with one layer difference.

In order to minimize the effect of the finite slab thickness and of the resulting coarse spacing of the bulk-like bands, we have performed RD calculations applying 23, 24, and 25 layers for every surface structure investigated. The final RD spectrum is obtained by first averaging over the spectra for 23 and 24, and 24 and 25 layers, and finally averaging over these results. This procedure reduces most of the finite size effects, although one should be aware that the interpretation of every small signature in the RD spectrum might not be sensible.

### 7.3 RDS spectra and interpretation

The goal of our calculations is to interpret the theoretical RD spectra with respect to transitions between electronic states. As we make use of the independent particle approximation a straightforward assignment of features in the imaginary dielectric function to transitions between one-electron states is possible and consequently also signatures in the real part of the dielectric function and the reflectance difference spectrum can be traced back to special excitations. For the assignment of states, we can make use of the fact that the independent particle dielectric function is obtained as a sum over specific  $k$ -point regions (as discussed before), and that we can therefore evaluate the RD spectrum for each  $k$ -point region separately. Additionally, the dielectric function can be analyzed with respect to the energy of the initial state, which provides together with the frequency of a specific feature information about the states contributing to this signal. For the Cu bulk, such an assignment was shown

in Fig. 6.5. Combining these two techniques, an interpretation of the dielectric function is possible. An assignment of RD features is slightly more complicated because not only the difference between the imaginary dielectric function for  $x$ - and  $y$ - polarized light, but also the difference in the real part contribute. These contributions are multiplied by the imaginary and real part of the bulk dielectric function and everything is finally divided by the norm of the bulk dielectric function, so that the origin of RD feature is more obscure than for the imaginary dielectric function.

While an assignment of a transition with respect to the energy of the initial band and the  $k$ -point region is in principle unique, it is nevertheless useful to consider selection rules and general properties of the band structure to disentangle possible transitions where the direct method only provides information about regions of energy and  $k$ -points.

In a first step, one can assume that transition probabilities are unity for all possible (= energetically allowed) excitations [see Eq. (2.75)], and that the dielectric function only depends on the number of states available. In this approximation the contribution to the dielectric function from transitions between the occupied band  $v$  to the unoccupied band  $c$  is proportional to the corresponding joint density of states:

$$J_{cv}(\epsilon) = \int_{BZ} \frac{2d\mathbf{k}}{(2\pi)^3} \delta[\epsilon_c(\mathbf{k}) - \epsilon_v(\mathbf{k}) - \epsilon]. \quad (7.3)$$

Employing the properties of the  $\delta$ -function, the density of states can be rewritten as a surface integral

$$J_{cv}(\epsilon) = \frac{2}{(2\pi)^3} \int_{\epsilon_c - \epsilon_v = \epsilon} \frac{dS}{|\nabla_{\mathbf{k}}[\epsilon_c(\mathbf{k}) - \epsilon_v(\mathbf{k})]|}. \quad (7.4)$$

Large contributions to the dielectric function therefore stem from "flat" bands

$$\nabla_{\mathbf{k}} \epsilon_c(\mathbf{k}) = \nabla_{\mathbf{k}} \epsilon_v(\mathbf{k}) = 0, \quad (7.5)$$

occurring frequently at high symmetry points of the Brillouin zone. Also if two bands are parallel

$$\nabla_{\mathbf{k}} \epsilon_c(\mathbf{k}) - \nabla_{\mathbf{k}} \epsilon_v(\mathbf{k}) = 0, \quad (7.6)$$

large contributions to the dielectric function can be expected.

In the previous consideration, the transition probabilities were not explicitly taken into account. For crystalline systems, group theory can be used to decide if transitions between bands at specific  $k$ -points are allowed according to their symmetry. For fcc and bcc bulk lattices, such dipole transition tables can e.g., be found in Ref. [101]. For the interpretation of the dielectric function of the bare and the adsorbate covered Cu(110) surfaces we consider the transition probabilities in an atomic like picture. To this end, the wavefunctions are projected onto atomic orbitals and transitions analyzed in terms of elementary atomic dipole selection rules. Such a procedure was e.g., applied by Smith [102] for the interpretation of the imaginary dielectric function of the Cu(111) and Cu(100) surface calculated with a simple semiempirical Hamiltonian. For electric dipole transitions the angular momentum number has to fulfill  $\Delta l = \pm 1$  (atomic dipole selection rule). Additionally, parity selection rules allow only electron excitations between states with different parity with respect to the

Table 7.1: Parity of atomic orbitals with respect to the  $x$ ,  $y$ , and  $z$  direction. Positive parity (+); Negative parity (-).

parity			
	$f(-x, y, z) = \pm f(x, y, z)$	$f(x, -y, z) = \pm f(x, y, z)$	$f(x, y, -z) = \pm f(x, y, z)$
$s$	+	+	+
$p_x$	-	+	+
$p_y$	+	-	+
$p_z$	+	+	-
$d_{xy}$	-	-	+
$d_{yz}$	+	-	-
$d_{zx}$	-	+	-
$d_{z^2}$	+	+	+
$d_{x^2-y^2}$	+	+	+

polarization-direction of the incident light. A transitions between e.g.,  $s$  and  $d$  bands would be forbidden because of the dipole selection rule. The parity selection rules allows e.g.,  $s \rightarrow p_x$ ,  $p_x \rightarrow d_{x^2-y^2}(d_{z^2})$ ,  $p_y \rightarrow d_{xy}$  transitions for light polarized along the  $x$ -direction, whereas e.g.,  $s \rightarrow p_y$ ,  $p_y \rightarrow d_{x^2-y^2}(d_{z^2})$ ,  $p_x \rightarrow d_{xy}$  transition are accessible by  $y$ -polarized light. In Tab. 7.3 the parity of atomic states is summarized for the  $x$ ,  $y$ , and  $z$  direction.

### 7.3.1 Band Structure

In this subsection, the band structure for the bare, and the oxygen and carbon-monoxide covered Cu(110) surface is discussed. The band structure or respectively its deviation from experiment is an important indicator, whether the one-electron KS results are sufficiently reliable for the description of the optical response. If discrepancies between the photoemission energies and the theoretical one-particle energies exist, they will lead to energy shifts of features in the dielectric function. If the experimental and the theoretical band structure agree at least qualitatively, errors in the relative energy position of the theoretical RD spectra can be traced back to these shifts in the band structure and comparison between RD and experimental photoemission data is still possible.

In Fig. 7.9, the band structure of the bare Cu(110) surface, in Fig. 7.10 the band structure of the oxygen induced Cu(110)-(2 × 1)O reconstruction (top) and the carbon-monoxide covered Cu(110)-(2 × 1)CO (bottom) are shown. The very same band structures for the bare and the adsorbate covered Cu(110) surfaces have already been presented in Refs. [91, 105] and have been discussed in more detail there.

The most significant feature in the band structure of the bare Cu(110) surface are the surface states at the  $\bar{Y}$  point. The deeper lying, occupied, surface states at -0.5 eV (experiment: -0.4 eV [92]) has predominantly  $p_y$  character, the second surface state at 1.5 eV (experimental: 1.8 eV [93])  $s$  and  $p_z$  character. The corresponding surface states at the  $\bar{X}$  point are both unoccupied. The width of the  $d$ -bands is overestimated as it is for the Cu bulk case. While the onset of the  $d$ -bands at -4 eV is almost identical for theory and experiments, the theoretical bandwidth is with 2.5 eV about 0.5 eV larger than suggested by the angle

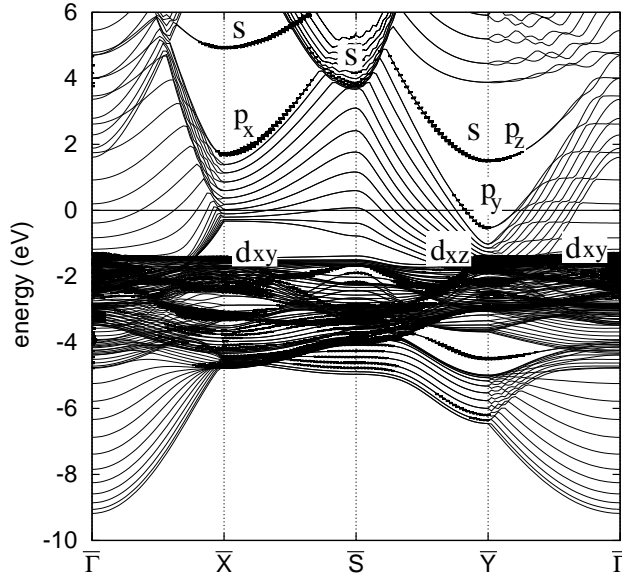


Figure 7.9: Band structure of the bare Cu(110) surface (24 layer slab) for lines between high symmetry points of the surface Brillouin zone.

resolved ultraviolet photoemission spectroscopy (ARUPS) measurements [95].

The band structure of the Cu(110)-(2×1)O added-row reconstruction is dominated by the features arising from the strongly bonded Cu-O-Cu rows aligned along the  $y$ -direction. The pronounced one-dimensional character of these rows can be seen from the strong dispersion of the O  $p_y$  state along the  $y$ -direction, whereas no dispersion appears along the  $x$ -direction. The O  $p_y$  antibonding counterpart can be observed at the  $\bar{Y}$  point as a weak resonance 0.5 eV above the Fermi level. While the O  $p_y$  states hybridize with the Cu  $s$ , Cu  $d_{x^2-z^2}$ , and Cu  $d_{z^2}$  states at the  $\bar{Y}$  point, the O  $p_x$  and O  $p_z$  states interact with the Cu  $d_{xy}$  and Cu  $d_{yz}$  states, respectively. The  $\bar{Y}$  surface states of the bare Cu(110) surface have been destroyed by the Cu(110)-(2×1)O surface reconstruction. In Fig. 7.11 a schematic overview of the energies observed in experiment and theory is provided. In the comparison the oxygen  $p$ -states and the Cu  $d$ -bands are shown. The bonding O  $p$  states have the same order in experiment and theory, the theoretical energies for the O  $p_y$  (−7.8 eV), O  $p_z$  (−6.0 eV), and O  $p_x$  (−5.5 eV) are equal or slightly larger than the measured ones (−7.8, −6.5, −6.1 eV). The character of the O  $p$  states above the Cu  $d$  bands has not been unambiguously determined in experiment. Only the position of the antibonding  $p_x$  state was confirmed at an energy of −1.2 eV (present work: −0.7 eV). The other two bands, of either  $p_y$ , or  $p_z$  type were reported at −0.2 eV, and −1.4 eV. Our calculations suggest a O  $p_z$  derived state at −1.0 eV and a O  $p_y$  related (unoccupied) state at 0.5 eV.

The band structure of the carbon-monoxide covered Cu(110)-(2×1)CO surface is shown in the bottom of Fig. 7.10. The signals arising from the carbon-monoxide are highlighted and labeled according to the CO molecular orbitals. The dispersion of the  $5\sigma$  and  $1\pi$  states at roughly −7.0 eV is small, only the  $5\sigma$  orbital hybridizes. The antibonding  $2\pi^*$  state is located at an energy of about 2 eV and distinctly visible between the  $\bar{\Gamma}$  and  $\bar{X}'$  point. In contrast to

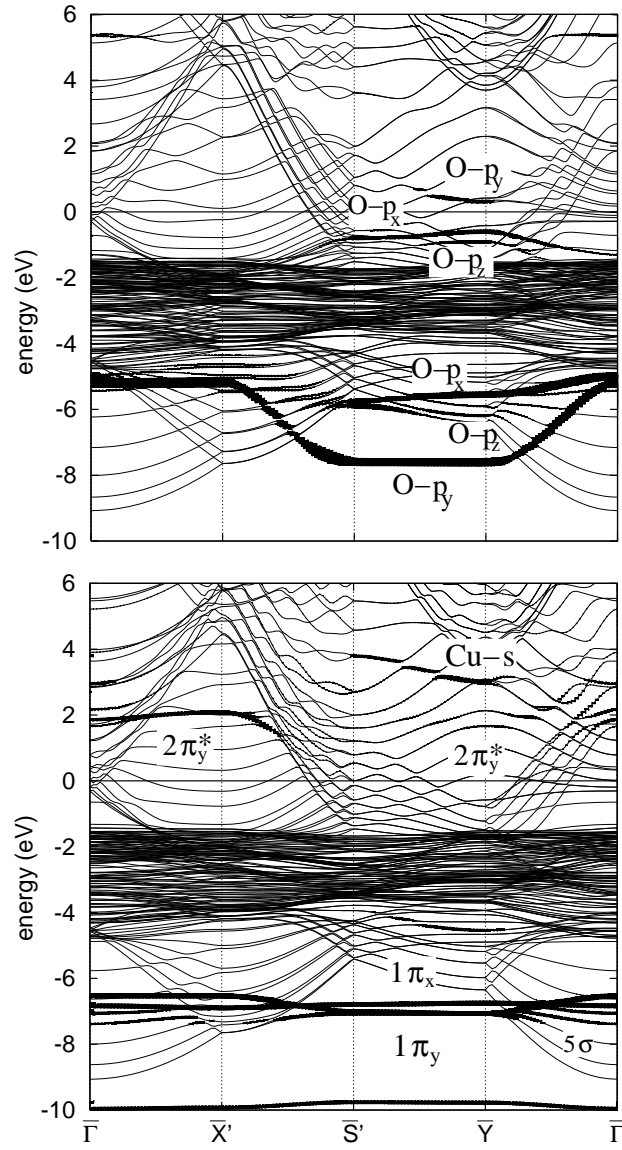


Figure 7.10: Band structure of the Cu(111)-(2 × 1)O (top) and Cu(111)-(2 × 1)CO surface (bottom). A 12 layer slab was used. Because of the doubled extension of the (2 × 1) cell, the Brillouin zone is folded back along the  $x$  direction, and the number of bands is doubled compared to the bare surface.

the Cu(111)-(2 × 1)O added-row reconstruction, the CO adsorption does not entirely destroy the characteristic surface states of the bare substrate. A Cu  $s$  like band can be found in the vicinity of the  $\bar{Y}$  point with an onset of about 3 eV, 1.5 eV above the corresponding surface state of the bare surface.

All in all, DFT describes the band structure of all three considered surfaces reasonably well. While the principle structure is reproduced, absolute energies sometimes exhibit sizeable errors, especially the Cu  $d$ -bandwidth is significantly overestimated. As a general trend,



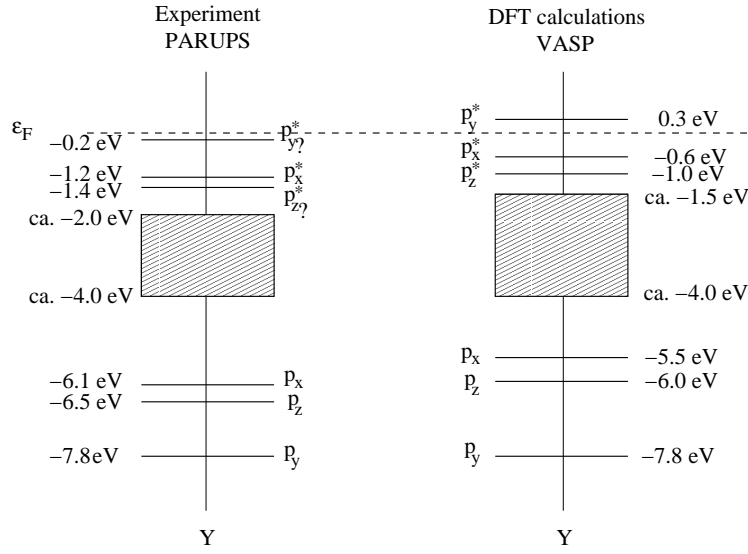


Figure 7.11: This figure schematically shows the experimental ([103] and [95]) and the ab-initio evaluated band structure for the Cu(110)-( $2 \times 1$ )O surface.

theoretical energies are shifted towards the Fermi energy, so that the energy of occupied bands is slightly too large, those of the unoccupied bands slightly too small.

### 7.3.2 Reflectance difference spectra

The final theoretical RD spectra for the bare, the oxygen, and the carbon-monoxide covered Cu(110) surface are shown in Fig. 7.12 together with the experimental data measured by Zeppenfeld *et al.* [55]. Theory succeeds in predicting the general features of all Cu(110) surfaces, but the frequencies of features are generally shifted to smaller values. This is a consequence of the beforehand discussed deviation between measured photoemission and KS-DFT eigenenergies, where the latter are shifted towards the Fermi level.

For the bare Cu(110) surface, the prominent maximum at about 2 eV is reproduced by the present calculations. Also the RD at higher frequencies, with the characteristic double minimum structure between 3 and 4 eV is obtained within the present theoretical approach. For the ( $2 \times 1$ )O added-row reconstruction, the large bare Cu(110) peak at 2 eV is significantly reduced, in accordance with the experimental findings. The minimum at about 3.8 eV is still present, although broadened compared to the measured RD signal. This might be related to spurious contributions due to the finite slab size, which could not be properly averaged out. For the carbon-monoxide covered Cu(110)-( $2 \times 1$ )CO surface the change from positive to negative RD values at small frequencies and the following rise of the RD spectrum is correctly reproduced by the present calculations. Only the minimum at about 3.8 eV is too deep. This discrepancy between theory and experiment is lifted in the case of the ( $3 \times 1$ )CO geometry. The reason for the very deep minimum in the Cu(110)-( $2 \times 1$ )CO spectrum lies in a transition involving a surface state. Since other experimental data exist that predict a much deeper minimum for the Cu(110)-( $2 \times 1$ )CO surface [52] than found by Zeppenfeld *et al.* [55], the discrepancy between the experimental data presented in [55] and our calculations might



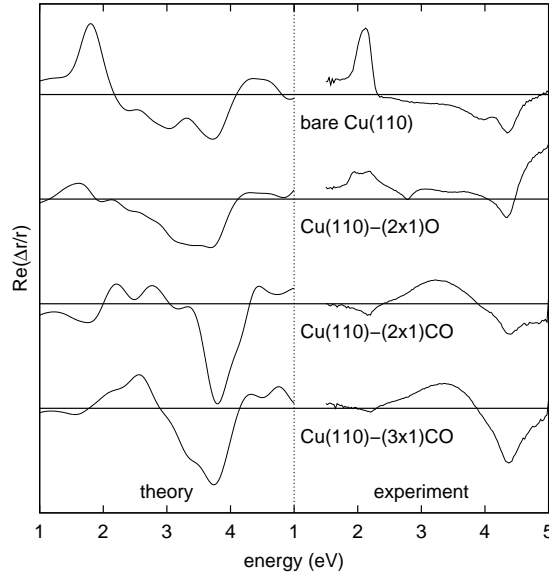


Figure 7.12: RD spectra for the bare, the oxygen induced Cu(110)-(2×1)O added-row reconstruction, the carbon-monoxide covered Cu(110)-(2×1)CO and Cu(110)-(3×1)CO surface. The theoretical spectra (left) are compared to the experimental results [55].

be related to a non-perfectly ordered experimental surface structure. On the other hand, an imprecise theoretical description of the relative position of the surface state can not be ruled out.

In the following, we will derive the origin of the main RD features by analyzing the energy and  $k$ -point origin of specific transitions. For the bare Cu(110) surface (see Fig. 7.13) the most prominent features of the RD spectrum is the large maximum at energies of about 2 eV and the double minimum structure at larger frequencies, where the second minimum occurs for all Cu(110) surfaces independently of the present adsorbate. The large maximum at about 2 eV was assumed to be connected to the characteristic bare Cu(110) surface states at the  $\bar{Y}$  point [52, 53, 58, 59, 60]. We find that transitions between the occupied surface state with  $p_y$  character and the unoccupied surface state with  $s$  character are indeed the main source for this strong absorption for  $y$ -polarized light. But in addition to this surface state – surface state transition, the final shape of this peak is determined by transitions from  $d_{xy}$  like bands at the top of the Cu  $d$ -bands to  $p_x$  states at the Fermi level near the  $\bar{X}$  point (positive RD contribution), and transitions to  $p_y$  like states between the  $\bar{\Gamma}$  and  $\bar{Y}$  point (negative RD contribution). In total these transitions result in a small positive RD shoulder at about 2 eV, as already proposed by Sun *et al.* [58]

The RD minimum at about 3.8 eV, which occurs for all Cu(110) surfaces studied in the present work, is not related to specific surface states but arises from the anisotropy of the Cu(110) surface itself. The origin of this minimum lies in transitions in the vicinity of the  $\bar{S}$  point from  $p_x$  and  $p_y$  like states at the Fermi energy to an unoccupied  $s$ -band at about 3.8 eV. Due to the fact that the surface contribution of  $p_x$  like orbitals is significantly stronger, the net absorption strength is larger (by about a factor of 2) for light polarized

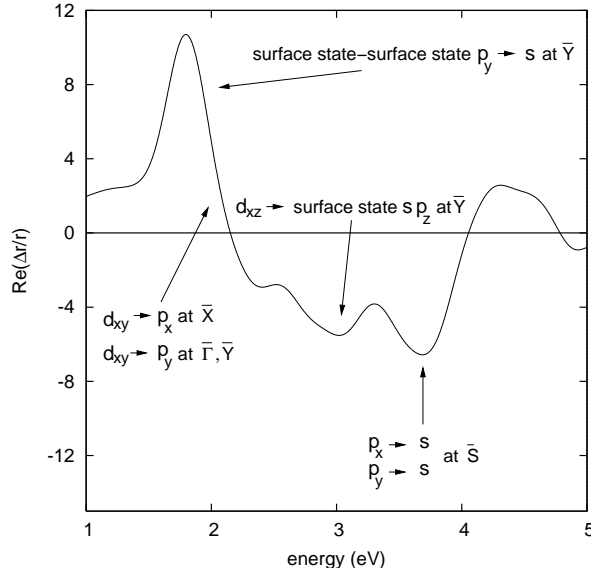


Figure 7.13: RD spectrum of the bare Cu(110) surface. Significant contributions are explicitly indicated.

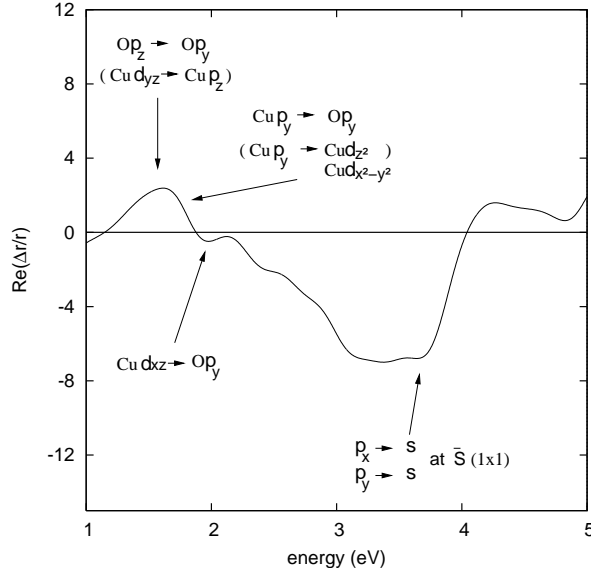


Figure 7.14: RD spectrum of the oxygen induced Cu(110)-(2 × 1)O added-row reconstruction and significant contributions to it.

along the  $x$  direction. The reason for this minimum is therefore not the different energy onset for the transitions from  $p_x$  and  $p_y$  states as proposed by Zeppenfeld *et al.* [54], but the difference in the absorption strength for these bands with different symmetry. Because the

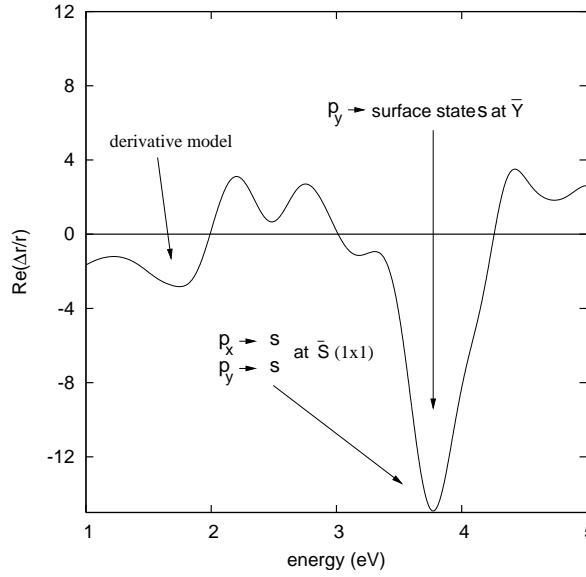


Figure 7.15: RD spectrum of the carbon monoxide covered Cu(110)- $(2 \times 1)$ CO surface and significant contributions to it.

contributing bands do not change with adsorption, the minimum at about 3.8 eV is present for all considered surfaces.

The last feature not yet explained for the bare Cu(110) surface is the second minimum at about 3 eV. It is another signature of the unoccupied surface state at the  $\bar{Y}$  point, with the initial state of  $d_{xz}$  character situated at the top of the Cu  $d$ -bands. The transition probabilities are not vanishing, due to the  $s$  and  $p_z$  character of the unoccupied surface state.

For both, the  $(2 \times 1)$ O and  $(2 \times 1)$ CO surface, the large maximum at 2 eV vanishes, to be replaced by a much smaller positive RD signal for the  $(2 \times 1)$ O, and even a negative signature for the  $(2 \times 1)$ CO surface. While for the  $(2 \times 1)$ O surface states associated with the adsorbed oxygen are responsible for the RD form at small frequencies, as will be shown later, the  $(2 \times 1)$ CO surface seems not to be influenced by specific transitions but by a general shift of the dielectric function for light polarized along  $x$ - and  $y$ - direction. This shift amounts to about +0.08 eV for  $y$  polarized light, so that the absorption in  $x$ -direction sets in slightly earlier causing the negative sign of the RD spectrum. Such a behavior can be explained by a derivative model [104]. For the  $(2 \times 1)$ O surface, this shift is overlaid by transitions to the unoccupied O  $p_y$  state at about 0.5 eV, with additional Cu  $d_{x^2-y^2}$ , Cu  $d_{z^2}$ , and Cu  $p_z$  character. Three different contributions can be observed: transitions from the O  $p_z$  state at  $-1.0$  eV to the O  $p_y$  state (positive RD contribution), transitions from Cu  $p_y$  like states at energies between  $-1.5$  and  $-1.0$  eV to the O  $p_y$  state (positive RD contribution), and transitions from Cu  $d_{xz}$  states slightly above the Cu  $d$ -bands ( $\approx -1.5$  eV) to the O  $p_y$  state (negative RD contribution). The last contribution gives rise to the small minimum at about 2 eV.

The Cu(110)-( $2 \times 1$ )O and Cu(110)-( $2 \times 1$ )CO RD spectra at higher frequencies are both dominated by the minimum at 3.8 eV described above. For the Cu(110)-( $2 \times 1$ )CO surface, this minimum is additionally deepened compared to the other surfaces. We found that this deepened minimum results from an additional transition between Cu- $p_y$  bulklike states to a ( $2 \times 1$ )CO  $\bar{Y}$  surface state at about 3 eV. This state has the same character as the unoccupied surface state of the bare Cu(110) surface ( $s$ -type), but is situated at a larger energy (3 eV compared to 1.5 eV for the bare surface), resulting in an absorption peak for  $y$ -polarized light at about 3.4 eV. In the RD, this feature manifests itself as a minimum around 3.7 eV. The negative sign of the RD contribution results from the increased importance of the real part of the surface dielectric anisotropy, as the imaginary part of the bulk dielectric function becomes larger than the respective real one.

The deviations between theoretical and experimental RD spectra concerning the depth of the minimum at 3.8 eV is lifted for the case of the Cu(110)-( $3 \times 1$ )CO surface. The depth of the minimum is now in agreement with the experimental data (see Ref. [55] and Fig. 7.12). Experiments suggest that the minimum at about 3.8 eV is very sensitive to surface defects and the roughness of the surface. The neglect of these contributions in the theoretical description of the RD ( $2 \times 1$ )CO spectrum, respectively, a quenching of the surface states by the roughened surface in experiments, might lead to the deviation for the depth of the minimum.

## Chapter 8

# Conclusions and Summary

This part of my thesis has been focused on the calculation of the reflectance difference spectra for the bare Cu(110), the oxygen covered Cu(110)-(2 × 1)O, and the carbon-monoxide covered Cu(110)-(2 × 1)CO and Cu(110)-(3 × 1)CO surfaces. The Cu(110) substrate was chosen because it is among the best studied metallic surfaces using RD spectroscopy and numerous of these measurements have been performed by our collaborators Peter Zeppenfeld and co-workers at the University of Linz [54, 55, 56, 57, 58].

The evaluation of the reflectance difference spectrum requires the (anisotropic) dielectric function of the considered surface as well as the optical response of the bulk material. Besides giving the RD spectrum, the present calculations were therefore also among the first applications of the PAW optical routines within the VASP code [21] for bulk metals as well as for the optical response of surfaces. For the correct description of the dielectric function of metallic systems, the expression for the intraband plasma frequency has been implemented in the VASP code, and was tested for various metallic systems in Sec. 6.1. The relationship between intraband transitions and interband transitions at small frequencies has been emphasized in subsection 7.2.3, and convergence tests for the surface dielectric function have been outlined in Sec. 7.2.

As the RD spectrum depends on the real and imaginary part of the bulk and surface dielectric function in a non-trivial way, the interpretation of the experimental RD spectra with respect to specific transitions is not straightforward. Therefore, an ab-initio calculation of the RD spectrum and the interpretation of this spectrum in terms of the underlying electronic transitions is of interest. In the independent particle approximation, which we used to describe the dielectric function, light can only be absorbed, if the frequency of the light corresponds to the energy difference between two one-electron eigenenergies. Agreement with experiment can only be expected if the one-electron eigenenergies correspond to the quasi-particle energies as measured in (inverse) photoemission spectroscopy. Band structure calculations for all considered Cu(110) surfaces and the comparison to experiment have been presented in subsection 7.3.1. We find that bulk like bands, surface states, and adsorbate associated features are in qualitative agreement with the experimental findings, although the theoretical one-particle energies are generally shifted towards the Fermi energy resulting in red-shifted dielectric functions and RD spectra. As we have shown in Sec. 9.1, GW calculations would improve the Cu bandstructure in some aspects, but unfortunately large scale calculations for enough  $k$ -points are yet not possible using GW due to the large

computational effort included.

For all Cu(110) surfaces, independent on the specific adsorbate, Zeppenfeld and co-workers find an RD minimum at an energy of about 4.4 eV. This feature, situated at 3.8 eV in the theoretical spectra, can be explained by transitions from  $p$ -like states near the Fermi energy to an unoccupied bulk-like  $s$  state at the  $\bar{S}$  point. Due to the surface anisotropy, the  $p_x$  character is stronger at this high symmetry point favoring absorption for light polarized along the  $x$ -direction. For the bare Cu(110) surface, the importance of the surface states for the RD could be confirmed. In the case of the oxygen covered surface, oxygen associated states are responsible for the RD maximum and the subsequent minimum in the low frequency range (1.5–2.5 eV). A surface state is found to be the reason for the deepened 3.8 eV minimum of the theoretical Cu(110)-(2  $\times$  1)CO structure, not present in the experimental spectrum. We think that this discrepancy might be related to a quenching of the surface state by disorder in the experimental setup.

For the Cu(110) bare, oxygen and carbon-monoxide covered surfaces, we find that the independent particle approximation provides a reasonable description of the surface optical response. The main features of the experimental RD spectra are reproduced but shifted to smaller energies. The RD spectra have been published in Ref. [105].

# Part III

## GW calculations

## Chapter 9

# Quasiparticle energies for metals

In the third part of my thesis, I will present GW quasiparticle calculations for *d*-metals, the noble metals Cu, Ag, and the magnetic transition metals Fe and Ni. Our results will be compared to previous calculations by other groups. An introduction to GW and to the evaluation of quasiparticle energies has been given in chapter 4. More details about the implementation of the GW routines in VASP and quasiparticle energies for semiconductors and insulators can be found in Refs. [25, 48]. The difference between semiconductors/insulators and metals is the existence of partially filled bands in the case of metals. This implies two important differences for the quasiparticle calculations of semiconductor/insulators and metals: First, the *k*-point convergence of the total quasiparticle energies is slower than for insulators, because it involves the calculation of the Fermi energy, which converges slowly with the number of *k*-points. Secondly, intraband transitions contribute to the dielectric function  $\epsilon(\mathbf{q})$ . For the long-wavelength limit  $\mathbf{q} \rightarrow 0$ , the intraband contribution is determined by the plasma frequency [Eq. (2.113)]. In order to take the long-wavelength intraband contributions into account, we evaluate the plasma frequency and add the corresponding Drude term to the interband dielectric function. If one does not include the Drude term, one neglects important contributions at the  $\Gamma$  point and thus a large number of *q*-points would be required.

In all quasiparticle calculations presented in this chapter we have used *GW* potentials. As a larger number of unoccupied bands are required for the GW calculations (and also for the ACFDT calculations presented in part IV of this thesis), it is important that the PAW pseudopotentials describe also the scattering properties of empty states accurately. Therefore special *GW* potentials are generated which reproduce the scattering properties of a spherical reference atom up to  $\approx 10$  Ry exactly. Details concerning the PAW potentials used in this chapter are summarized in Tab. 9.1.

### 9.1 Noble metals - Cu and Ag

In the following we will present  $G_0W_0$  quasiparticle energies for the noble metals Cu and Ag. Both Cu and Ag crystallize in an fcc structure with an experimental lattice constant of 3.615 Å and 4.086 Å, respectively. The *d*-bands are fully occupied with the highest DFT *d*-states<sup>1</sup> found at  $-1.56$  eV and  $-2.74$  eV for Cu and Ag, respectively, which is about 0.5

---

<sup>1</sup>The band structures obtained applying the LDA or the PBE exchange-correlation potential are very similar for the noble metals.



Table 9.1: PAW potentials used in the present section. Cutoff radii  $r_c^l$  applied for the generation of the pseudo partial waves with angular quantum number  $l$  are denoted in a.u. The number of partial waves and projectors is specified. The energy cutoff  $E_{\text{cut}}$  refers to the one specified in the POTCAR file. In the third column, the states treated as valence are indicated. The local potentials have been generated by replacing the AE potential by a soft pseudopotential within the cutoff radius  $r_{\text{loc}}$  (a.u.) specified in the fourth column. For Ag, the pseudopotential for the  $4f$  state was used as local potential. For more details, see Ref. [15].

name		valence	local	$r_c^l$ (a.u.)				$E_{\text{cut}}$
				$s$	$p$	$d$	$f$	(eV)
Cu	Cu_GW	4s 3d	1.5	2×2.2	2×2.2	2×1.9		417
Cu-3p	Cu_pv_GW	3p 4s 3d	1.5	2×2.2	2×1.5	2×1.9		467
Ag	Ag_GW	5s 4d	4f	2×2.5	2×2.6	2×2.4		250
Ag- $f$	Ag_f_GW	5s 4d	1.4	2×2.5	2×2.6	2×2.4	2×2.6	250
Fe	Fe_GW	4s 3d	1.7	2×2.3	2×2.3	2×2.1		321
Fe-3p	Fe_pv_GW	3p 4s 3d	1.6	2×2.3	2×1.7	2×2.0		365
Fe-3p3s	Fe_sv_GW	3s 3p 4s 3d	0.7	1.3 2×1.8	2×1.6	2×1.9		443
Ni	Ni_GW	4s 3d	1.7	2×2.3	2×2.3	2×2.0		357
Ni-3p	Ni_pv_GW	3p 4s 3d	1.3	2×2.1	2×1.7	2×2.0		368

eV and 1.2 eV higher than the experimental onset. For a comparison of the experimental and theoretical band structure of Cu see Fig. 6.3.

Previous calculations by Marini *et al.* suggested that  $G_0W_0$  improves the agreement between the experimental and theoretical  $d$ -band position for both Cu [41] and Ag [42] significantly. But those calculations were performed using pseudopotentials, an approximation which suffers from an inaccurate representation of the valence wavefunctions in the core region and the neglect of core-valence interactions (see Ref. [25] Sec. II F). As a consequence, keeping the Cu  $3s$  and  $3p$  electrons in the pseudopotential calculations in the core e.g., moved the highest occupied  $d$ -bands above the Fermi level, as reported in Ref. [41]. Such a drastic error ( $> 2$  eV) is not expected for the PAW method since we calculate the core-valence interaction on the HF level (see Sec. 4.2) but the influence of the deeper lying  $3p$  states will be nevertheless tested for Cu. For Ag, the inclusion of  $f$ -projectors for the representation of the unoccupied Ag  $f$ -states at  $\approx 11$  eV above the Fermi level is considered.

Besides the applied potentials, the  $k$ -point dependence, the influence of the number of unoccupied bands, the dependence on  $\eta$  for the evaluation of the dielectric function (Lorentzian broadening), the maximal rank of the response function determined by ENCUTGW, and the maximal angular momentum number LMAXFOCKAE up to which the true charge density is reconstructed on the plane wave grid have been tested.

The present  $G_0W_0$  calculations have been performed at the experimental lattice constants. The LDA was used for the evaluation of the DFT eigenenergies, which are considered as the starting point for the  $G_0W_0$  correction. The DFT-LDA band structures of Cu (left) and Ag (right) are shown in Fig. 9.1 and states at high-symmetry points are labeled. For the initial DFT calculations a Methfessel-Paxton Fermi integration of first order with a smearing width of 0.4 eV was used, if not otherwise mentioned. The use of the tetrahedron method is

Table 9.2:  $k$ -point dependence of the Cu  $G_0W_0$  quasiparticle energies. The Fermi energy is evaluated by the tetrahedron method and the quasiparticle energies are specified with respect to the Fermi energy  $E_F$ .

$x \times x \times x$ $k$ -point	4	6	8	10	12
$\Gamma_1$	-9.66	-9.58	-9.50	-9.49	-9.45
$\Gamma_{25'}$	-3.03	-3.02	-2.98	-2.97	-2.96
$\Gamma_{12}$	-2.31	-2.27	-2.24	-2.24	-2.22
$L_1$	-4.93	-4.93	-4.92	-4.89	-4.88
$L_3$	-3.07	-3.04	-3.01	-3.01	-3.00
$L_3$	-1.74	-1.71	-1.68	-1.67	-1.65
$L_{2'}$	-1.43	-1.35	-1.30	-1.28	-1.25
$L_1^*$	3.74	3.80	3.87	3.90	3.91
$X_1$	-4.68	-4.62	-4.65	-4.66	-4.65
$X_3$	-4.24	-4.22	-4.21	-4.22	-4.21
$X_2$	-1.77	-1.74	-1.71	-1.72	-1.70
$X_5$	-1.59	-1.55	-1.52	-1.52	-1.51
$X_4^*$	1.17	1.23	1.29	1.32	1.35
$\Gamma_{12}$ - $\Gamma_{25}$	0.73	0.75	0.74	0.73	0.74
$X_5$ - $X_3$	2.66	2.67	2.69	2.70	2.71
$X_5$ - $X_1$	3.09	3.07	3.13	3.14	3.14
$L_3$ - $L_3$	1.33	1.33	1.33	1.33	1.34
$L_3$ - $L_1$	3.19	3.22	3.24	3.22	3.22
$X_5$ - $X_2$	0.18	0.19	0.19	0.20	0.19
Fermi energy	5.36	5.33	5.28	5.25	5.23

not possible yet, because the intraband plasma frequency and hence the intraband dielectric function is not evaluated for this setting, which would result in a slower  $k$ -point convergence of the  $G_0W_0$  results. The energy cutoff for the representation of the plane waves was chosen to be 400 eV for Cu and 350 eV for Ag. Tests have shown that an energy cutoff of 250 eV would not change the results for Ag significantly. The results are therefore essentially fully converged with respect to the plane wave energy cutoff. The energy cutoff determining the rank of the response function ENCUTGW was set to 200 eV, which gives well converged results for Ag and Cu.

We will first focus on the convergence tests performed for Cu. The conclusions can, in most cases, be transferred to the case of Ag as well. It is known that the convergence of  $G_0W_0$  quasiparticle energies with the number of empty bands is very slow. We find that for 55 additional unoccupied bands, errors are smaller than 0.02 eV, which is enough for the present purpose. Another important test concerns the number of required  $k$ -points because an increase of this quantity enlarges the computational time drastically. For insulators and semiconductors a  $\Gamma$ -centered  $4 \times 4 \times 4$   $k$ -point grid has shown [25] to result already in reasonable quasiparticle energies. For metals, the convergence might be slower due to partially occupied states at the Fermi energy. In Tab. 9.2 both, absolute quasiparticle energies and

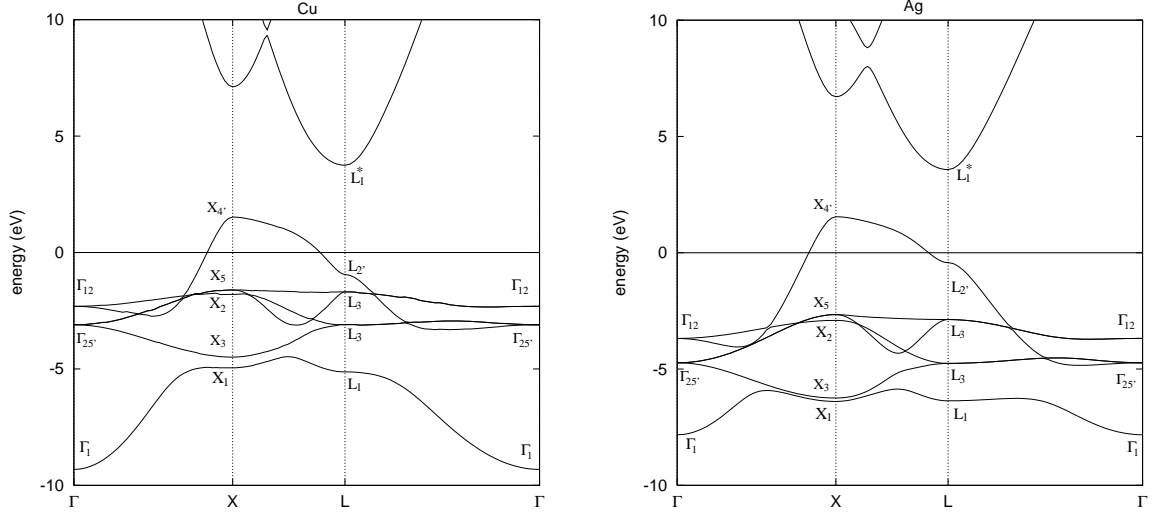


Figure 9.1: DFT band structure of Cu (left) and Ag (right) and assignment of bands at high-symmetry  $k$ -points.

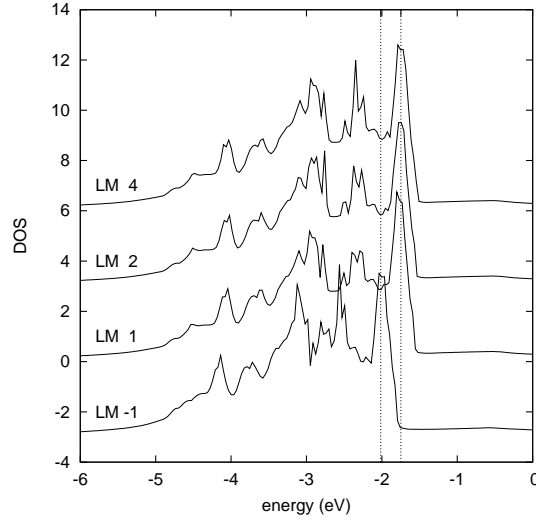


Figure 9.2: Cu quasiparticle DOS evaluated for different maximal angular momentum numbers LMAXFOCKAE up to which the exact wavefunction is restored on the plane wave grid. The energies stem from a  $8 \times 8 \times 8$   $k$ -points calculation for the Cu GW potential. The positions of the first maxima ( $\approx 0.3$  eV difference) are highlighted by vertical lines.

energy differences at high symmetry Brillouin zone points, are presented for various  $k$ -point grids. The  $k$ -point convergence is slightly dependent on the considered band, with slower convergence for the  $\Gamma_1$ ,  $L_{2'}$ ,  $L_1^*$ , and the  $X_4^*$  state. The  $k$ -point induced errors are somewhat smaller for  $d$ -bands and especially the energy differences are well reproduced already for a  $4 \times 4 \times 4$   $k$ -point grid (errors  $< 0.05$  eV). The Fermi energy evaluated using the tetrahedron

method seems to converge faster than the Fermi energy obtained applying the Methfessel-Paxton smearing, so that we use the tetrahedron method for the evaluation of the  $G_0W_0$  Fermi energy throughout this work. But it should be kept in mind, that even applying the tetrahedron method the Fermi energy for a  $8 \times 8 \times 8$   $k$ -point grid (both for DFT and GW) is not better converged than  $\approx 0.06$  eV. Differences between  $12 \times 12 \times 12$  and  $10 \times 10 \times 10$  results are however well below 50 meV, for most energies below 20 meV, which suffices for the present purpose.

Further tests show that the  $G_0W_0$  quasiparticle energies are hardly affected by choosing the smearing width 0.2 or 0.4 eV in the initial DFT calculation. Furthermore, reducing the imaginary shift  $\eta$  for the evaluation of the self energy and the polarizability from 0.1 eV to 0.01 eV leads to almost no change in the quasiparticle energies. Only the  $X_1$  state is shifted upwards by 0.06 eV. The largest effect on the quasiparticle energies, nevertheless, is caused by the introduction or the neglect, respectively, of LMAXFOCKAE. By setting LMAXFOCKAE to an angular momentum number  $l$ , all components of the difference between AE and PS partial densities up to this momentum are reconstructed on a plane wave grid and consequently the form of the AE density is approximately reconstructed (see Sec. 2.7). In Fig. 9.2 the Cu  $G_0W_0$  density of states obtained neglecting the AE reconstruction (LM  $-1$ ), and results for increasing values of LMAXFOCKAE are shown. If the form of the AE density is not recovered, the topmost  $d$ -bands start at lower energies (the first maximum of the  $d$ -bands is highlighted by a vertical line) resulting in a reduction of the bandwidth from 3.3 eV with LMAXFOCKAE = 4 to 3.0 eV for LMAXFOCKAE =  $-1$ . Although the position of the  $d$ -bands agrees better with experiment if LMAXFOCKAE =  $-1$ , this is an artefact of the crude approximation of the exact charge density. Interestingly, the results stemming from setting the maximal angular momentum to 1 or 4 do not differ much. For the heavier Ag, the difference between considering the AE reconstruction or not is much smaller than for Cu. The reason for these observations is that the exact Cu  $3d$  wavefunctions are spatially strongly contracted, and VASP usually only attempts to restore the moments of the charge density without any consideration of the exact shape of the  $3d$  wavefunctions. This causes an overestimation of the  $3d$ - $3d$  screened exchange interaction. By restoring the correct spatial charge distribution on the plane wave grid, the screened exchange interaction is well approximated. These issues are less critical for  $4d$  states, which are spatially less contracted, thus the Ag results are less dependent on LMAXFOCKAE.

In Tab. 9.3 the Cu  $G_0W_0$  quasiparticle energies obtained for two different Cu potentials, one without, one with the  $3p$  electrons included in the valence, are shown. A  $12 \times 12 \times 12$   $k$ -point grid and LMAXFOCKAE = 4 were applied. Additionally, the energies calculated by Marini *et al.* [41] employing a pseudopotential plane wave code and by Zhukov *et al.* [106] using the full potential LMTO approximation are presented. We first note that LDA results are little changed by the choice of the PAW potential, whereas the GW results depend on the treatment of the  $3p$  electrons. The most significant error in the DFT one-electron energies is the wrong description of the absolute position and the bandwidth of the  $d$ -states. The highest  $d$ -band (see  $X_5$  state) is located at  $-1.56$  eV in LDA, whereas experiments suggest  $-2.01$  eV, a difference of 0.45 eV. The error in the low energy  $d$  onset (see  $X_1$ ) is smaller (0.2 eV), so that, as a consequence, the bandwidth (in Tab. 9.3 in italic letters) is 3.42 eV in DFT versus 3.17 eV in experiment. Unfortunately, our  $G_0W_0$  results can not correct this behavior and the uppermost  $d$ -bands are shifted to even slightly higher energies (about 0.1

Table 9.3: Cu  $G_0W_0$  quasiparticle energies evaluated for two different potentials and a  $12 \times 12 \times 12$   $k$ -point grid. The results are compared to the pseudopotential plane wave (PPW) values obtained by Marini *et al.* Ref. [41] and the full potential linear muffin-tin orbital (FP-LMTO) calculations by Zhukov *et al.* [106]. Experimental data are taken from Ref. [90], if not otherwise stated.

	LDA Cu	LDA Cu-3p	$G_0W_0$ Cu	$G_0W_0$ Cu-3p	$G_0W_0$ [41]	$G_0W_0$ [106]	Exp.
$\Gamma_1$	-9.43	-9.47	-9.45	-9.68	-9.24	-9.35	-8.60
$\Gamma_{25'}$	-3.11	-3.12	-2.96	-2.94	-3.41	-3.17	-3.59
$\Gamma_{12}$	-2.27	-2.27	-2.22	-2.19	-2.81	-2.36	-2.78
$L_1$	-5.19	-5.20	-4.88	-4.99	-5.07	-5.20	-5.16
$L_3$	-3.16	-3.15	-3.00	-2.98	-3.50	-3.21	-3.62
$L_3$	-1.73	-1.70	-1.65	-1.61	-2.24	-1.78	-2.25
$L_{2'}$	-1.05	-1.08	-1.25	-1.33	-0.57	-0.92	-0.85
$L_1^*$	3.65	3.64	3.91	3.81	4.19	3.86	4.10
$X_1$	-4.98	-4.98	-4.65	-4.74	-4.94	-5.00	-5.18
$X_3$	-4.54	-4.53	-4.21	-4.25	-4.53	-4.55	-4.80
$X_2$	-1.74	-1.71	-1.70	-1.65			-2.30 [107]
$X_5$	-1.59	-1.56	-1.51	-1.45	-2.04	-1.63	-2.01
$X_4'^*$	1.42	1.39	1.35	1.29			2.3 [108]
$\Gamma_{12}-\Gamma_{25}$	0.84	0.85	0.74	0.76	0.60	0.81	0.81
$X_5-X_3$	2.95	2.97	2.71	2.80	2.49	2.92	2.79
$X_5-X_1$	<b>3.39</b>	<b>3.42</b>	<b>3.14</b>	<b>3.29</b>	<b>2.90</b>	<b>3.37</b>	<b>3.17</b>
$L_3-L_3$	1.43	1.45	1.34	1.38	1.26	1.43	1.37
$L_3-L_1$	3.46	3.50	3.22	3.39	2.83	3.42	2.91

eV). Together with an upward shift of the lower  $d$ -states the  $G_0W_0$  bandwidth (3.29 eV) is in better agreement with experiment (3.17 eV), but the entire  $d$ -band is shifted to too high energies. In contrast to our data, the quasiparticle  $d$ -band energies obtained by Marini *et al.* [41] undergo a drastic shift to lower energies resulting in a good agreement with experiment. This might be a fortuitous effect of the errors introduced by the pseudopotential method, which is supported by our observations for  $LMAXFOCKAE = -1$ . Additionally, another calculation [106] performed using a full potential LMTO method could also not confirm the  $d$ -band onset calculated by Marini *et al.*

Beside  $G_0W_0$ , Marini *et al.* [109] have performed  $GW_0$  calculations where the eigenenergies entering the Green's functions were updated in each quasiparticle iteration [see Eq. (4.15)] but the polarization and consequently the screened Coulomb interaction  $W$  were kept fixed. They observed, that with each iteration, the energy difference between  $d$ -bands becomes smaller and the bandwidth decreases from 2.90 eV, to 2.31 eV, to 1.92 eV, and this does not yet seem to be the converged value. In order to check this result, we also performed  $GW_0$  calculations applying a  $8 \times 8 \times 8$   $k$ -point grid. The results are presented in Tab. 9.4 together with the energy differences by Marini *et al.* [109] (in bold letters). While we observe a slight decrease of the energy differences by updating the Green's function, the effect is by

Table 9.4:  $G_0W_0$  quasiparticle energies for Cu. The Cu potential without  $3p$  electrons and a  $8 \times 8 \times 8$   $k$ -point grid is applied. Our data are compared to the results of Marini *et al.* [109]. Their quasiparticle energies are written in **bold** letters.

	$G_0W_0$	<b><math>G_0W_0</math></b>	$G_1W_0$	<b><math>G_1W_0</math></b>	$G_2W_0$	<b><math>G_2W_0</math></b>	exp.[90]
$\Gamma_{12}-\Gamma_{25'}$	0.74	<b>0.60</b>	0.71	<b>0.38</b>	0.71	<b>0.23</b>	0.81
$X_5-X_3$	2.69	<b>2.49</b>	2.65	<b>1.99</b>	2.64	<b>1.65</b>	2.79
$X_5-X_1$	3.13	<b>2.90</b>	3.11	<b>2.31</b>	3.11	<b>1.92</b>	3.17
$L_3-L_3$	1.33	<b>1.26</b>	1.30	<b>1.03</b>	1.29	<b>0.90</b>	1.37
$L_3-L_1$	3.24	<b>2.83</b>	3.21	<b>2.13</b>	3.20	<b>1.65</b>	2.91
$L_1^*-L_{2'}$	5.18	<b>4.76</b>	5.22	<b>4.78</b>	5.22	<b>3.77</b>	4.95

far not as strong as in Ref. [109]. Furthermore, from the second iteration on (we performed 6 iterations - not all shown in Tab. 9.4), our energy differences do not change anymore. From our point of view this suggests that the code of Marini contained a severe bug, making the previous results indeed very disputable. In Tab. 9.5 the quasiparticle energies obtained for Ag are summarized. For Ag, the unoccupied  $f$ -states were included by introducing  $f$  partial waves and  $f$ -projectors in the generation of the PAW potentials. The DFT failure for the description of the Ag  $d$ -bands follows the same trend as for Cu, but the discrepancy between theory and experiment is even larger. Now both the upper and lower edge of the bands are significantly shifted to too high energies, 1.2 eV for the upper edge, and 0.9 eV for the lower edge. The theoretical bandwidth is consequently 0.3 eV larger than the experimental one (3.7 eV vs. 3.40 eV). As in the case of Cu, our  $G_0W_0$   $d$ -states are still lying too high, but at least a shift in the right direction is observed. The  $X_5$  state (upper  $d$ -band edge) is downshifted by  $\approx 0.6$  eV, the  $X_1$  state (lower  $d$ -band edge) by 0.3 eV, reducing the LDA bandwidth from 3.7 eV to 3.44 eV. The introduction of the  $f$ -projector thereby contributes almost 0.3 eV shift for the  $X_5$  state and generally decreases the  $d$ -band energies. Again pseudopotential calculations [42] result in a much better agreement with the experiments, probably due to errors in the description of the wavefunctions.

In summary, for both Cu and Ag,  $G_0W_0$  results in a better description of the  $d$ -bandwidth, but in both cases the  $d$ -bands are located too high in energy, 0.65 eV in the case of Ag and 0.56 eV in the case of Cu. A similar behavior was observed by Miyake *et al.* [44] for the semicore  $d$ -states in ZnS. Experimentally, the  $d$ -band of this material is observed at an energy of about  $-9.0$  eV, whereas LDA predicts the lowest  $d$ -state to be located at  $-6.42$  eV. While  $G_0W_0$  leads to a decrease in energy (to  $-7.17$  eV) it is still far from the experimental value. Interestingly, also if the  $G_0W_0$  starts from LDA+U results, which can bring the  $d$ -bands in agreement with experiment, the quasiparticle  $G_0W_0$  energies shift upwards in energy back to  $-7.82$  eV.

## 9.2 Ferromagnets: Fe, Ni

In this section, quasiparticle energies for ferromagnetic Fe and Ni will be presented. Fe crystallizes in a bcc structure with a lattice constant of 2.866 Å and has a magnetic moment

Table 9.5: Ag  $G_0W_0$  quasiparticle energies evaluated for various potentials and a  $10 \times 10 \times 10$   $k$ -point grid. The results are compared to the pseudopotential plane wave (PPW) values obtained by Marini *et al.* [42]. If not otherwise mentioned, experimental data are taken from Ref. [42] which are based on the energies averaged over different experimental data presented in Ref. [110].

Method	LDA	LDA	$G_0W_0$	$G_0W_0$	$G_0W_0$	Exp.
Potential	Ag	Ag- $f$ proj.	Ag	Ag- $f$ proj.	PPW [42]	
$\Gamma_1$	-7.89	-7.90	-7.99	-7.85		
$\Gamma_{25'}$	-4.83	-4.82	-5.07	-5.28	-5.75	-6.06
$\Gamma_{12}$	-3.77	-3.76	-4.08	-4.34	-4.81	-4.95
$L_1$	-6.45	-6.45	-6.61	-6.69	-7.11	-7.09
$L_3$	-4.84	-4.84	-5.11	-5.32	-5.79	-6.14
$L_3$	-2.97	-2.95	-3.25	-3.54	-3.94	-4.15
$L_{2'}$	-0.49	-0.50	-0.56	-0.35		-0.20 [112]
$L_1^*$	3.50	3.50	3.82	3.71		3.8 [111]
$X_1$	-6.47	-6.47	-6.66	-6.76	-7.23	-7.37
$X_3$	-6.34	-6.33	-6.50	-6.64	-7.11	-7.32
$X_2$	-2.99	-2.98	-3.31	-3.60	-4.01	-4.53
$X_5$	-2.76	-2.74	-3.02	-3.32	-3.72	-3.97
$X_4'^*$	1.48	1.48	1.56	1.76		2.10 [111]
$\Gamma_{12}-\Gamma_{25}$	1.06	1.06	0.99	0.95	0.94	1.11
$X_5-X_3$	3.58	3.59	3.49	3.32	3.39	3.35
$X_5-X_1$	3.72	3.73	3.65	3.44	3.51	3.40
$L_3-L_3$	1.88	1.88	1.87	1.78	1.85	1.99
$L_3-L_1$	3.48	3.49	3.36	3.15	3.17	2.94

of  $2.13 \mu_B$ . Ni possesses an fcc structure with a lattice constant of  $3.524 \text{ \AA}$  and the exchange splitting is significantly smaller than for Fe leading to an experimental magnetic moment of  $0.57 \mu_B$ . The band structures for Fe (left) and Ni (right) are shown in Fig. 9.3. Previous calculations by Aryasetiwan [43] showed that the  $G_0W_0$  quasiparticle energies of Ni are in quite good agreement with experiments, but that the exchange splitting was not reduced compared to the too large LDA value. For both, Fe and Ni, the influence of the  $3p$  states has been tested. A plane wave energy cutoff of 350 eV was used throughout all calculations. While ENCUTGW was set to 200 eV for Cu and Ag, we found that this reduction leads to slight errors in the quasiparticle energies for Fe and Ni, so that ENCUTGW was set to the plane wave energy cutoff. The initial DFT calculation has again been performed applying a smearing width of 0.4 eV, and  $\eta$  was set to 0.1 eV. Changing the width from 0.4 eV to 0.2 eV, and the shift  $\eta$  from 0.1 to 0.01 eV had again hardly any effect on the quasiparticle energies.

As for Cu, the largest effect on the quasiparticle energies was the one caused by the reconstruction of the AE charge density triggered by setting LMAXFOCKAE. In Fig. 9.4 the quasiparticle density of states for Fe (left) and Ni (right) obtained by setting LMAXFOCKAE to 4 (reconstruction of the AE charge density up to an angular momentum of 4) or not



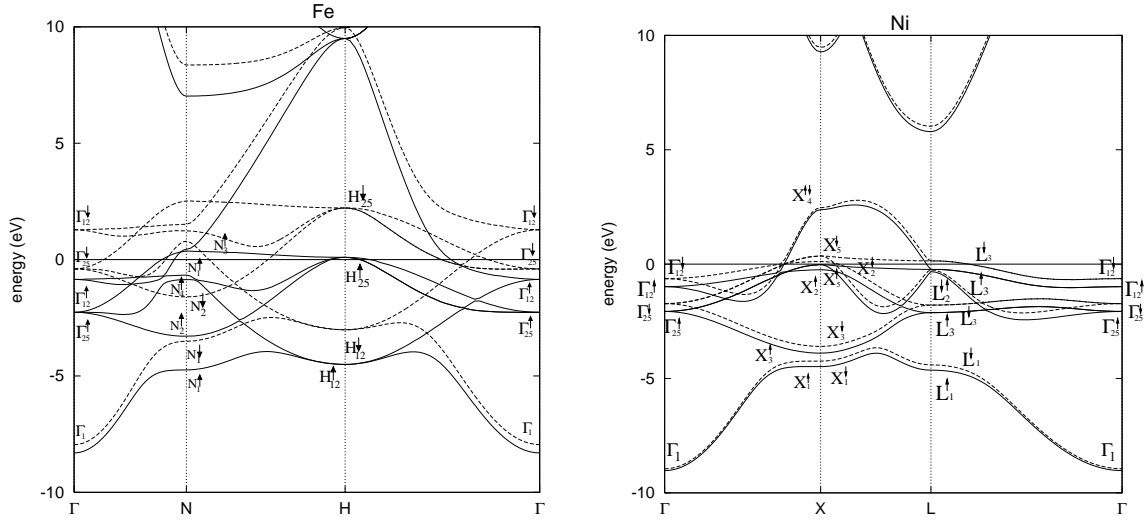


Figure 9.3: DFT band structure for Fe (left) and Ni (right) and assignment of bands at high-symmetry  $k$ -points.

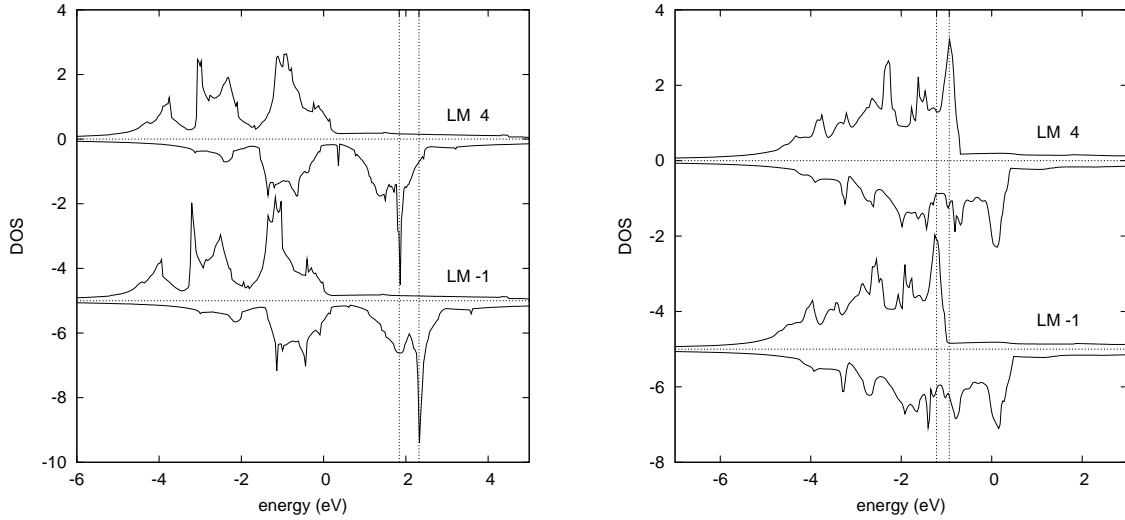


Figure 9.4: Quasiparticle  $G_0W_0$  density of states for Fe (left) and Ni (right) choosing either LMAX-FOCKAE (LM) is 4 which corresponds to a reconstruction of the AE charge density on the plane wave grid up to an angular momentum number  $l = 4$  or setting LMAXFOCKAE not at all (LM  $-1$ ).

restoring the AE charge density at all (LMAXFOCKAE =  $-1$ ), are shown. In both cases, Fe and Ni, the correction of the charge density results in a smaller exchange splitting.

In Tab. 9.6 the  $G_0W_0$  quasiparticle energies for Fe are collected. For Fe, the agreement between LDA one-particle energies and experiment is satisfactory. The largest error concerns the up and down component of the  $H_{12}$  state (0.8 eV for  $H_{12\uparrow}$ , 0.5 eV for  $H_{12\downarrow}$ ), but all other



Table 9.6: Fe  $G_0W_0$  quasiparticle energies for different potentials. A  $10 \times 10 \times 10$   $k$ -point grid has been applied. The experimental values have been measured by Turner *et al.* [113], if not otherwise quoted.

Method Potential	LDA	$G_0W_0$ Fe	$G_0W_0$ Fe-3p	$G_0W_0$ Fe-3p3s	Exp.		
$\langle \Gamma_{1\uparrow\downarrow} \rangle$	-8.13	-8.60	-9.20	-9.07	-8.15		
$\Gamma_{25'\uparrow}$	-2.19	-2.01	-2.17	-2.26	-2.35	-2.55	[115]
$\Gamma_{12\uparrow}$	-0.91	-0.96	-1.03	-1.09	-0.78	-1.2	[114]
$\Gamma_{25'\downarrow}$	-0.40	-0.13	-0.21	-0.23	-0.27	-0.41	[115]
$\Gamma_{12\downarrow}^*$	1.36	1.50	1.64	1.79		1.5	[116]
$H_{12\uparrow}$	-4.55	-4.15	-4.52	-4.69	-3.80		
$H_{12\downarrow}$	-2.98	-2.65	-2.90	-2.96	-2.50		
$H_{25\uparrow}^*$	0.14	0.14	0.18	0.17		0.12	[116]
$H_{25\downarrow}^*$	2.18	2.20	2.40	2.54		1.9	[116]
$N_{1\uparrow}$	-4.72	-4.46	-4.86	-4.96	-4.50		
$N_{2\uparrow}$	-3.24	-2.91	-3.18	-3.30	-3.00		
$N_{1\downarrow}$	-0.89	-0.91	-0.98	-1.03	-0.70	-1.02	[115]
$N_{4\uparrow}$	-0.73	-0.77	-0.82	-0.86	-0.70		
$N_{1\downarrow}$	-3.50	-3.26	-3.64	-3.67	-3.60		
$N_{2\downarrow}$	-1.60	-1.26	-1.42	-1.48	-1.40		
$N_{3\uparrow}^*$	0.40	0.37	0.44	0.45		0.4	[116]
Exchange splitting							
$\Gamma_{25'}$	1.80	1.87	1.96	2.03	2.08		
$H_{12}$	1.57	1.50	1.62	1.73	1.30		
$N_2$	1.63	1.65	1.76	1.82	1.60		

$d$ -band positions are well described already on the LDA level. Also the exchange splitting are only slightly overestimated within LDA.  $G_0W_0$  leads to relatively modest corrections to the LDA one-particle energies and consequently does not give huge deviations from experiment. Interestingly, the introduction of the  $3p$  electrons in the valence predominantly and strongly effects the deeper lying  $d$ -states  $H_{12}$  and  $N_1$ , and shifts the  $G_0W_0$  energies obtained without  $3p$  electrons (which are in good agreement with experiment) back to the DFT values. As we find that the influence of the  $3p$  electrons is largest for Fe, we also tested a potential in which both,  $3p$  and  $3s$  electrons are treated as valence. Although the difference between the quasiparticle energies obtained from the Fe-3p and the Fe-3p3s potential is significantly smaller than between the energies from the Fe and the Fe-3p potential, the change in the energies amount still up to 0.17 eV for the  $H_{12\uparrow}$  state. The magnetic moment, which is 2.17  $\mu_B$  for the LDA, becomes 2.21  $\mu_B$  applying  $G_0W_0$  no matter which potential has been used and is thus larger than the experimental value of 2.13  $\mu_B$ .

For Ni the agreement of the  $G_0W_0$  quasiparticle energies and experiment worsens drastically. In Fig. 9.7 the quasiparticle energies for Ni are presented. Due to the small exchange splitting in Ni the distinction of experimental up and down components is not possible for

Table 9.7: Ni  $G_0W_0$  quasiparticle energies for different potentials. A  $10 \times 10 \times k$ -point grid has been chosen. The theoretical quasiparticle energies of Aryasetiawan [43] have been obtained applying the full potential linear augmented plane wave method (FP-LAPW). The experimental values have been measured by Eberhardt *et al.* [118], if not otherwise quoted.

Method Potential	LDA	$G_0W_0$ Ni	$G_0W_0$ Ni-3p	$G_0W_0$ [43]	Exp.
$\langle \Gamma_{1\uparrow\downarrow} \rangle$	-8.99	-9.63	-9.96	-9.0	-8.8
$\Gamma_{25'\uparrow}$	-2.34	-2.34	-2.41	-1.7	
$\Gamma_{25'\downarrow}$	-1.75	-1.60	-1.66	-1.1	$\langle -1.1 \rangle$
$\Gamma_{12\uparrow}$	-1.18	-1.37	-1.39	-0.9	
$\Gamma_{12\downarrow}$	-0.65	-0.64	-0.65	-0.3	$\langle -0.4 \rangle$
$L_{1\uparrow}$	-4.78	-4.74	-4.91	-4.3	
$L_{1\downarrow}$	-4.43	-4.35	-4.51	-4.0	$\langle -3.6 \rangle$
$L_{3\uparrow}$	-2.33	-2.33	-2.39	-1.9	
$L_{3\downarrow}$	-1.81	-1.64	-1.69	-1.3	$\langle -1.3 \rangle$
$L_{2'\uparrow}$	-0.29	-1.18	-1.22	-1.3	
$L_{2'\downarrow}$	-0.28	-1.17	-1.21	-1.3	$\langle -1.0 \rangle$
$L_{3\uparrow}$	-0.49	-0.76	-0.75		-0.2
$L_{3\downarrow}^*$	0.12	0.17	0.18		0.16
$X_{1\uparrow}$	-4.58	-4.47	-4.62	-4.3	
$X_{1\downarrow}$	-4.26	-4.06	-4.21	-3.9	$\langle -3.3 \rangle$
$X_{3\uparrow}$	-4.11	-3.92	-4.01	-3.5	
$X_{3\downarrow}$	-3.62	-3.33	-3.44	-2.9	$\langle -2.8 \rangle$
$X_{2\uparrow}$	-0.44	-0.75	-0.75	-0.5	-0.24 [117]
$X_{2\downarrow}$	0.10	0.12	0.13	0.2	-0.04 [117]
$X_{5\uparrow}$	-0.33	-0.62	-0.59		-0.11 [117]
$X_{5\downarrow}^*$	0.34	0.35	0.39		0.22 [117]
Exchange splitting					
$L_3$	0.61	0.93	0.94		0.36
$X_2$	0.54	0.87	0.88	0.7	0.20
$\Gamma_{12\uparrow}$	0.52	0.73	0.74	0.6	

most of the states. Therefore the averaged values are given. For all occupied bands, except the  $L_{2'}$  state, LDA predicts too low energies. The error, in some cases, is as large as 1 eV. Applying the  $G_0W_0$  correction does scarcely change the positions of the  $d$ -bands, only the  $L_{2'}$  band moves nearer to experiment and the  $\Gamma_1$  state further away. Additionally, the exchange splitting is enlarged and deviates strongly from experiment. The inclusion of the  $3p$  electrons in the valence, as for Fe, influences mostly the deep lying  $d$ -states ( $L_1$  and  $X_1$ ). The fact that  $G_0W_0$  hardly changes the position of the  $d$ -bands is especially unsatisfactory because early calculations by Aryasetiawan applying the full potential linearized augmented plane-wave method (no pseudopotentials) suggested that  $G_0W_0$  results in an improved description of the  $d$ -band positions. I think that further tests will be necessary to clarify our

results for Ni.

For the ferromagnets Fe and Ni, our  $G_0W_0$  calculations have lead to relatively small changes of the LDA one-particle energies. As the LDA description is rather good for Fe and exhibits large errors in the case of Ni, the same holds for the  $G_0W_0$  results. The inclusion of the  $3p$  states in the valence mainly influences the position of the  $d$ -bands at low energies. We believe that the observed errors in the  $d$ -bands for all four considered materials is a result of the spurious selfinteractions in the GW approximation. This causes an upshift of the  $d$  bands for Cu and Ag (0.6 eV error) and pronounced errors for Ni and Fe, where GW predicts too large band-widths and overestimated the exchange splitting. Only the inclusion of vertex corrections in  $\Sigma$  (i.e.,  $\Sigma = iGWT$ ) would lift this problem, but such calculations are currently not possible.



## Part IV

# Total energies from ACFDT

Although the ACFDT formalism was introduced more than 30 years ago [27, 28, 29], and similar approaches within many-body perturbation theory (see e.g., [19]) are even older, the calculation of (RPA)-ACFDT energies has for a long time been restricted to model systems such as jellium bulk [132] and jellium slabs and surfaces [29, 119, 120]. The reason for this "delay" is the large computational cost to calculate the response function for an arbitrary system. First RPA calculations for molecules have been presented by Furche in 2001 [121]. Other RPA calculations for molecules [122, 123, 124, 125, 126, 127] and solids [128, 129, 130] followed shortly afterwards. Although the RPA (setting  $f_{xc} = 0$ ) accounts for long-range correlation effects such as the van der Waals interaction, molecules have been shown to be standardly too weakly bonded with a mean absolute error similar to the one found for DFT-PBE. Absolute correlation energies, on the other hand, are throughout too large if the RPA is applied (see e.g., Ref. [35] for the homogenous electron gas). An improvement should be expected if an appropriate exchange-correlation kernel is introduced for the calculation of the response function of the interacting system. Such attempts have, so far, been only applied to molecular systems [122, 125, 126] [with the exception of the homogenous electron gas (HEG)]. In all molecular calculations,  $f_{xc}$  was chosen to be independent of the frequency (static - or adiabatic - approximation). An extensive study of atomization energies obtained for exchange-correlation kernels of the form  $f_{xc}(\mathbf{r}, \mathbf{r}') = \delta^2 E_{xc} / \delta n(\mathbf{r}) \delta n(\mathbf{r}')$  derived from different approximations to the exchange-correlation energy (LDA, PBE, BP86, B3LYP, PBE0) has been performed in Ref. [126]. The authors found that improvement over the RPA can only be obtained if the exchange-correlation kernel is non-local (as it is in the case of B3LYP and PBE0). Similar tests for solids have not been performed so far, but calculations for the homogenous electron gas [35] suggest that the non-locality of the  $f_{xc}$  is important also in the case of solids.

As the RPA does not fulfill the homogenous electron gas limit a different route to an improvement was supposed by Kurth and Perdew [131]. They included an additional correction term to the RPA correlation energy,  $\Delta E_c$ , which is introduced in a LDA like way:  $\Delta E_c = E_c^{LDA} - E_c^{LDA-RPA}$ , where  $E_c^{LDA}$  is the standard LDA correlation energy based on the exact correlation energy for the homogenous electron gas and  $E_c^{LDA-RPA}$  an LDA term based on the RPA energy of the homogenous electron gas. This method is referred to as RPA+ and results in the correct correlation energy for the HEG per definition. The computational cost to calculate the correction term is negligible compared to the RPA energy evaluation. Unfortunately, the RPA+ does not provide an improvement over RPA atomization energies [121], although Fuchs *et al.* [122] report that absolute correlation energies are improved. Lattice constants and bulk moduli are almost the same for RPA and RPA+ [130].

In this part of my thesis I will present results obtained within the ACFDT formalism, which has been introduced in chapter 3. Throughout the present work we will make use of the RPA for the evaluation of the density-density response function of the interacting system. In chapter 10, we will discuss technical issues concerning the calculation of the RPA correlation energy in more detail. In chapter 11, RPA energies for molecules (Sec. 11.1), rare gas solids (Sec. 11.2), and extended insulating, semiconducting, and metallic systems (Sec. 11.5) will be discussed. For the extended systems, besides the lattice constants and bulk moduli, also the RPA atomization energies are evaluated. Atomization energies of extended systems have, to the best of our knowledge, not been performed before. This is connected to the difficulty to evaluate atomic energies within a plane wave basis code.

## Chapter 10

# Implementation of the ACFDT routines

The total RPA energy is given as a sum of the Hartree-Fock energy evaluated for the KS-DFT wavefunctions (in the following simply referred to as HF energy), and the RPA correlation energy [see Eq. (3.36)]:

$$E = T_s[\{\psi^{KS}\}] + E_H[n] + E_x[\{\psi^{KS}\}] + E_c^{RPA}[\{\psi^{KS}, \epsilon^{KS}\}] = E_{HF}[\{\psi^{KS}\}] + E_c^{RPA}.$$

As we will use the RPA throughout this work, we disregard the index *RPA* and abbreviate the RPA correlation energy as  $E_c$ . The RPA correlation energy  $E_c$  is obtained by evaluating Eq. (3.35):

$$E_c = \int_0^\infty \frac{d\omega}{2\pi} \sum_{\mathbf{q} \in BZ} \sum_{\mathbf{G}} \left\{ (\ln[1 - \chi^{KS}(\mathbf{q}, i\omega)] \nu(\mathbf{q}))_{\mathbf{G}, \mathbf{G}} + \nu_{\mathbf{G}, \mathbf{G}}(\mathbf{q}) \chi_{\mathbf{G}, \mathbf{G}}^{KS}(\mathbf{q}, i\omega) \right\}.$$

Three steps are required for the calculation of the total RPA energy:

(i) Hartree-Fock energy: The Hartree-Fock energy  $E_{HF}$  is evaluated for the KS wavefunctions determined in a DFT calculation. A high energy cutoff  $E_{\text{cut}}$  and dense  $k$ -point grids are required for accurate Hartree-Fock energies. Therefore, the settings for the Hartree-Fock calculation might differ from the respective values applied in the evaluation of the RPA correlation energy.

(ii) Pre-run for RPA correlation energy: For the evaluation of the RPA correlation energy, the KS-DFT wavefunctions and eigenenergies of a large number of unoccupied states are required. In this pre-run, all  $N_{PW}$  (number of plane wave) solutions of the KS eigenvalue problem are evaluated by an exact diagonalization of the  $N_{PW} \times N_{PW}$  Hamilton matrix  $H_{\mathbf{G}, \mathbf{G}'}$ . The number of plane waves is related to the energy cutoff  $E_{\text{cut}}$  by the constraint  $|\mathbf{G} + \mathbf{k}|^2/2 < E_{\text{cut}}$ . For a fixed energy cutoff  $E_{\text{cut}}$ , the number of plane waves  $N_{PW}$  is proportional to the volume of the real space cell  $V$ , so that this step can become demanding for large volumes  $V$ . The importance of unoccupied bands also requires special care for the construction of the PAW potentials. For the calculation of the RPA correlation energies so called *GW* potentials have been constructed that describe scattering properties very accurately up

to  $\approx 10$  Ry. Furthermore, a  $d$ -projector has been introduced for the third row elements, and a  $f$ -projector for Ag. These states, while unoccupied, are not too high in energy and therefore contribute to the response function  $\chi^{KS}$ .

(iii) RPA correlation energy: The response function  $\chi_{\mathbf{G},\mathbf{G}'}^{KS}(\mathbf{q}, i\omega)$  is calculated from the wavefunctions and eigenenergies evaluated in the previous step and the RPA correlation energy is determined via Eq. (3.35). Some details concerning the evaluation of this expression have already been discussed in Sec. 3.3. What remains to be analyzed is the dependence of the RPA correlation energy on the rank of the response function  $\chi_{\mathbf{G},\mathbf{G}'}^{KS}$ . The sum over reciprocal lattice vectors in Eq. (3.35) has to be truncated at some maximal vector  $\mathbf{G}_{\text{cut}}$ , which is determined by the relation  $|\mathbf{G} + \mathbf{q}|^2/2 < E_{\text{cut}}^\chi$ . The dependence of the correlation energy on the energy cutoff  $E_{\text{cut}}^\chi$  will be discussed in Sec. 10.1. Besides the summation over reciprocal lattice vectors, the evaluation of the correlation energy requires an integration along the frequency axis. In Sec. 10.2 different frequency integration schemes will be discussed and convergence tests with respect to the number of frequency points will be presented. Sec. 10.3 deals with the calculation of RPA correlation energies for metals. For metals the long-wavelength ( $\mathbf{q} = 0$ ) response function  $\chi$  (or more precisely  $\nu\chi$ ) also contains contributions arising from intraband transitions. In Sec. 10.3 several ways will be considered, how to include the intraband term for the evaluation of the correlation energy.

## 10.1 Dependence on dimension of the response function

For the calculation of the RPA correlation energy, the dependence on the rank of the response function or the energy cutoff  $E_{\text{cut}}^\chi$ , respectively, is among the most critical issues. The energy cutoff  $E_{\text{cut}}^\chi$  determines at which point the sum over reciprocal lattice vectors in Eq. (3.35) is truncated, and the convergence of the correlation energy with the maximal considered lattice vector turns out to be very slow. This slow convergence is not unique to plane wave basis set codes. If the RPA correlation energy is calculated using a local basis set the highest angular momentum quantum number in the atomic basis set determines the convergence of the correlation energy (see Furche [121]).

The calculation of the fully converged correlation energy is not possible, because an increase in  $E_{\text{cut}}^\chi$  implies that also the energy cutoff for the plane wave expansion,  $E_{\text{cut}}$ , and the number of bands have to be increased. As a consequence, such calculations will become intractable. On the other hand, if an analytic dependence of the correlation energy on  $E_{\text{cut}}^\chi$  were known, it would be enough to evaluate the correlation energy for smaller values of  $E_{\text{cut}}^\chi$  and extrapolate the correlation energies according to this dependence. In the following, we will derive the  $E_{\text{cut}}^\chi$  dependence of the RPA correlation energy for the homogenous electron gas (HEG). Under the assumption that the "correlation error" introduced by the neglect of high energy components in the response function behaves similar for the homogenous electron gas and an inhomogeneous system, the determined  $E_{\text{cut}}^\chi$  dependence can also be applied to any other material.

The correlation energy for the HEG, as for any other system, can be evaluated from the difference between the interacting and the independent-particle response function [see Eq. (3.24)], which are coupled by the Dyson equation [Eq. (3.29) if the RPA is applied]. With the independent-particle response function of the HEG, the Lindhard function  $\chi^{\text{Lind}}$ ,



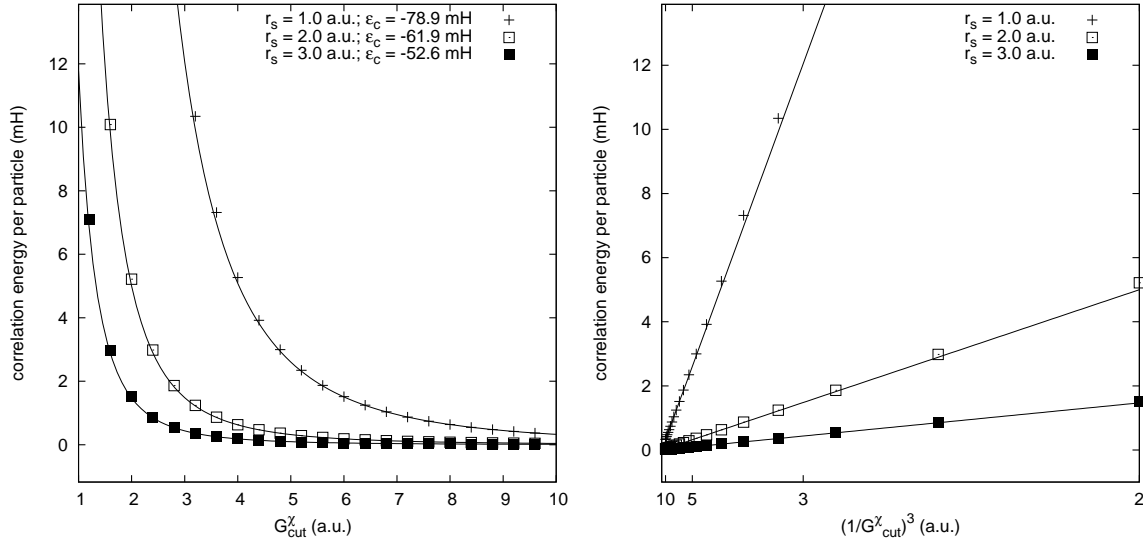


Figure 10.1: Dependence of the HEG RPA correlation energy  $\epsilon_c(q)$  on the maximal  $q$  value,  $G_{\text{cut}}^\chi$ , up to which the  $q$  integration is performed. For sufficiently large values of  $G_{\text{cut}}^\chi$ , the error introduced by truncating the  $q$  integration behaves like  $1/(G_{\text{cut}}^\chi)^3$  (solid lines). Presented are energies with respect to the extrapolated value  $\epsilon_c^\infty$  which is reached for  $G_{\text{cut}}^\chi \rightarrow \infty$ .

the RPA correlation energy per particle can be expressed as:

$$\epsilon_c = -\frac{1}{4\pi^3 n} \int_0^\infty dq q^2 \int_0^1 d\lambda \int_0^\infty d\omega \nu(q) \frac{[\chi^{\text{Lind}}(q, i\omega)]^2 \lambda \nu(q)}{1 - \lambda \nu(q) \chi^{\text{Lind}}(q, i\omega)}, \quad (10.1)$$

with the Coulomb kernel  $\nu(q) = 4\pi/q^2$ . The Lindhard function is given by [132]:

$$\begin{aligned} \chi^{\text{Lind}}(q, i\omega) = & \\ = \frac{k_F}{2\pi^2} \left\{ \frac{Q^2 - u^2 - 1}{4Q} \ln \frac{u^2 + (Q+1)^2}{u^2 + (Q-1)^2} - 1 + u \arctan \frac{1+Q}{u} + u \arctan \frac{1-Q}{u} \right\} \end{aligned} \quad (10.2)$$

with

$$Q = \frac{q}{2k_F} \quad u = \frac{w}{qk_F} \quad k_F^3 = 3\pi^2 n.$$

In practice, the integration over  $q$  has to be truncated at some value  $G_{\text{cut}}^\chi$ . We estimate the error introduced by this truncation by calculating

$$\epsilon_c(G_{\text{cut}}^\chi) = -\frac{1}{4\pi^3 n} \int_0^{G_{\text{cut}}^\chi} dq q^2 \int_0^1 d\lambda \int_0^\infty d\omega \nu(q) \frac{[\chi^{\text{Lind}}(q, i\omega)]^2 \lambda \nu(q)}{1 - \chi^{\text{Lind}}(q, i\omega) \lambda \nu(q)}. \quad (10.3)$$

for values of  $G_{\text{cut}}^\chi$  ranging from 1 to 10 a.u. Additionally, we evaluate  $\epsilon_c(G_{\text{cut}}^\chi)$  for different densities or Wigner Seitz radii  $r_s = (3/4\pi n)^{1/3}$  of the HEG, respectively. The frequency integration was performed by applying a Gauss-Legendre integration with 36 supporting points and assuming an exponential decay with respect to the frequency. The maximal

frequency was chosen to be 20 a.u. For the  $q$  integration an equidistant grid was used and the distance between two  $q$  points fixed to  $10^{-3}$ . Such a dense grid is only required to reproduce the correct integration for small  $q$  points, which is in principle not important when investigating the dependence on  $G_{\text{cut}}^\chi$ , but we additionally want to evaluate the absolute correlation energies  $\epsilon_c(r_s)$  and compare them to published data. The integration over  $\lambda$  was performed on a grid with 200 points.

For all considered densities we find the following dependence for the correlation energy

$$\epsilon_c(G_{\text{cut}}^\chi) = \epsilon_c^\infty + \frac{A}{(G_{\text{cut}}^\chi)^3} = \epsilon_c^\infty + \frac{A'}{(E_{\text{cut}}^\chi)^{3/2}}, \quad (10.4)$$

for sufficiently large values of  $G_{\text{cut}}^\chi$ . The higher the density of the HEG, the larger the energy from which on Eq. (10.4) holds. In the VASP calculation, not  $|\mathbf{G}_{\text{cut}}^\chi|$ , but the energy cutoff  $E_{\text{cut}}^\chi$  is specified, which determines  $|\mathbf{G}_{\text{cut}}^\chi|$  via  $|\mathbf{G}_{\text{cut}}^\chi + \mathbf{q}|^2/2 < E_{\text{cut}}^\chi$ .

In Fig. 10.1, the errors in the correlation energies  $\epsilon_c(G_{\text{cut}}^\chi) - \epsilon_c^\infty$  for three different densities  $r_s = 1.0, 2.0$ , and  $3.0$  a.u. are shown. The value  $\epsilon_c^\infty$  is evaluated by applying Eq. (10.4) and the fits are plotted using solid lines. The HEG RPA correlation energies  $\epsilon_c^\infty$  obtained by extrapolation are  $-78.9$ ,  $-61.9$ , and  $-52.6$  mH for  $r_s = 1.0, 2.0$ , and  $3.0$  a.u., respectively. The corresponding values calculated by von Barth and Hedin [132] are  $-78.7$  mH,  $-61.7$  mH, and  $-52.7$  mH. Differences between our correlation energies and the one evaluated in [132] probably stem from the region of small  $q$  values, where we have not tried to achieve perfectly converged values.

To this point, we have found that the correlation energy of the HEG exhibits a  $1/(E_{\text{cut}}^\chi)^{3/2}$  dependence. In the next paragraph we will take a closer look at the  $E_{\text{cut}}^\chi$  dependence of the total and the relative correlation energies for realistic systems. For the  $\text{H}_2$ ,  $\text{N}_2$ , and  $\text{O}_2$  molecules which will be discussed in detail in section 11.1, we find that the  $1/(E_{\text{cut}}^\chi)^{3/2}$  behavior is well reproduced, both for absolute and relative correlation energies. Also for the rare gas solids which will be the topic of section 11.2, the correlation energy nicely follows a  $1/(E_{\text{cut}}^\chi)^{3/2}$  dependence.

In section 11.5, lattice constants, bulk moduli, and atomization energies evaluated for representative bulk systems will be presented. For many of the considered systems as e.g., SiC, Na, Al, ..., the  $1/(E_{\text{cut}}^\chi)^{3/2}$  behavior is given already for the total bulk correlation energies. This is not the case, if the correlation energy is calculated applying potentials for which electrons from deeper lying shells are treated as valence. Such potentials have been generated for Mg (used for MgO), Na (NaCl, NaF), Li (LiF), and Si (Si). The fact that we do not observe the HEG behavior for the energies  $E_{\text{cut}}^\chi$  considered for these materials, does not imply that it cannot be reached for higher energies. As we have seen in Fig. 10.1 for the HEG, the  $q$ -value from which on the correlation energy follows the  $1/q^3$  behavior depends on the density. If we e.g., calculate the correlation energy for Si bulk using a potential including 2s2p3s3p electrons in the valence ( $\text{Si}_2$  potential) the density increases from 4 electrons/atom in the standard 3s3p ( $\text{Si}_1$ ) potential to 12 electrons/atom. Besides the fact, that the  $1/(E_{\text{cut}}^\chi)^{3/2}$  dependence is not exactly fulfilled if deeper lying electronic states are treated as valence, the difference between the correlation energy at the largest considered  $E_{\text{cut}}^\chi$  and the extrapolated value is significantly larger than for the standard potentials. But if the correlation contribution to the atomization energies, namely the difference between the bulk correlation energy and the atomic correlation energy is considered, the dependence on

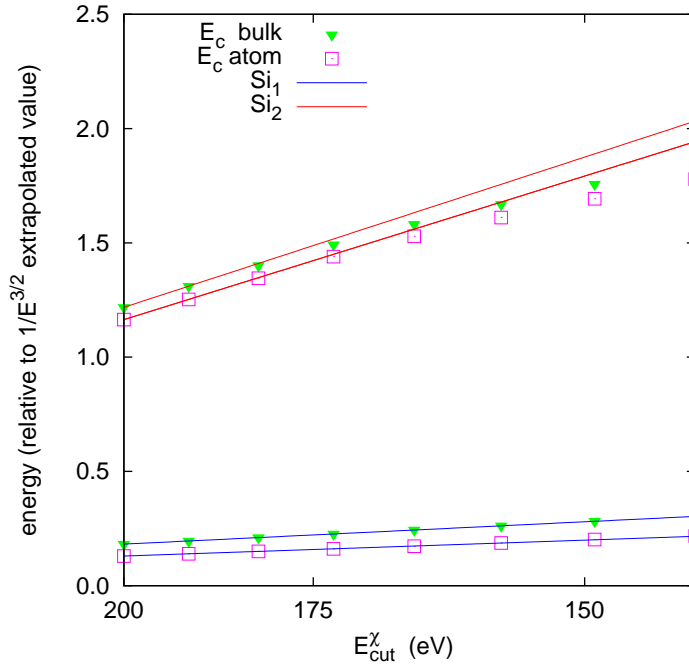


Figure 10.2: Dependence of the correlation energy on the energy cutoff  $E_{\text{cut}}^x$  for Si. The correlation energy (plotted versus  $1/(E_{\text{cut}}^x)^{3/2}$ ) for the bulk (green triangles) and the atom (pink squares) is presented. Two different Si potentials were considered: fits for the  $\text{Si}_2$  potential (2s2p3s3p electrons) are shown in red, fits for the standard,  $\text{Si}_1$ , potential (3s3p electron) are blue.

$E_{\text{cut}}^x$  becomes (i) weaker, because the dependence for atom and bulk cancel to a large degree (ii) and the  $1/(E_{\text{cut}}^x)^{3/2}$  dependence is almost recovered.

As an example we will discuss the Si correlation energies obtained from the  $\text{Si}_1$  (3s3p electrons as valence) and the  $\text{Si}_2$  (2s2p3s3p electrons) potential. In Fig. 10.2 the correlation energies of bulk Si (green triangles) and of the Si atom (pink squares) are plotted versus the energy cutoff  $E_{\text{cut}}^x$ . A  $1/(E_{\text{cut}}^x)^{3/2}$  scale is chosen, and consequently the relation given in Eq. (3.46) and Eq. (10.4) is fulfilled, if the correlation energies for different  $E_{\text{cut}}^x$  lie all on one straight line. The largest value of  $E_{\text{cut}}^x$  is 200 eV and the  $1/(E_{\text{cut}}^x)^{3/2}$  fit is only performed for the largest two values of the energy cutoff in order to best visualize the deviation from the correct behavior. The red lines represent the fits for the  $\text{Si}_2$  correlation energies, the blue lines for the  $\text{Si}_1$  correlation energies. All energies are plotted with respect to  $E_c^\infty$  obtained from these fits. Two main differences can be observed for the correlation energies of the  $\text{Si}_1$  and the  $\text{Si}_2$  potentials. First, the  $\text{Si}_2$  correlation energies, both for the bulk and the atom, show a much stronger dependence on the energy cutoff  $E_{\text{cut}}^x$  than the  $\text{Si}_1$  energies. Second, the  $1/(E_{\text{cut}}^x)^{3/2}$  dependence is perfectly fulfilled, if the  $\text{Si}_1$  potential is applied, but not if the  $\text{Si}_2$  potential is used. But, we find that the difference  $\Delta E_c = [E_c(\text{bulk}) - E_c(\text{atom})]$  converges significantly faster and does not deviate from the  $1/(E_{\text{cut}}^x)^{3/2}$  behavior. We have calculated the bulk and atomic correlation energies for different energy cutoffs. Because the  $1/(E_{\text{cut}}^x)^{3/2}$  behavior is not fulfilled for the  $\text{Si}_2$  correlation energies of the bulk and the atom, the extrapolated correlation energies depend on the extrapolation range. For the bulk

correlation energy we find an extrapolated correlation energy of  $-17.437$  eV for the  $E_{\text{cut}}^{\chi}$  range  $[140,200]$  eV,  $-19.016$  eV for  $[215,300]$  eV, and  $-19.386$  eV for  $[250,350]$  eV. But because the extrapolated correlation energies of both the bulk and the atom show a very similar dependence on the extrapolation range, the difference  $\Delta E_c$  is  $-1.522$  eV for  $[140,200]$  eV,  $-1.509$  eV for  $[215,300]$  eV, and  $-1.508$  eV  $[250,350]$  eV, and it is therefore possible to obtain well converged atomization energies even if the individual contributions to the energy are not completely converged.

For the lattice constant and bulk moduli determined in section 11.5, we find that values with and without  $1/(E_{\text{cut}}^{\chi})^{3/2}$  extrapolation can differ significantly (by up to 1.5% in the volume), whereas the dependence on the specific interpolation range is small, also for systems where the  $1/(E_{\text{cut}}^{\chi})^{3/2}$  dependence is not strictly fulfilled.

In the latest VASP version the correlation energy is standardly evaluated for 8 cutoff energies  $E_{\text{cut}}^{\chi}$  starting with the value of ENCUTGW set in the INCAR file and decreasing in steps of 5 % of ENCUTGW. The extrapolated correlation energy is written to the OUTCAR file together with the correlation energies at the single values of  $E_{\text{cut}}^{\chi}$ .

## 10.2 Frequency integration

We calculate the correlation energy from the linear response function at imaginary frequencies. The response function  $\chi(i\omega)$  is a smooth function of the frequency and the frequency integration therefore does not constitute a fundamental problem. As the number of frequency points enters the computational time linearly, an optimal choice for the frequency grid is nevertheless desirable.

All integration schemes presented in the following are based on a Gauss-Legendre integration. The weights and supporting points for a Gauss-Legendre integration in the interval  $[0,1]$  are tabulated in VASP for up to 64 supporting points. According to the Gauss-Legendre integration scheme, the integral of a polynomial of degree  $2N - 1$  is exactly determined by a  $N$ -point sum

$$\int_0^1 f(x) dx = \sum_i^N w_i f(x_i), \quad (10.5)$$

where  $w_i$  and  $x_i$  are the Gauss-Legendre weights and supporting points, respectively. For the frequency integration as present in the evaluation of the correlation energy, an integral of the type

$$E_c = \int_0^\infty g(\omega) d\omega \quad (10.6)$$

has to be calculated. The integrand  $g(\omega) = \ln(1 - \nu\chi) + \nu\chi$  exhibits an exponential decay over a wide range of frequencies<sup>1</sup>. In order to make use of Eq. (10.5), a weighting function

---

<sup>1</sup>If only one single transition contributes to the response function  $\chi(i\omega)$ , the frequency dependence of the response function is proportional to  $\Delta\epsilon/(\Delta\epsilon^2 + \omega^2)$ ,  $\Delta\epsilon$  being the energy difference between the contributing states [consider Eq. (2.35) for imaginary frequencies]. For large frequencies, the correlation energy thus decays  $\propto 1/\omega^4$ . Nevertheless, fast convergence is found by assuming an exponential decay.

$v(\omega)$  is introduced in Eq. (10.6), which exhibits a similar energy dependence as  $g(\omega)$ :

$$\int_0^\infty g(\omega) d\omega = \int_0^\infty \left[ \frac{g(\omega)}{v(\omega)} \right] v(\omega) d\omega. \quad (10.7)$$

In order to rewrite the integral in Eq. (10.7) into an integral of the form given in Eq. (10.5), we perform the following transformation of variables:

$$dx = v(\omega) d\omega \quad \rightarrow \quad x = \int_0^\omega v(\omega') d\omega' + c. \quad (10.8)$$

The constant  $c$  is thereby chosen as to obtain an integration interval  $[0,1]$  for an integration over  $x$ . Eq. (10.7) can then be written as

$$\int_0^1 \left[ \frac{g(\omega(x))}{v(\omega(x))} \right] dx \stackrel{(10.8)}{=} \int_0^1 g(\omega(x)) \left[ \frac{d\omega}{dx} \right] dx \stackrel{(10.5)}{=} \sum_i^N w_i g(\omega(x_i)) \left[ \frac{d\omega}{dx} \right] (x_i). \quad (10.9)$$

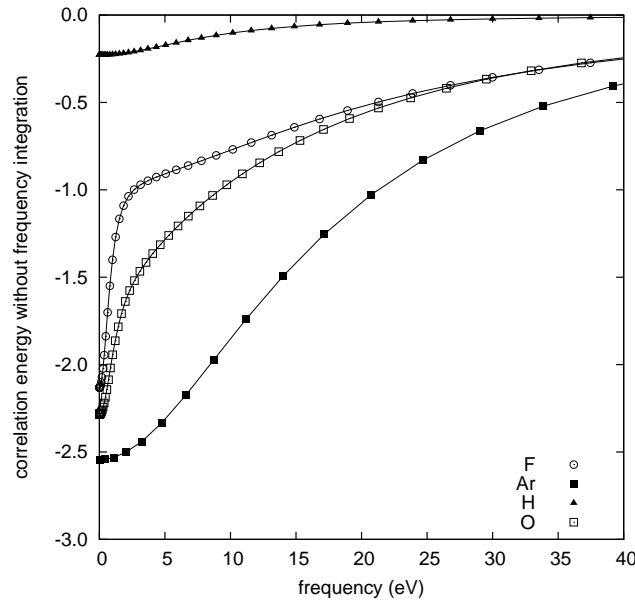


Figure 10.3: Correlation contribution before applying the frequency integration (arbitrary scale). Shown are the results for the H, O, F, and Ar atom. The smaller the fundamental gap of the system, the more structure in the small energy range is observed.

For the ACFDT frequency integration, several integration schemes have been implemented, which differ in the chosen weighting functions  $v(\omega)$ . These schemes can be addressed by setting OMEGAGRID in the INCAR file. Possible values are OMEGAGRID = 4, 40, 41, and 44. Additionally, the number of supporting points (NOMEGA) and the value of the maximal frequency  $\omega_{\max}$  (OMEGATL in eV) have to be specified. The basic (but not standard) integration routine is called by setting OMEGAGRID = 41 and determines frequency

Table 10.1: Lattice constant  $a_0$ , bulk modulus  $B_0$ , and energy error  $\Delta E_0$  of bulk Si as obtained for a different number of frequency points and for different integration schemes. For the method OMEGAGRID = 40, two different values for the smallest frequency point are presented.

NOMEGA	OMEGAGRID	SIGMA	$a_0$ (Å)	$B_0$ (GPa)	$\Delta E_0$ (meV)
8	41		5.438	99.4	-233
12	41		5.437	93.0	-19
16	41		5.433	94.2	1
8	44		5.433	94.4	-2
12	44		5.433	94.5	-1
16	44		5.433	94.5	0
8	40	0.2	5.437	93.6	-10
12	40	0.2	5.433	94.5	0
16	40	0.2	5.433	94.5	0
8	40	0.05	5.438	92.7	8
12	40	0.05	5.433	94.6	0
16	40	0.05	5.433	94.5	0

points by using an exponential weighting function, so that

$$\begin{aligned}
 v(\omega) &= \alpha e^{-\alpha\omega} \\
 x(\omega) &= 1 - e^{-\alpha\omega} \\
 \omega(x) &= -\frac{1}{\alpha} \ln(1-x) \\
 \frac{d\omega}{dx} &= \frac{1}{\alpha} \frac{1}{1-x}.
 \end{aligned} \tag{10.10}$$

For 12 frequency points, which is the standard choice for the number of frequency points in the present work, this integration scheme provides well converged correlation energies, if the band gaps are not too small. For small gap systems or metals, the resulting number of small frequency supporting points might not be enough. In order to illustrate this,  $g(\omega)$  is shown for several atoms in Fig. 10.3. Whereas the integrand exhibits not much structure for small frequencies in the case of the H and the Ar atom, a strong increase of  $|g(\omega)|$  at small frequencies is observed for the F and O atom. The extra small frequency structure for the F and O atom is related to excitations between states with small energy differences. A coarse frequency grid for small energies neglects these contributions altogether. Therefore an integration scheme that provides a higher frequency density at small frequencies has been introduced. It is called by setting OMEGAGRID = 44 and is defined as

$$\begin{aligned}
 v(\omega) &= \frac{\alpha}{B} \omega^{(1/B-1)} e^{-\alpha\omega^{1/B}} \\
 x(\omega) &= 1 - e^{-\alpha\omega^{1/B}} \\
 \omega(x) &= \frac{1}{\alpha} [-\ln(1-x)]^B \\
 \frac{d\omega}{dx} &= \frac{B}{\alpha} [-\ln(1-x)]^{(B-1)} \frac{1}{1-x}.
 \end{aligned} \tag{10.11}$$

Finally, a third kind of integration scheme was introduced, which guarantees a denser frequency grid at smaller frequencies than provided by OMEGAGRID = 41, but yields a similar behavior for large frequencies. By choosing OMEGAGRID = 4 or 40, the frequency points are determined according to

$$\omega(x) = -\frac{1}{\alpha} \ln [(1-b)(1-x) + b(1-x)^2] \quad (10.12)$$

$$\frac{d\omega}{dx} = \frac{1}{\alpha} \frac{(1-b) + 2b(1-x)}{(1-b)(1-x) + b(1-x)^2}. \quad (10.13)$$

This integration scheme occurs in two flavors. For OMEGAGRID = 4, which is the standard setting for ACFDT calculations, a fixed value is chosen for  $b$ , for OMEGAGRID = 40, the smallest frequency is set to the value of SIGMA provided in the INCAR file<sup>2</sup>. Numerous tests have confirmed that OMEGAGRID = 4 or OMEGAGRID = 40 provide a very good compromise between the number of frequency points and the accuracy of the frequency integration.

One of the systems for which the convergence with the number of frequency points is especially slow is bulk Si. In table 10.1 the Si equilibrium lattice constant  $a_0$ , the bulk modulus  $B_0$ , and the energy error  $\Delta E_0$  obtained from different integration schemes and different number of frequency points are summarized. A  $4 \times 4 \times 4$  k-point grid has been used. For all, but the simple exponential Gauss-Legendre integration (OMEGAGRID = 41), 12 frequency points provide well converged lattice constants, bulk moduli and total energies.

### 10.3 k-point convergence and $\Gamma$ -point correction for metals

Although metals do not represent a fundamental problem for (RPA-)ACFDT calculations, they require more attention with respect to the  $k$ -point convergence than semiconductors and insulators. In fact, already the sampling of the metallic Fermi surface in standard DFT calculations requires a denser  $k$ -point grid. Here the  $k$ -point grid affects the precision in two ways, first because  $\chi(\mathbf{q})$  is only evaluated using a finite set of  $k$ -points, second because  $\chi(\mathbf{q})$  is only summed over a finite grid of  $q$ -points. These two grids, the  $k$ -point grid used in the calculation of  $\chi(\mathbf{q})$  and the  $q$ -point grid used in the final evaluation of the correlation energy, are independent from each other, but they will be chosen identical throughout this work. A second difficulty arises for metals from the existence of intraband transitions within one partially-filled band crossing the Fermi level. These contributions to  $\chi(\mathbf{q})\nu(\mathbf{q})$  are routinely calculated for  $q \neq 0$ , but for the long-wavelength limit  $q \rightarrow 0$ , a direct evaluation of these terms leads to an indefinite expression (see Sec. 2.8). This indefiniteness in the long-wavelength intraband term of  $\nu\chi$  can however be lifted and the intraband contributions (or Drude term) can be expressed via the plasma frequency  $\bar{\omega}$  [see Eq. (2.106)]. In the following, we will discuss the influence of the Drude term on the correlation energy for the example of the homogenous electron gas (HEG) and present different ways how to include the intraband long-wavelength contribution.

---

<sup>2</sup>If ISMEAR is set  $\geq 0$  in the INCAR, the one-electron levels are broadened or smeared. The parameter SIGMA controls the width of the broadening function. It is reasonable to expect that the user will chose values corresponding roughly to the smallest excitation energies in the system under consideration.

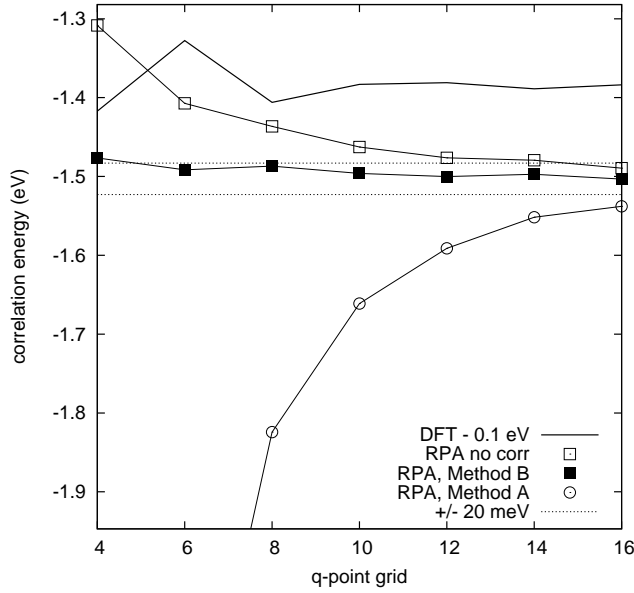


Figure 10.4: Correlation energy (eV) of the homogenous electron gas at a density  $r_s = 2.5$  a.u. Empty squares denote the energy without including the Drude term. Circles represent energies obtained when incorporating the Drude term as defined in Method A, and filled squares are values obtained from applying Method B.

In the first approximation, we do not include the Drude term in the description of the response function at all. The response function, therefore, lacks contributions at the  $\Gamma$  point that arise from the long-wavelength intraband transitions. Consequently, the absolute correlation energy is expected to be too small. The error introduced by the neglect of the long-wavelength intraband contributions (or Drude contributions) depends on the number of  $q$ -points, because the relative weight of the  $\Gamma$  point to the Brillouin zone sum becomes negligible for a sufficiently dense  $q$ -point grid. But a very dense  $q$ -point grid is not a feasible option, if one considers the large computational costs for the ACFDT correlation energies, so that the correct (or approximated) inclusion of the long-wavelength intraband, or Drude term, is highly desirable. In Fig. 10.4 the  $q$ -(and  $k$ -point) dependence of the HEG correlation energy is shown for different methods applied for the inclusion of the Drude contribution. The correlation energy without considering the Drude term at all is shown using empty squares. The DFT energies (solid line) are also given for comparison. As expected, the absolute correlation energy increases for a larger number of  $k$ -points, because the error introduced by the neglect of the Drude term at the  $\Gamma$  point is of less consequence if a denser  $k$ -point grid is applied for the Brillouin zone integration.

In the following, we will consider two different methods to include the Drude term in or after the calculation of the RPA-ACFDT correlation energy. In the first approach (referred to as Method A), the expression  $\chi(\mathbf{q})\nu(\mathbf{q})$  is directly complemented by the Drude term

$$\chi_{\mathbf{G},\mathbf{G}'}^{KS}(\mathbf{q},i\omega)\nu_{\mathbf{G},\mathbf{G}'}(\mathbf{q}) \rightarrow \chi_{\mathbf{G},\mathbf{G}'}^{KS}(\mathbf{q},i\omega)\nu_{\mathbf{G},\mathbf{G}'}(\mathbf{q}) + \frac{\bar{\omega}_{\alpha\beta}^2}{\omega^2} \delta_{\mathbf{G},\mathbf{G}'}\delta(\mathbf{q}) =: \bar{\epsilon}^{\Gamma}(\mathbf{q},i\omega), \quad (10.14)$$



where the plasma frequency tensor is given by Eq. (2.106). If we performed a  $\mathbf{q}$ -integration over the Brillouin zone, Eq. (10.14) would result in an exact expression for the correlation energy. But as we approximate the Brillouin zone integration as a sum over discrete  $q$ -points and since we consequently replace the integral over the  $\Gamma$ -centered volume  $V(\Gamma)$  by the integrand evaluated at the  $\Gamma$ -point times  $V(\Gamma)$ , i.e.,

$$\frac{V}{(2\pi)^3} \int_{V(\Gamma)} d^3q \{ \ln [1 - \bar{\varepsilon}^\Gamma(\mathbf{q}, i\omega)] + \bar{\varepsilon}^\Gamma(\mathbf{q}, i\omega) \} \rightarrow \frac{V}{(2\pi)^3} V(\Gamma) \{ \ln [1 - \bar{\varepsilon}^\Gamma(0, i\omega)] + \bar{\varepsilon}^\Gamma(0, i\omega) \}, \quad (10.15)$$

method A strongly overestimates the contribution caused by the Drude term. The absolute correlation energies evaluated applying method A will therefore be too large, especially for a coarse  $q$ -point grid which results in large volumes  $V(\Gamma)$ . This can be also seen from Fig. 10.4, where correlation energies obtained from Method A are given by empty circles.

A second, denser  $q'$ -point grid could be introduced around the  $\Gamma$  point in order to allow a better numerical integration for small values of  $q$ . But this would still require an increased number of  $\chi_{\mathbf{G}, \mathbf{G}'}^{KS}(\mathbf{q}, i\omega) \nu_{\mathbf{G}, \mathbf{G}'}(\mathbf{q})$  evaluations. We proceed along this line, but replace the KS response function  $\chi^{KS}$  of the considered system by the independent-particle response function of the HEG, the Lindhard function  $\chi^{\text{Lind}}(\mathbf{q})$  [see Eq. (10.2)]. The density of the HEG,  $n^*$ , is thereby chosen as to obey the free electron relation for the plasma frequency calculated for the respective system (Method B):

$$\bar{\omega}^2 = \frac{4\pi e^2 n^* \hbar^2}{m}. \quad (10.16)$$

For metals with high, cubic symmetry, this is well defined since  $\bar{\omega} := \bar{\omega}_{xx} = \bar{\omega}_{yy} = \bar{\omega}_{zz}$ . For low symmetry systems, one could consider the density corresponding to  $\bar{\omega}^2 = \text{Tr}[\bar{\omega}_{\alpha,\beta}^2]/3$ . The evaluation of the respective correlation correction  $E_c^\Gamma$

$$E_c^\Gamma = \frac{V}{(2\pi)^3} \int_{V(\Gamma)} d^3q \int_0^\infty d\omega \left\{ \ln [1 - \chi^{\text{Lind}}(\mathbf{q}, i\omega; \bar{\omega}) \nu(\mathbf{q})] + \chi^{\text{Lind}}(\mathbf{q}, i\omega; \bar{\omega}) \nu(\mathbf{q}) \right\} \quad (10.17)$$

can be performed numerically and independently of the actual RPA calculations. The correction calculated from Eq. (10.17) is then simply added to the RPA correlation energy obtained without inclusion of the Drude term. More technical details about the integration of Eq. (10.17) will be discussed in the next subsection. In Fig. 10.4 the correlation energies calculated from Method B are shown using black squares. The convergence with respect to the number of  $q$ -points is now significantly improved compared to the correlation energies without considering the Drude term (empty squares).

### 10.3.1 $\Gamma$ -point corrections: Technical details

The  $\Gamma$ -point correction  $E_c^\Gamma$  is evaluated by summing over

$$E_c^\Gamma(\mathbf{q}_i) := \int_0^\infty d\omega \left\{ \ln [1 - \chi^{\text{Lind}}(\mathbf{q}_i, i\omega; \bar{\omega}) \nu(\mathbf{q}_i)] + \chi^{\text{Lind}}(\mathbf{q}_i, i\omega; \bar{\omega}) \nu(\mathbf{q}_i) \right\} \quad (10.18)$$

Table 10.2: Tests for different frequency integration schemes at a fixed  $q'$  value of  $0.005 \text{ \AA}^{-1}$ . OMEGAGRID = 4 refers to a Gauss-Legendre integration, which is exact for an exponential decaying function; OMEGAGRID = 40 introduces a denser grid for smaller frequencies and allows to chose a minimal frequency  $\omega_{\min}$  (see Sec. 10.2).

	T1	T2	T3	T4	T5
OMEGAGRID	4	4	40	40	40
nr. of $\omega$	64	24	24	24	48
$\omega_{\min}$	-	-	0.03	0.003	0.003
$\omega_{\max}$					
80	-16.12103	-15.78955	-16.16447	-16.12142	-16.12102
200	-16.12010	-11.29112	-16.16799	-16.11489	-16.12103
400	-16.18106	-6.59418	-16.17142	-16.10677	-16.12103
800	-15.59202	-3.41346	-16.17724	-16.31622	-16.12101

for a set of  $q'$ -points. The  $q'$ -point grid for the numerical integration is chosen to be a Monkhorst-Pack grid centered around the  $\Gamma$  point and is constrained to the volume around the  $\Gamma$  point,  $V(\Gamma)$ . To select the  $q'$ -points a minimum image convention or Wigner-Seitz like construction is used so that the points  $\mathbf{q}'$  are always closer to  $\Gamma$  than to any other  $q$ -point used to sample the Brillouin zone. In this section, tests concerning the frequency integration from  $\omega = 0$  to  $\omega = \infty$  are presented. Furthermore, the convergence with the number of  $q'$  points is analyzed.

For the calculation of  $E_c^\Gamma$ , Eq. (10.18) has to be evaluated for small  $q'$  values. But  $\chi^{\text{Lind}}(\mathbf{q}', i\omega; \bar{\omega}) \nu(\mathbf{q}')$  is numerical unstable for small values of  $q'$  (especially for large frequencies). Small values of  $q'$  can either occur if the number of  $q'$  points in  $V(\Gamma)$  is large and/or a sizable real-space cell and consequently a small  $\Gamma$ -point volume  $V(\Gamma)$  is present. The instability is due to the term

$$(Q^2 - u^2 - 1) \ln \frac{u^2 + (Q + 1)^2}{u^2 + (Q - 1)^2} \quad (10.19)$$

in the Lindhard function [Eq. (10.2)], because the  $\ln$  term approaches 0 for large  $\omega$  and small  $q'$  and at the same time the term in front of the  $\ln$  diverges. This instability becomes significant for  $q' < 0.005 \text{ \AA}^{-1}$ . We therefore expand this term for small values of  $q'$  and replace Eq. (10.19) by

$$\frac{4Q(Q^2 - u^2 - 1)}{u^2 + 1 + Q^2}. \quad (10.20)$$

Next we test different frequency integration schemes (see section 10.2), number of frequency points, and maximal and minimal frequencies  $\omega_{\max}$  and  $\omega_{\min}$ . The tests are performed for  $q' = 0.005 \text{ \AA}^{-1}$  because the frequency integration is most demanding for small  $q'$  values. The results are shown in Table 10.2. Let us consider the results obtained by the last test, T5, first. It has been performed with the integration scheme OMEGAGRID = 40, which results in a high density of points in the small frequency regime, and a total of 48 frequency

Table 10.3:  $\Gamma$ -point corrections for different  $q$ -point grids depending on the number of  $q'$ -points used in the integration over the  $\Gamma$ -point volume. All values are given in meV(!).

$q$ -points ( $n$ ) $\rightarrow$	4	6	8	12	16
$q'$ -points $\downarrow$					
$(12 \times 12 \times 12)$	-159.374	-79.691	-47.602	-22.484	-13.042
$(24 \times 24 \times 24)$	-159.291	-79.647	-47.576	-22.472	-13.035
$(36 \times 36 \times 36)$	-159.276	-79.639	-47.571	-22.470	-13.034

points. The smallest frequency,  $\omega_{\min}$ , was set to 0.003 eV. In this case, the same value is obtained no matter how large the maximal frequency  $\omega_{\max}$  is chosen. That indicates that in the present case no contribution arises from frequencies larger than 80 eV and that enough frequency points are present in the small frequency region. If the very same settings, but 24 instead of 48  $\omega$ -points are used (T4), the small frequency range is not sampled well enough, if  $\omega_{\max}$  is chosen too large. If we additionally change the minimal frequency  $\omega_{\min}$  from 0.003 eV to 0.03 eV (T3), we recognise that the small frequency sampling is not accurate anymore, reflected by the change from  $-16.121$  eV in the case of  $\omega_{\min} = 0.003$  eV to  $-16.164$  eV for  $\omega_{\min} = 0.03$  eV. All calculations up to this point have been performed with the integration scheme OMEGAGRID = 40. If we use OMEGAGRID = 4, which introduces a coarser integration grid for small frequencies, we find that 24 frequency points (T2) lead to results far from the correct values. And even for 64 points a correct sampling of the small frequency range is not guaranteed anymore for large values of  $\omega_{\max}$ .

Now that we have tested the frequency integration, we can finally evaluate  $E_c^\Gamma$  and analyze the dependence on the number of  $q'$ -points. We consider an fcc cell and a plasma frequency of  $\bar{\omega} = 122$  eV. For the frequency integration, OMEGAGRID = 40 and 48 frequency points are considered. The maximal and minimal frequency points were placed at 0.003 and 80 eV (corresponding to test T5 shown above). The correction  $E_c^\Gamma$  is calculated for a grid of  $n \times n \times n$  ( $n=4, 6, 8, 12$ , and 16)  $q$ -points and consequently different volumes  $V(\Gamma)$  around the  $\Gamma$  point. It is expected that the convergence with the number of  $q'$  points is slower for a small number of  $q$  points, because then the smallest  $q'$  value is larger and therefore important contributions near the  $\Gamma$ -point are neglected. In Tab. 10.3, the  $\Gamma$ -point correction  $E_c^\Gamma$  (meV) for different  $q$  and  $q'$ -point grids is shown. Even for the coarsest  $q$ -point grid,  $4 \times 4 \times 4$ , the difference between a  $(12 \times 12 \times 12)$  and  $(24 \times 24 \times 24)$   $q'$ -point grid amounts only to  $84 \times 10^{-6}$  eV. For  $8 \times 8 \times 8$   $q$ -points it reduces to  $26 \times 10^{-6}$  eV to finally become  $7 \times 10^{-6}$  eV for  $16 \times 16 \times 16$   $q$ -points. Compared to the error of the correlation energy without  $\Gamma$ -point corrections, all these small changes in the energy can confidently be neglected. Concerning the dependence of the  $\Gamma$ -point correction on the number of  $q$ -points, we found that  $E_c^\Gamma$  scales approximately like  $1/n^{7/4}$ , where  $n$  is the number of  $q$ -points along one direction.

## Chapter 11

# Application of the ACFDT

### 11.1 Molecules - H<sub>2</sub>, O<sub>2</sub>, N<sub>2</sub>

The following calculations of the H<sub>2</sub>, O<sub>2</sub>, and N<sub>2</sub> atomization energies provide a test for our implementation of the RPA-ACFDT routines. Our results will be compared to the ones obtained by Furche [121] using a local basis set code. His RPA routines have been implemented in the Møller-Plesset (MP2) module MPGRAD [133] of the program TURBOMOLE [134] and a cc-pVXZ (correlation consistent polarized valence electron X zeta) basis set was applied. Similar to the slow convergence of our correlation energies with the maximal reciprocal lattice vector determined by  $E_{\text{cut}}^X$  (see section 10.1), Furche's correlation energies exhibit a

$$E_c^{RPA}(X) = E_c^{RPA}(\infty) + A/X^3 \quad (11.1)$$

dependence on the maximal angular momentum  $X$  used for the construction of the basis set. If we compare to his correlation energies, we always refer to his extrapolated values.

For a test set of 12 molecules including e.g., results for HF, CO, CO<sub>2</sub>, H<sub>2</sub>O, Furche found that the RPA leads to a general underestimation of the atomization energy  $\Delta E = \sum E(\text{atom}) - E(\text{mol})$ . The RPA atomization energies for H<sub>2</sub>, N<sub>2</sub>, O<sub>2</sub>, F<sub>2</sub>, and Si<sub>2</sub> (errors smaller than 9 kcal/mol  $\approx$  0.4 eV) are improved compared to the DFT-PBE results. For the other molecules, PBE atomization energies are closer to experiment. The Hartree-Fock atomization energies  $\Delta E_{HF} = \sum E_{HF}(\text{atom}) - E_{HF}(\text{mol})$  are in all cases much too small, deviating from the experimental energies by 25 kcal/mol<sup>1</sup>  $\approx$  1.1 eV for H<sub>2</sub>, 117 kcal/mol  $\approx$  5.1 eV for N<sub>2</sub>, and 155 kcal/mol  $\approx$  6.7 eV for CO<sub>2</sub>.

In the present work, we focus on the atomization energies for H<sub>2</sub>, O<sub>2</sub>, and N<sub>2</sub>. The bond length is fixed to the experimental value (0.7413 Å for H<sub>2</sub>, 1.208 Å for O<sub>2</sub>, and 1.098 Å for N<sub>2</sub>). The generalized gradient approximation by Perdew, Burke, and Ernzerhof (PBE) [12] was used for the representation of the exchange-correlation energy in the calculation of the KS-DFT eigenenergies and wavefunctions. In order to achieve very accurate results for oxygen and nitrogen, we applied different potentials for the evaluation of the HF energy,  $E_{HF}$ , and the RPA correlation energy,  $E_c$ . For the calculation of the Hartree-Fock energy,  $E_{HF}$ , potentials with small core-radii have been considered. For the RPA correlation energy, where unoccupied states have to be correctly represented, *GW* potentials that describe scattering

---

<sup>1</sup>1 kcal/mol = 43.364 meV

Table 11.1: Cutoff radii  $r_c$  for the PAW potentials. For nitrogen and oxygen, different potentials have been applied for the evaluation of DFT and HF energies and the calculation of the RPA correlation energy,  $E_c$ . If the cutoff radii differ for specific quantum numbers, they are specified for each channel using subscripts.

		$r_c$ (a.u.)	$r_c$ (a.u.)
valence		(PBE, HF)	RPA
H	1s	1.1	1.1
N	2s 2p	1.1	1.2 <sub>s</sub> 1.5 <sub>pd</sub>
O	2s 2p	1.1	1.2 <sub>s</sub> 1.5 <sub>pd</sub>

properties very accurately up to  $\approx 10$  Ry, have been applied. The core radii  $r_c$  for these two types of PAW potentials are summarized in Tab. 11.1. The energy cutoff was chosen as high as  $E_{\text{cut}} = 1000$  eV for the DFT-PBE and HF calculations. A supercell with a side-length of  $10 \text{ \AA}$  resulted in converged atomization energies (i.e., an error smaller than  $0.05$  kcal/mol).

For the evaluation of the RPA-ACFDT correlation energy, an energy cutoff of  $E_{\text{cut}} = 600$  eV was sufficient. As described in section 10.1, the convergence with the dimension of the response function (determined by the energy  $E_{\text{cut}}^x$ ) is improved by extrapolating to the known  $1/(E_{\text{cut}}^x)^{(3/2)}$  dependence. For the molecular calculations, the extrapolated values were obtained from a fit to the correlation energies using  $E_{\text{cut}}^x = 300$  and  $350$  eV. The frequency integration was carefully tested. Errors smaller than  $3$  meV can be achieved, if 16 frequency points, a maximal frequency of  $800$  eV, and the integration scheme  $\text{OMEGAGRID} = 44$  (see section 10.2) is applied.

The convergence of the correlation energy difference with respect to the lateral extension of the supercell is relatively fast. For sufficiently large volumes, the correlation contribution to the atomization energy shows a  $1/V^2$  dependence due to spurious, stabilizing van der Waals interactions between repeated images. The deviation between the correlation energy difference,  $\Delta E_c = E_c(\text{mol}) - 2 E_c(\text{atom})$ , when evaluated for the largest applied volume (a  $7.2 \times 6 \times 6 \text{ \AA}$  box), and when using an  $1/V^2$  extrapolation, is  $0.8$  kcal/mol  $\approx 30$  meV for  $N_2$  and  $0.3$  kcal/mol  $\approx 10$  meV for  $O_2$ .

Before finally presenting the values for the atomization energies, we will briefly comment on the influence of two quantities. The first quantity is `ENCUTFOCK` and determines the energy cutoff for the FFT grid used to Fourier transform the cell periodic part of the exchange density  $\phi_a(\mathbf{r})\phi_i(\mathbf{r})$  (see subsection 2.7.1 and Ref. [21]). In principle, the charge density contains Fourier components up to 2 times the number of plane wave components  $G_{\text{cut}}$ . The full  $2 \times G_{\text{cut}}$  grid is considered if `ENCUTFOCK` is not set (`ENCUTFOCK` =  $-1$ ). If `ENCUTFOCK` =  $0$ , a fast Fourier transformation box that just contains all required plane waves is used. The error introduced for the correlation energy by choosing `ENCUTFOCK` =  $0$  is smaller than  $1$  meV and consequently negligible for all three systems considered.

The second quantity is related to the proper treatment of the shape of the exact AE charge density in the calculation of the response function. This point has been discussed in more detail in Sec. 2.7.1. The parameter that defines the quality of the charge density is `LMAXFOCKAE`. The integer value assigned to this parameter determines up to which angular momentum number the AE charge density is reconstructed on the plane wave grid.

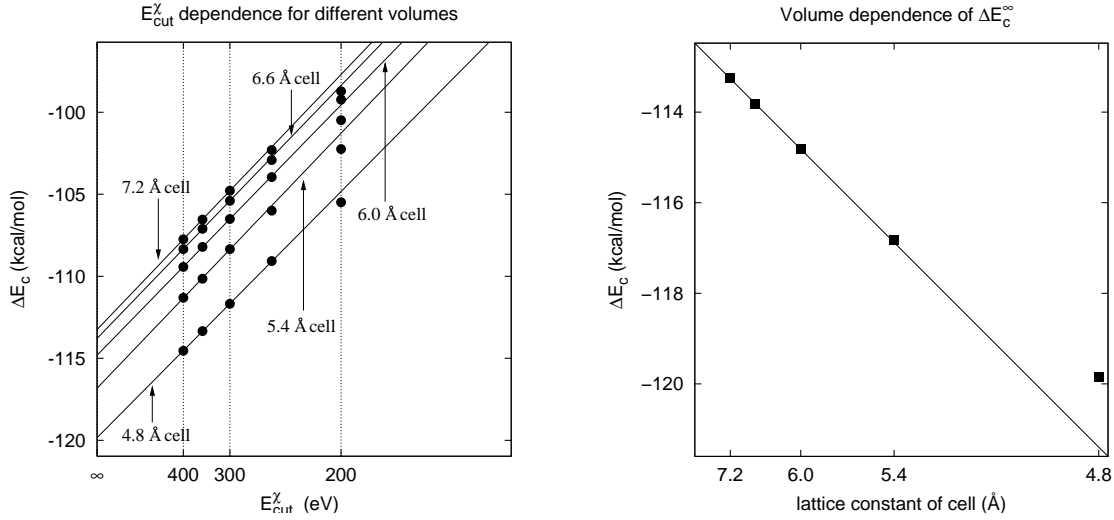


Figure 11.1: Left: Dependence of the  $\text{N}_2$  correlation energy difference ( $\Delta E_c = E_c^{\text{N}_2} - 2 E_c^{\text{N}}$ ) on the energy  $E_{\text{cut}}^X$ , which determines the rank of the response function matrix [ $(E_{\text{cut}}^X)^{-3/2}$  scale]. Shown are results for different supercell volumes (circles) and the fit to  $E_{\text{cut}}^X = 350$  and 300 eV (solid lines). Right: The volume dependence of the extrapolated values  $\Delta E_c^\infty$  is displayed ( $V^{-2}$  scale).

Table 11.2: Correlation energy difference (kcal/mol) for a  $6.6 \times 5.5 \times 5.5$  Å cell. The influence of the quality of the charge density on the plane wave grid determined by LMAXFOCKAE (= LM), and the change introduced by the extrapolation with respect to  $E_{\text{cut}}^X$  are shown for  $\text{H}_2$ ,  $\text{O}_2$ , and  $\text{N}_2$ .

	$\text{H}_2$		$\text{O}_2$		$\text{N}_2$	
$E_{\text{cut}}^X$	LM=-1	LM=2	LM=-1	LM=2	LM=-1	LM=2
350	-23.3	-23.5	-84.5	-86.6	-103.5	-107.1
extra.	-24.6	-24.9	-86.1	-88.3	-109.3	-113.7

It should be typically chosen to be twice the number of the highest angular momentum in the PAW projectors. In this case, we only compare LMAXFOCKAE = 2 to calculations with no corrections at all. The correlation energy differences  $\Delta E_c = E_c(\text{mol}) - 2 E_c(\text{atom})$  evaluated for LMAXFOCKAE = 2 and LMAXFOCKAE = -1 are shown in the Tab. 11.2. Additionally, the values with and without extrapolation with respect to  $E_{\text{cut}}^X$  are given. The correlation energy differences have been determined for a  $6.6 \times 5.5 \times 5.5$  Å cell. For all three considered molecules, the reconstruction of the AE charge density on the plane wave grid (LMAXFOCKAE = 2) leads to a sizeable effect. Especially for  $\text{O}_2$  and  $\text{N}_2$ , absolute correlation energy differences without setting LMAXFOCKAE = 2 are far too small. The error introduced by not including the LMAXFOCKAE correction amounts to as much as 2.2 kcal/mol  $\approx$  0.1 eV for  $\text{O}_2$  and 4.4 kcal/mol  $\approx$  0.2 eV for  $\text{N}_2$ . For the evaluation of total energies, the reconstruction of the AE charge density on the plane wave grid is therefore necessary.

Table 11.3: Atomization energies (kcal/mol) for H<sub>2</sub>, N<sub>2</sub>, and O<sub>2</sub> from standard DFT-PBE calculations (PBE) and from ACFDT calculations applying the RPA (RPA). Additionally the contribution to the total ACFDT atomization energy from ACFDT correlation (corr.) and from the HF energy (HF) are shown. The experimental values (Exp.) are taken from [121].

		PBE	HF	corr.	RPA	Exp.
H <sub>2</sub>	present	105	84	25	109	109
	[121]	105	84	25	109	
N <sub>2</sub>	present	244	111	113	224	228
	[121]	244	111	112	223	
O <sub>2</sub>	present	143	25	88	113	121
	[121]	144	25	88	113	

In Tab. 11.3 the DFT-PBE (PBE), Hartree-Fock (HF), RPA correlation energy (corr.), and the total energy obtained within the RPA-ACFDT formalism (RPA) are summarized and compared to the results of Furche [121]. The correlation energies were obtained for a  $7.2 \times 6 \times 6$  Å cell. The energy was extrapolated according to a  $1/(E_{\text{cut}}^{\chi})^{(3/2)}$  dependence for  $E_{\text{cut}}^{\chi} = 300$  and 350 eV. On-site corrections were included by choosing LMAXFOCKAE = 2. Obviously Furche's results agree very well with ours. For the standard DFT calculations, the atomization energy shows only a small deviation for the O<sub>2</sub> molecule. The HF energies (more exactly: the Hartree-Fock energy evaluated for DFT-PBE wavefunctions) resulting from the plane wave (present work) and the local basis set (Furche) approach agree within 1 kcal/mol. Also the RPA-ACFDT correlation energies are close to each other. The difference for N<sub>2</sub> is reduced by applying the  $1/V^2$  volume extrapolation. While the N<sub>2</sub> correlation energy difference amounts to  $-113.3$  kcal/mol for the  $7.2 \times 6 \times 6$  Å cell, the  $1/V^2$  extrapolated value is  $-112.5$  kcal/mol and comes closer to the result of Furche (112 kcal/mol). For all molecules considered here, the RPA provides better agreement with experiment than the DFT-PBE results. But this is not the case for all molecules considered by Furche, as discussed at the beginning of this section.

Finally, we show the dependence of the correlation energy  $\Delta E_c$  on the energy cutoff  $E_{\text{cut}}^{\chi}$  (Fig. 11.1, left) and the volume dependence of the extrapolated values (Fig. 11.1, right). Here, the volume is denoted by the longer side of the supercell, which lies along the binding direction of the molecule (e.g. 7.2 Å cell for the  $7.2 \times 6.0 \times 6.0$  Å cell).

## 11.2 Rare-gas solids - Ne, Ar, Kr

The rare gas solids are the standard example of extended systems bonded only by weak dispersion forces. As the rare gas atoms possess a closed-shell electronic configuration, they do not exhibit any covalent interactions. The nature of their binding is only due to the van der Waals interaction, which exhibits the typical  $-1/R^6$  behavior for sufficiently large distances. The source of the attractive van der Waals interaction is the energy gained by the interaction of fluctuating dipoles. While the rare gas atoms have no permanent dipole



moment, quantum fluctuations introduce an instantaneous dipole moment. In a qualitative picture of two atoms at a distance  $R$ , the dipole moment on atom 1,  $p_1$ , results in an electric field  $E \propto p_1/R^3$ . The electric field introduces a dipole moment on atom 2,  $p_2$ , which is proportional to the electric field  $p_2 \propto E(R) \propto p_1/R^3$ . The energy of a dipole moment in an electric field is given by  $V = -p_2 E$  which, in total, results in a potential  $V \propto -p_1 p_2 / R^6$ . How strongly an atom can be polarized by an electric field depends on its polarizability. Consequently, this quantity enters the van der Waals potential as a prefactor.

The nature of the van der Waals interaction is non-local, because it describes the reaction of an atom at position  $\mathbf{r}$  to the density fluctuations of a second atom at position  $\mathbf{r}'$ . Such a correlation contribution is not captured in any local (LDA) or semilocal (GGA) approximation of the correlation energy as normally used in DFT calculations (see also Ref. [32]). This failure of standard DFT becomes evident in the description of rare gas molecules and solids, where LDA strongly overbinds, while GGA underbinds. Other prominent examples are graphite and h-BN, for which GGA does not provide an interlayer binding between the graphene and h-BN sheets at all, while LDA binds only because of a spurious cancellation of errors in the description of the exchange and correlation energy. Therefore, it is common to include the van der Waals potential as an additional energy contribution  $\propto C_6^{(ab)} / R_{(ab)}^6$ , and to sum over all pairs of atoms  $(a, b)$  present in the system (see e.g., [135]). In order to avoid strong interactions at very small distances, the  $1/R^6$  potential is damped for small values of  $R$ . This approach thus resembles the introduction of a Lennard-Jones potential:

$$V_{ab}(R_{ab}) = \frac{C_{12}^{ab}}{R_{ab}^{12}} - \frac{C_6^{ab}}{R_{ab}^6} \quad (11.2)$$

The coefficient  $C_6$  can be calculated from the ab-initio atomic polarizability.

Beside the difficulties of determining the damping factor and the correct calculation of the atomic polarizability, a fundamental problem lies in the assumption that the correct  $R$  dependence of the correlation can be obtained by summing over terms of the form given in Eq. (11.2). While the summation over the  $1/R^6$  terms gives the correct energy behavior in leading order of  $1/R$  (not necessarily the correct prefactors) for an insulating system, it can be shown [32, 33] that for metals not even the correct long-range behavior can be reproduced. Thus, this semi-empirical treatment can not be the proper solution for the description of van der Waals bonded systems.

The ACFDT formulism provides an exact (non-local) expression for the correlation energy, and therefore naturally also includes the van der Waals interaction. Even within the RPA, it has been shown [34] that the correct long-range  $1/R^6$  behavior for two atoms (respectively the correct dependence on the distance  $R$  for any system) can be reproduced. Only the coefficients are altered by the RPA approximation, so that e.g., the  $C_6$  coefficients describing the interaction between two distant atoms are determined by the RPA atomic polarizabilities instead of the exact ones.

In this chapter, we will present RPA cohesive energies for the fcc rare-gas crystals of Ne, Ar, and Kr. The applied potentials were generated as to guarantee good scattering properties for the isolated atoms for up to  $\approx 10$  Ry. The parameters of these potentials are summarized in Tab. 11.4. For the Hartree-Fock energy,  $E_{HF}$ , a  $12 \times 12 \times 12$   $k$ -point grid was used. This dense  $k$ -point grid was necessary in order to obtain convergence on the meV level. For the RPA correlation energies, a  $6 \times 6 \times 6$   $k$ -point grid already leads to relatively smooth energy-



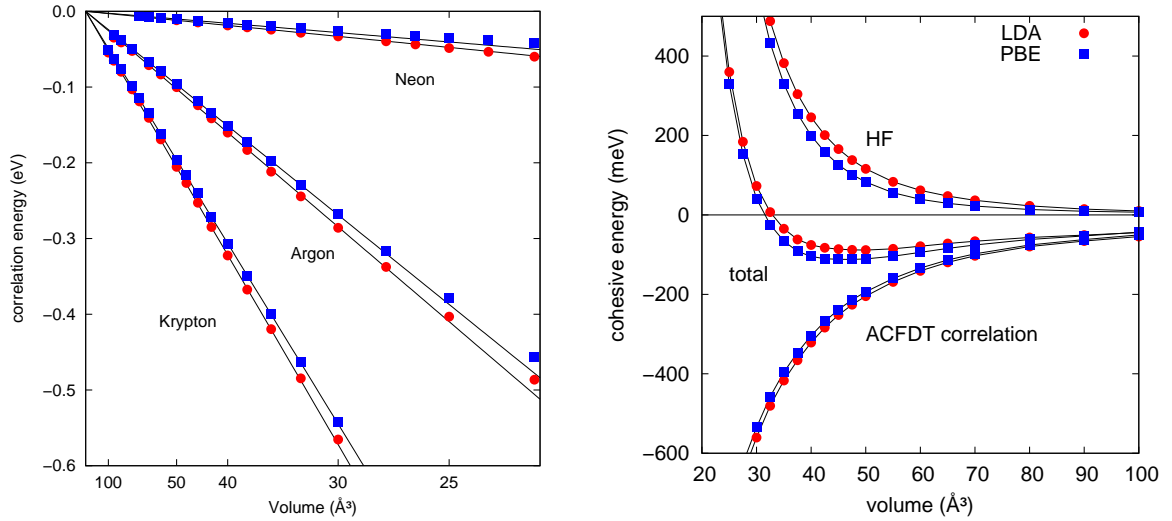


Figure 11.2: Left: RPA correlation energy based on LDA (circles) and PBE (squares) wavefunctions and eigenenergies. The correlation energy is plotted over  $1/V^2$ . The energies are given with respect to the (extrapolated) correlation energy of the isolated atom. Right: Kr RPA cohesive energy (meV) and contributions arising from the HF part  $E_{HF}$  and the correlation energy  $E_c$  only. Energies based on DFT-LDA wavefunctions are given by circles, values based on DFT-PBE by squares.

Table 11.4: Cutoff radii  $r_c$  for the rare gas PAW potentials. For the rare gas solids the same potentials have been used for the HF contribution  $E_{HF}$  and for the evaluation of the correlation energy  $E_c$ .

	valence	$r_c$ (a.u.)	$E_{\text{cut}}$ (HF)	$E_{\text{cut}}$ (corr.)
Ne	2s 2p	1.4 <sub>s</sub> 1.8 <sub>pd</sub>	900	650
Ar	3s 3p	1.5 <sub>s</sub> 1.9 <sub>pd</sub>	390	390
Kr	4s 4p	1.8 <sub>s</sub> 2.3 <sub>pd</sub>	340	340

volume curves. The extrapolation to  $E_{\text{cut}}^{\chi} \rightarrow \infty$  was performed using the correlation energies obtained at  $E_{\text{cut}}^{\chi} = 300, 275, 250$ , and  $225$  eV for Ne and for  $225, 200$ , and  $175$  eV for Ar. It is noted that the choice of the  $E_{\text{cut}}^{\chi}$  values and the extrapolation is automated in the current version of VASP.

For the evaluation of the cohesive energy, the Hartree-Fock and the RPA correlation energy of the isolated atom are required. The atomic Hartree-Fock energy contribution was calculated directly. Very large supercells would have been required to obtain RPA correlation energies of an accuracy in the meV range. This step was circumvented by extrapolating the correlation energy of the fcc solid according to a  $1/V^2 \propto 1/R^6$  behavior and taking the extrapolated value as the correlation energy of an isolated atom. The validity of such a procedure is demonstrated in Fig. 11.2 (left panel). The correlation energy is plotted over  $1/V^2$ , so that all points lie on a straight line, if the correct  $1/R^6$  dependence is fulfilled. For all three considered rare gas solids the  $1/V^2$  dependence holds already for volumes as small

Table 11.5:  $C_6$  (eVÅ<sup>6</sup>) coefficients for the noble gas solids, where  $C_6$  determines the strength of the long-range  $C_6/R^6$  interaction ( $R$  is the nearest neighbor distance). This value equals twice the slopes of the curves shown in Fig. 11.2, left panel. The “experimental” values are estimated by fitting the experimental zero-point corrected equilibrium energies and equilibrium volumes [136] to a Lennard-Jones pair potential.

	Exp.	LDA	PBE
Ne	47	62	53
Ar	455	512	484
Kr	895	1030	980

as 30 Å<sup>3</sup> for both LDA or PBE wavefunctions and eigenenergies. The slope of the correlation energy versus  $1/V^2$  corresponds to half the coefficient  $C_6$ , which determines the van der Waals energy contributions  $C_6/R^6$ ,  $R$  being the nearest neighbor distance in the fcc crystal. The corresponding values are given in Tab. 11.5 for Ne, Ar, and Kr. The “experimental” reference values were obtained by fitting the zero-point corrected equilibrium energies and volumes taken from [136] to a Lennard-Jones potential. The “experimental” and theoretical values for  $C_6$  agree rather satisfactorily, particularly in the GGA-PBE case. The slight overestimation of the coefficient is related to the fact that RPA polarizabilities evaluated from LDA and PBE wavefunctions and eigenenergies are normally overestimated, more so for the LDA than for the PBE case. Whether LDA or PBE wavefunctions and eigenenergies are used as input for the RPA energy, does not only effect the RPA correlation energy. In Fig. 11.2, right panel, the total RPA energy of the Kr crystal is split into the contribution arising from the Hartree-Fock and the correlation energy. For the correlation energy, we have already seen in the left panel that using LDA wavefunctions and eigenenergies yields a larger absolute value for the correlation energy. This goes hand in hand with the fact that the LDA polarizability is larger than the PBE one (see Tab. 11.5). For the Hartree-Fock contribution, however, PBE wavefunctions result in smaller energies so that in total PBE wavefunctions give smaller RPA cohesive energies for the rare gas solids than LDA ones.

In Fig. 11.3, the cohesive energies are shown for all three considered rare gas solids. Besides the standard DFT results (solid line: LDA, dashed line: PBE) the RPA-ACFDT energies are plotted as obtained using LDA (circles) and PBE (squares) wavefunctions and eigenenergies as input. The experimental lattice constants and cohesive energies (corrected by zero point contributions) as taken from Ref. [136] are plotted using diamonds. In Tab. 11.6, the equilibrium properties are summarized. Besides the lattice constants and cohesive energies obtained from DFT LDA and PBE calculations, the RPA values resulting from LDA and PBE input are given. Additional to our data, the CCSD(T) values from Ref. [136] are specified. The experimental reference data are taken from Ref. [136]. The DFT lattice constants of the rare gas solids follow the general LDA and PBE trend, respectively: LDA-DFT lattice constants are too small, PBE-DFT lattice constants too large. The LDA error becomes slightly smaller for the heavier rare gas atoms, while the opposite trend is observed for PBE. The performance of the RPA for the calculation of the lattice constants is significantly better, and for DFT-PBE wavefunctions and eigenenergies, the errors of the RPA lattice constant is 3.4, 1.3, and 1.6 % for Ne, Ar, and Kr, respectively, compared to −10.3 % error

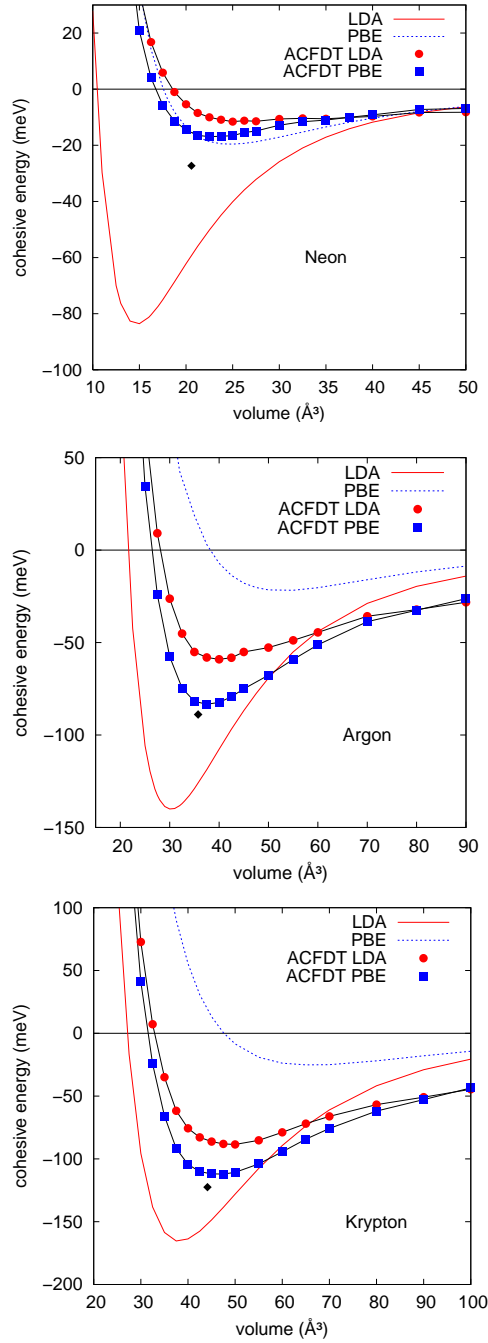


Figure 11.3: Cohesive energy (meV) as a function of the primitive cell volume for the fcc noble gas crystals Ne, Ar, and Kr. Besides the cohesive energies obtained from the RPA-ACFDT calculations based on LDA (circles) and PBE (squares) wavefunctions and eigenenergies, standard DFT results within the LDA (solid line) and PBE (dashed line) are shown. The experimental values (without zero-point energy) are given by black diamonds.

Table 11.6: Equilibrium lattice constants and cohesive energies of the noble gas fcc crystals Ne, Ar, and Kr. The DFT results are compared to RPA-ACFDT values and experiment. The zero-point energy is neglected and the experimental lattice constants are extrapolated to zero temperature (see Ref. [136]).

	DFT- LDA	ACFDT- LDA	DFT- PBE	ACFDT- PBE	Exp.	Ref. [136]
lattice constant ( $\text{\AA}$ )						
Ne	3.9	4.7	4.6	4.5	4.35	4.314
Ar	4.9	5.4	6.0	5.3	5.23	5.284
Kr	5.3	5.8	6.4	5.7	5.61	5.670
absolute value of cohesive energy (meV)						
Ne	83	11	20	17	27.3	26.44
Ar	140	59	22	83	88.9	82.81
Kr	165	88	25	112	122.5	114.44

in the Ne LDA lattice constant, or 14.1 % for the Kr PBE values.

In summary, for the cohesive energies, DFT overbinds in the case of the LDA, and underbinds for PBE. The error introduced by the LDA is about  $-50$  meV for all three rare gas solids, while the PBE error increased from 7 meV for Ne, to 67 meV for Ar, to 100 meV for Kr. Also with respect to the cohesive energies, the RPA results in an improved description compared to both LDA and PBE. With the exception of Ne, where PBE-DFT is closer to experiment, RPA gives better agreement with experiment. If PBE wavefunctions and eigenenergies are used as input for the RPA energies, the error never exceeds 11 meV. For Ar and Kr, the RPA-PBE lattice constants and cohesive energies are very close to the CCSD(T) values reported by Paulus *et al.* [136].

For the rare gas crystals of Ne, Ar, and Kr we found that the RPA provides an improved description of lattice constants and cohesive energies compared to DFT based on the LDA or PBE. Additionally, RPA correctly accounts for the  $1/R^6$  dependence, and the corresponding coefficients are well described within the RPA.

### 11.3 Homogenous electron gas

Because the correct RPA-ACFDT correlation energies for the homogenous electron gas are known (see e.g., Ref. [11, 132]), the HEG represents the ideal test system for RPA calculations of metallic systems. In this section, we will mainly focus on the  $k$ -point convergence of the RPA correlation energy, a topic that has already been addressed in section 10.3. Additionally, we will aim at a comparison between calculated RPA correlation energies and values presented in the literature.

The RPA correlation energies have been calculated applying energy cutoffs of  $E_{\text{cut}} = 250$

eV and  $E_{\text{cut}}^{\chi} = 150$  eV. For the frequency integration, method OMEGAGRID = 40 (see Sec. 10.2) with 24 supporting points and a minimal and maximal frequency of 0.05 eV and 200 eV has been applied. Changing the energy cutoffs to 350/150 and 450/250 changes the correlation energies by less than 1 meV. The same holds if the maximal frequency is increased to 800 eV and the number of supporting points to 64.

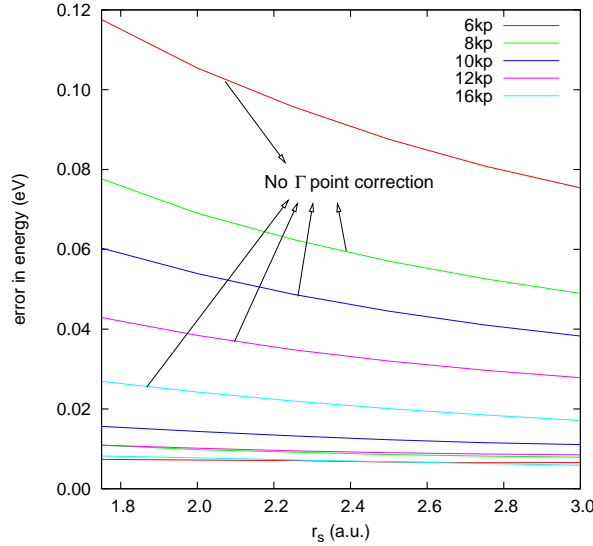


Figure 11.4: Difference between correlation energies calculated for different  $k$ -(and  $q$ )-point grids and the values stemming from the RPA parameterization by Perdew and Wang [11]. Both, results obtained with and without the  $\Gamma$ -point correction are shown.

The convergence of the RPA-ACFDT energy with the number of  $q$ -points is determined by the correct treatment of the small- $q$  integrand. In Method B described in section 10.3, the intraband contributions from the vicinity of the  $\Gamma$  point are calculated by a numerical integration over the HEG expression. If applied to the HEG, this method is exact provided that the numerical integration is accurate enough. The remaining error stems from errors in the  $k$ -point sampling of the Brillouin zone, when evaluating the response function  $\chi(\mathbf{q})$ .

In Fig. 11.4 the differences between our correlation energies and the values obtained from the parameterization of Perdew and Wang [11] for different  $k(q)$ -point grids and densities are shown. Both, the errors with and without the applied  $\Gamma$ -point corrections, are displayed. The  $k$ -point error without applying the  $\Gamma$ -point correction is significantly larger, and especially the correlation energy for large densities (small Wigner-Seitz radii) is underestimated. Applying the  $\Gamma$ -point correction, the  $k$ -point error and the dependence on the densities is much reduced. For all  $k$ -point values starting from  $6 \times 6 \times 6$   $k$ -points and for all densities, the error applying  $\Gamma$ -point correlations is smaller than 20 meV. This large improvement compared to the uncorrected correlation energies highlights the importance of including the Drude term for metals.

For the data presented in Fig. 11.4 the extrapolation to  $E_{\text{cut}}^{\chi} \rightarrow \infty$  has been applied (see Sec. 10.1). In Fig. 11.5, the 16  $k$ -point correlation energies for a response function energy cutoff of  $E_{\text{cut}}^{\chi} = 150$  eV (black squares) are shown together with the extrapolated energies

with (empty circles) and without (empty squares) applying the  $\Gamma$ -point correction. Evidently, the  $E_{\text{cut}}^{\chi}$  extrapolation is essential in order to obtain accurate correlation energies.

The number of points used in the frequency integration (NOMEGA) could play a more important role for metals than for semiconductors due to the existence of small frequency transitions. Although the Drude term is treated separately (as done in Method B), a dense  $q$ -point grid will lead to small  $q$ -point transitions and consequently small intraband excitations. Nevertheless, we found that the frequency integration is unproblematic, at least in the case of the HEG. If the integration scheme OMEGAGRID = 4 is used (see Sec. 10.2), converged energies are obtained already for 16 frequency points. We therefore observe that the intraband contributions are well manageable. Only if band crossings occur near the Fermi surface, as for Al and the transition metals, faster convergence is obtained if extremely small frequency points are not considered (see next section).

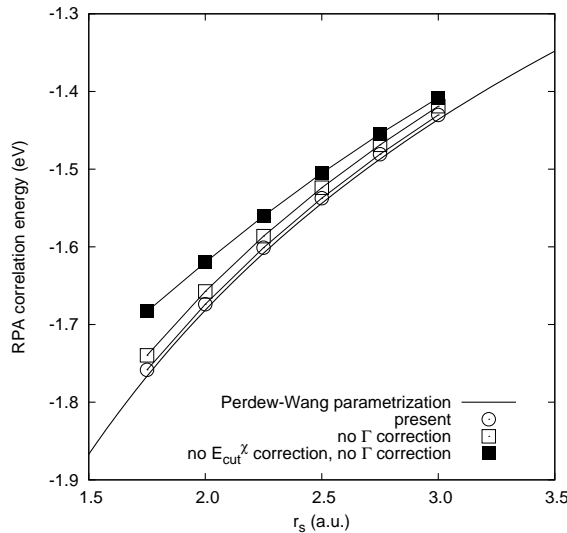


Figure 11.5: Influence of the  $E_{\text{cut}}^{\chi}$  extrapolation and of the  $\Gamma$ -point correction on the HEG RPA correlation energy.

Finally we address the reproducibility of published data with our implementation of the RPA energy in VASP. Published data for the HEG RPA correlation energy [132] were calculated numerically by evaluating Eq. (10.1). Here, we compare to the parameterization of the HEG RPA correlation energies as provided by Perdew and Wang [11]. Our calculations have been performed for densities corresponding to Wigner-Seitz radii between 1.75 and 3.0. The energy cutoff  $E_{\text{cut}}$  was chosen to be 250 eV and for the response function plane wave components with an energy of up to  $E_{\text{cut}}^{\chi} = 150$  eV were considered. The  $E_{\text{cut}}^{\chi}$  extrapolation was performed as described in Sec 10.1. The final RPA correlation energies (empty circles in Fig. 11.5) stem from a 16  $k$ -point calculation and the  $\Gamma$  point correction was applied. For the frequency integration the scheme OMEGAGRID = 40 was employed and the smallest frequency was chosen to be SIGMA = 0.05 eV. For all considered densities the difference between our calculated RPA correlation energies and the literature values [11] is smaller than 9 meV.

## 11.4 Metals - Na, Al, Cu, Rh, Pd

In this section, RPA calculations of the metals Na, Cu, Al, Rh, and Pd will be presented. We will focus on the convergence of the lattice constant, the bulk modulus, and the total energy with respect to the  $k$ -point grid used in the evaluation of the HF energy and the RPA-ACFDT correlation energy. Additionally, the influence of the  $\Gamma$ -point correction (= inclusion of the Drude term) for the RPA correlation energy (see Sec. 10.3) is investigated for all five metals. We have applied the same energy cutoffs  $E_{\text{cut}}$  and  $E_{\text{cut}}^{\chi}$  as specified in Tab. 11.9. The parameters of the frequency integration, the integration method, the number of frequency points, and the maximal/minimal frequency are also summarized in Tab. 11.9. For Na, we used a PAW potential that treats only the 3s electrons as valence, referred to as Na<sub>1</sub> potential in section 11.5.

In the previous section, the RPA correlation energy of the homogenous electron gas (HEG) has been calculated and the inclusion of the  $\Gamma$ -point corrections was found to significantly improve the  $k$ -point convergence. As sodium can be considered to be a nearly free electron like metal, the Na bcc crystal represents the first step from the HEG to a real metallic system. The total energy ( $E_{\text{HF}} + E_c$ ) of the Na bcc crystal is shown in Fig. 11.6. Three different cases are considered: In the top panel, the RPA correlation energy is not corrected for by the  $\Gamma$ -point contributions and the HF energy is always evaluated using a  $16 \times 16 \times 16$   $k$ -point grid. In the middle panel, the HF part is treated as before, but the  $\Gamma$ -point correction is added to the RPA correlation energy. In the bottom panel, the HF part is calculated using the same  $k$ -point grid as employed for the correlation energy, and the  $\Gamma$ -point correction is applied. The lattice constants, bulk moduli, and total energies of Na and the other metals are summarized in Tab. 11.7. If no  $\Gamma$ -point correction is added and a  $16 \times 16 \times 16$   $k$ -point grid is considered for the HF energy (top panel of Fig. 11.6), the energy error is dominated by errors in the correlation energy. The general form of the Na energy versus volume curve is basically maintained for all chosen  $k$ -point grids, with a slight overestimation of the lattice constant for coarser grids. The absolute value of the correlation energy is too small for a  $6 \times 6 \times 6$   $k$ -point grid (by  $\approx 70$  meV) and continuously increases towards a denser  $k$ -point grid. Adding the  $\Gamma$ -point correction (middle panel of Fig. 11.6), leads to a significant improvement of the energy convergence (30 meV error for  $6 \times 6 \times 6$   $k$ -points,  $< 10$  meV for more  $k$ -points.) The  $k$ -point error for the lattice constants also decreases. If the HF energy is evaluated at a  $16 \times 16 \times 16$  grid, and  $\Gamma$ -point corrections are applied for the correlation energy, the lattice constant stemming from the  $8 \times 8 \times 8$   $k$ -point correlation energy differs only by 0.05 % from the converged result. The error in the total energy only amounts to 7 meV. Much slower convergence of the lattice constants and energies is obtained, if the same  $k$ -point grid is applied for the HF and the correlation energy. The resulting energy-volume curves are presented in the bottom panel of Fig. 11.6. The difference between the  $8 \times 8 \times 8$  and  $16 \times 16 \times 16$   $k$ -point lattice constants now amounts to 0.2 % and the total energy varies by 25 meV.

For Cu, the lattice constants and total energies calculated with and without  $\Gamma$ -point correction and different  $k$ -point settings for the HF part are summarized in Tab. 11.7. In contrast to Na, both the valence  $s$ -electron and the  $d$ -electrons contribute to the correlation energy of the Cu fcc crystal. As a consequence, the Drude like contribution around the  $\Gamma$ -point is not as dominant as in the case of Na. Even without considering the  $\Gamma$ -point

Table 11.7: Lattice constants  $a_0$  (Å), bulk moduli  $B_0$  (GPa), and energies  $E_0$  (eV) for Na, Cu, Al, Rh, and Pd evaluated for different  $k$ -point grids applied for the RPA correlation energy. Values obtained if including or not including  $\Gamma$ -point corrections for the correlation energy are presented. Furthermore, both values resulting from using the same  $k$ -point grid for the HF and the correlation energy [HF( $\leftarrow$ )] and a denser  $k$ -point grid for the HF energy are shown.

Na									
$k$ -point grid	HF(16kp)/no $\Gamma$			HF(16kp)/ $\Gamma$			HF( $\leftarrow$ )/ $\Gamma$		
	$a_0$	$B_0$	$E_0$	$a_0$	$B_0$	$E_0$	$a_0$	$B_0$	$E_0$
$8 \times 8 \times 8$	4.262	7.45	-2.990	4.256	7.53	-3.021	4.264	7.37	-3.003
$10 \times 10 \times 10$	4.258	7.48	-3.004	4.254	7.54	-3.024	4.257	7.46	-3.014
$12 \times 12 \times 12$	4.258	7.48	-3.011	4.255	7.52	-3.026	4.264	7.41	-3.022
$14 \times 14 \times 14$	4.257	7.52	-3.017	4.255	7.55	-3.028	4.256	7.57	-3.029
$16 \times 16 \times 16$	4.255	7.54	-3.020	4.254	7.56	-3.028	4.254	7.56	-3.028
Cu									
$k$ -point grid	HF(16kp)/no $\Gamma$			HF(16kp)/ $\Gamma$			HF( $\leftarrow$ )/ $\Gamma$		
	$a_0$	$B_0$	$E_0$	$a_0$	$B_0$	$E_0$	$a_0$	$B_0$	$E_0$
$6 \times 6 \times 6$	3.606	146	-18.261	3.605	146	-18.320	3.604	149	-18.276
$8 \times 8 \times 8$	3.599	153	-18.256	3.598	153	-18.291	3.620	164	-18.291
$10 \times 10 \times 10$	3.602	154	-18.265	3.601	154	-18.289	3.604	145	-18.278
$12 \times 12 \times 12$	3.601	157	-18.268	3.601	157	-18.285	3.592	157	-18.292
Al									
$k$ -point grid	HF(20kp)/no $\Gamma$			HF(20kp)/ $\Gamma$			HF( $\leftarrow$ )/ $\Gamma$		
	$a_0$	$B_0$	$E_0$	$a_0$	$B_0$	$E_0$	$a_0$	$B_0$	$E_0$
$6 \times 6 \times 6$	4.031	65.9	-10.087	4.042	64.3	-10.195	4.078	60.0	-10.457
$8 \times 8 \times 8$	4.036	68.8	-10.191	4.042	67.7	-10.255	4.052	87.3	-10.342
$10 \times 10 \times 10$	4.027	73.4	-10.239	4.031	72.5	-10.281	4.021	65.7	-10.267
$12 \times 12 \times 12$	4.033	74.5	-10.225	4.035	74.1	-10.255	4.053	79.0	-10.295
$14 \times 14 \times 14$	4.033	75.0	-10.250	4.035	74.8	-10.272	4.019	76.8	-10.269
$16 \times 16 \times 16$	4.032	75.6	-10.247	4.034	75.5	-10.264	4.036	78.6	-10.289
Rh									
$k$ -point grid	HF(16kp)/no $\Gamma$			HF(16kp)/ $\Gamma$			HF( $\leftarrow$ )/ $\Gamma$		
	$a_0$	$B_0$	$E_0$	$a_0$	$B_0$	$E_0$	$a_0$	$B_0$	$E_0$
$8 \times 8 \times 8$	3.799	259	-31.211	3.797	261	-31.246	3.810	250	-31.147
$10 \times 10 \times 10$	3.806	258	-31.250	3.805	259	-31.273	3.813	249	-31.159
$12 \times 12 \times 12$	3.813	255	-31.298	3.812	256	-31.314	3.815	252	-31.261
$16 \times 16 \times 16$	3.810	254	-31.230	3.810	254	-31.239	3.810	254	-31.239
Pd									
$k$ -point grid	HF(16kp)/no $\Gamma$			HF(16kp)/ $\Gamma$			HF( $\leftarrow$ )/ $\Gamma$		
	$a_0$	$B_0$	$E_0$	$a_0$	$B_0$	$E_0$	$a_0$	$B_0$	$E_0$
$8 \times 8 \times 8$	3.874	186	-26.780	3.871	187	-26.807	3.896	180	-26.910
$10 \times 10 \times 10$	3.888	193	-26.835	3.887	193	-26.853	3.873	185	-26.922
$12 \times 12 \times 12$	3.868	229	-26.885	3.867	230	-26.898	3.869	229	-26.867
$16 \times 16 \times 16$	3.873	200	-26.846	3.872	200	-26.854	3.872	200	-26.854



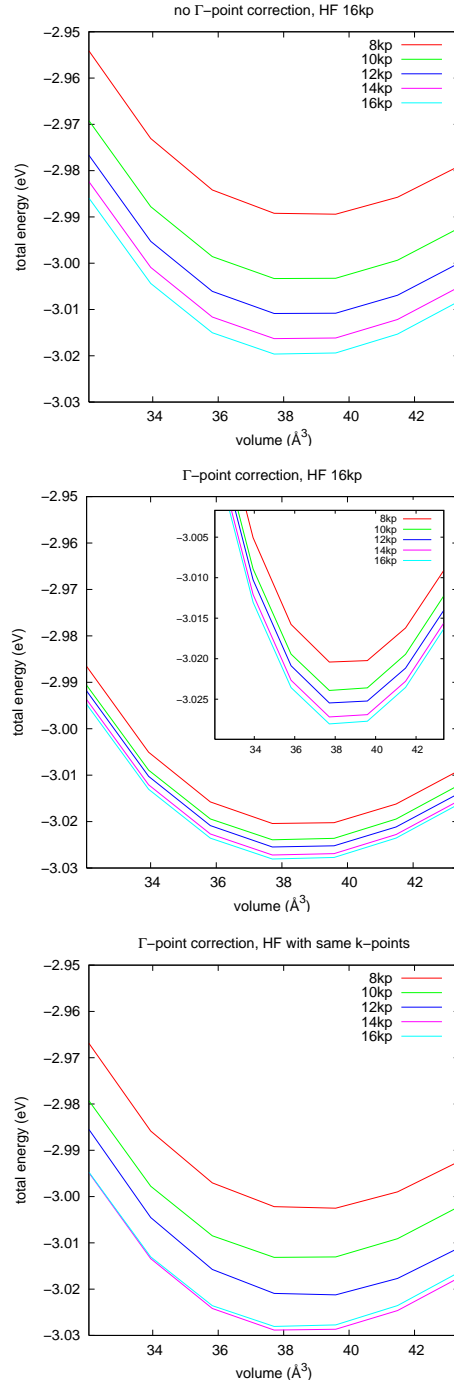


Figure 11.6: Total energy of the Na bcc crystal determined with (middle and bottom) and without (top)  $\Gamma$ -point corrections. The HF energy evaluated at 16  $k$ -points was used (top and middle), or the same  $k$ -point set as for the correlation energy was applied for the HF calculations (bottom).

correction, both the lattice constant and the total energy converge fast with the number of  $k$ -points. On the contrary, the  $\Gamma$ -point contribution overcorrects the  $6 \times 6 \times 6$   $k$ -point result by almost 30 meV. If the number of  $k$ -points is chosen the same for the calculation of the HF and the RPA correlation energy, the  $k$ -point convergence of both, the lattice constant and the total energy, is slower than if evaluating the HF energy at a denser  $k$ -point grid. Especially the  $k$ -point dependence of the lattice constant becomes significantly stronger. As for Na,  $k$ -point converged Cu lattice constants (error  $< 0.08$  %), bulk moduli (error  $< 2.5$  %), and total energies (error  $< 7$  meV) can be already obtained using a  $8 \times 8 \times 8$   $k$ -point grid for the determination of the RPA correlation energy. The HF energies, however, have to be evaluated applying a denser  $k$ -point grid. The  $k$ -point convergence of the Ag lattice constant, bulk modulus, and total energy is very similar to the one of Cu, and is therefore not explicitly addressed in this section. So far, we have considered bulk systems

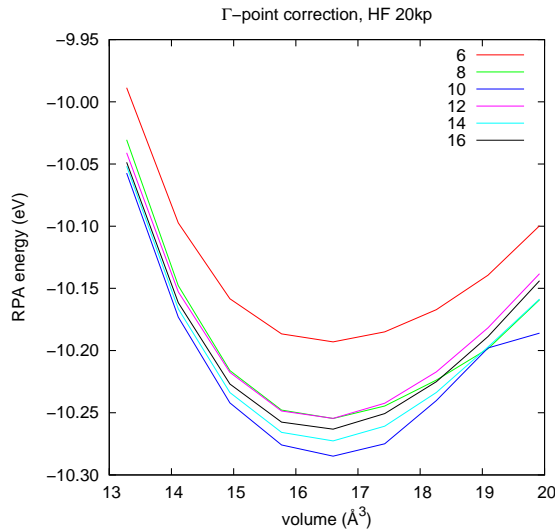


Figure 11.7: RPA energy for Al.  $\Gamma$ -point corrections have been applied for the correlation energy and the HF energy has been evaluated using a  $20 \times 20 \times 20$   $k$ -point grid.

with only one valence band crossing the Fermi level. If band crossings occur near the Fermi surface, transitions with very small excitation energies are possible. As the strength of these transitions depends strongly on the location of the band crossings with respect to the Fermi surface, the contributions to the correlation energy can change significantly, if the volume of the cell is altered. Additionally, the influence of the band crossings sensitively depends on the chosen  $k$ -point grid and the relative distance between the band crossing and the considered  $k$ -points.

As a test case for a simple metal that exhibits such band crossings we have chosen fcc Al. In Fig. 11.7 the energy dependence on the volume of the cell is shown. A  $20 \times 20 \times 20$   $k$ -point grid is used for the HF energy and  $\Gamma$ -point corrections are added to the RPA correlation energy. Lattice constants and energies obtained from fits to the curves presented in Fig. 11.7 are summarized in Tab. 11.7. In contrast to Na (and also Cu), where all energy-volume curves shared the same general form, now some curves show spurious kinks. The  $10 \times 10 \times 10$   $k$ -point curve, e.g., exhibits a stronger increase starting at a volume of  $17 \text{ \AA}^3$  followed by

a kink at  $19 \text{ \AA}^3$ . A similar behavior can be observed for the  $8 \times 8 \times 8$   $k$ -point grid. The kinks in these energy-volume curves are large enough to question if fits to the  $8 \times 8 \times 8$  and  $10 \times 10 \times 10$   $k$ -point curves are meaningful at all. Furthermore, the  $k$ -point convergence of the Al HF energies is especially slow. If the same  $k$ -point grids are applied for the HF and the correlation energy, the lattice constant changes by 0.4 % for different  $k$ -point grids and the error in the energy is also significantly larger than for a dense HF  $k$ -point grid.

Finally, we consider the convergence of lattice constants and total energies for the transition metals Rh and Pd. Both metals have only partially filled  $3d$  states and due to the large number of  $d$  bands near the Fermi level the effect caused by band crossings is even stronger than for Al. The  $k$ -point convergence is indeed harder to achieve for Rh and Pd than for all other metals considered so far. For Al, we have found that the energy volume curve can exhibit spurious kinks for specific  $k$ -point grids, but the  $k$ -point convergence of the lattice constant, the bulk modulus, and the total energy was nevertheless reasonable fast. For the transition metals, the lattice constants undergo larger variations for different  $k$ -point grids than was the case for the other considered metals, and for Pd a  $12 \times 12 \times 12$   $k$ -point grid leads to a significantly altered shape of the energy-volume curve with a bulk modulus which is 13 % off the values obtained for the other  $k$ -point settings. Also the  $k$ -point convergence of the Rh and Pd total energy is slower than for the other considered metals. If the HF energy is evaluated applying a dense  $k$ -point mesh, the energy difference for using a  $8 \times 8 \times 8$  or  $12 \times 12 \times 12$   $k$ -point grid for the evaluation of the correlation energy amounts to 70 and 90 meV for Rh and Pd, respectively. The same difference is only 5 meV for Na and 6 meV for Cu. In contrast to the other metals, the  $k$ -point dependence of the total energy is not worsened, if the HF energy is evaluated applying the same  $k$ -point grid as used for the RPA correlation energy.

The spurious influence of transitions between states with small energy differences can be somewhat diminished by avoiding to evaluate the response function for very small frequencies. This can be done by choosing the first supporting point for the frequency integration relatively large. To this end, the frequency integration scheme OMEGAGRID = 40 (see Sec. 10.2) has been applied which allows to set the smallest frequency by SIGMA. We found that SIGMA = 0.2 eV reduces the effect of the small energy transitions and at the same time seems to capture most of the "desirable" part of the correlation energy.

We have found that for both, Na and Cu, the  $k$ -point convergence of the lattice constant, the bulk modulus, and the total energy is unproblematic. For Al, band crossings near the Fermi energy can lead to spurious contributions to the correlation energy for specific cell volumes and  $k$ -point grids. For these three metals, it is not recommended to use the same  $k$ -point grid for the HF and the correlation energy, because the HF contributions seem to converge significantly slower with the number of  $k$ -points than the correlation energy. From Tab. 11.7 it is clear that a convergence to 10 meV in the energy and 0.1 % in the lattice constant can be obtained for Na, Cu, and Al. For the transition metals Rh and Pd, the  $k$ -point convergence is slower, which is related to the large number of band crossings near the Fermi surface caused by the high density of  $3d$  states near the Fermi level. Errors, also for dense  $k$ -point grids, still amount to 0.2 % in the lattice constant and 20 meV in the total energy.

Table 11.8: PAW potentials used in the present section. Cutoff radii  $r_c^l$  applied for the generation of the partial waves with angular quantum number  $l$  are denoted in a.u. The number of partial waves and projectors is specified. The energy cutoff  $E_{\text{cut}}$  refers to the one specified in the POTCAR file, the energy cutoffs applied in the HF and RPA calculations are given in Tab. 11.9. In the third column, the states treated as valence are indicated. As local potential a pseudopotential was generated for the states indicated in the column "local". For some elements (Li, Cu, Rh, Pd, Ag<sub>2</sub>), the local potential was generated by replacing the AE potential by a soft potential within the cutoff radius  $r_{\text{loc}}$  (a.u.), which, in these cases, is provided in the "local" column. For more details see Ref. [15].

	name	valence	local	$r_c^l$ (a.u.)				$E_{\text{cut}}$ (eV)
				$s$	$p$	$d$	$f$	
Li	Li_sv_GW	1s 2s	1.0	3×1.2	2×1.5			433
B	B_GW	2s 2p	3d	2×1.5	2×1.7			319
C	C_GW	2s 2p	3d	2×1.2	2×1.5			414
O	O_GW	2s 2p	3d	2×1.2	2×1.5			414
F	F_d_GW	2s 2p	4f	3×1.1	2×1.4	2×1.4		487
Na <sub>1</sub>	Na_d_GW	3s	4f	2×2.5	2×3.0	2×2.5		82
Na <sub>2</sub>	Na_sv_GW	2s 2p 3s	4f	3×1.6	2×2.0	2×2.2		260
Al	Al_d_GW	3s 3p	4f	2×1.9	2×1.9	2×1.9		241
Si <sub>1</sub>	Si_d_GW	3s 3p	4f	1.5 1.9	2×1.9	2×1.9		246
Si <sub>2</sub>	Si_sv_GW	2s 2p 3s 3p	4f	2×1.2 1.4	3×1.5	2×1.6		475
P	P_d_GW	3s 3p	4f	2×1.9	2×1.9	2×2.0		255
Cl	Cl_d_GW	3s 3p	4f	2×1.7	2×1.9	2×1.9		262
Cu	Cu_GW	4s 3d	1.5	2×2.2	2×2.2	2×1.9		417
Rh	Rh_f_GW	5s 4d	1.6	2×2.4	2×2.8	2×2.4	2×2.6	247
Pd	Pd_f_GW	5s 4d	1.6	2×2.4	2.4 2.6	2×2.4	2×2.6	250
Ag <sub>1</sub>	Ag_GW	5s 4d	4f	2×2.5	2×2.6	2×2.4		250
Ag <sub>2</sub>	Ag_f_GW	5s 4d	1.4	2×2.5	2×2.6	2×2.4	2×2.6	250

## 11.5 Solids

In this section, RPA-ACFDT lattice constants, bulk moduli, and atomization energies of representative insulators, semiconductors, and metals will be presented. The considered materials range from covalently bonded systems like C and Si to strongly ionic ones (NaF, NaCl), from simple *sp*-metals (Na, Al) to the *d*-metals Cu, Ag, Rh and Pd.

For the calculation of the RPA-ACFDT correlation energy the formalism introduced in chapter 3 is applied. More technical details have been addressed in chapter 10 and have already been discussed for practical applications in Sec. 11.1 (molecules) and Sec. 11.2 (rare gas solids). Convergence tests for metals have been the topic of Sec. 11.3 and Sec. 11.4 and will not be considered here anymore. Correlation energies for metals are evaluated by including the  $\Gamma$ -point correction (Method B in section 10.3) and the HF energy part is calculated at a dense  $k$ -point grid (denser than for the correlation energy). The theoretical (DFT-PBE, DFT-LDA, HF, RPA-ACFDT) equilibrium volume ( $V_0$ ), bulk moduli ( $B_0$ ), and bulk energy

Table 11.9: Settings for HF and RPA-ACFDT correlation calculations. The (different) energy cutoffs  $E_{\text{cut}}$  (eV) and  $k$ -point grids ( $\Gamma$ -centered  $\text{kp} \times \text{kp} \times \text{kp}$ ) used for HF and ACFDT calculations are labeled with  $HF$  and  $AC$ , respectively. The last three columns give the value of LMAXFOCKAE (short: LM), the frequency grid (number of frequency points - NOMEGA / maximal frequency OMEGATL), and the method used for the frequency integration. Convergence tests employing different energy cutoffs (or LMAXFOCKAE for the case of AIP) are referred to as calculation (1) and (2). The potentials are labeled as in Tab. 11.8.

name	structure	$E_{\text{cut}}^{HF}$	$\text{kp}^{HF}$	$E_{\text{cut}}^{AC}$	$\text{kp}^{AC}$	LM	$\omega$	method
C	A4 (diamond)	700	12	460/250	8	2	16/800	40(0.10)
Si <sub>1</sub> C	B3 (zinc blende)	500	12	460/250	6	2	16/800	4
Si <sub>1</sub>	A4 (diamond)	500	12	360/200	8	2	16/500	40(0.10)
Si <sub>2</sub>	A4 (diamond)	700	8	500/200	6	4	16/800	40(0.05)
BP	B3 (zinc blende)	360	10	360/200	6	2	12/800	4
AIP (1)	B3 (zinc blende)	360	10	360/200	6	2	12/800	4
AIP (2)	B3 (zinc blende)	360	10	360/200	6	4	12/800	4
MgO	B1 (NaCl)	900	8	460/250	6	2	12/800	4
LiF (1)	B1 (NaCl)	900	8	600/350	6	2	12/800	4
LiF (2)	B1 (NaCl)	900	8	460/250	6	2	12/800	4
Na <sub>2</sub> F	B1 (NaCl)	800	8	460/250	6	2	12/800	4
Na <sub>2</sub> Cl	B1 (NaCl)	460	8	460/250	6	2	12/800	4
Na <sub>1</sub>	A2 (bcc)	200	16	200/120	16	2	12/800	40(0.4)
Na <sub>2</sub>	A2 (bcc)	600	14	360/200	10	2	16/800	40(0.4)
Al	A1 (fcc)	360	20	300/200	16	2	16/800	40(0.4)
Cu	A1 (fcc)	600	16	460/250	12	4	16/800	40(0.2)
Ag <sub>1</sub> (1)	A1 (fcc)	460	16	460/250	10	4	16/800	40(0.2)
Ag <sub>1</sub> (2)	A1 (fcc)	460	16	300/200	12	4	16/800	40(0.2)
Ag <sub>2</sub>	A1 (fcc)	460	16	300/200	12	4	16/700	40(0.2)
Rh	A1 (fcc)	360	16	300/200	16	4	16/700	40(0.2)
Pd	A1 (fcc)	360	16	300/200	16	4	16/700	40(0.2)

( $E_0$ ) are obtained by evaluating the total energies at seven volume points centered around the experimental volume and differing by 5 % each. A Birch-Murnaghan equation of states is fitted to these energies and volumes:

$$E(V) = E_0 + \frac{9V_0B_0}{16} \left\{ \left[ (V_0/V)^{\frac{2}{3}} - 1 \right]^3 B'_0 + \left[ (V_0/V)^{\frac{2}{3}} - 1 \right]^2 \left[ 6 - 4(V_0/V)^{\frac{2}{3}} \right] \right\}. \quad (11.3)$$

If the theoretical volume is far from the experimental one, as is e.g., the case for the HF values for metals, additional volume points are introduced. In the following we aim at an (technical) accuracy of 0.3 % for the volume ( $\approx 0.1$  % in the lattice constant) and of about 3% for the bulk modulus. In Tab. 11.8, the potentials applied in this section are presented. The states treated as valence, the type of the local potential, and the cutoff radii used for the construction of the pseudized partial waves and the projectors are summarized. Additional, the energy cutoff  $E_{\text{cut}}$  specified in the POTCAR files is denoted. The actual energy cutoffs applied in calculation of the HF and RPA correlation energy are summarized in Tab. 11.9.

Throughout this section, special *GW* potentials are used. These potentials are constructed as to describe the scattering properties of a spherical atom accurately up to an energy of  $\approx 10$  Ry and therefore are also suited to represent unoccupied states properly. Due to the inclusion of unoccupied states in the ACFDT formalism, *d*-projectors have been introduced for the row 3 elements (Na, Al, Si, P), where the *3d* states, while unoccupied, are situated very close to the Fermi energy. Due to the same reason, a  $\text{Ag}_2$  potential including *f*-projectors has been constructed. The potential without *f*-projectors is referred to as  $\text{Ag}_1$  potential. *f*-projectors are also added for Rh and Pd. For two cases, Si and Na, the effect introduced by treating deeper lying electrons as valence has been tested. In the standard Si potential,  $\text{Si}_1$ , all electrons, but the *3s* and *3p* electrons, are kept fixed in the core. For the  $\text{Si}_2$  potential the *2s* and *2p* electrons have been included in the valence. Both potentials have already occurred in Sec. 10.1 where the dependence on  $E_{\text{cut}}^{\chi}$  has been discussed. Both potentials,  $\text{Si}_1$  and  $\text{Si}_2$ , result in very similar lattice constants and bulk moduli, as will be shown later. Thus, the frozen core approximation seems also to be valid for the calculation of correlation energies. For Na the situation is slightly more complex. Here two potentials,  $\text{Na}_1$  and  $\text{Na}_2$ , have been constructed, with the *3s* ( $\text{Na}_1$ ) and *2s2p3s* ( $\text{Na}_2$ ) electrons in the valence, respectively. For NaF and NaCl the inclusion of the *2s* and *2p* electrons is necessary already on the DFT level since the F *2s* and the Cl *3s* states are close to the Na *2p* states. The  $\text{Na}_2$  potential is therefore used in all calculations of these materials. For the Na bulk, significant differences between the lattice constant and the bulk modulus are obtained using the  $\text{Na}_1$  and  $\text{Na}_2$  potential, respectively. This difference will be discussed in more detail later.

Tab. 11.9 lists the materials for which RPA-ACFDT energies have been calculated in this section. Besides the considered structures, *k*-point grids, and energy cutoffs for the HF energy and for the RPA correlation energy are summarized. In most cases, the number of *k*-points and the energy cutoff are not the same for the HF and the RPA-ACFDT calculations. Since the calculation of the HF energy requires a denser *k*-point grid and a larger energy cutoff, we have found that an independent choice of the *k*-point grid and energy cutoff  $E_{\text{cut}}$  for the HF and the correlation energy is advantageous. For the evaluation of the correlation energy additional parameters have to be considered. Beside the energy cutoff  $E_{\text{cut}}$ , the maximal dimension of the response function as determined by  $E_{\text{cut}}^{\chi}$  is relevant. In Tab. 11.9 this quantity is specified together with the energy cutoff  $E_{\text{cut}}$  used in the ACFDT calculations:  $E_{\text{cut}}/E_{\text{cut}}^{\chi}$ . In the next column the maximal angular momentum number LMAXFOCKAE (LM) up to which the exact all-electron charge density is reconstructed for the evaluation of the response function is summarized. The last two columns list the parameters used in the frequency integration. The number of frequency points and the maximal frequency as well as the frequency integration method (see Sec. 10.2) are specified. The settings used for the evaluation of the HF and the RPA correlation energy have been extensively tested. The *k*-point numbers and the value of the energy cutoff cited in Tab. 11.9 guarantee atomization energies that are technical converged to  $\approx 20$  meV (volume convergence of atomic energies excluded). For the evaluation of converged lattice constants and bulk moduli generally coarser *k*-point grids can be applied.

For some systems, lattice constants, bulk moduli, and atomization energies obtained using different technical parameters will be presented. For AlP results using LMAXFOCKAE = 2 and 4 will be presented, for LiF and  $\text{Ag}_1$  the influence of different energy cutoffs will be considered. The different calculations are referred to as calculation (1) and (2).

Table 11.10: Lattice constants in Å. Values in parenthesis are deviations from the experimental lattice constant in percent. Bold letters refer to data obtained from DFT-LDA wavefunctions and eigenenergies. In all other cases DFT-PBE input has been used. Theoretical lattice constants are not corrected for zero-point vibrations or finite temperature effects. All experimental data (except for AlP [138]) have been taken from Ref. [139] (and correspond to the ones cited in Ref. [37, 140, 141]).

name	PBE		LDA		HF		RPA		Exp.
C	3.569	(0.1)	3.534	(−0.9)	3.540	(−0.8)	3.572	(0.1)	3.567
C	LDA eigenen. and wavefunc.				<b>3.540</b>	(−0.8)	<b>3.574</b>	(0.2)	3.567
Si <sub>1</sub> C	4.378	(0.5)	4.332	(−0.6)	4.351	(−0.2)	4.366	(0.2)	4.358
Si <sub>1</sub>	5.466	(0.7)	5.404	(−0.5)	5.482	(1.0)	5.431	(0.0)	5.430
Si <sub>1</sub>	LDA eigenen. and wavefun.				<b>5.479</b>	(0.9)	<b>5.432</b>	(0.0)	5.430
Si <sub>2</sub>	5.480	(0.9)	5.405	(−0.5)	5.497	(1.2)	5.435	(0.1)	5.430
BP	4.546	(0.2)	4.493	(−1.0)	4.566	(0.6)	4.536	(−0.0)	4.538
AlP (1)	5.501	(0.9)	5.435	(−0.3)	5.514	(1.2)	5.468	(0.3)	5.451
AlP (2)	5.501	(0.9)	5.435	(−0.3)	5.514	(1.2)	5.471	(0.4)	5.451
MgO	4.259	(1.2)	4.169	(−0.9)	4.173	(−0.8)	4.225	(0.4)	4.207
LiF (1)	4.069	(1.5)	3.913	(−2.4)	3.991	(−0.5)	3.998	(−0.3)	4.010
LiF (2)	4.069	(1.5)	3.913	(−2.4)	3.991	(−0.5)	4.004	(−0.1)	4.010
Na <sub>2</sub> F	4.707	(2.1)	4.511	(−2.1)	4.614	(0.1)	4.625	(0.3)	4.609
Na <sub>2</sub> Cl	5.697	(1.8)	5.469	(−2.3)	5.778	(3.3)	5.588	(−0.1)	5.595
Na <sub>1</sub>	4.183	(−1.0)	4.051	(−4.1)	4.453	(5.4)	4.254	(0.7)	4.225
Na <sub>2</sub>	4.196	(−0.7)	4.056	(−4.0)	4.494	(6.4)	4.182	(−1.0)	4.225
Al	4.035	(0.1)	3.983	(−1.2)	4.104	(1.8)	4.034	(0.1)	4.032
Cu	3.634	(0.9)	3.523	(−2.2)	3.968	(10.1)	3.601	(−0.1)	3.603
Ag <sub>1</sub> (1)	4.146	(1.9)	4.003	(−1.6)	4.504	(10.7)	4.097	(0.7)	4.069
Ag <sub>1</sub> (2)	4.146	(1.9)	4.003	(−1.6)	4.504	(10.7)	4.096	(0.7)	4.069
Ag <sub>2</sub>	4.146	(1.9)	4.002	(−1.6)	4.507	(10.8)	4.089	(0.5)	4.069
Rh	3.824	(0.7)	3.753	(−1.2)	3.748	(−1.3)	3.810	(0.3)	3.798
Pd	3.935	(1.4)	3.830	(−1.3)	3.972	(2.3)	3.872	(−0.2)	3.881

### 11.5.1 Lattice constants and bulk moduli

In this subsection, structural properties arising from RPA-ACFDT energies are presented. Lattice constants (Tab. 11.10) and bulk moduli (Tab. 11.11) have been obtained by fitting the energy for different volume points to the Birch-Murnaghan equation of states. In addition to the RPA values, lattice constants and bulk moduli from DFT-LDA and DFT-PBE energies and from HF energies are presented. The HF energies stem from an evaluation of the HF energy expression for DFT wavefunctions. The (total) RPA energies equal the sum of these HF energies and the RPA correlation energy. If not otherwise mentioned, HF energies and RPA correlation energies are calculated from DFT-PBE wavefunctions and eigenenergies. Results from test calculations employing DFT-LDA input are highlighted by bold letters. In addition to the absolute values of the lattice constants and the bulk moduli, the errors (%) with respect to the experimental values are given in parenthesis. Before discussing the results in detail, the settings required in order to obtain accurate geometrical properties



should be considered. For metals this topic has already been discussed in Sec. 11.4, so that we will here focus only on semiconductors and insulators. In Tab. 11.9 the settings for the  $k$ -point grid and for the energy cutoff used for the present calculations have been summarized. These dense  $k$ -point grids and large energy cutoffs have been applied to obtain accurate atomization energies (no  $\text{Si}_2$  atomization energies have been calculated). In most cases, less effort is required for the geometrical properties. As an example we consider the Si and C lattice constants and bulk moduli for different settings. For the Si lattice constant and bulk modulus presented in Tab. 11.10 and Tab. 11.11, a  $12 \times 12 \times 12$  ( $8 \times 8 \times 8$ )  $k$ -point grid and an energy cutoff of 500 eV (360 eV) have been applied for the calculation of the HF (RPA correlation) energy. In fact, very accurate HF values (5.481 Å, 108 GPa) are already obtained for a  $6 \times 6 \times 6$   $k$ -point grid and an energy cutoff of 360 eV. But the reduction from the 12 to the 6  $k$ -point grid leads to an error of almost 60 meV in the total HF energy. For an  $8 \times 8 \times 8$  grid the error has reduced to slightly over 20 meV. Also for the RPA correlation energy, a reduction of the  $k$ -point grid (from 8 to 6) and reduction of the energy cutoff (from 360 eV to 300 eV) results in almost the same RPA lattice constant and bulk modulus. The effect of the  $k$ -point reduction on the energy is smaller than for the HF part and amounts to  $\approx 10$  meV. For diamond, the same behavior as for Si can be observed for the HF related quantities. Again, a reduction of the HF  $k$ -point grid from  $12 \times 12 \times 12$  to  $6 \times 6 \times 6$  does not alter the lattice constant and the bulk modulus, but the total HF energy is reduced by almost 60 meV. For the RPA correlation energy of diamond, the  $8 \times 8 \times 8$   $k$ -point grid could be reduced to  $6 \times 6 \times 6$  without changing to the energy. Like for Si and C, the HF  $k$ -point grids can be safely reduced for all insulators and semiconductors, if only geometrical properties are of interest. For all considered semiconductors and insulators (Si being the exception) a  $4 \times 4 \times 4$  grid for the RPA correlation energy results in accurate lattice constants and bulk moduli.

We now focus on the lattice constants and bulk moduli summarized in Tab. 11.10 and Tab. 11.11. The systems are grouped by their bonding type, ranging from covalent to ionic to metallic and within each group the systems are arranged according to their atomic weight. The relative errors of the theoretical lattice constants for semiconductors/insulators and metals are visualized in Fig. 11.8 and Fig. 11.9. The DFT lattice constants and bulk moduli follow the general PBE and LDA trend: Lattice constants are too small if the LDA is applied, whereas PBE normally overestimates the equilibrium volume. Accordingly, LDA predicts too large bulk moduli, and PBE too small ones. The only system that deviates from this trend is Na. Here both PBE and LDA underestimate the lattice constant and predict a too large bulk modulus. The DFT-PBE and DFT-LDA errors become larger when moving from covalent to ionic systems. The largest error in the lattice constant occurs for the sodiumhalogenides, where DFT-PBE yields a deviation of 2.1 % for NaF and DFT-LDA -2.3 % for NaCl. In the next step, the equilibrium geometries stemming from HF energies, and thus neglecting correlation effects altogether, will be considered. The lattice constants as obtained from the HF energy expression evaluated for DFT(-PBE) wavefunctions are listed in Tab. 11.10 (HF). The presented HF lattice constants are not only of interest for a comparison to the RPA lattice constants but are also interesting per se. In fact, only few data on HF energies for solids can be found in the literature. Although RPA-ACFDT calculations for solids require the evaluation of the HF energy for periodic systems, and although such RPA-ACFDT calculations have been presented before [128, 129, 130] (performed using the



Table 11.11: Bulk Moduli in GPa. Values in parenthesis are deviations from the experimental bulk modulus in percent. Bold letters refer to data obtained from DFT-LDA wavefunctions and eigenenergies. In all other cases DFT-PBE input has been used. Theoretical lattice constants are not corrected for zero-point vibrations or finite temperature effects. All experimental data (except for AlP [142]) have been taken from Ref. [139] (and correspond to the one cited in Ref. [37, 140, 141]).

name	PBE		LDA		HF		RPA		Exp
C	434	(-2)	465	(5)	512	(16)	442	(-0)	443
C	LDA eigenen. and wavefun.				<b>509</b>	(15)	<b>439</b>	(-1)	443
Si <sub>1</sub> C	212	(-6)	229	(2)	253	(12)	223	(-1)	225
Si <sub>1</sub>	89	(-11)	97	(-3)	108	(9)	99	(-0)	99.2
Si <sub>1</sub>	LDA eigenen. and wavefun.				<b>108</b>	(9)	<b>98</b>	(-1)	99.2
Si <sub>2</sub>	87	(-12)	96	(-3)	105	(6)	95	(-4)	99.2
BP	161	(-2)	175	(6)	181	(9)	170	(3)	165
AlP (1)	83	(-4)	90	(5)	100	(16)	93	(8)	86 <sup>a</sup>
AlP (2)	83	(-4)	90	(5)	100	(16)	92	(6)	86 <sup>a</sup>
MgO	149	(-10)	173	(5)	196	(19)	168	(2)	165
LiF (1)	68	(-3)	87	(24)	80	(15)	76	(9)	69.8 <sup>a</sup>
LiF (2)	68	(-3)	87	(24)	80	(15)	79	(14)	69.8 <sup>a</sup>
Na <sub>2</sub> F	45	(-12)	61	(19)	54	(4)	53	(3)	51.4
Na <sub>2</sub> Cl	24	(-11)	32	(20)	22	(-15)	29	(8)	26.6
Na <sub>1</sub>	8.0	(7)	9.4	(25)	5.6	(-25)	7.6	(1)	7.5
Na <sub>2</sub>	7.9	(5)	9.1	(21)	5.4	(-27)	8.4	(12)	7.5
Al	77	(-3)	84	(6)	61	(-24)	75	(-5)	79
Cu	138	(-3)	186	(31)	32	(-77)	157	(11)	142
Ag <sub>1</sub> (1)	90	(-17)	138	(27)	26	(-76)	107	(-2)	109
Ag <sub>1</sub> (2)	90	(-17)	138	(27)	26	(-76)	105	(-3)	109
Ag <sub>2</sub>	90	(-17)	138	(27)	27	(-75)	101	(-7)	109
Rh	255	(-5)	317	(18)	318	(18)	254	(-6)	269
Pd	162	(-17)	226	(16)	112	(-43)	200	(3)	195

<sup>a</sup> experimental bulk moduli obtained from different measurements can exhibit sizable differences. For AlP in Ref. [142] a second value of 93.1 GPa is cited. The experimental bulk moduli for LiF is stated to be as large as 76.9 GPa in Ref. [143].

ABINIT/SELF-code in Ref. [129, 130]), we have not found any publication presenting HF energies, lattice constants, and bulk moduli evaluated with this code. To the best of our knowledge, the only code routinely used to calculate HF lattice constants, bulk moduli, and atomization energies for solids is the CRYSTAL code, which relies on Gaussian-type basis functions. But achieving convergence of HF energies (lattice constants and bulk moduli) applying a Gaussian basis set seems to be difficult [145]. Furthermore, the use of the same basis set for the solid and the reference atom leads to fairly large basis set superposition errors. In order to fulfill the different requirements for the basis set of the solid and the reference atom, counterpoise corrections can be applied to the energy of the reference atoms. More details and the effect of these counterpoise corrections (applied to metallic systems)

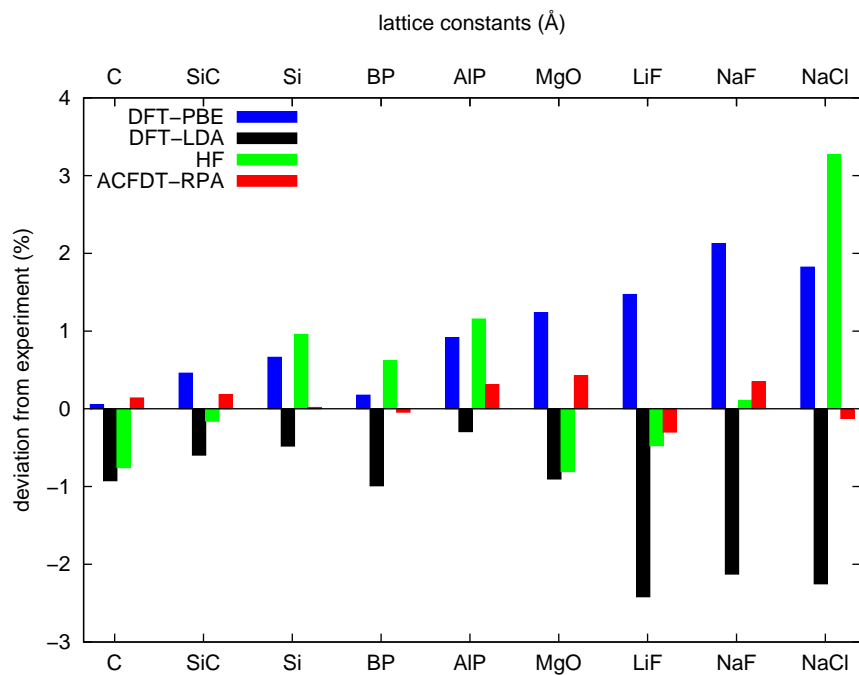


Figure 11.8: Relative error (%) of the theoretical lattice constants of semiconductors and insulators.

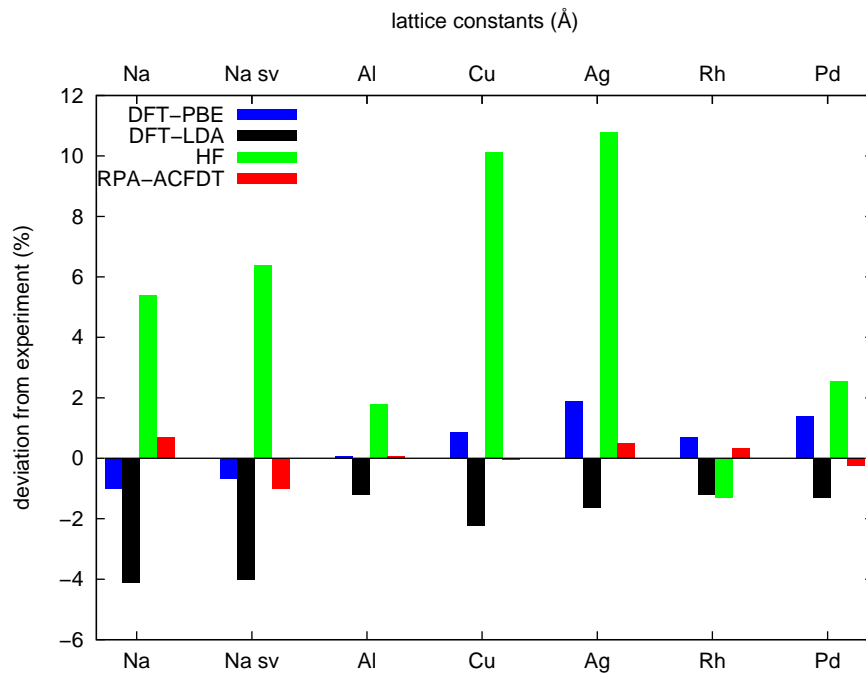


Figure 11.9: Relative error (%) of the theoretical lattice constants of metals.

Table 11.12: HF and DFT-LDA lattice constants ( $\text{\AA}$ ) from the present work and from literature. The HF lattice constants in the second column stem from non-selfconsistent (NSC) HF energies evaluated from PBE wavefunctions and correspond to the values shown in Tab. 11.10. In the next column, lattice constants obtained from self-consistent (SC) HF calculations are summerized. The core-valence interaction is thereby evaluated for HF core wavefunctions. All previous HF lattice constants have been obtained from the CRYSTAL code, which uses Gaussian orbitals. The importance of the chosen basis set and treatment of counterpoise corrections can be seen by comparing  $^{b1,b2}$  and  $^{f1,f2}$  data.

name	HF lattice constants ( $\text{\AA}$ )					LDA lattice constants ( $\text{\AA}$ )		
	NSC	SC	literature			present	literature	
C	3.540	3.552	3.577 <sup>b1</sup>	3.574 <sup>b2</sup>	3.58 <sup>d</sup>	3.534	3.544 <sup>a</sup>	3.56 <sup>d</sup>
SiC	4.351	4.372	4.438 <sup>b1</sup>	4.390 <sup>b2</sup>		4.332	4.351 <sup>a</sup>	
Si	5.482	5.512	5.558 <sup>b1</sup>	5.501 <sup>b2</sup>	5.49 <sup>d</sup>	5.404	5.426 <sup>a</sup>	5.40 <sup>d</sup>
BP	4.566	4.588	4.656 <sup>b1</sup>	4.598 <sup>b2</sup>	4.5836 <sup>e</sup>	4.493		
AlP	5.514	5.546	5.598 <sup>b1</sup>	5.553 <sup>b2</sup>	5.55 <sup>d</sup>	5.435	5.47 <sup>d</sup>	
MgO	4.173	4.197	4.21 <sup>d</sup>			4.169	4.156 <sup>a</sup>	4.18 <sup>d</sup>
LiF	3.991	4.003	4.02 <sup>c</sup>			3.913	3.904 <sup>a</sup>	
NaF	4.614		4.63 <sup>c</sup>			4.511	4.505 <sup>a</sup>	
NaCl	5.778		5.80 <sup>c</sup>	5.79 <sup>d</sup>		5.469	5.471 <sup>a</sup>	5.48 <sup>d</sup>
Na	4.494		4.42 <sup>f1</sup>	4.57 <sup>f2</sup>		4.051	4.049 <sup>a</sup>	4.05 <sup>f</sup>
Al	4.104					3.983	4.008 <sup>a</sup>	
Cu	3.968		3.89 <sup>f1</sup>	4.06 <sup>f2</sup>		3.523	3.530 <sup>a</sup>	3.52 <sup>f</sup>
Ag	4.507		4.38 <sup>f1</sup>	4.49 <sup>f2</sup>		4.003	3.997 <sup>a</sup>	4.01 <sup>f</sup>

<sup>a</sup> [144] GAUSSIAN code, Gaussian type orbitals

<sup>b</sup> [145] CRYSTAL code, Gaussian type orbitals, <sup>b1</sup> 6-21G basis set, <sup>b2</sup> 6-21G\* basis set

<sup>c</sup> [146] CRYSTAL

<sup>d</sup> [147] CRYSTAL

<sup>e</sup> [148] CRYSTAL

<sup>f</sup> [149] CRYSTAL, <sup>f1</sup> no counterpoise corrections, <sup>f2</sup> counterpoise corrections

can be found in Ref. [149]. Our HF lattice constants therefore provide the first summary of HF lattice constants and atomization energies for solids obtained using a plane wave basis set code, or more precisely, the lattice constants and atomization energies stemming from a non-selfconsistent evaluation of the HF energy for DFT wavefunctions. In order to estimate the effect of selfconsistency, we calculated the selfconsistent HF lattice constants and bulk moduli for C, Si, and MgO. Our self-consistent HF values stem from a frozen core Hartree-Fock calculation, and the core-valence exchange interaction is evaluated using AE DFT-PBE core wavefunctions. This limitation can be lifted and it is possible to recalculate the core-valence interactions using AE HF core wavefunctions. The respective lattice constants have been evaluated by Martijn Marsman [150]. The HF lattice constant and bulk modulus calculated from the selfconsistent HF case are 3.546  $\text{\AA}$  and 501 GPa for diamond, if the core-valence interaction is evaluated using AE PBE-wavefunctions. This amounts to a change of +0.2 % in the lattice constant and of -2 % in the bulk modulus with respect to our

non-selfconsistent HF values. If the core states stem from a HF reference calculation, the selfconsistent HF lattice constant further increases to 3.552 Å (+0.3 % compared to the non-selfconsistent HF value). For Si and MgO, the selfconsistent HF lattice constants become 5.493 Å (+0.2 %) and 4.187 Å (+0.3%), the bulk moduli 105 GPa (−3 %) and 185 GPa (−6 %), if the core-valence interaction is recalculated using PBE core wavefunctions. Using HF core wavefunctions enhances the difference, and the selfconsistent HF lattice constants become 5.512 Å (+0.5 %) and 4.197 Å (+0.6%) for Si and MgO, respectively. Also for the other considered materials, selfconsistency leads to an increase of the HF lattice constant (see Tab. 11.12). If the core-valence interaction is recalculated using HF core wavefunctions, the corresponding lattice constants are 0.3 % to 0.6 % larger than the values stemming from non-selfconsistent HF calculations based on PBE wavefunctions. In Tab. 11.12, our HF lattice constants are compared to values obtained using the CRYSTAL code. In addition, selfconsistent HF lattice constants recalculating the core-valence interaction with HF core wavefunctions as evaluated by Martijn Marsman are presented. Even on the level of DFT-LDA, lattice constants obtained using a local and a plane wave basis set can differ by  $\approx 0.4$  %. For most considered systems, the plane wave LDA lattice constants are smaller than the ones evaluated using Gaussian type orbitals. It is evident that HF lattice constants evaluated using CRYSTAL show large deviations for different basis sets applied. In Ref. [145], lattice constants have been calculated for C, SiC, Si, BP, and AlP using the CRYSTAL code. The results, labeled with <sup>b1</sup> and <sup>b2</sup> in Tab. 11.12, have been obtained for two different local basis sets, 6-21G and 6-21G\*, where the latter includes polarization functions. For SiC, Si, BP, and AlP, the difference between the HF lattice constants obtained from the 6-21G and 6-21G\* basis set amounts to  $\approx 1\%$ . If we take the 6-21G\* lattice constant as a reference, the difference between our self-consistent lattice constants and the CRYSTAL values is 0.6 % for diamond and  $<0.4$  % for the other materials, which is smaller than the error observed for different local basis sets. For metallic systems, the basis set superposition error plays an important role. The inclusion of counterpoise corrections leads to a change of up to 4 % (Cu) in the lattice constant. The difference between the counterpoise corrected lattice constants from Ref. [145] and our (non-selfconsistent) HF values is 1.5 % for Na, 2.3 % for Cu, and −0.4 % for Ag.

For semiconductors and insulators (see Fig. 11.8), the HF lattice constants (errors in green) are not worse than DFT-LDA (black) and DFT-PBE (blue). As a general trend, too small lattice constants are obtained for the lighter systems and too large ones for solids formed of heavier atoms. An illustrative example are the alkali halides LiF, NaF, and NaCl where the error in the lattice constant increases from −0.5 to 0.1 to 3.3 %. The same trend as observed in the present work was also found by Prencipe and coworkers [147] (see values in Tab. 11.12), who performed HF calculations for alkali halides. They ascribed the increase in the HF lattice constant when going from F to Cl to two effects: first, due to the lack of correlation, the HF ions are too large. Secondly, dispersion forces (which are neglected if only the HF contribution is considered) are proportional to the polarization of the atoms and the polarization is again larger for heavier atoms. The neglect of the attractive polarization effects therefore leads to an increase of the lattice constant with the atomic mass. For the presently considered semiconductors and insulators the HF bulk moduli are normally too large. The only exception from this trend is NaCl, where the bulk modulus is underestimated by −15 %.

Almost all HF lattice constants (bulk moduli) presented in Tab. 11.10 (Tab. 11.11) have been evaluated on top of DFT-PBE wavefunctions. Only for C and Si, values resulting from DFT-LDA input are shown as well (bold numbers). The effect of the different exchange-correlation potential is very small. Another test concerns the effect introduced if deeper lying states are included in the valence. For two materials, Si and Na, such potentials have been generated and are referred to as  $\text{Si}_2$  and  $\text{Na}_2$ . For Si, the effect resulting from the increased number of valence electrons amounts to a change of +0.3 % in the lattice constant. For Na, the difference in the lattice constant related to the use of either the  $\text{Na}_1$  or  $\text{Na}_2$  potential is with an 1.0 % change significantly larger. The magnitude of this change is too large to be related to an insufficient  $k$ -point grid or energy cutoff, it has to be related to the choice of the potentials. One reason why the inclusion of  $2s$  and  $2p$  electrons results in larger deviations for Na than for Si can be found in the energetic vicinity of these states to the outer shell states for the case of Na. While the  $2s$  and  $2p$  states are situated  $-133$  eV and  $-90$  eV below the Fermi energy for Si, they are only  $-53$  eV and  $-25$  eV below the Fermi energy for Na. Thus the inclusion of these states is more important for the description of Na. In Fig. 11.10 and Fig. 11.11 the HF energy for Si and Na, respectively, are shown on the left hand side. We will return to the inclusion of deeper lying states when discussing the influence of the RPA correlation energy on the equilibrium volume of Si and Na.

In contrast to the case of semiconductors and insulators, where HF provides a reasonable estimate for the lattice constants and (to a lesser extend) for the bulk moduli, HF fails dramatically for the description of metals. For all considered metals, except for Rh, the HF lattice constants are too large with errors being up to  $\approx 6$  % for Na and 10 % for Cu and Ag. The bulk moduli, which have been overestimated for almost all considered insulators and semiconductors, are now severely underestimated (again with the exception of Rh). The errors in the HF lattice constants and bulk moduli are most severe for the free-electron like metals Na, Cu, and Ag. For Al, and especially for the transition metals Rh and Pd, where the covalent contribution to the binding is significantly stronger, HF yields closer agreement to experiment. In the case of Rh, HF even underestimates the lattice constant, and overestimates the bulk modulus.

We finally focus on the RPA lattice constants and bulk moduli (errors are given in red in Fig. 11.8 and Fig. 11.9). The inclusion of correlation effects drastically improves the geometrical properties of the metallic systems compared to HF. For sodium, the error in the lattice constant is reduced from over 6 % to under 1 % (mind the relative large deviations of values obtained using the  $\text{Na}_1$  and  $\text{Na}_2$  potential). For the noble metals Cu and Ag, the relative errors are  $-0.1$  % for Cu and  $0.5$  % for Ag compared to a 10 % mismatch in the HF case. A similar improvement is observed for the bulk moduli. For the semiconductors and insulators, the quality of the RPA lattice constants is even better than for the metals, with a maximal error of  $0.4$  % for AlP and MgO, although the improvement compared to the already relative good HF values is not as impressive. In contrast to the DFT lattice constants, which exhibit increasing errors when the ionic character of the material prevails, and the HF values, for which the error depends on the atomic weight, the RPA lattice constants give constantly good results for covalent, ionic, and metallic systems and show no dependence on the weight. The RPA bulk moduli tend to exceed the experimental values. All in all, we find that the RPA provides a very good description of geometrical properties for metals, semiconductors, and insulators.

Some tests of the computational settings for the RPA calculations are also provided in Tab. 11.10 and Tab. 11.11. First, the influence on the exchange-correlation potential used for the calculation of the DFT wavefunctions and eigenenergies has been tested for C and Si, where RPA lattice constants obtained from DFT-LDA (bold) are shown together with results from DFT-PBE. For the RPA lattice constant, the deviations are small, 0.06 % for C and 0.02 % for Si. Also the bulk moduli do not differ by more than 1 %. Another test concerns the energy cutoffs  $E_{\text{cut}}/E_{\text{cut}}^{\chi}$  used in the calculation of the RPA correlation energy. Lattice constants obtained for different energy cutoffs have been analyzed for LiF and Ag (Ag<sub>1</sub> potential). LiF constitutes the material with the highest requirement on the energy cutoff that is considered in the present work. For this material the increase from 460/250 eV to 600/350 eV for  $E_{\text{cut}}/E_{\text{cut}}^{\chi}$  still leads to a change of 0.15 % in the lattice constant and 4 % in the bulk modulus. Additionally, the 460/250 eV correlation energies exhibit a considerable roughness with the volume, which is almost smoothed out for 600/350 eV. For Ag, where the large cutoff of 460/250 eV was chosen for test reasons only, a reduction to 300/200 eV hardly changes the lattice constant and bulk modulus. This test also confirms that reliable geometrical properties can already be obtained if the absolute RPA energies are not converged with the energy cutoff  $E_{\text{cut}}$ , as this is the case for LiF and Ag. A similar test for the atomization energies will be the topic of the next section. The influence of the inclusion of deeper lying (core) electrons in the valence has already been discussed for the HF lattice constants and bulk moduli. In Fig. 11.10 and Fig. 11.11 the contributions solely stemming from the HF and the RPA correlation energy (left hand side), as well as the total RPA correlation energy arising from the sum of these contributions (right hand side), are presented for Si and Na, respectively. Results obtained using both - potentials including

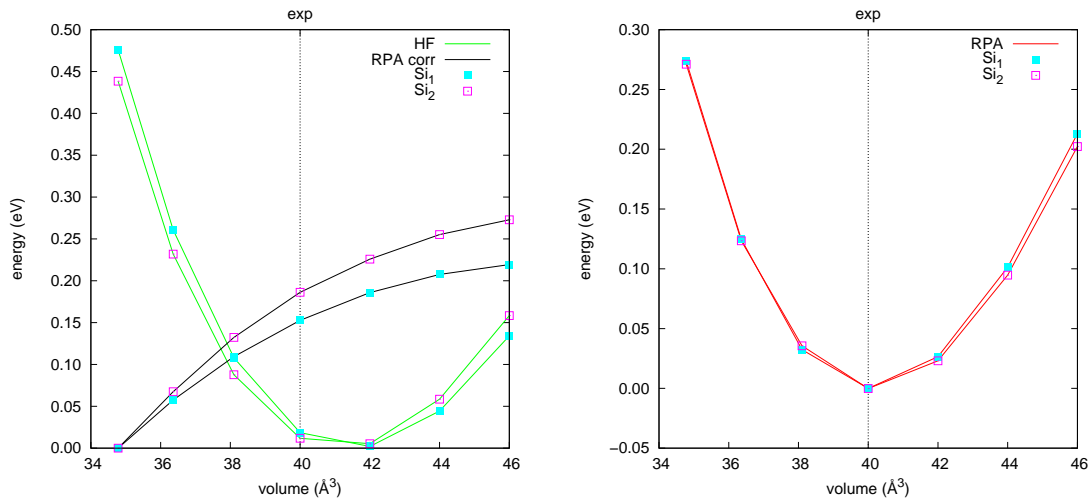


Figure 11.10: On the left hand side, the HF energy (green) and the RPA correlation energy (black) evaluated for the Si<sub>1</sub> potential (valence: 3s3p) and Si<sub>2</sub> potential (valence: 2s2p3s3p) are shown. The HF energy is given with respect to the energy minimum, the RPA correlation energy with respect to the energy for the smallest volume. On the right hand side, total RPA energies are shown for the two potentials.

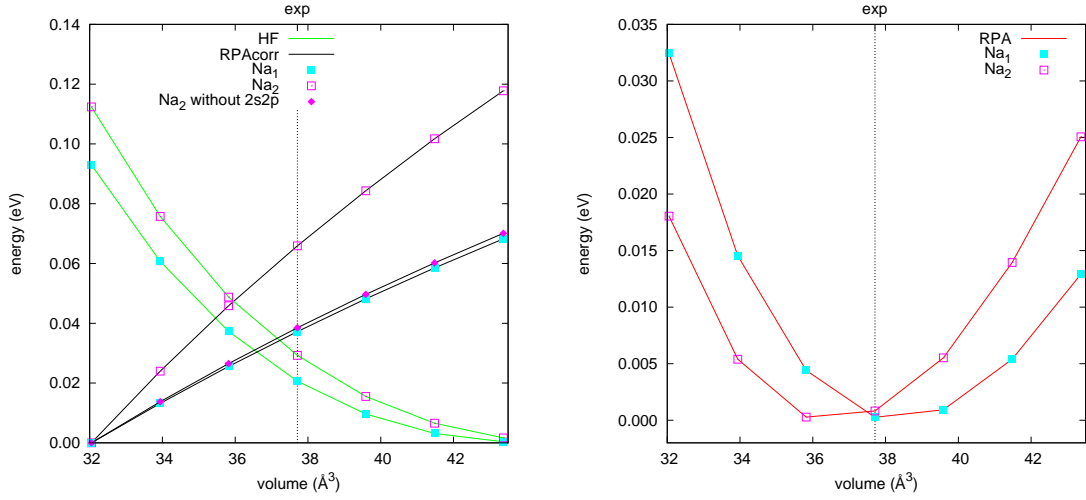


Figure 11.11: On the left hand side, the HF energy (green) and the RPA correlation energy (black) evaluated for the  $\text{Na}_1$  potential (valence:  $3s$ ) and  $\text{Na}_2$  potential (valence:  $2s2p3s$ ) are shown. Additionally, the correlation energy evaluated from the  $\text{Na}_2$  potential, but omitting the contributions of the  $2s2p$  states, is presented. The HF energy is given with respect to the energy minimum, the RPA correlation energy with respect to the energy for the smallest volume. On the right side, the total RPA energy is shown for the two potentials.

only the outermost electrons ( $\text{Si}_1$  and  $\text{Na}_1$ ) and potentials treating also the  $2s$  and  $2p$  states as valence ( $\text{Si}_2$  and  $\text{Na}_2$ ) - are compared. Again, the influence of the different potentials is smaller for Si than for Na. For Si, the difference in the RPA lattice constants obtained from the  $\text{Si}_1$  and  $\text{Si}_2$  potentials amounts only to 0.07 %, and thus is smaller than the difference in the HF lattice constant (0.3 %). The slope of the correlation energy is stronger for the  $\text{Si}_2$  than for  $\text{Si}_1$  potential, the difference in the HF lattice constants is counterbalanced, and the final volume over total RPA energy curves are almost the same for  $\text{Si}_1$  and  $\text{Si}_2$ . For Na, the effect of the  $2s$  and  $2p$  states is stronger and the  $\text{Na}_2$  HF lattice constant is 1 % larger than the  $\text{Na}_1$  one. The addition of the RPA correlation energy does not diminish this difference, but, on the contrary, leads to an overcorrection and the  $\text{Na}_2$  lattice constant is now -1.7 % smaller than the  $\text{Na}_1$  one. In order to isolate the source of this large discrepancy and to eliminate the possibility of an inaccurate construction of the potentials, we calculate the correlation energy stemming from the  $\text{Na}_2$  potential, but exclude the contributions arising from the  $2s$  and  $2p$  states. The resulting energies are shown on the left hand side of Fig. 11.11. The difference between the  $\text{Na}_2$  correlation energy excluding the  $2s$  and  $2p$  electrons and the  $\text{Na}_1$  correlation energy is minimal. Thus the large deviation between the  $\text{Na}_1$  and  $\text{Na}_2$  lattice constant is not due to an inappropriateness of the potentials, but stems from the correlation contributions arising from the polarizability of the core states which obviously can not be neglected for Na.

Finally, some comments on the choice of the maximal angular momentum number up to which the AE charge density (determined by  $\text{LMAXFOCKAE} = \text{LM}$  in Tab. 11.10 and Tab. 11.11) is recovered are in place. For AIP, geometrical properties (and later atomization energies) have been calculated for  $\text{LMAXFOCKAE} = 2, 4$ . Additionally, the number of points



at which the AE charge density is reconstructed was raised from 1 for LMAXFOCKAE = 2 to 2 for LMAXFOCKAE = 4. For these two settings, the lattice constants deviate by a modest 0.05 %, the bulk moduli by 1 %, although the total energy for AIP is changed by  $\approx 0.1$  eV. For AIP these changes can be traced back to the increase of the number of fitting points from 1 to 2 rather than to the increase of LMAXFOCKAE from 2 to 4. For most materials (including e.g., C and Si) reliable lattice constants and bulk moduli can be already obtained if LMAXFOCKAE is not set at all. But exceptions exist: For MgO, for example, the lattice constant is underestimated by almost 0.4 % if LMAXFOCKAE is not set and it therefore seems reasonable to normally make use of this correction.

Table 11.13: Lattice constants for Si and NaCl. Our LDA and RPA values are compared to the results obtained by Marini *et al.* [130]. Only lattice constants obtained by evaluating the HF plus LDA correlation energy (HF+LDAcorr) have been presented in Ref. [130].

Si lattice constants (Å)				NaCl lattice constants (Å)			
method	Ref. [130]	present	diff.	method	Ref. [130]	present	diff.
DFT-LDA	5.382	5.404	-0.4 %	DFT-LDA	5.535	5.469	1.2 %
HF+LDAcorr	5.334	5.397	-1.2 %	HF+LDAcorr	5.503	5.671	-3.0 %
RPA	5.361 <sup>a</sup>	5.431	-1.4 %	RPA	5.503 <sup>a</sup>	5.588	-1.5 %
exp.	5.430	5.430		exp.	5.595	5.595	

<sup>a</sup> The values in Ref. [130] are RPA+ values. As stated in [130], the authors claim that their RPA and RPA+ lattice constants are very similar.

RPA calculations for (realistic) periodic systems are relatively rare. Geometrical properties have been reported for h-BN [41] and Si and NaCl [130]. These values have been calculated using a plane wave basis set and pseudopotentials. We summarize the Si and NaCl lattice constants obtained by Marini *et al.* [130] in Tab. 11.13 and compare their values to our results. Unfortunately, no (pure) HF lattice constants have been published by Marini *et al.* Therefore, we have performed HF+LDA-correlation calculations for which the respective values have been given in Ref. [130] (there denoted as EXX/LDA). Additionally, the RPA+ [131] was used for the calculation of the energies in [130], but the influence on the lattice constant is believed to be small. The agreement between our data and the lattice constants as calculated by Marini *et al.* is unfortunately rather poor, interestingly already on the DFT-LDA level for NaCl. For Si, the DFT-LDA values are still close, but both the HF+LDA and RPA values deviate by more than 1 %. For NaCl, the disagreement of Marini's and our value is even larger. Starting with an error of 1.2 % in the DFT-LDA lattice constant, the error increases to -3.0 % for the HF-LDA values and finally becomes -1.5 % for the RPA lattice constant. The reason for the HF and the RPA discrepancies might be related to the use of pseudopotentials in Ref. [130]. We found that it is not easy to construct good potentials for the HF calculations and these problems will become especially important if one does not deal with AE but pseudo-wavefunctions. Also for the RPA correlation part, it seems to be important, at least for some materials, to deal with the true wavefunction (see the results for LMAXFOCKAE).

In this subsection we have presented lattice constants and bulk moduli obtained from



(non-selfconsistent) HF calculations and from the evaluation of the RPA correlation energy. The agreement of the HF equilibrium properties with experiment is not too bad in the case of semiconductors and insulators, but lattice constants are vastly overestimated for metals. The RPA gives lattice constants which are drastically improved for metals, and it also yields satisfactory equilibrium distances for semiconductors and insulators.

### 11.5.2 Atomization energies

In the previous subsection, we have concentrated on the RPA equilibrium properties. Now the atomization energies calculated from HF and RPA energies will be considered. The atomization energy describes the energy which is required to split a material into its fragments:

$$\Delta E = - \left( E_{\text{bulk}} - \sum_i E_{\text{atom}_i} \right). \quad (11.4)$$

In contrast to the sign convention which we used in Sec. 11.2 for the cohesive energy, larger atomization energies mean stronger binding and vice versa.

In order to calculate the atomization energy, the energy of the isolated atom has to be evaluated. For the RPA correlation energies this step is involved, because the calculation of the correlation energy scales like  $V^3$  with the volume of the supercell  $V$ , and it is necessary to use supercells with an extension of at least  $8 \times 8 \times 8 \text{ \AA}$ . Due to the large number of plane waves that can easily exceed 10.000 even the DFT prerun with the large number of empty bands (= number of plane waves) can become tedious. For atoms with large atomic radii, like Li and Na, Mg, and Cu and Ag, the volume convergence of both the DFT energy and the RPA correlation energy is especially slow. Additionally, these elements are described by potentials with high energy cutoffs, which are required because electrons from lower shells are included (Li, Na, Mg) or because  $d$ -electrons (Cu, Ag) are present. This further complicates the calculation of the correlation energy. Therefore, the correlation energies for these atoms exhibit relatively large error bars and consequently RPA atomization energies can not be specified with an accuracy better than 50 meV for NaCl and NaF, 40 meV for LiF, and 20 meV for Ag and Cu. In Tab. 11.14 atomization energies calculated using DFT-PBE, DFT-LDA, HF, and ACFDT-RPA are summarized. All atomization energies are given per atom (e.g. for AlP,  $\text{energy/atom} = 1/2 \times \text{energy/unit cell}$ ) and the deviation from experiment (in parenthesis) is given in eV/atom. Fig. 11.12 and Fig. 11.13 visualize these errors for semiconductors and insulators, and for metals, respectively. Negative errors indicate that the method underbinds the material, positive errors indicate overbinding. The HF and RPA atomization energies all have been calculated using PBE wavefunctions. The use of the LDA wavefunctions and eigenenergies for the atomic calculations turned out to be problematic, a point to which we will return later.

DFT-PBE describes the atomization energies well, although it does not reach chemical accuracy ( $\approx 40 \text{ meV}$ ). The error introduced by the PBE approximation can be positive (e.g., C) or negative (e.g., Ag). The largest errors for the considered set of materials are 0.35 eV for C and  $-0.43 \text{ eV}$  for Ag, the average absolute error is 0.15 eV. The errors of the DFT-LDA atomization energies are for all considered systems larger than for DFT-PBE and a too strong tendency towards forming a 3D solid is observed. In average, the atomization energy is by 0.76 eV (17 %) too large.

Table 11.14: Atomization energies (eV/atom). Values in parenthesis are absolute deviations from experiment in eV/atom. DFT-PBE wavefunctions and eigenenergies have been used as input for the HF and RPA-ACFDT calculations. If not otherwise stated the experimental atomization energies are taken from [140]. Errors are normally calculated with respect to the energies reported in [140].

name	PBE		LDA		HF		ACFDT		Exp
C	7.72	(0.35)	9.01	(1.64)	5.19	(-2.18)	7.02	(-0.36)	7.35 [147]; 7.37 7.35 [147]; 7.37
Si <sub>1</sub> C	6.40	(0.06)	7.45	(1.11)	4.36	(-1.98)	6.03	(-0.31)	6.34
Si <sub>1</sub>	4.55	(-0.08)	5.34	(0.71)	2.82	(-1.81)	4.39	(-0.24)	4.68 [147]; 4.63
BP	5.28	(0.24)	6.29	(1.25)	3.23	(-1.82)	4.96	(-0.08)	5.04
AlP (1)	4.09	(-0.07)	4.87	(0.71)	2.53	(-1.63)	4.07	(-0.09)	4.163 [147]
AlP (2)	4.09	(-0.07)	4.87	(0.71)	2.53	(-1.63)	4.06	(-0.10)	4.163 [147]
MgO	4.98	(-0.17)	5.88	(0.73)	3.47	(-1.68)	4.90	(-0.25)	5.15
							4.92	(-0.23)	5.15
LiF (1)	4.33	(-0.07)	4.94	(0.54)	3.25	(-1.15)	4.18	(-0.22)	4.40
							4.22	(-0.18)	4.40
LiF (2)	4.33	(-0.07)	4.94	(0.54)	3.25	(-1.15)	4.20	(-0.20)	4.40
							4.25	(-0.15)	4.40
Na <sub>2</sub> F	3.82	(-0.09)	4.38	(0.48)	2.79	(-1.11)	3.74	(-0.16)	3.90
							3.79	(-0.11)	3.90
Na <sub>2</sub> Cl	3.10	(-0.21)	3.50	(0.19)	2.54	(-0.78)	3.14	(-0.17)	3.31
							3.17	(-0.14)	3.31
Na <sub>1</sub>	1.09	(-0.04)	1.26	(0.13)	0.22	(-0.89)	0.98	(-0.16)	1.13
Na <sub>2</sub>	1.08	(-0.04)	1.26	(0.13)	0.23	(-0.89)	0.98	(-0.16)	1.13
							1.03	(-0.10)	1.13
Al	3.44	(0.05)	4.04	(0.65)	1.33	(-2.06)	3.21	(-0.18)	3.39
Cu	3.48	(-0.13)	4.55	(1.06)	0.03	(-3.46)	3.42	(-0.07)	3.49
Ag (1)	2.52	(-0.43)	3.64	(0.69)	0.52	(-2.43)	2.68	(-0.27)	2.95
Ag (2)	2.52	(-0.43)	3.64	(0.69)	0.52	(-2.43)	2.68	(-0.27)	2.95
Ag <sub>2</sub>	2.58	(-0.43)	3.64	(0.69)	0.52	(-2.43)	2.63	(-0.32)	2.95
							2.65	(-0.30)	2.95

The HF atomization energies are always too small, thus the energy gain due to the crystal formation is always underestimated. The same trend was already observed for molecular atomization energies in section 11.1 (see Tab. 11.3). The reason that HF misses important contributions to the atomization energy can be explained with the simple example of the H<sub>2</sub> molecule. For the isolated H atom, the HF approximation is exact because no correlation effects have to be considered for the description of one single electron. In the case of the H<sub>2</sub> molecule with its two electrons, the HF energy is underestimating the binding energy, since the correlation energy is entirely neglected in the HF case: i.e., inclusion of additional Slater determinants to the single reference HF wavefunction will lower the energy. The HF atomization energy of H<sub>2</sub> is therefore too small. For solids, the error introduced by the HF approximation ranges from -2.18 eV for diamond to -0.78 eV for NaCl. Relative errors for

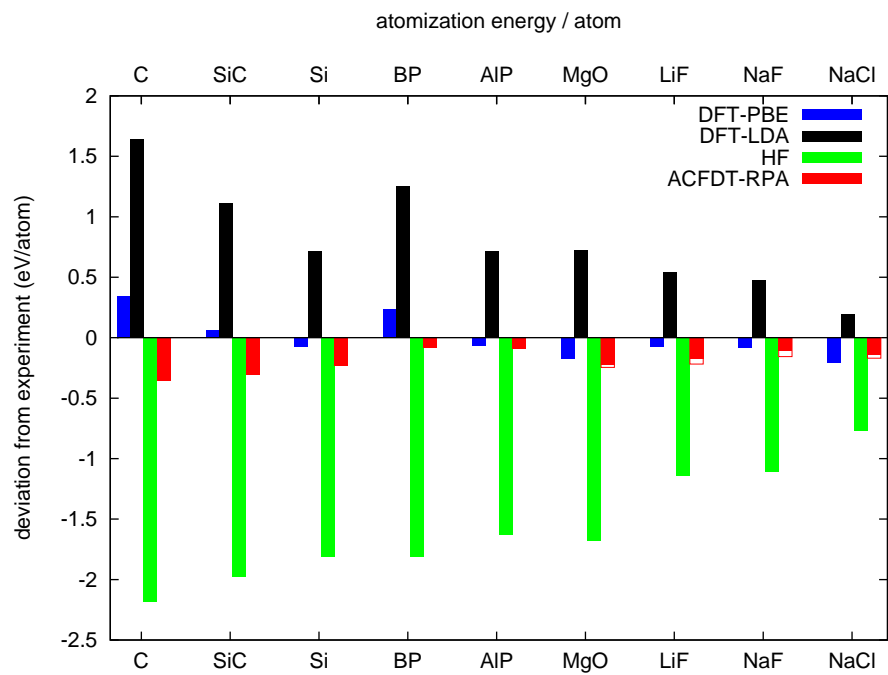


Figure 11.12: Absolute error (eV/atom) of the atomization energy of semiconductors and insulators.

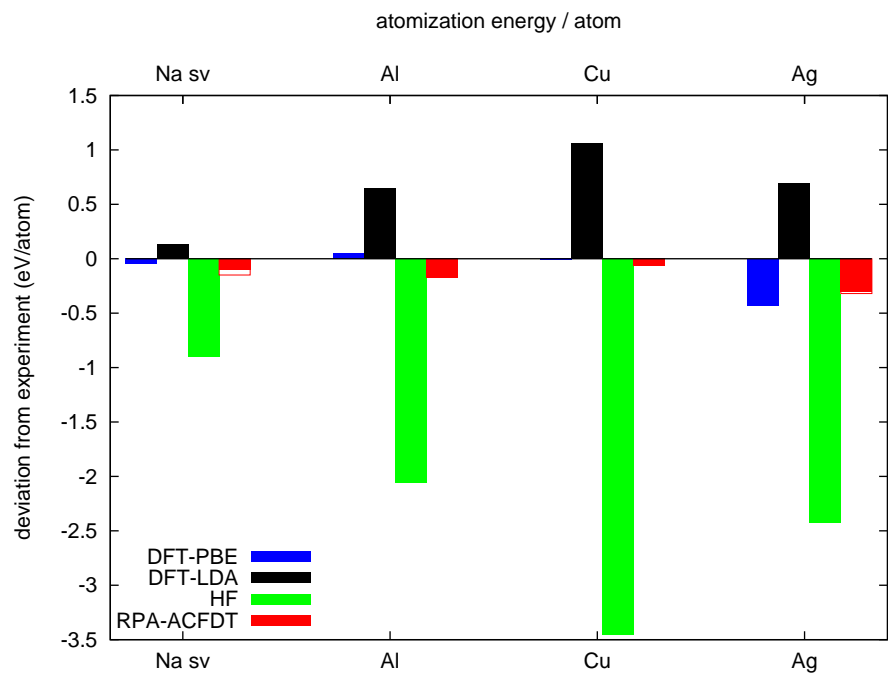


Figure 11.13: Absolute error (eV/atom) of the atomization energy for metals.

semiconductors and insulators lie between 20 and 40 % of the total atomization energy. For the metallic systems errors are considerably larger, going up to  $-3.46$  eV/atom and 99 % of the total atomization energy for the case of Cu. For all metals considered in the present work, the HF error is never smaller than 60 % of the experimental atomization energy, which manifests the importance of correlation contributions to the metallic binding. In Tab. 11.15

Table 11.15: HF atomization energies from the literature compared to the present work. Our HF energies have not been calculated selfconsistently, but stem from the evaluation of the HF energy using DFT wavefunctions.

	HF atomization energies (eV/atom)					
	C	Si	AlP	LiF	NaF	NaCl
present	5.19	2.82	2.53	3.25	2.79	2.54
literature	5.42 <sup>a</sup>	3.06 <sup>a</sup>	2.71 <sup>a</sup>	3.45 <sup>b</sup>	2.97 <sup>b</sup>	2.69 <sup>b</sup>
	5.37 <sup>c</sup>	3.09 <sup>c</sup>				

<sup>a</sup> Ref. [147]

<sup>b</sup> Ref. [151]

<sup>c</sup> Ref. [152]

our HF atomization energies are compared to energies obtained using the CRYSTAL code. No one-to-one comparison is possible, because our atomic and bulk energies do not stem from selfconsistent HF calculations, but from the evaluation of the HF energy using DFT wavefunctions. Nevertheless, the literature values are fairly well reproduced in the present work. Furthermore, the CRYSTAL atomization energies, similar to the CRYSTAL lattice constants, are very sensitive to the Gaussian basis set used (see Ref. [145]). Generally, the literature values are larger than our atomization energies with a typical difference of  $\approx 0.2$  eV. This could be related to basis set superposition errors that always yield too large binding energies for the solid. If atomization energies are calculated from RPA-ACFDT energies, correlation energy contributions are included. As can be seen in Tab. 11.14 visualized in Fig. 11.12 (semiconductors and insulators) and Fig. 11.13 (metals), RPA-ACFDT atomization energies recover the largest part of the experimental atomization energies. The error bars introduced by the slow volume convergence of the Li, Na<sub>2</sub>, and Mg atom are visualized in Fig. 11.12 and Fig. 11.13 by empty areas with red borders. In Tab. 11.14 both maximal and minimal values for the corresponding atomization energies are specified. For all materials considered in this section, the RPA atomization energy is slightly too small and the crystals are therefore too weakly bonded. This relative preference for the atomic state has already been observed for molecular systems in Sec. 11.1 and for the rare gas solids in Sec. 11.2. For the N<sub>2</sub> and the O<sub>2</sub> molecule, the error introduced by the RPA is  $-0.2$  eV and  $-0.3$  eV, respectively. The RPA atomization energies of the bulk systems exhibit similar errors as the molecular ones presented in Sec. 11.1. Nevertheless, for semiconductors and insulators, at least 95 % of the atomization energy are recovered by the RPA. Absolute errors range from  $-0.36$  eV for C to  $-0.08$  eV for BP. The improvement over the HF atomization energies is best visualized in Fig. 11.14, where bars representing the absolute atomization energies obtained from HF and RPA are put on top of each other and are compared to the experimental results. In green the contribution to the atomization energy arising from the HF energy is given. The remaining

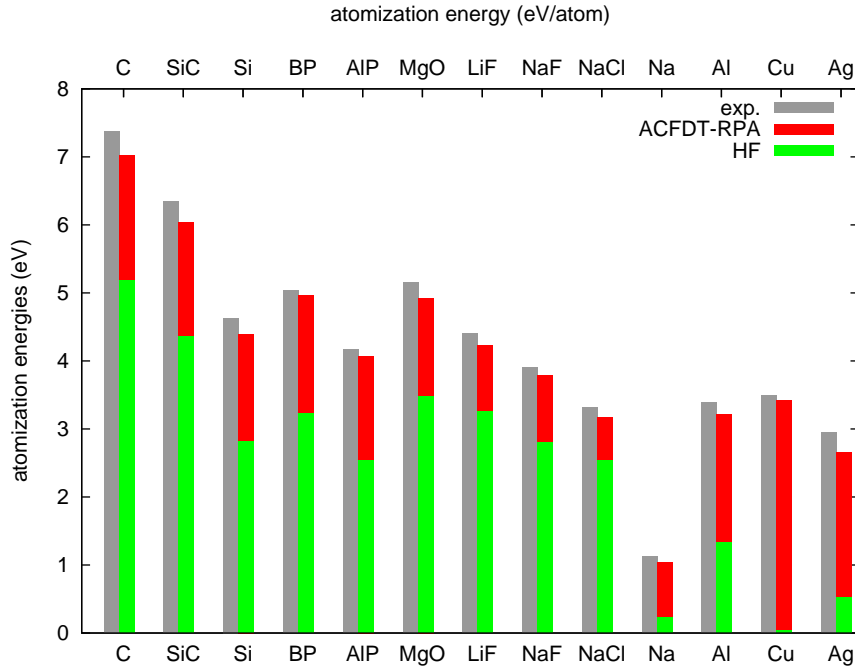


Figure 11.14: Experimental and theoretical atomization energies (eV/atom).

red area displays the part of the atomization energy which is related to the RPA correlation energy.

For two of the considered metals, Na and Ag, the fraction of the atomization energy which is recovered by the RPA is with 90 % slightly smaller than that for the insulators and semiconductors. But for the considered metals, the correlation energy accounts for 80 % of the atomization energy, so that an error in the correlation energy effects the quality of the total energy most. An interesting example is Cu, where HF alone leads to hardly any binding at all. In this case more than 99 % of the atomization energy seem to be due to correlation effects and the RPA describes most of it. Although the RPA leads to a significant improvement over HF atomization energies, chemical accuracy is not reached. The mean absolute error is with 0.16 – 0.18 eV even larger than for DFT-PBE (0.14 eV).

Finally, we like to comment on the difference of RPA atomization energies calculated using DFT-LDA and DFT-PBE wavefunctions and eigenenergies. For the lattice constants and bulk moduli presented in the former subsection, we have shown for C and Si that the actual approximation to the exchange-correlation energy in the initial DFT run hardly effects the geometrical properties. We do not calculate the RPA correlation energy selfconsistently by generating an RPA exchange-correlation potential and updating wavefunctions and eigenenergies. It is therefore reassuring that the result is not that sensitive to the actual input (LDA or PBE wavefunctions and eigenenergies). Naturally, one would also hope that the atomization energies do not change much if either LDA or PBE wavefunctions are used. In Ref. [127], RPA atomization energies have been evaluated for the  $H_2$ ,  $Li_2$ ,  $LiH$ , and the  $N_2$  molecule and very similar results have been found for both LDA and PBE applied for the calculation of the DFT wavefunctions. We have tested the influence of the exchange-correlation potential used

in the KS-DFT calculations on the atomization energies of bulk Si and C, and the O<sub>2</sub> and N<sub>2</sub> molecule. The most significant difference between LDA and GGA (here PBE) eigenenergies of atoms and molecules is the strong tendency of the LDA to yield symmetric atoms, i.e., to distribute electrons equally over  $p_x$ ,  $p_y$ , and  $p_z$  orbitals, thus giving non-integer occupancies for the one-electron orbitals. For elements with subshells that are neither half nor fully filled (like it is the case for B, C, O, F, Al, Si, S, Cl) this results in very small energy gaps between the highest occupied and lowest unoccupied state. For heavier atoms the splitting becomes even smaller and for some cases the eigenenergies are degenerated. For Si, e.g., the LDA leads to a solution where all spin-up 3p states are equally occupied by 2/3 electrons per state. The PBE lifts this degeneracy and the gap between occupied and unoccupied 3p states becomes  $\approx 0.25$  eV. A similar behavior is observed for C (LDA one-electron gap: 0.06 eV, PBE gap: 0.54 eV) and O (LDA one-electron gap: 0.26 eV, PBE gap: 1.14 eV). If the highest occupied and the lowest unoccupied band differ by the spin or the angular quantum number (like it is the case for H, He, Li, Be, N, Ne, ...) both the LDA and PBE one-electron gaps are considerably larger and the relative difference introduced by the use of LDA or PBE is significantly smaller.

How does this difference between LDA and PBE eigenstates effect the HF atomization energy? For the evaluation of the HF expression only the KS-DFT wavefunctions are required, and the HF atomization energy for LDA and PBE wavefunctions should therefore only depend on the difference in the corresponding wavefunctions and not on the different description of the eigenenergies. In fact, we find that the HF energy is additionally very sensitive to the existence or non-existence of partially filled states. For the Si atom, the LDA solution consists of three partially filled 3p spin-up states. Due to the energy degeneracy of these states, the total atomic energy does not change, if 2 of these states are fully occupied and 1 is entirely unoccupied. Although the LDA energy is not changed by this "trick", the consequence on the Si HF energy is significant. For the Si atom with the partially filled states, the HF energy becomes  $-4.91$  eV, whereas for the Si atom with integer occupancies the energy decreases to  $-7.66$  eV (which is comparable to the HF energy for PBE wavefunctions). This highlights the importance of avoiding partial occupancies for atoms if non-selfconsistent HF energies are evaluated. The difference of HF atomization energies determined from LDA or PBE wavefunctions is of the order of 10 meV if all states possess integer occupancies. For the Si and C bulk, the difference between the LDA and PBE HF atomization energy is 20 and 25 meV/atom, respectively, under the assumption that integer occupation number are chosen for the Si atom. For the molecular test systems, O<sub>2</sub> and N<sub>2</sub>, the difference is found to be 10 and 20 meV/molecule, respectively. We thus conclude, that the results are indeed insensitive to the KS potential, as long as integer occupancies are enforced for atoms.

As we have seen, the effect introduced by the different wavefunctions (LDA or PBE) is relatively small. For the evaluation of the RPA correlation energy both KS-DFT eigenenergies and wavefunctions are required, thus the tendency of the LDA to underestimate the energy difference between occupied and unoccupied bands comes into play. For bulk C (diamond) we find that the RPA-PBE atomization energy, which is 7.02 eV, differs by almost 0.3 eV from the RPA-LDA energy of 6.74 eV. The difference stems from the significantly larger absolute value of the correlation energy for the LDA C atom than for the PBE C atom. We ascribe this difference to the small one-electron gap between the highest occupied and the lowest unoccupied 2p spin-up state and to the large relative deviation between LDA and PBE

for this quantity. To test this assumption we calculate the RPA correlation energy from the symmetric LDA and PBE solutions of the C atom. The spin-up  $2p$  states are then partially occupied with  $2/3$  electrons for both LDA and PBE and the next fully unoccupied states are the spin-down  $2p$  states. The symmetrized and symmetry-broken PBE correlation energy ( $-4.73$  eV and  $-5.18$  eV) differ by  $0.45$  eV, but they are much closer than the corresponding HF energies (symmetrized:  $-7.97$  eV, symmetry-broken:  $-12.43$  eV). Using the symmetrized RPA correlation energy (and symmetry-broken HF energy), the diamond atomization energy becomes  $7.45$  eV for both LDA and PBE wavefunctions. Analogous to the case of diamond, a relatively large difference of  $0.4$  eV is found for the  $O_2$  atomization energy calculated from LDA and PBE wavefunctions. The O atom, like the C atom, has a partly filled  $2p$  spin component explaining this difference. For the  $N_2$  molecule the  $2p$  subshell is half-filled and the energy between the highest occupied (spin-up) and lowest unoccupied (spin-down) state is comparable large. The  $N_2$  RPA atomization energies stemming from LDA and PBE input thus only differ by  $10$  meV, which confirms the result by Dahlen *et al.* [127]. All other molecules studied in this reference ( $H_2$ ,  $Li_2$ ,  $LiH$ ) consist of "unproblematic" atoms with a half-filled  $s$  subshell, and the effect of LDA or PBE input is expected to be small.

## Chapter 12

# Conclusions and Summary

This part of my thesis has been dedicated to the calculation of correlation energies on the basis of the adiabatic connection fluctuation-dissipation theorem (ACFDT). The ACFDT has already been introduced in chapter 3. Here we have focused on more technical issues concerning the implementation of the ACFDT routines (chapter 10) and on the results, which have been obtained within the random phase approximation (RPA) (chapter 11).

Having discussed the technical aspects, which are required to obtain converged RPA correlation energies in chapter 10, chapter 11 focuses on the application of the ACFDT formalism. First of all, RPA atomization energies were calculated for a set of molecules –  $\text{H}_2$ ,  $\text{O}_2$ , and  $\text{N}_2$  (Sec. 11.1). These energies have previously been evaluated by Furche [121] using a local basis set code and it was therefore possible to compare to already published data. The agreement of Furche’s and our results is excellent, which proves that using a plane wave basis set we are able to calculate RPA correlation energies even for strongly localized electrons. But, as the computational cost for the determination of RPA correlation energies scales like  $V^3$  if plane waves are applied, calculations utilizing large supercells are computationally demanding. For the considered molecules the RPA predicts better atomization energies than DFT-PBE, but shows a tendency to underbind.

For many molecules considered by Furche [121] DFT-PBE provides a good, and sometimes better description than RPA. But for van der Waals (vdW) bonded systems, like the rare gas solids, DFT possesses a fundamental shortcoming, if the correlation energy is approximated using local or semilocal functionals. Van der Waals (dispersion) forces can be ascribed to the interaction of fluctuating dipoles. The long-range part of this contribution to the correlation energy leads to an attractive interaction for fragments with non-overlapping densities and is therefore not correctly described in a (semi)local description e.g., in the LDA or GGA-PBE. As the RPA correlation energy is based on the non-local response function, the vdW interaction is an integral part of the RPA correlation energy. This makes the rare gas solids Ne, Ar, and Kr, which are the topic of Sec. 11.2, interesting test systems for the performance of the RPA. Indeed, for all three solids we find that the correct long-range vdW  $-1/R^6$  behavior is fulfilled and the prefactors are within 10 % of experiment. The lattice constants and cohesive energies, while not in perfect agreement with experiment, are improved compared to the DFT-LDA and DFT-PBE values. The RPA results for the molecules and the rare gas solids have been published in Ref. [153].

In Sec. 11.3 and Sec. 11.4 we focused on metallic systems. The RPA correlation energy



for the homogenous electron gas has been evaluated in Sec. 11.3 and is in agreement with published data with an error of less than 10 meV. The  $k$ -point convergence of the lattice constants and the energies was tested for metals in Sec. 11.4. By the introduction of the intraband contributions, the convergence of the energy was improved, especially for Na. While the  $k$ -point convergence for Na and Cu was satisfactory, Al exhibits spurious jumps in the energy at specific volumes and for specific  $k$ -point grids, which are related to the existence of bands that cross near the Fermi surface. The influence of these spurious jumps becomes even stronger for the transition metals Rh and Pd. Although the existence of band crossings near the Fermi energy can make the calculation of RPA correlation energies for metals particularly difficult, reasonable convergence could be achieved for all considered metals.

In Sec. 11.5 we applied the RPA formulism to a larger set of materials, ranging from insulators, semiconductors to metals, and from covalent to ionic bonded systems. Published data for RPA lattice constants only exist for Na [128], NaCl [130], and Si [130, 128] and are too sparse and furthermore afflicted by the use of pseudopotentials to reveal trends. We have bridged this gap. In this section, we calculated the RPA lattice constants, the bulk moduli, and the atomization energies. In order to assess the influence of the correlation energy, the respective quantities were also determined for the Hartree-Fock (HF) energy evaluated for DFT wavefunctions. Lattice constants and bulk moduli obtained from the HF energies are reasonable as long as semiconductors and insulators are considered, implying that these systems are well described by a single Slater determinant. For HF, the mean absolute relative error of the lattice constants of semiconductors and insulators is with 0.92 % slightly smaller than for DFT-PBE (0.99 %). For metals, however, geometrical properties based on the HF energies are far from the experimental ones. For Cu and Ag, where the error is largest, the lattice constant is overestimated by more than 10 %, and the error in the bulk modulus is almost 80 %. The mean absolute relative error for the six considered metals amounts to 5.45 % compared to 0.93 % error obtained from DFT-PBE calculations. The RPA, on the other hand, describes the equilibrium volume very well for semiconductors, insulators, and metals. The mean absolute relative error of the lattice constants of all 15 considered systems amounts to 0.27 % and the RPA lattice constants are consequently much closer to experiment than the DFT-PBE (0.97 %) and HF (2.73 %) ones are. For metals, the improvement compared to the HF results is most impressive (RPA mean absolute relative error: 0.36 %) and for Cu and Ag, which have been particularly badly described using HF, the error in the lattice constants is now smaller than 0.5 % and the bulk modulus is within 9 % of experiment. The fact that the RPA provides lattice constants and bulk moduli in good agreement with experiment indicates that the energy dependence on the volume is well reproduced, although it is well known that the absolute RPA correlation energy is almost 30 % too large.

Energetic differences have been tested by calculating the RPA atomization energies for 13 systems (no atomization energies have been evaluated for Rh and Pd). Atomization energies for bulk systems (except for jellium, and jellium surfaces) have not been published before, because RPA calculations for atoms are demanding, if a plane wave basis set is applied. For some atoms, such as Li, Na, and Mg, we have been unable to obtain correlation energies with an accuracy better than 40 meV. Nevertheless, general trends for the RPA atomization energies could be obtained. If correlation effects are totally neglected, and the HF energies are used to calculate the atomization energies, important contributions to the binding are

missing. For insulators and semiconductors, the HF atomization energy in average amounts to  $\approx 70$  % of the experimental atomization energy. For Al, HF contributes 40 % to the experimental atomization energy, while for Na, Cu, and Ag less than 20 % of the total binding energy are recovered. This emphasizes the importance of the correlation for the metallic binding. If the RPA correlation energy is included, in average 96 % and at least 94 % of the total atomization energy is reproduced for insulators and semiconductors. For the metals, where HF has performed so poorly, an agreement of at least 90 % with experiment is obtained. Although RPA is able to reduce the HF error, the mean absolute error in the atomization energy is with 0.19 eV/atom slightly larger than the DFT-PBE one (0.14 eV/atom). This is certainly disappointing, but we believe that the error is predominantly in the energies of the atoms, and that methods for correcting this error can be found.

# Bibliography

- [1] P. Hohenberg, W. Kohn, Phys. Rev. **136**, B 864 (1964).
- [2] M. Levy, Proc. Natl. Acad. Sci. **76**, 6062 (1979).
- [3] W. Kohn, L.J. Sham, Phys. Rev. **140**, A1133 (1965).
- [4] P.W. Ayers, M. Levy, Chem. Phys. Lett. **415**, 211 (2005).
- [5] D. Mazziotti, Phys. Rev. Lett. **93**, 213001 (2004).
- [6] L.H. Thomas, Proc. Cambridge Philos. Soc. **23**, 542 (1927).
- [7] E. Fermi, Z. Phys. **61**, 126 (1930).
- [8] E. Teller, Rev. Mod. Phys. **34**, 627 (1962).
- [9] E.H. Lieb and B. Simon, Phys. Rev. Lett. **31**, 681 (1973).
- [10] D.M. Ceperley and B.J. Alder, Phys. Rev. Lett. **45**, 566 (1980).
- [11] J.P. Perdew, Y. Wang, Phys. Rev. B **45**, 13244 (1992).
- [12] J.P. Perdew, K. Burke, M. Ernzerhof, Phys. Rev. Lett. **77**, 3865 (1996).
- [13] M.C. Payne, M.P. Teter, D.C. Allan, T.A. Arias, J.D. Joannopoulos, Rev. Mod. Phys. **64**, 1045 (1992).
- [14] P.E. Blöchl, Phys. Rev. B **50**, 17953 (1994).
- [15] G. Kresse and D. Joubert, Phys. Rev. B **59**, 1758 (1999).
- [16] H.J. Monkhorst und J.D. Pack, Phys. Rev. B **13**, 5188 (1976).
- [17] E. Runge and E.K.U. Gross, Phys. Rev. Lett. **52**, 997 (1984).
- [18] *Time-Dependent Density Functional Theory*, Eds. M.A.L. Marques, C.A. Ullrich, F. Nogueira, A. Rubio, K. Burke, E.K.U. Gross, (Springer, Berlin 2006).
- [19] D. Pines and P. Nozières, *The theory of quantum liquids* (Benjamin, New York 1966).
- [20] P. Ziesche and G. Lehmann, *Elektronentheorie der Metalle* (Springer, Berlin 1983).

- 
- [21] M. Gajdoš, K. Hummer, G. Kresse, J. Furthmüller, F. Bechstedt, Phys. Rev. B **73**, 045112 (2006).
- [22] S.L. Adler, Phys. Rev. **126**, 413 (1962).
- [23] N. Wiser, Phys. Rev. **129**, 62 (1963).
- [24] A. Rubio, J.A. Alonso, X. Blase, L.C. Balbás, S.G. Louie, Phys. Rev. Lett. **77**, 247 (1996).
- [25] M. Shishkin and G. Kresse, Phys. Rev. B **74**, 035101 (2006).
- [26] N.W. Ashcroft, N.D. Mermin, *Solid State Physics*, (Thomson Learning, London, 1976).
- [27] D.C. Langreth and J.P. Perdew, Solid State Commun. **17**, 1425 (1975).
- [28] O. Gunnarsson and B.I. Lundqvist, Phys. Rev. B **13**, 4274 (1976).
- [29] D.C. Langreth and J.P. Perdew, Phys. Rev. B **15**, 2884 (1977).
- [30] D.L. Freeman, Phys. Rev. B **15**, 5512 (1977).
- [31] L.D. Landau and E.M. Lifshitz, *Statistical Mechanics*, (Addison-Wesley, Reading 1969).
- [32] J.F. Dobson, K. McLennan, A. Rubio, J. Wang, T. Gould, H.M. Le, B.P. Dinte, Aust. J. Chem. **54**, 513 (2001).
- [33] J.F. Dobson, A. White, A. Rubio, Phys. Rev. Lett. **96**, 073201 (2006).
- [34] J.F. Dobson in *Time-dependent Density Functional Theory*, Eds. M.A.L. Marques, C.A. Ullrich, F. Noqueira, A. Rubio, K. Burke, E.K.U. Gross (Springer, Berlin 2006).
- [35] M. Lein, E.K.U. Gross, J.P. Perdew, Phys. Rev. B **61**, 13431 (2000).
- [36] Y.M. Niquet, M. Fuchs, X. Gonze, Phys. Rev. A **68**, 032507 (2003).
- [37] J. Paier, R. Hirschl, M. Marsman, G. Kresse, J. Chem. Phys. **122**, 234102 (2005).
- [38] F. Aryasetiawan and O. Gunnarsson, Rep. Prog. Phys. **61**, 237 (1998).
- [39] G. Onida, L. Reining, A. Rubio, Rev. Mod. Phys. **74**, 601 (2002).
- [40] R.W. Godby, P. García-González in *A Primer in Density Functional Theory* Eds. C. Fiolhais, F. Nogueira, M. Marques, (Springer, Berlin 2003).
- [41] A. Marini, G. Onida, R. Del Sole, Phys. Rev. Lett **88**, 016403 (2002).
- [42] A. Marini, R. Del Sole, G. Onida, Phys. Rev. B **66**, 115101 (2002).
- [43] F. Aryasetiawan, Phys. Rev. B **46**, (1992) 13051.
- [44] T. Miyake, P. Zhang, M.L. Cohen, S.G. Louie, Phys. Rev. B **74**, 245213 (2006).
- [45] S.V. Faleev, M. van Schilfgaarde, T. Kotani, Phys. Rev. Lett. **93**, 126406 (2004).

- [46] M. van Schilfgaarde, T. Kotani, S.V. Faleev, Phys. Rev. Lett. **96**, 226402 (2006).
- [47] M. Shishkin and G. Kresse, Phys. Rev. Lett. **99**, 246403 (2007).
- [48] M. Shishkin and G. Kresse, Phys. Rev. B **75**, 235102 (2007).
- [49] D.E. Aspnes, A.A. Studna, Appl. Opt. **14**, 220 (1975).
- [50] D.E. Aspnes, J.P. Harbison, A.A. Studna, L.T. Florez, J. Vac. Sci. Technol. A, **6**, 1327 (1988).
- [51] D.S. Martin, P. Weightman, Surf. Int. Anal. **31**, 915 (2001).
- [52] Ph. Hofmann, K.C. Rose, V. Fernandez, A.M. Bradshaw, W. Richter, Phys. Rev. Lett. **75**, 2039 (1995).
- [53] K. Stahrenberg, Th. Herrmann, N. Esser, W. Richter, Phys. Rev. B **61**, 3043 (2000).
- [54] L.D. Sun, M. Hohage, P. Zeppenfeld, R.E. Balderas-Navarro, K. Hingerl, Surf. Sci. **527**, L184 (2003).
- [55] L.D. Sun, M. Hohage, P. Zeppenfeld, R.E. Balderas-Navarro, phys. stat. sol. (c) **0**, 3022 (2003).
- [56] L.D. Sun, M. Hohage, P. Zeppenfeld, R.E. Balderas-Navarro, K. Hingerl, Phys. Rev. Lett. **90**, 106104 (2003).
- [57] L.D. Sun, M. Hohage, P. Zeppenfeld, Phys. Rev. B **69**, 045407 (2004).
- [58] L.D. Sun, M. Hohage, P. Zeppenfeld, R.E. Balderas-Navarro, Surf. Sci. **589**, 153 (2005).
- [59] P. Monachesi, M. Palummo, R. Del Sole, R. Ahuja, O. Eriksson, Phys. Rev. B **64**, 115421 (2001).
- [60] P. Monachesi, M. Palummo, R. Del Sole, A. Grechnev, O. Eriksson, Phys. Rev. B **68**, 035426 (2003).
- [61] P. Monachesi and L. Chiodo, Phys. Rev. Lett. **93**, 116102 (2004).
- [62] J.D.E. McIntyre, D.E. Aspnes, Surf. Sci. **24**, 417 (1971).
- [63] O.S. Heavens, *Optical properties of Thin Solid Films*, (Butterworth, London, 1955).
- [64] R.J. Cole, B.G. Fredrick, P. Weightman, J. Vac. Sci. Technol. A **16**, 3088 (1998).
- [65] G. Onida, L. Reining, A. Rubio, Rev. Mod. Phys. **74**, 601 (2002).
- [66] L. Kipp, D.K. Biegelsen, J.E. Northrup, L.-E. Swartz, R.D. Bringans, Phys. Rev. Lett. **76**, 2810 (1996).
- [67] O. Pulci, G. Onida, R. Del Sole, L. Reining, Phys. Rev. Lett. **81**, 5374 (1998).
- [68] M. Palummo, G. Onida, R. Del Sole, B.S. Mendoza, Phys. Rev. B **60**, 2522 (1999).

- 
- [69] R. Del Sole, G. Onida, Phys. Rev. B **60**, 5523 (1999).
- [70] W.G. Schmidt, E.L. Briggs, J. Bernholc, F. Bechstedt, Phys. Rev. B **59**, 2234 (1999).
- [71] M. Marsili, N. Witkowski, O. Pulci, O. Pluchery, P.L. Silvestrelli, R. Del Sole, Y. Borenstein, Phys. Rev. B **77**, 125337 (2008).
- [72] Th. Herrmann, M. Gensch, M.J.G. Lee, A.I. Shkrebtii, N. Esser, W. Richter, Ph. Hofmann, Phys. Rev. B **69**, 165406 (2004).
- [73] M. Mebarki, A. Ziane, S. Bouarab, M.A. Khan, Surf. Sci. **454**, 433 (2000).
- [74] S. Bouarab, M. Mebarki, A. Ziane, M.A. Kahn, Phys. Rev. B **63**, 195409 (2001).
- [75] A. Ziane and S. Bouarab, Phys. Rev. B **67**, 235419 (2003).
- [76] W.G. Schmidt, N. Esser, A.M. Frisch, P. Vogt, J. Bernholc, F. Bechstedt, M. Zorn, Th. Hannappel, S. Visbeck, F. Willig, W. Richter, Phys. Rev. B **61**, R16335 (2000).
- [77] P.H. Hahn, W.G. Schmidt, F. Bechstedt, Phys. Rev. Lett. **88**, 016402 (2002).
- [78] W.G. Schmidt, S. Glutsch, P.H. Hahn, F. Bechstedt, Phys. Rev. B **67**, 085307 (2003).
- [79] W.G. Schmidt, phys. stat. sol. (b) **242**, 2751 (2005).
- [80] M. Rohlfing, S.G. Louie, phys. stat. sol. (a) **175**, 17 (1999).
- [81] M. Rohlfing, M. Palummo, G. Onida, R. Del Sole, Phys. Rev. Lett. **85**, 5440 (2000).
- [82] A. Marini, G. Onida, R. Del Sole, Phys. Rev. B **64**, 195125 (2001).
- [83] D.Y. Smith, B. Segall, Phys. Rev. B **34**, 5191 (1986).
- [84] O. Hunderi, J. Phys. F **6**, 1223 (1976).
- [85] T. Inagaki, L.C. Emerson, E.T. Arakawa, M.W. Williams, Phys. Rev. B **13**, 2305 (1976).
- [86] P.B. Johnson, R.W. Christy, Phys. Rev. B **6**, 4370 (1972).
- [87] E.G. Maksimov, D.Yu. Savrasov, S.Yu. Savrasov, Phys. Usp. **40**, 337 (1997).
- [88] G.R. Parkins, W.E. Lawrence, R.W. Christy, Phys. Rev. B **23**, 6408 (1981).
- [89] K. Stahrenberg, Th. Herrmann, K. Wilmers, N. Esser, W. Richter, M.J.G. Lee, Phys. Rev. B **64**, 115111 (2001).
- [90] R. Courths and S. Hüfner, Phys. Rep. **112**, 53 (1984).
- [91] J. Harl, diploma thesis.
- [92] S. Kevan, Phys. Rev. B **28**, 4822 (1983).
- [93] A. Goldmann, V. Dose, G. Borstel, Phys. Rev. B **32**, 1971 (1985).

- [94] G. Chiarotti (Ed.), Landolt-Börnstein New Series III-24b (Springer, Berlin, 1995).
- [95] R. Courths, S. Hüfner, P. Kemkes, G. Wiesen, Surf. Sci. **376**, 43 (1997).
- [96] S.Y. Liem, G. Kresse, J.H.R. Clarke, Surf. Sci. **415**, 194 (1998).
- [97] J. Harl, G. Kresse, Surf. Sci. **600**, 4633 (2006).
- [98] Ph. Hofmann, K.-M. Schindler, S. Bao, V. Fritzsche, A.M. Bradshaw, D.P. Woodruff, Surf. Sci. **337**, 169 (1995).
- [99] D. Brust, Phys. Rev. B **2**, 818 (1970).
- [100] F. Szmulowicz, B. Segall, Phys. Rev. B **24**, 892 (1981).
- [101] W. Eberhardt, F.J. Himpsel, Phys. Rev. B **21**, 5572 (1980).
- [102] N.V. Smith, Phys. Rev. B **19**, 5019 (1979).
- [103] R. Courths, B. Cord, H. Wern, H. Saalfeld, S. Hüfner, Solid State Commun. **63**, 619 (1987).
- [104] U. Rossow, L. Mantese, and D.E. Aspnes, J. Vac. Sci. Technol. B **14**, 3070 (1996).
- [105] J. Harl, G. Kresse, L.D. Sun, M. Hohage, P. Zeppenfeld, Phys. Rev. B **76**, 035436 (2007).
- [106] V.P. Zhukov, E.V. Chulkov, P.M. Echenique, Phys. Rev. B **68**, 045102 (2003).
- [107] P. Thiry, D. Chandessris, J. Lecante, C. Guillot, R. Pinchaux, Y. Pétroff, Phys. Rev. Lett. **43**, 82 (1979).
- [108] W. Altmann, K. Desinger, V. Dose, A. Goldmann, Solid State Commun. **65**, 1411 (1988).
- [109] A. Marini, R. Del Sole, A. Rubio, G. Onida, Phys. Rev. B **66**, 161104(R) (2002).
- [110] G. Fuster, J.M. Tyler, N.E. Brener, J. Callaway, D. Bagayoko, Phys. Rev. B **42**, 7322 (1990).
- [111] B. Reihl, R.R. Schlittler, Phys. Rev. B **29**, 2267 (1984).
- [112] H. Wern, R. Courths, G. Leschik, S. Hüfner, Z. Phys. B: Condens. Matter **60**, 293 (1985).
- [113] A.M. Turner, A.W. Donoho, and J.L. Erskine, Phys. Rev. B **29**, 2986 (1984).
- [114] E. Kisker, K. Schröder, M. Campagna, W. Gudat, Phys. Rev. Lett. **52**, 2285 (1984).  
E. Kisker, K. Schröder, W. Gudat, M. Campagna, Phys. Rev. B **31**, 329 (1985).
- [115] Y. Sakisaka, T. Rhodin, D. Mueller, Solid State Commun. **53**, 793 (1985).
- [116] A. Santoni, F.J. Himpsel, Phys. Rev. B **43**, 1305 (1991).

- 
- [117] P. Heimann, F.J. Himpsel, D.E. Eastman, Solid State Commun. **39**, 219 (1981).
- [118] W. Eberhardt, E.W. Plummer, Phys. Rev. B **21**, 3245 (1980).
- [119] J.M. Pitarke and A.G. Eguiluz, Phys. Rev. B **57**, 6329 (1998).
- [120] J.F. Dobson and J. Wang, Phys. Rev. Lett. **82**, 2123 (1999).
- [121] F. Furche, Phys. Rev. B **64**, 195120 (2001).
- [122] M. Fuchs and X. Gonze, Phys. Rev. B **65**, 235109 (2002).
- [123] F. Aryasetiawan, T. Miyake, K. Terakura, Phys. Rev. Lett **88**, 166401 (2002), **90**, 189702 (2003).
- [124] N.E. Dahlen, U. von Barth, Phys. Rev. B **69**, 195102 (2004).
- [125] M. Fuchs, Y.M. Niquet, X. Gonze, K. Burke, J. Chem. Phys. **122**, 094116 (2005).
- [126] F. Furche and T. van Voorhis, J. Chem. Phys. **122**, 164106 (2005).
- [127] N.E. Dahlen, R. van Leeuwen, U. von Barth, Phys. Rev. A **73**, 012511 (2006).
- [128] T. Miyake, F. Aryasetiawan, T. Kotani, M. van Schilfgaarde, M. Usuda, and K. Terakura, Phys. Rev. B **66**, 245103 (2002).
- [129] A. Marini, P. García-González, and A. Rubio, Phys. Rev. Lett. **96**, 136404 (2006).
- [130] P. García-González, J.J. Fernández, A. Marini, and A. Rubio, J. Phys. Chem. A **111**, 12458 (2007).
- [131] S. Kurth, J.P. Perdew, Phys. Rev. B **59**, 10461 (1999).
- [132] U. von Barth, L. Hedin, J. Phys. C **5**, 1629 (1972).
- [133] F. Haase and R. Ahlrichs, J. Comput. Chem. **14**, 907 (1993).
- [134] R. Ahlrichs, M. Bär, M. Häser, H. Horn, Ch. Kölmel, Chem. Phys. Lett. **162**, 165 (1989).
- [135] F. Ortmann, F. Bechstedt, W.G. Schmidt, Phys. Rev. B **73**, 205101 (2006).
- [136] K. Rościszewski, B. Paulus, P. Fulde, H. Stoll, Phys. Rev. B **60**, 7905 (1999).
- [137] J.G. Ángyán, I.C. Gerber, A. Savin, J. Toulouse, Phys. Rev. A **72**, 012510 (2005).
- [138] *Landolt-Börnstein, New Series, Group III*, edited by G. Chiarotti (Springer) Volume 24a.
- [139] J. Heyd, G.E. Scuseria, J. Chem. Phys. **121**, 1187 (2004).
- [140] J. Paier, M. Marsman, K. Hummer, G. Kresse, I. C. Gerber, J.G. Ángyán, J. Chem. Phys. **124**, 154709 (2006), J. Chem. Phys. **125**, 249901 (2006).



- 
- [141] J. Paier, M. Marsman, G. Kresse, J. Chem. Phys. **127**, 024103 (2007).
- [142] *Landolt-Börnstein, New Series, Group III*, edited by O. Madelung, U. Rössler and M. Schulz (Springer) Volume 41A1a.
- [143] S. Haussühl, Z. Phys. **159**, 223 (1960).
- [144] V.N. Staroverov, G.E. Scuseria, J. Tao, J.P. Perdew, Phys. Rev. B **69**, 075102 (2004).
- [145] R. Orlando, R. Dovesi, C. Roetti, V.R. Saunders, J. Phys.: Condens. Matter **2**, 7769 (1990).
- [146] M. Prencipe, A. Zupan, R. Dovesi, E. Aprà, V.R. Saunders, Phys. Rev. B **51**, 3391 (1995).
- [147] A. Zupan, M. Causà, Int. J. Quant. Chem. **56**, 337 (1995).
- [148] S. Kalvoda, B. Paulus, P. Fulde, H. Stoll, Phys. Rev. B **55**, 4027 (1997).
- [149] B. Paulus, K. Rościszewski, J. Phys.: Condens. Matter **19**, 346217 (2007).
- [150] M. Marsman, to be published.
- [151] K. Doll, H. Stoll, Phys. Rev. B **56**, 10121 (1997).
- [152] B. Paulus, P. Fulde, H. Stoll, Phys. Rev. B **51**, 10572 (1995).
- [153] J. Harl, G. Kresse, Phys. Rev. B **77**, 045136 (2008).



# List of Publications

- 1 J. Harl, G. Kresse, *Density functional theory studies on stress stabilization of the Cu(110) striped phase*, Surf. Sci. **600**, 4633 (2006).
- 2 J. Harl, G. Kresse, L.D. Sun, M. Hohage, P. Zeppenfeld, *Ab initio reflectance difference spectra of the bare and adsorbate covered Cu(110) surfaces*, Phys. Rev. B **76**, 035436 (2007).  
Selected for the 13th August, 2007 issue of the Virtual Journal of Nanoscale Science and Technology.
- 3 J. Harl, G. Kresse, *Cohesive energy curves for noble gas solids calculated by adiabatic connection fluctuation-dissipation theory*, Phys. Rev. B **77**, 045136 (2008).
- 4 R. Westerström, C.J. Weststrate, A. Resta, A. Mikkelsen, J. Schnadt, J.N. Andersen, E. Lundgren, M. Schmid, N. Seriani, J. Harl, F. Mittendorfer, G. Kresse, *Stressing Pd atoms: Initial oxidation of the Pd(110) surface*, Surf. Sci. **602**, 2440 (2008).



# Acknowledgments

Thanks to Georg Kresse who has offered me the best support I could wish for. My colleges Kerstin, Alessandro, Joachim, Doris, Roman, Nicola, Andreas, Martijn who listened to my problems and helped me to get closer to the solutions (or at least to coffee and chocolate). Thanks especially to Florian Mittendorfer. He read most of my thesis and helped to decrease the number of errors. Finally, I am grateful for all the encouragement from my parents, my brother, and my friends.



# Curriculum vitae

Judith Harl

## Personal information

Date of Birth	September 18, 1979
Place of Birth	Linz, Austria
Nationality	Austria
Parents	Christine Harl, Dipl. Ing. Josef R. Harl
Home address	Adolf-Gstöttnergasse 6/19 A-1200 Wien
Email	judith.harl@univie.ac.at

## Education

2005 - (2008)	Doctoral studies in Physics at the University of Vienna PhD thesis : "The linear response function in density functional theory: Optical spectra and improved description of the electron correlation" Supervisor : Univ. Prof. Dr. Georg Kresse
June 2005	Graduation with distinction, awarding the academic degree <i>Mag. rer. nat.</i>
1998 - 2005	Studies in Physics at the University of Vienna Diploma thesis : "Ab-initio Untersuchung der Cu(110) Streifenphase: Quantum size effects und Spannungsstabilisierung" Supervisor : Univ. Prof. Dr. Georg Kresse